Mechanics and Applications of Titanium Isotope Fractionation in Terrestrial Magmas

Liam Hoare

School of Earth and Environmental Sciences

Cardiff University

Submitted in partial fulfilment of the requirements for the degree of

Doctor of Philosophy

October 2021

"Science is magic that works"

Kurt Vonnegut, Cat's Cradle (1963)

"She ionizes and atomizes

Then turns to sunlight

He realizes and itemizes

Pulls harder than gravity

She ionizes and atomizes

Then turns to sunlight

Fluorescent lightbulbs will make

An absence of dark, but

The light just ain't there still and she said

I'm feeling empty,

The real lights can make you heavy but

Never ever really empty

Fluorescent lights will always equal empty."

Modest Mouse, Ionizes & Atomizes, This Is a Long Drive for Someone with Nothing to Think About, Up Records, 1996

Declaration

This work has not been submitted in substance for any other degree or award at this or any other university or place of learning, nor is being submitted concurrently in candidature for any degree or other award.

Statement 1

This thesis is being submitted in partial fulfilment of the requirements for the degree of PhD.

Statement 2

This thesis is the result of my own independent work/investigation, except where otherwise stated, and the thesis has not been edited by a third party beyond what is permitted by Cardiff University's Policy on the Use of Third Party Editors by Research Degree Students. Other sources are acknowledged by explicit references. The views expressed are my own.

Statement 3

I hereby give consent for my thesis, if accepted, to be available online in the University's Open Access repository and for inter-library loan, and for the title and summary to be made available to outside organisations.

Abstract

This thesis investigates the systematics of mass dependent titanium (Ti) isotope variation in magmatic processes on Earth. Titanium is a relatively abundant minor element that has five stable isotopes and possess a single valence state under terrestrial conditions (Ti^{4+}). The most common Ti-bearing minerals are oxides such as ilmenite, rutile and titanomagnetite. As a refractory lithophile element, Ti is generally considered to be incompatible and fluid-immobile during magmatic processes. All these properties make Ti an attractive prospect to be utilised as a novel isotopic tool to investigate a range of magmatic processes. During fractional crystallisation of a magma, Ti is enriched in the remaining melt until the onset of Fe-Ti oxide crystallisation. The crystallisation of Fe-Ti oxides produces Ti isotope fractionation due to the contrast in co-ordination state of Ti in Fe-Ti oxides relative to silicate melt. Titanium occupies a lower spatial coordination in silicate melts relative to Fe-Ti oxides, which results in lighter isotopes of Ti being preferentially partitioned into Fe-Ti oxides. Consequently, the remaining melt is progressively enriched in heavy isotopes of Ti during fractional crystallisation. This observation enables Ti isotopes to be utilised as a novel tracer of magmatic evolution, particularly Fe-Ti oxide-melt equilibria.

High precision measurements of Ti isotope ratios are performed using a double spike technique, which involves doping the sample solution with a synthetic solution of a known isotope composition to account for instrumental isotope fractionation during analysis via mass spectrometry. The Ti isotope measurements are performed using a multi-collector inductively coupled plasma mass spectrometer (MC-ICP-MS), with Ti isotope compositions of analysed samples reported in the delta notiation relative to a reference standard; $\delta^{49/47}Ti_{OL\text{-}Ti}$ (where OL-Ti is the Origins Lab Ti reference material).

This thesis reports the Ti isotope compositions of igneous rocks and their mineral constituents to better constrain the mechanics of Ti isotope fractionation in magmatic

systems with the aim of developing Ti isotopes as a novel isotopic tool that can be applied to investigating processes occurring in the Earth's mantle and crust.

Chapter 3 presents a comprehensive set of Ti isotope data for a range of well-characterised magmatic differentiation suites from different tectonic settings; a tholeiitic mid oceanic ridge and subduction zone magmas, calc-alkaline subduction zone, and intraplate magma suites. Evolved magmas from intraplate settings display significantly more variation in their Ti isotope compositions relative to magmas from other tectonic settings at similar SiO_2 contents. This is due to high initial TiO_2 concentrations in their parental magmas which enables high degrees of Fe-Ti crystallisation, both ilmenite and titanomagnetite, which produces a greater magnitude of Ti isotope fractionation. In addition, calc-alkaline subduction zone magmas exhibit higher $\delta^{49/47}$Ti values at a given Mg# relative to tholeiitic magmas. Calc-alkaline magma possess higher water contents which enables Fe-Ti oxides to crystallise earlier as the crystallisation of other minerals such as plagioclase is suppressed in the presence of water. Thus calc-alkaline magmas display increased $\delta^{49/47}$Ti at higher Mg# relative to tholeiitic magmas due to the earlier onset of Fe-Ti oxide crystallisation.

Chapter 4 presents Ti isotope fractionation factors for different Fe-Ti oxide minerals, namely titanomagnetite, ilmenite and rutile, which have been derived from crystal-groundmass pairs in lavas from Santorini (calc-alkaline subduction zone) and Heard Island (intraplate), and from rutile-melt experiments. Selected oxides and groundmass/glass were extracted via micro-mill for MC-ICP-MS analysis. The results show that titanomagnetites display the largest mineral/melt Ti isotope fractionation, followed by ilmenite, then rutile. This is consistent with stable isotope theory which dictates that lighter isotopes prefer longer bonds, with Ti-O bond length decreasing from titanomagnetite to ilmenite and rutile. Furthermore, the titanomagnetite-melt fractionation factor also increases as a function of titanomagnetite TiO_2 content, with magnetite from Heard Island (>20 wt% TiO_2) consistently displaying a greater fractionation factor in comparison to Santorini (≤15 wt% TiO_2). This data enables the

calculation of oxide-melt Ti isotope fractionation factors as a function of temperature, and TiO_2 content in the case of titanomagnetite. These fractionation factors are then applied to successfully model melting of the Earth's mantle and to reproduce the $\delta^{49/47}$Ti evolution the magmatic differentiation suites from Chapter 3 using constraints from mineral compositions and modal proportions in lavas from the differentiation suites.

Chapter 5 combines the enhanced quantitative understanding of Ti isotope fractionation in magmatic systems gained from the previous chapter to apply Ti isotopes as a novel tool to probe the geodynamic origin of The Oman ophiolite. Primitive (Mg# >60) lavas and dikes from Oman, filtered from an overall database of >1200 samples, show large variations in concentrations and ratios of redox-sensitive elements. Importantly, the range of variation in these elements and ratios increases both spatially and temporally throughout the ophiolite. Mantle melting models considering varying source redox state indicate that the trace element systematics of the lavas and sheeted dikes can be replicated by melting of a progressively oxidised source. The trace element systematics are complemented by the first Ti isotope study of Oman lavas and dikes, to evaluate the redox state of mantle melts. The earliest phase of Oman magmatism display Ti isotope evolution pathways that require the presence of elevated water contents and are distinct from tholeiitic suites typical of mid oceanic ridge settings. The second phase of magmatism possess Ti isotope signatures that are comparable to hydrous arc magmas from mature subduction zones. Overall, the trace element and Ti isotope systematic of Oman ophiolite magmas suggest the progressive introduction of water in the active melting column under the Oman ophiolite and thus its likely formation in close proximity to a nascent subduction zone.

Authors note and status of publications

Chapter 3 presents a paper published in an international, peer-reviewed journal. Whilst the text, figures and tables are largely the same as those in the published paper, the content has been re-formatted and edited to be suitable for the thesis layout and to avoid repetition. Furthermore, Chapter 4 presents a paper that as of the time of writing this thesis has been submitted to a journal and is currently under review, again the content of this chapter has been re-formatted for consistency.

The status of the papers are as follows (correct as of thesis submission):

Chapter 3 – Hoare, L., Klaver, M., Saji, N.S., Gillies, J., Parkinson, I.J., Lissenberg, C.J. and Millet, M.A., 2020. Melt chemistry and redox conditions control titanium isotope fractionation during magmatic differentiation. *Geochimica et Cosmochimica Acta*, *282*, pp.38-54. https://doi.org/10.1016/j.gca.2020.05.015

Chapter 4 – Hoare, L., Klaver, M., Muir, D.D., Klemme, S., Barling, J., Parkinson, I.J., Lissenberg, C.J. and Millet, M.A., 2021. Empirical and Experimental Constraints on Fe-Ti Oxide-Melt Titanium Isotope Fractionation Factors. *Geochimica et Cosmochimica Acta.* **(In review, submitted 10/08/21)**

Acknowledgements

Embarking on a PhD is often an arduous journey filled with a great many peaks and a lot more troughs, and this is when the world is in a relatively 'normal' state. Given that we are currently in the midst of a global pandemic, this additional caveat is the equivalent of being the straw that broke the camel's back, even though the camel had just previously been struck by a high-speed train. So, with that I would like to say that anyone who is starting or in the middle of PhD during COVID-19, you are an absolute hero, hang in there! I would like to extend this same sentiment to all the staff at the School of Earth and Environmental Sciences at Cardiff University, from admin, to technicians, post-docs, and lecturers. Even when up against a certain institution of higher education and Westminster government, all of whom were keen to increase precarity through pension cuts, increased workloads, and more marketisation of higher education, even prior to the pandemic, you all kept on going, despite the odds, and for that you have my eternal admiration and gratitude.

First and foremost, I would like to thank my dynamic duo of supervisors Marc-Alban Millet and Johan Lissenberg. Marc has provided a limitless amount of encouragement and guidance, which has been instrumental in making me a better scientist. Our scientific discussions were always thought-provoking, and our off-topic ones ranged from insightful to humorous. Marc's patience, openness, and support was also infinite, which created a positive environment in which I never felt discouraged by mistakes or unsuccessful analyses in the lab. Johan has similarly provided ample support, advice, and encouragement. Johan was never afraid to reign me in from a tangential scientific flight of fancy, taught me to think more critically and to listen more carefully to what the rocks were telling me. I also owe a great deal of thanks to Martijn Klaver who has provided me with an immense amount of support and advice on all things isotope geochemistry. Martijn's methodical and meticulous ways in the lab are infectious and as a result my skills and confidence in the lab have grown exponentially. I would also like to thank Ian Parkinson, my co-supervisor and

previously one of my lecturers at the University of Bristol, if you hadn't brought this position to my attention, I wouldn't be writing this. Particularly as this came at a time following a successive string of rejections for other positions which left me feeling despondent about my future academic prospects. Honourable mentions are also extended to Nikitha Saji, Morten Andersen, Katy Chamberlain, Jane Barling, Jon Blundy, Stephan Klemme, and Chris MacLeod for their involvement, input, and discussion during the various stages of this project.

I would like to thank Duncan Muir for assistance and training on the SEM and for orchestrating the Bute Park Bobble, and Tony Oldroyd for sample preparation. During this PhD I also benefitted from the support of the CELTIC team (past and present) in Cardiff, particularly Lindsey Owen who has put in a herculean effort to keep the lab running during the pandemic. Additionally, I owe many thanks to Ian Thomas particularly for his assistance with writing the double spike code in Python, and more generally for help/advice with coding during my PhD.

I also would like to acknowledge support from a NERC GW4+ Doctoral Training Partnership studentship (NE/L002434/1) which provided the funding for this research.

My PhD journey would not have been the same or as enjoyable without the support of the PhD/Post-doc community at Cardiff, from students who had at started at a similar time to me and the grizzled veterans already deep in their studies, all made Cardiff feel like a new home. General chin-wagging and numerous tea/coffee breaks were an essential part of the day, particularly in the company of not-so-secret Tea Club (Bob, Joanna, Kate, Matt P and J. Panton) and regular trips to Cardiff's premier caffeine provider, Brodies, with Aidan, Caps, George, Harry, Martijn, Max, Matt G, J. Panton, Jereon, Will et al. Special mentions go to J. Panton for numerous beers, gigs and culinary adventures; Aidan Starr and Harry Leah for being great housemates, and more importantly friends with whom I shared many an adventure both within and around Cardiff; Max Jansen for many adventures, beers, sharing his ophiolite knowledge and insightful discussions both scientific and otherwise. Also, I couldn't forget the legendary sport of T-ball to which I was introduced at the start of my PhD.

whilst it was outlawed during my PhD, it resurfaced like a phoenix rising from the ashes, albeit in a more clandestine nature towards the end, which certainly helped the writing process become more bearable.

Outside of the department at Cardiff, I'm lucky to have a great network of friends and family to keep me motivated, grounded and, relatively sane; from Abertillery to my days at the University of Bristol and beyond.

And of course, I'd like to thank my partner Erín for putting up with me over the last year or so, you have been there for celebrating the highs and supporting me through the lows. Thanks, you're alright.

Finally, I'd like to thank my Mam and Dad for their endless encouragement and support in all my endeavours, big and small. It goes without saying but I wouldn't be where I am today without you guys.

For Nan, Grandma, and Grandad

Table of Contents

Table of Figures

Chapter 1: Introduction

The field of isotope geochemistry utilises the variations in the isotopic composition of elements to study a range of geologic phenomena ranging from the formation of planets to changes in past climate. The existence of radioactive isotopes was first postulated by Soddy (1913), and shortly confirmed experimentally thereafter by Thomson (1913) who described the first mass spectrographs, the progenitor of the modern mass spectrometer. Despite its infancy, the development of isotope analysis in the early 20th century was marked by the rapid construction of mass spectrometers for routine analysis (Mattauch and Herzog, 1934; Nier, 1940). Isotope geochemistry became a burgeoning field in the mid 20th century, marked by pioneering studies describing the isotopic variation of elements such as hydrogen, oxygen and sulphur (e.g. Bigeleisen and Mayer, 1947; Urey, 1947; Urey, 1948; Bigeleisen, 1965 and references therein). The arrival of modern mass spectrometry was heralded by the arrival of the first automated mass spectrometer built by Wasserburg (1969) which possessed the capacity for digital data storage.

Traditional stable isotope geochemistry involves the application of light elements such as hydrogen (H), carbon (C), nitrogen (N), oxygen (O) and sulphur (S), which are principally measured using gas-source mass spectrometry (see Eiler et al., 2014; and Valley and Cole, 2018 for an overview). The elements that comprise the roster of 'traditional' stable isotopes possess several common characteristics such as: low atomic mass, large relative mass difference between their isotopes, they form highly covalent bonds, multiple valence states (C, N and S), and the abundance of their rare isotopes. These characteristics enabled them to be analysed with the available analytical capability of the mid-20th century. The recent development of multi-collector inductively coupled plasma mass spectrometry (MC-ICP-MS) which affords greater sensitivity and higher precision has enabled geochemists to utilise and measure new so called 'non-traditional' stable isotopes which do not adhere to all of the criteria of the traditional stable isotopes, such as iron (Fe; see reviews by Dauphas

and Rouxel, 2006; and Dauphas et al., 2017), magnesium (Mg; Young and Galy, 2004; Teng, 2017) and, the focus of this body of work, titanium (Ti; Millet and Dauphas, 2014; Millet et al., 2016).

1.1 Stable Isotope Theory

Natural variation in isotope ratios can either be attributed to mass-dependent or mass-independent fractionation. The natural variation observed within *stable* isotope ratios are predominantly influenced by mass-dependent fractionation, where fractionation refers to a change in an isotope ratio because of a physico-chemical or geologic process, such as fractional crystallisation of a magma or terrestrial weathering (for an overview see Teng et al., 2017). Mass-dependent stable isotopic fractionation is a function of the mass difference between isotopes of the same element (Bigeleisen and Mayer, 1947; Urey, 1947; Schauble, 2004), with the degree of fractionation scaling with the mass difference between isotopes. Mass-independent fractionations, which as the name suggests are un-related to the mass difference between isotopes and are often related to processes such as radioactive decay and the distribution and sources of elements during the formation of the solar system (e.g. Clayton et al., 1973; Thiemens, 2006; Trinquier et al., 2009). The foundations of stable isotope theory, particularly the calculations concerning the directions, magnitudes and temperature dependence of equilibrium isotopic fractionation was the result of seminal work by Urey (1947) and Bigeleisen and Mayer (1947).

1.1.1 Mechanics of Mass Dependent Isotope Fractionation

Studies of stable isotopes are predominantly concerned with variations driven by mass-dependent fractionation. The physico-chemical process which drives variations in stable isotopes, mass fractionation, is the process by which isotopes of the same element are preferentially partitioned between two different phases which causes them to inherit different isotope ratios. The magnitude of this partitioning is termed the fractionation factor or $\alpha_{A\text{-}B}$:

Eq. 1-1

$$\alpha_{A-B} = {R^A_{i,j}}\Big/{R^B_{i,j}}$$

Where $R_{i,j}$ represents the isotope ratio of i over j in phase A or B, respectively.

1.1.2 What Factors Control Mass Dependent Isotope Fractionation?

First order controls on mass-dependent fractionation are related to the co-ordination number (number of ligands attached to the central ion) and the vibrational energy of the bonding site (Bigeleisen and Mayer, 1947; Urey, 1947; Schauble, 2004). Second order effects related to physico-chemical factors such as temperature (Bigeleisen and Mayer, 1947; Urey, 1947; Schauble, 2004), redox state (e.g. Sossi et al., 2012; Dauphas et al., 2014; Prytulak et al., 2016; Sossi et al., 2018) and even pressure (Polyakov and Kharlashina, 1994; Horita et al., 2002; Polyakov, 2009; Young et al., 2015) can exert an influence on the magnitude of stable isotopic fractionation.

Most mass dependent isotopic fractionation pertains to equilibrium isotopic fractionation. Equilibrium fractionation is the separation of heavy and light isotopes in chemical equilibrium facilitated by contrasts in the vibrational energy between atoms of different masses (Bigeleisen and Mayer, 1947; Urey, 1947; Schauble, 2004). Equilibrium fractionations result from a reduction in vibrational energy (particularly the zero-point energy) as a heavy isotope is substituted for an isotope of lower mass (Bigeleisen and Mayer, 1947; Urey, 1947; Schauble, 2004). Bond stiffness is an important concept in controlling mass-dependent fractionation, with the stiffest bonds being short and strong (e.g., highly covalent bonds: Bigeleisen and Mayer, 1947; Urey, 1947; Schauble, 2004). Stiff bonds possess high force constants, with the force required to extend bond lengths (in this case, molecular vibrations) being proportional to extension in accordance with Hooke's law (Schauble, 2004). O'Neil (1986) established several rules pertaining to the factors which result in the enrichment of heavy isotopes in substances:

- The degree of isotopic fractionation decreases as temperature increases in proportion to $1/T^2$. Thus, in high temperature settings such as magmatic systems stable isotopic fractionation is predicted to be minimal.
- The degree of stable isotopic fractionation is greatest in light elements and for elements that possess large differences in mass between their respective isotopes.
- Heavy isotopes are concentrated in the substance which possess the stiffest or highest energy bonds (i.e., highest bond force constants). The magnitude of isotopic fractionation is approximately proportional to the contrast in bond stiffness between substances. Short, strong bonds possess the highest bond stiffness. Bond stiffness is related to:
  a. Oxidation state, with a higher oxidation state resulting in a greater fractionation factor which can be observed in isotopes of elements such as iron and vanadium (e.g. Sossi et al., 2012; Dauphas et al., 2014; Prytulak et al., 2016; Sossi et al., 2018).
  b. Highly covalent bonds present between atoms of similar electronegativities
  c. Low co-ordination number

Therefore, to summarise, heavy isotopes prefer to occupy substances with a low co-ordination number which consequently possess high bond stiffness (and thus higher zero-point energy; Bigeleisen and Mayer, 1947; Urey, 1947; Schauble, 2004), with the magnitude of isotopic fractionation being greatest at lower temperature (Bigeleisen and Mayer, 1947; Urey, 1947; Schauble, 2004).

Stable isotopic fractionation can also occur via kinetic fractionations, which are one-directional, non-equilibrium processes, which result in incomplete isotopic exchange between substances e.g., evaporation of liquid H_2O in a vacuum (Young et al., 2002; Schauble, 2004). In kinetic isotopic fractionation, isotopic exchange can be restricted by the presence of energy barriers – the activation energy – which must be satisfied for isotopic exchange to occur (Young et al., 2002). For non-traditional stable

isotopes such as titanium, the major driving forces behind kinetic isotopic fractionation relate to the effects of diffusion, activation energy and atomic velocities, and how they scale with isotopic mass (Young et al., 2002; Schauble, 2004). Extensive experimental studies have demonstrated that lighter isotopes have higher diffusivities (i.e., diffuse faster) than heavier isotopes (e.g. Mg; Richter et al., 2003; Richter et al., 2008). A major geological example of kinetic isotopic fractionation is diffusive exchange between crystals and melt in a magma chamber (e.g. Oeser et al., 2015; Oeser et al., 2018) via which isotopic fractionation occurs due to a chemical gradient between crystal and melt, along which lighter isotopes diffuse in/out of the crystal faster than heavy ones (e.g. Richter et al., 2003). This has been observed with Fe and Mg isotopes in olivine crystals, as Mg diffuses out and Fe diffuses in, producing isotopic zoning and a negative correlation between Mg and Fe isotopes within the crystal (Oeser et al., 2015; Oeser et al., 2018). Experimental work has also shown thermal (Soret) diffusion can produce significant stable isotopic fractionation due to the presence of thermal gradients, with significant enrichments in heavier isotopes at the colder end of the piston cylinder apparatus (Richter et al., 2003; Richter et al., 2008).

1.1.3 Mass Independent Isotope Fractionation

Mass independent fractionation does not scale relative to isotopic mass and thus produces deviations from mass dependent fractionations as there is no systematic separation of light and heavy isotopes according to their mass (see Thiemens, 2006 for a detailed review). Mass independent fractionations are related to processes such as radioactive decay, nucleosynthesis and the degree of mixing of isotopic sources in the solar protoplanetary disk (e.g. Thiemens, 1999; Leya et al., 2008; Young et al., 2008; Trinquier et al., 2009; Larsen et al., 2011; Burkhardt et al., 2014)

Clayton (1973) first recognised mass independent effects within the oxygen isotopic composition of calcium-aluminium inclusions within the carbonaceous chondrite, Allende, and later other meteorites (Clayton et al., 1976). The origin of these

mass-independent effects continues to be a matter of contentious debate (see Thiemens, 2006 for a detailed review).

Mass independent effects relating to nucleosynthetic anomalies have been observed in the bulk ^{46}Ti and ^{50}Ti isotopic composition of meteorites which could provide insights into the evolution of the solar proto-planetary disk (e.g. Leya et al., 2008; Trinquier et al., 2009). ^{46}Ti and ^{50}Ti have distinct nucleosynthetic origins, neutron rich ^{50}Ti is thought to produced be type 1A supernovae, whereas ^{46}Ti originates from type 2 supernovae (Woosley and Weaver, 1995). However, Trinquier et al. (2009) observed correlated anomalies in ^{46}Ti and ^{50}Ti despite their different stellar sources within Orguiel Cl chondrite. This isotopic heterogeneity was interpreted as the result of varying degrees of thermal processing of molecular cloud material that was initially sourced from an isotopically homogeneous or well-mixed protoplanetary disk (Trinquier et al., 2009).

1.1.4 Reference Geo-Standards and Delta Notation

Stable isotope data is commonly reported in what is referred to as delta (δ) notation. The δ value expresses the deviation of the isotopic ratio of a sample from the ratio of a well-known reference standard in units of per mil (‰). Mass dependent variation in titanium isotopes, is reported as $\delta^{49/47}Ti_{OL\text{-}Ti}$ (Eq. 1-2), the δ value is expressed as the deviation of the ^{49}Ti/^{47}Ti ratio of a sample relative to the Origins Laboratory Ti standard (OL-Ti) developed by Millet and Dauphas (2014) as:

Eq. 1-2

$$\delta^{49/47}Ti_{OL-Ti}\ (‰) = \left[\frac{\left({}^{49}Ti/{}_{47}Ti\right) Sample}{\left({}^{49}Ti/{}_{47}Ti\right)\ OL-Ti} - 1\right] * 10^3$$

(where the ^{49}Ti/^{47}Ti of OL-Ti = 0.7497666). Prior to the development of OL-Ti by Millet and Dauphas (2014), NIST SRM3162, a pure Ti solution had been used as a reference standard (Zhang et al., 2011). However, NIST SRM3162 exhibits significant

fractionation in comparison to terrestrial igneous standards BCR-2 and BIR-1 and thus is not an appropriate reference standard for investigations of stable titanium isotopes in magmatic systems (Millet and Dauphas, 2014).

The Origins Laboratory titanium standard (OL-Ti) was obtained from a pure-Ti metal rod and has been shown to exhibit a Ti stable isotopic composition much closer to that of terrestrial igneous rocks, OL-Ti also exhibits a homogeneous δ^{49}Ti composition across the length of the metal rod from which it was sourced (Millet and Dauphas, 2014). The bar of pure Ti used to create OL-Ti has now been transferred to SARM (Nancy, France), where it can be requested for use. Therefore OL-Ti complies with the criteria for reference standards recommended by Teng et al. (2017) which are as follows:

- The isotope composition should be demonstrably homogeneous within current analytical precision
- The reference material should be a pure element or chemical compound that is easily dissolved in diluted acids
- The reference material should have an isotope composition that is geologically relevant, i.e., its isotope composition is within the range of natural variability and is ideally comparable to a major geologic reservoir
- The reference material should be measured at high precision for all its isotopes to identify any potential anomalies
- The choice of the reference material and its associated notation should be a community driven effort and its application must be consistent
- Reference materials should be widely accessible and held by organisations that have no conflict of interest

1.2 Elemental and Isotopic Characteristics of Titanium

1.2.1 The Geo-chemical Characteristics of Titanium

Titanium is a transition metal that possesses an atomic number of 22 and an atomic mass of 47.867, which possess 5 stable isotopes: ^{46}Ti: 8.01%; ^{47}Ti: 7.33%; ^{48}Ti:

73.81%; ^{49}Ti: 5.50%; ^{50}Ti: 5.35% (Berglund and Wieser, 2011). Titanium is a refractory lithophile element (McDonough and Sun, 1995; Palme and O'Neill, 2014) that is considered fluid immobile during most geologic processes (Cann, 1970; Pearce and Norry, 1979; Van Baalen, 1993) and exhibits moderately incompatible behaviour in Earth's mantle (McDonough et al., 1992; Prytulak and Elliott, 2007). Under terrestrial conditions Ti exists primarily as Ti^{4+}, but has the potential to exist as Ti^{3+} under more reducing conditions such as the lunar mantle (Papike et al., 2005; Papike et al., 2016; Simon and Sutton, 2017; Simon and Sutton, 2018). In magmatic systems Ti can exist in several coordination states; it primarily occupies a V-fold coordination in silicate melts but can also occupy IV and VI coordination in silicic and mafic melts respectively (Farges et al., 1996b; Farges and Brown, 1997; Mysen and Richet, 2018; Ackerson et al., 2020). Additionally, V-fold coordinated Ti in silicate melts transitions to VI-fold coordination during the crystallisation of Ti-bearing oxide minerals such as ilmenite, rutile and titanomagnetite (Farges and Brown, 1997). Thus in accordance with stable isotope theory (Schauble, 2004), the mass dependent fractionation of Ti stable isotopes should be driven by contrasts in the coordination environment between silicates melts and Ti-bearing oxides. Hence Ti isotopes have the potential to trace oxide-melt equilibria during magmatic processes.

1.2.2 Titanium Isotope Composition of the Terrestrial Mantle

Millet and Dauphas (2014) produced the first analyses of the Ti isotope composition of terrestrial samples which included five well characterised basaltic rock standards and eight subduction zone basalts (Fig. 1.1). Millet and Dauphas (2014) observed no resolvable variations between terrestrial basalts and the Ol-Ti reference standard, with a mean of $\delta^{49/47}$Ti = +0.004 ± 0.062‰ which they interpreted as a robust proxy for the composition of the upper mantle. Millet et al. (2016) expanded that data set by measuring a larger and more diverse array of terrestrial samples including mid-ocean ridge, island arc, and intraplate basalts, alongside mantle-derived rocks and

eclogites (Fig. 1.1). Using this expanded sample set, Millet et al. (2016) derived a $\delta^{49/47}$Ti composition for the bulk silicate earth (BSE) of +0.005 ± 0.005‰ (Fig. 1.1).

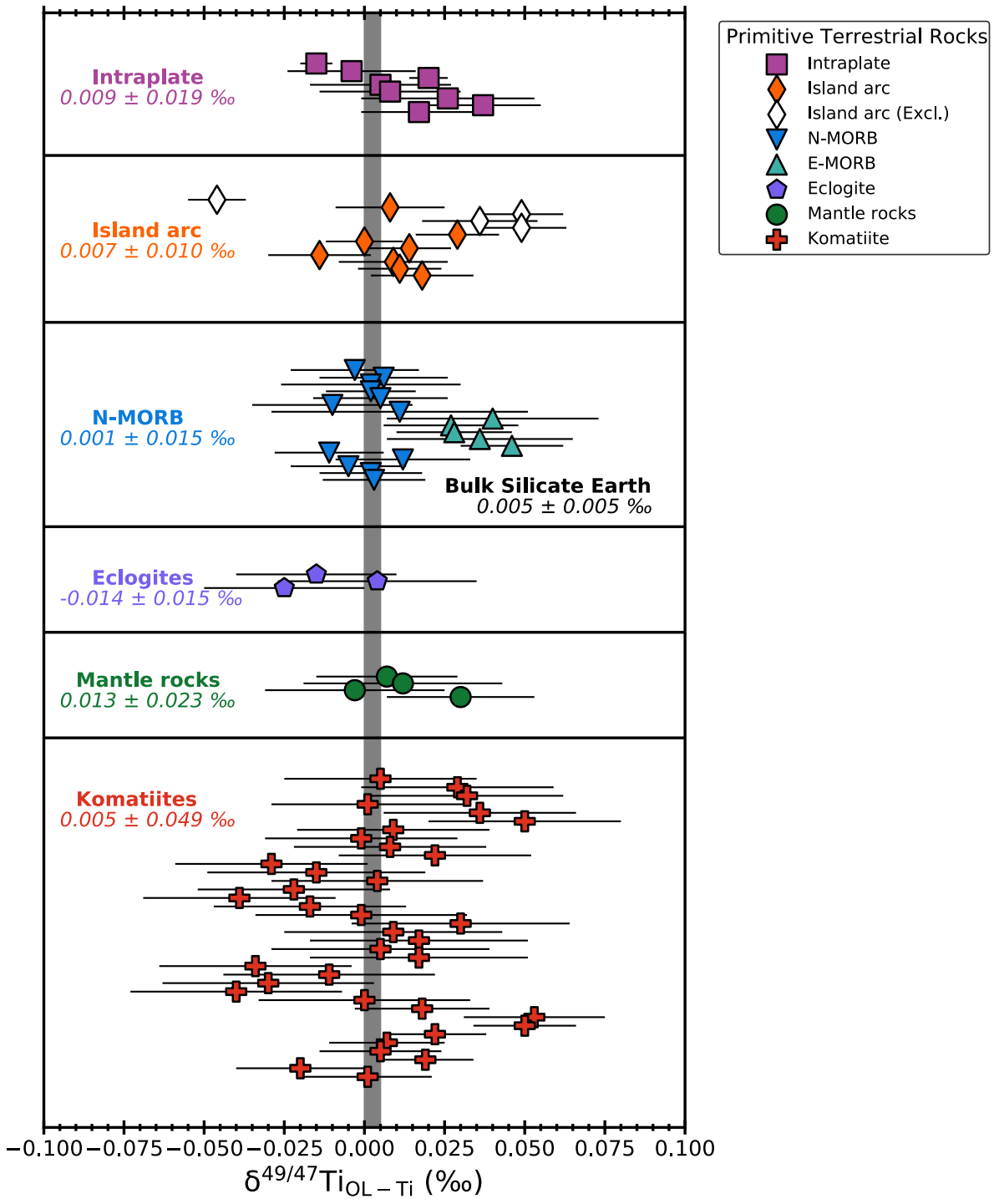

Fig. 1.1 $\delta^{49/47}$Ti compositions of primitive terrestrial rocks (Millet and Dauphas, 2014; Millet et al., 2016; Greber et al., 2017b; Deng et al., 2018). Island arc samples with open symbols have experienced fractionation or accumulation of Ti oxides and were excluded from the mean value. The $\delta^{49/47}$Ti composition of the BSE is indicated by the shaded grey bar (+0.005 ± 0.005‰). The plot shows the bulk of primitive terrestrial igneous rocks are within error of the BSE despite differing geologic settings and petrogenetic histories.

As Ti behaves as a moderately incompatible element during the melting of both spinel and garnet-bearing peridotite (Prytulak and Elliott, 2007) and is efficiently extracted during basalt petrogenesis, this suggests basalts should record the Ti isotopic composition of their mantle source (Millet and Dauphas, 2014; Millet et al., 2016). The Ti isotopic composition of the bulk primitive terrestrial basalts from a variety of geodynamic settings in Fig. 1.1 demonstrates that Earth's upper mantle possess a homogeneous Ti isotope composition which is indistinguishable from the composition of mantle-derived samples, which suggests mantle melting induces no fractionation of Ti isotopes (Millet and Dauphas, 2014; Millet et al., 2016). This is further evidenced by the observation that the vast majority of komatiites, the product of high degrees of melting (e.g. Walter, 1998), are within error of the BSE (Fig. 1.1; Greber et al., 2017). However, Deng et al. (2018) observed a subtle offset in the $\delta^{49/47}$Ti composition of enriched (E) mid-ocean basalts relative to normal (N) mid-ocean ridge basalts (Fig. 1.1). Deng et al. (2018) attributed this variation to the recycling of isotopically light residues, formed during continental crust formation in the Archean, into the mantle source of N-MORB and late-Archean komatiites. However, this interpretation remains controversial and requires further analysis of a global data set of well-characterised mid-ocean basalts coupled with radiogenic isotope systematics (e.g., Pb-Pb, Sm-Nd, Rb-Sr) to be fully validated.

Whilst the mobility of Ti in subduction zone fluids is highly debated (e.g. Kessel et al., 2005), the indistinguishable Ti isotope compositions of N-MORB and island arc basalts suggests that dehydration of subduction zone fluids exerts no influence on the Ti isotope budget of basalts (Millet et al., 2016). In addition, eclogites and subduction-zone related serpentinites exhibit similar Ti isotope compositions to MORB (Fig. 1.1), despite having experienced substantial dehydration. This further supports the notion that Ti is largely immobile in subduction zones and that the recycling of oceanic lithosphere does not produce resolvable Ti isotope fractionation (Millet et al., 2016).

1.2.3 Titanium Isotopes as Tracers of Magmatic Differentiation

In addition to providing constraints on the Ti isotope composition of the terrestrial mantle, Millet et al. (2016) demonstrated the efficacy of Ti isotopes as tracers of Fe-Ti oxide-melt equilibria during magmatic differentiation. Millet et al. (2016) observed that evolved magmatic rocks from the Agung volcano (Sunda arc, Indonesia) exhibited a pronounced enrichment in heavy Ti isotopes in comparison to their more mafic counterparts (Fig. 1.2). The increase in $\delta^{49/47}$Ti is positively correlated with indices of magmatic differentiation such as increasing SiO_2 content (Fig. 1.2). The moderately to highly incompatible behaviour of Ti coupled with its relatively low concentrations in major silicate minerals (e.g. pyroxenes, olivine, and plagioclase; McDonough et al., 1992), suggest the crystallisation of silicate minerals is unlikely to induce any significant Ti isotope fractionation during magmatic differentiation. Therefore, the Ti isotope budget of evolved melts is likely to be controlled by the onset of Fe-Ti oxide crystallisation (Millet et al., 2016). The fractionation of Ti isotopes during magmatic differentiation is driven by a contrast in co-ordination number between silicate melt and Fe-Ti oxides, with Ti predominantly occupying a V-fold co-ordination, in silicate melts compared to VI-fold co-ordination in Fe-Ti oxides (e.g. Farges et al., 1996). As heavier isotopes prefer to occupy low co-ordination number sites, and thus stronger and stiffer bonds (Schauble, 2004), light Ti isotopes are preferentially sequestered into Fe-Ti oxides and thus as a consequence the remaining melt will be enriched in heavy Ti isotopes during fractional crystallisation (Fig. 1.2; Millet et al., 2016).

Furthermore, Deng et al. (2019) observed that at a given SiO_2 content, lavas from TiO_2 rich intraplate magmas display significantly greater variation in $\delta^{49/47}$Ti relative to the Agung differentiation suite from Millet et al. (2016; Fig. 1.2). Deng et al. (2019) postulated that this contrast is the result of delayed onset of Fe-Ti oxide crystallisation in intraplate magmas relative to arc magmas due to lower oxygen fugacities (fO_2) in intraplate mantle sources. Fractional crystallisation of olivine and plagioclase under reduced conditions produces substantial enrichments in TiO_2 in mafic to intermediate

intraplate lavas compared to arc lavas, which Deng et al. (2019) argued results in a greater magnitude of Ti isotope fractionation with respect to SiO_2 contents at the onset of Fe-Ti oxide crystallisation.

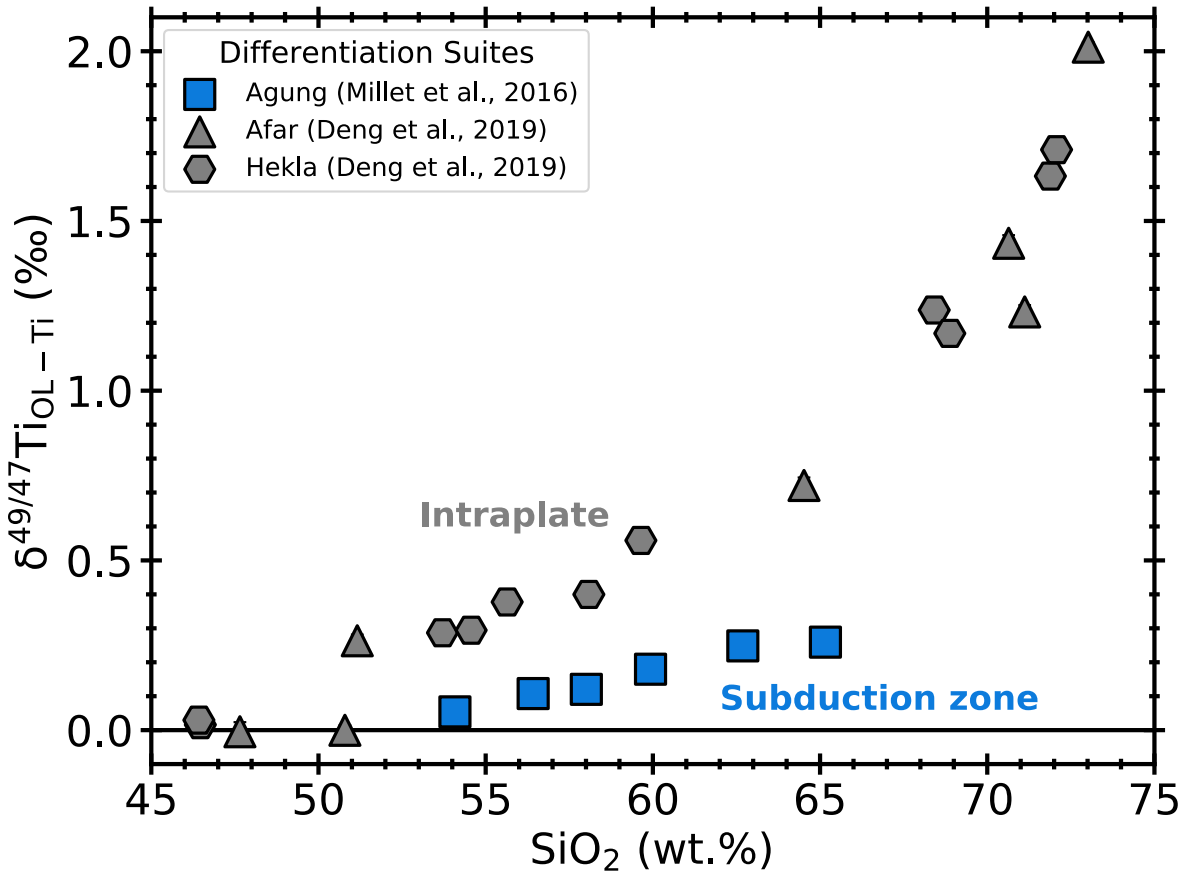

Fig. 1.2 Variations in $\delta^{49/47}$Ti relative to SiO_2 contents for the Agung differentiation suite from the Sunda arc, Indonesia (Millet et al., 2016), compared to intraplate differentiation suites from Hekla (Iceland) and the Afar rift (East Africa) from Deng et al. (2019). Samples display co-variation between $\delta^{49/47}$Ti and SiO_2 due to Fe-Ti oxide crystallisation during magmatic differentiation.

1.2.4 Titanium Isotopes as Recorders of Continental Crust Formation

Greber et al. (2017a) conducted a study of the Ti isotope composition of shales of various ages to elucidate the chemical composition of continental crust exposed to weathering, particularly its SiO_2 content to estimate the relative proportion of mafic and felsic rocks in the continental crust through time. The Ti isotopic composition of shales is unlikely to be affected by numerous processes in terrestrial surface environments that effect the composition of sedimentary rocks such as weathering and diagenesis as Ti is highly insoluble (Orians et al., 1990). Titanium is biologically

inert (Orians et al., 1990), thus is also immune to the implications of large-scale biogeochemical changes that transpired at the Archean-Proterozoic boundary. During mechanical sorting in riverine and oceanic transport, Ti is preferentially incorporated into clay and silt fractions (Taboada et al., 2006), which removes any potential grain size bias. Therefore, the Ti stable isotopic composition of shales will likely reflect that of their source rocks prior to erosion and weathering.

Previous studies have postulated that the continental crust was predominantly mafic in composition during the Archean, only transitioning to a more felsic composition towards 3 – 2 Ga (e.g. Tang et al., 2016), concurrent with the onset of subduction-driven plate tectonics after 3.0 Ga (Dhuime et al., 2015; Tang et al., 2016). Shales exhibit a substantial amount of variability in their δ^{49}Ti composition ranging from -0.018 to +0.791‰, but are predominantly heavier in comparison to mafic rocks (Greber et al., 2017a). On the basis of coupled $\delta^{49/47}$Ti and Ni/Co systematics, Greber et al. (2017a) argued the $\delta^{49/47}$Ti compositions of shales of all ages could only be explained if the crust was comprised of predominantly felsic material since approximately 3.5 Ga, and hence argued subduction related magmatism was already in operation much earlier in the Archean than previously estimated.

1.2.5 Titanium Isotope Compositions of Lunar and Planetary Materials

The analysis of the Ti stable isotopic composition of lunar rocks has significant potential to provide further insight into the magmatic evolution of the Moon and address unresolved questions regarding the crystallisation of the Lunar Magma Ocean (LMO). Millet et al. (2016) conducted the first survey of the stable Ti isotopic composition of the Moon, analysing nine lunar samples: three low-Ti basalts, a single green glass sample, and five high-Ti basalts. Low-Ti basalts and the green glass exhibit a Ti stable isotopic composition ranging from δ^{49}Ti = -0.008 to +0.011‰ like that of the Earth's mantle (Millet et al., 2016). Furthermore, Millet et al. (2016) argued that low-Ti basalts also serve as the best estimate of the Ti isotope composition of the lunar mantle (δ^{49}Ti = -0.003 ± 0.014‰, n=4). Consequently, the similarity observed in the δ^{49}Ti

composition of low-Ti lunar basalts and terrestrial basalts (Millet et al., 2016), provides further evidence to support models postulating the involvement of an compositionally Earth-like impactor in the giant Moon-forming impact event (e.g. Dauphas et al., 2014a; Mastrobuono-Battisti et al., 2015). In contrast to low-Ti lunar basalts, Millet et al. (2016) observed that high-Ti lunar basalts extend to lighter Ti isotope compositions ($\delta^{49/47}$Ti = -0.022 to +0.033‰), which may have arisen due to Ti isotope fractionation induced by the precipitation of ilmenite during the generation of the mantle source of high-Ti basalts during the late-stage crystallisation of the lunar magma ocean (e.g. Snyder et al., 1992). In addition, Greber et al. (2017b) measured a KREEPy (Potassium, Rare-Earth Element and Phosphorous) impact melt breccia (SaU 169), which exhibited a $\delta^{49/47}$Ti value of +0.330 ± 0.034‰, which correlates with KREEP's represent origins as residual melt left over from the ilmenite crystallisation stage of the lunar magma ocean (e.g. Warren and Wasson, 1979).

Greber et al. (2017b) conducted the first substantial survey of the mass dependent Ti isotope composition of various meteoritic and planetary materials. Ordinary, enstatite and, carbonaceous chondrites, yield and average $\delta^{49/47}$Ti composition of +0.004 ± 0.010‰ (Greber et al., 2017b), indistinguishable from the estimate for the BSE and the lunar mantle estimated by Millet et al. (2016), thus implying the Earth and Moon possess a chondritic Ti isotope composition. Similarly, the average $\delta^{49/47}$Ti of basaltic meteorites from the Howardite-Eucrite-Diogenite parent body (probably 4 Vesta; +0.011 ± 0.021‰), the Angrite parent body (+0.007 ± 0.038‰), and Mars (+0.021 ± 0.03‰) are within uncertainty of the chondritic value (Greber et al., 2017b). However, Greber et al. (2017b) did observe variability in the $\delta^{49/47}$Ti composition of aubrite meteorites and attributed this to isotope fractionation driven by the co-existence of Ti^{3+} and Ti^{4+} in aubrite melts due to the extremely reducing conditions under which the aubrite parent body differentiated (e.g. Keil, 2010)

1.2.6 Mass Independent Variations in Titanium Isotopes

Prior to recent investigations of the mass dependent isotope variation in Ti, the major focus of Ti isotope geochemistry concerned studies of isotope abundance anomalies i.e., mass independent effects observed within meteorites related to nucleosynthetic or cosmogenic processes occurring before or during the formation of the solar system (e.g. Niederer et al., 1980; Niemeyer and Lugmair, 1984; Papanastassiou and Brigham, 1989; Leya et al., 2008; Trinquier et al., 2009). Leya et al. (2008) observed that carbonaceous chondrites exhibit enrichments in $^{50}Ti/^{47}Ti$ and $^{46}Ti/^{47}Ti$, and slight depletion in $^{48}Ti/^{47}Ti$ relative to the Earth, Moon, Mars, HED's and ordinary chondrites. It was also observed that these Ti isotopic anomalies were not just confined to special phases in refractory calcium aluminium inclusions (CAI's), but were distributed within a range of phases present in carbonaceous chondrites not just CAI's (Leya et al., 2008). As galactic cosmic-ray exposure close to the early sun cannot produce enrichments in $^{50}Ti/^{47}Ti$, the isotopic anomalies must be related to nucleosynthetic processes, which resulted in carbonaceous chondrites receiving distinct mixture of pre-solar material compared to the Earth, which in conjunction with their characteristic depletion in volatile elements is consistent with an accretionary origin in the outer solar system, further away from the terrestrial planet forming region (Leya et al., 2008).

However, Trinquier et al. (2009) observed correlated isotopic anomalies in Orgueil Cl chondrite between ^{46}Ti and ^{50}Ti, despite these isotopes originating from different stellar sources (e.g. Woosley and Weaver, 1995). The presence of a correlated anomaly in ^{46}Ti and ^{50}Ti suggests that pre-solar material was initially well-mixed in the protoplanetary disk and subsequent thermal processing related to volatile element depletion in the inner solar system has imparted isotopic heterogeneity at the planetary scale (Trinquier et al., 2009). Moreover, Davis et al. (2018) observed the same linear correlation between ^{46}Ti and ^{50}Ti in 46 CAI's from the Allende CV chondrite. Davis et al. (2018) also measured mass dependent $\delta^{49/47}Ti$ variations and observed that most CAI's exhibit no variation within a 95% confidence interval. However, a select

few CAI's exhibited significant fractionation with $\delta^{49/47}$Ti ranging from ~-4 to ~+4. Coincidently, the CAI's that possess the highest ^{50}Ti anomalies exhibit more dispersion in their $\delta^{49/47}$Ti compositions which further suggests that thermal processing plays an important role in imparting Ti isotopic anomalies to CAI's and bulk meteorites (Davis et al., 2018).

1.3 Thesis outline

Magmas erupted at the surface of our planet offer a wide range of opportunities to investigate chemical heterogeneity of the Earth, from the dynamics of the terrestrial mantle to the evolution of Earth's crust. In the past classical geochemical tools often provide incomplete or ambiguous answers to an array of questions such as: what minerals are involved in the evolution of magma? How much water is present in different mantle sources and the magmas that originate from them? Can the chemical composition of magmas tell us about the tectonic setting of ancient volcanism?

As demonstrated in this section Ti isotopes show great promise as a novel isotopic tool to trace magmatic processes (Millet et al., 2016; Greber et al., 2017b; Deng et al., 2019). The aim of this thesis is three-fold and are explored in detail in Chapters 3, 4 and 5:

- Chapter 3 - To build upon the foundations laid by previous studies (Millet et al., 2016; Deng et al., 2019) on the mechanics and controls of Ti isotope fractionation during magmatic differentiation. This will be achieved by expanding the current dataset with high precision measurements of the $\delta^{49/47}$Ti compositions of differentiation suites comprised of well-characterised lavas from different tectonic settings. The results of this work will enable us to better quantify the behaviour of Ti isotopes during magma evolution across different tectonic settings and to establish the extent to which different factors such as the composition of melts and Fe-Ti oxide minerals (namely ilmenite and titanomagnetite), redox conditions and water contents influence Ti isotope fractionation during magmatic differentiation.

- Chapter 4 – Whilst preliminary measurements of Fe-Ti oxide mineral separates (Johnson et al., 2019; Mandl, 2019) and ab-initio studies (Leitzke et al., 2018; Wang et al., 2020) have confirmed that oxides are isotopically light relative to silicate melts or minerals, there is currently no data for individual oxide-melt Ti isotope fractionation factors. In order to derive Ti isotope fractionation factors for titanomagnetite, ilmenite and rutile, selected oxides and groundmass, and glass were extracted in-situ via micro-mill from crystal-groundmass pairs in lavas from Santorini (calc-alkaline arc) and Heard Island (intraplate), and from rutile-melt experiments Klemme et al. (2005). The resulting Ti isotope fractionation factors can then be incorporated into petrologic models to facilitate quantitative investigation of processes such as magmatic differentiation and mantle melting. Ultimately, this will enable Ti isotopes to become a mature petrologic tool.
- Chapter 5 – In this chapter, the quantitative methods and understanding of Ti isotopes in magmatic systems gained in Chapters 3 and 4 will be applied to ascertain the efficacy of Ti isotopes as a novel tool to elucidate the geodynamic setting of past volcanism, with a focus on the Oman ophiolite. The Ti isotope compositions of a temporally and spatially representative set of lavas and dikes from the ophiolite will be used to address the long-standing debate as to whether the Oman ophiolite formed at a true mid-ocean ridge or subduction zone setting.

Chapter 2: Methods

2.1 An Introduction to Multi-Collector Inductively Coupled Plasms Mass Spectrometry

The accurate and precise determination of stable isotope ratios has been of vital importance to geochemists due to its importance in broad range of applications in geoscience. Historically, Thermal Ionisation Mass Spectrometry (TIMS) has been the de facto method of choice for acquiring the highest levels of precision and accuracy (e.g. Platzner et al., 1997 and references therein). However, since it was first utilised by Walder et al. (1993), the rapid development of multi-collector inductively coupled plasma mass spectrometry (MC-ICP-MS) has played a crucial role in measuring mass dependent isotope variations in a variety of elements, and can achieve levels of precision comparable with TIMS (e.g. Woodhead, 2002; Albarede et al., 2004; Weis et al., 2006).

An MC-ICP-MS instrument consists of numerous components; a sample introduction system, an inductively coupled argon plasma, ion transfer system and a mass detector system (Wang, 2009, Lu et al., 2017). Multi-collector inductively coupled plasma mass spectrometry has numerous other advantages over TIMS such as high sample throughput (Lu et al., 2017) and highly efficient ionisation and high mass resolution (Albarede et al., 2004; Yang, 2009; Epov et al., 2011; Lu et al., 2017) have only served to facilitate its rapid development and utilisation in the geochemistry community. In mass spectrometry, mass resolution is typically defined at the minimum separation required between two mass spectral peaks of both equal height and width in order to create a detectable 'valley' between them. As such, mass resolution power is defined as $m_1/(m_2-m_1)$.

Importantly, MC-ICP-MS has paved the way for analysis for a multitude of so called 'non-traditional' stable isotopes (e.g. Fietzke and Eisenhauer, 2006; Petit et al., 2008; Dauphas et al., 2009; Huang et al., 2009; Wombacher et al., 2009; Zhang et al., 2011; Gall et al., 2012; Millet and Dauphas, 2014; Nanne et al., 2017; Inglis et al., 2018).

The optimisation of the MC-ICP-MS instrument in the analysis of stable Ti isotopes is crucial in obtaining ultra-precise isotopic compositions required resolve the often-small variations that occur during high temperature magmatic processes. However, there are many challenges facing the acquisition of ultra-precise Ti stable isotope data such as: mass dependent fractionation due to non-quantitative yields produced during sample preparation, instrumental mass bias and the presence of isobaric interferences (Millet and Dauphas, 2014). The development of a double spike technique (Millet and Dauphas, 2014) which can correct for fractionation that can occur during both sample preparation and the operation of the instrument was a fundamental stage in the optimisation of Ti stable isotope analysis via MC-ICP-MS.

2.1.1 Standard-Sample Bracketing

Standard-sample bracketing (SSB) is a widespread technique used in MC-ICP-MS analysis in order to correct for mass bias (e.g. Albarede et al., 2004). Mass bias refers to artificial changes in isotope ratios i.e., isotopic fractionation that is induced by the instrument due to the variable transmission of the ion beam in the mass spectrometer (Andrén et al., 2004), which in MC-ICP-MS occurs mainly in the plasma and interface portions of the machine. The SSB analytical sequence consists of bracketing a sample between standards of known isotopic composition, the mass bias correction factor is then determined by the bracketing standards (Albarede et al., 2004; Yang, 2009; Lu et al., 2017). Prior to analysis the SSB method requires that the concentration of the target element is the same in both the sample and standard, and that the samples have undergone extensive purification to minimize interference because of sample-matrix mismatch (Albarede et al., 2004; Yang, 2009; Lu et al., 2017). If matrix is introduced during column separation this can lead to the failure of the SSB technique which has detrimental implications for the accuracy and precision of isotope data (e.g. Pietruszka and Reznik, 2008).

2.1.2 Double Spike Deconvolution, Calibration and Optimisation

Double-spike (DS) deconvolution is an effective mass bias correction method that can efficiently tackle issues with isotope fractionation that can occur during sample preparation that was first demonstrated experimentally by Dietz et al. (1962). The mathematical framework of double spike deconvolution was established by Dodson (1963; 1970), and is illustrated in Fig. 2.1. The relationship between the sample/standard and the spike is described by resolving Eq. 2-1 (e.g. Albarède and Beard, 2004; Rudge et al., 2009):

Eq. 2-1

$$R_m = \left[\left((1-f)\left(R_{Standard}(i_x/i_n)^{\alpha}\right)\right) + fR_{Spike}\right](i_x/i_n)^{\beta}$$

where R_m, $R_{Standard}$ and R_{Spike} represent the isotopic ratio of the measured sample, standard and spike (Fig. 2.1; Eq. 2-1), i_n is the normalised isotope for ratios, i_x is any other isotope of the target element, f is the proportion of the normalising isotope related to the spike in the sample-spike mixture, α is the natural fractionation between the sample and the reference standard, and β represents the instrumental fractionation factor (Fig. 2.1; Eq. 2-1; Albarède and Beard, 2004; Rudge et al., 2009; Millet and Dauphas, 2014; Klaver and Coath, 2019). Eq. 2-1 consists of three unknowns f, α and β, which indicates a minimum of three isotopes is required to resolve equation Eq. 2-1 by creating at least 3 versions of the equation. This calculation assumes that the sample and the standard are related via exponential mass dependent fractionation law for all the 3 input isotope ratios, which is appropriate for instrumental fractionation in MC-ICP-MS (Rudge et al., 2009; Klaver and Coath, 2019). If an isotope that exhibited mass independent variations (e.g., nucleosynthetic anomalies) or analytical errors were to be involved in the calculation, it would produce inaccurate results (e.g. Millet and Dauphas, 2014). ^{50}Ti exhibits distinct mass independent signatures within meteorites and lunar samples as a result of nucleosynthetic anomalies and cosmogenic effects (e.g. Niederer et al., 1980; Leya et al., 2008; Trinquier et al., 2009), and thus ^{50}Ti is not

included in double-spike resolution equations. ^{46}Ti also displays MIF signatures in meteorites (Zhang et al., 2011), however the variation is much smaller in comparison to ^{50}Ti (-0.03 to +0.06 vs. -0.13 to+ 0.37). Terrestrial samples do not display any ^{46}Ti anomalies and are always related to one another by mass-dependent fractionation in ^{46}Ti-^{47}Ti-^{48}Ti-^{49}Ti space (Millet and Dauphas, 2014), however extra-terrestrial materials that exhibit isotopic anomalies are analysed both spiked and un-spiked to elucidate their true isotopic composition (e.g. Niederer et al., 1980).

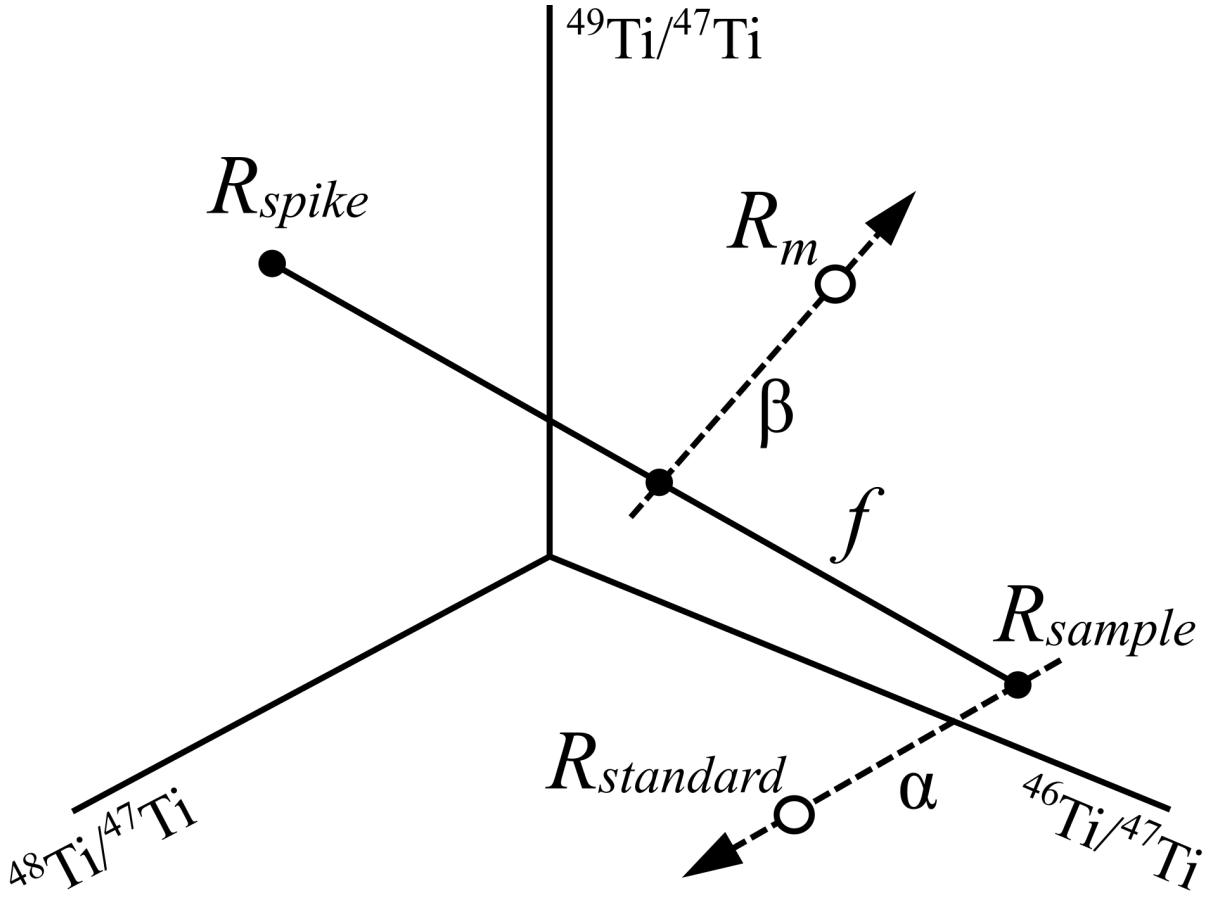

Fig. 2.1 Conceptual diagram of the double spike technique (not to scale, modified after Klaver and Coath, 2019). Ti is used an example, in four-isotope space, the isotope ratio of a natural sample (R_{sample}) and double spike (R_{spike}) have very different compositions. The measured isotope ratio (R_m) lies on a mixing line and contains a mixture of the R_{sample} and R_{spike} (where *f* is the proportion of double spike). The R_m is displaced from the mixing line along an instrumental mass fractionation (IMF) line, but the degree of fractionation, β, is unknown. Similarly, the degree of fractionation in the natural sample relative to a reference standard ($R_{standard}$), is expressed as α, the natural fractionation factor. As the value of R_{spike} is known, measurement of R_m and $R_{standard}$ are required to solve the double spike equation to yield values for α, β, and *f*. As a result, α can utilised to calculate the value of R_{sample}.

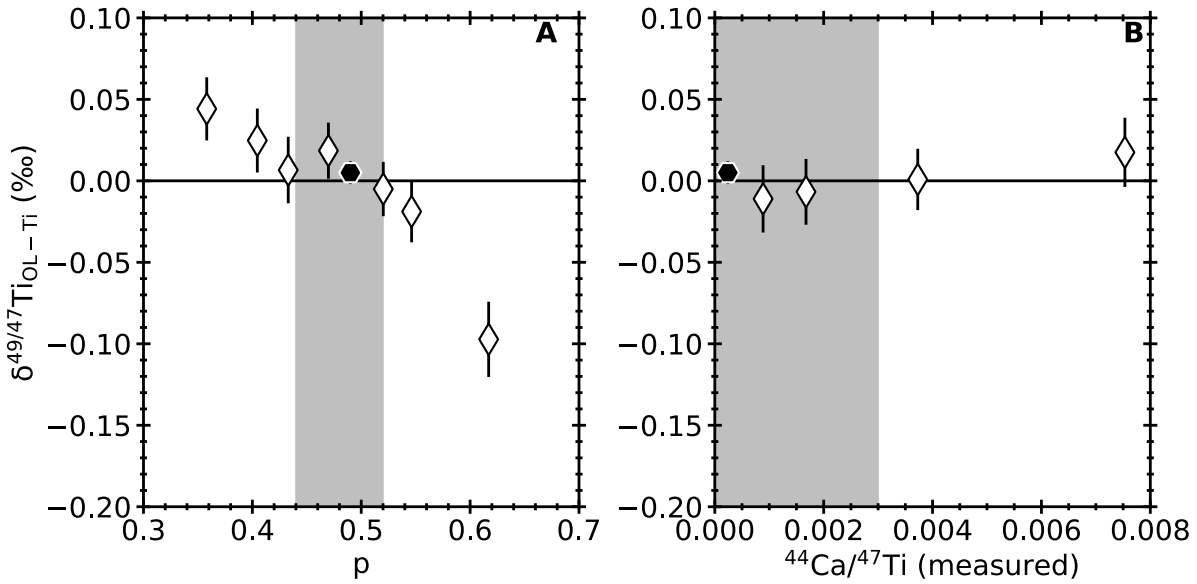

Fig. 2.2 Robustness of $\delta^{49/47}$Ti results. A) $\delta^{49/47}$Ti of the OL-Ti reference standard with variable proportion of double spike (p), in the sample-spike mixture. The shaded grey region shows the range of p for samples measured in 3 separate analytical sessions during October 2020 and hence the lack of bias on $\delta^{49/47}$Ti due to variable sample:spike proportions; B) $\delta^{49/47}$Ti of OL-Ti solutions doped with different Ca concentrations. In both figures the filled (black) hexagon represents the mean of un-doped OL-Ti solutions that were measured as unknows (n=9).

The optimisation of spiking methods is a matter of some debate, particularly regarding whether double or triple spikes provide better errors (e.g. Galer and Abouchami, 1998). In developing their "double spike toolbox" Rudge et al. (2009) proposed the best optimum double spike composition for Ti involves ^{50}Ti, but the calculations did not incorporate the effect of isotopic anomalies. Millet and Dauphas (2014) developed a refined spike composition Monte-Carlo simulations to evaluate all double and triple spike compositions in ^{46}Ti-^{47}Ti-^{48}Ti-^{49}Ti space, the results of the simulation were displayed in a tetrahedron, the bases of which are defined by three pure spikes, with the Ti standard at the apex. The areas with the lowest error were consistently confined to edges of the selected ternary error map, with error increasing with proximity to the centre (Millet and Dauphas, 2014). This demonstrates that for Ti, double spikes consistently provide better errors than triple spikes, with the optimal double spike composed of 50% ^{47}Ti and 50% ^{49}Ti, which provides the lowest errors when mixed in 48:52 proportions with the sample (Millet and Dauphas, 2014).

During the course of this study a calibration check was performed in order to re-confirm the ideal sample:spike proportion first proposed by Millet and Dauphas (2014; Fig. 2.2). In the process, this also enabled an assessment of the extent to which variable sample:spike proportions can bias the $\delta^{49/47}$Ti compositions of the OL-Ti standard used for standard-sample bracketing. The results of this calibration check are shown in Fig. 2.2, and suggest the optimal range of the double spike proportion (p) is ~0.47-0.53 (Fig. 2.2). Doping of OL-Ti with varied amounts of Ca was also carried out (Fig. 2.2) to test the effect of ^{46}Ca and ^{48}Ca, which are isobaric interferences (Millet and Dauphas, 2014) and the ability of the Ca interference built into the data reduction code. Fig. 2.2 illustrates the correction of isobaric interferences is accurate to < 0.01 V of measured ^{44}Ca/^{47}Ti.

2.2 Titanium Isotope Sample Preparation

For the duration of this study sample preparation first requires digestion of 10-60 mg (amount is dependent on the TiO_2 concentration of the sample to achieve at least 5 μg of natural Ti) of fine-powdered silicate rock sample or geo-standard in concentrated 1:1 mixture of HNO_3 and HF at 120°C for a period of at least 48 hours. An additional 2 ml of concentrated HNO_3 is then added and evaporated to incipient dryness. Following this step, each sample is taken up in 500 μl of concentrated HNO_3 and dried down, this step is repeated 3 times. The sample is then taken up in 6 M HCl with the addition of ~30 mg of H_3BO_3 into the solution to ensure the removal of any fluorides that would sequester Ti out of the sample solution. Finally, an aliquot containing 5-10 μg of Ti is taken from the sample solution and mixed with a ^{47}Ti-^{49}Ti double spike in a 48:52 ratio based on the calibration of Millet and Dauphas (2014).

2.3 Titanium Isotope Cation-Exchange Chromatography

The following procedures were performed at the clean laboratory housed in the Cardiff Earth Laboratory for Trace Element and Isotope Chemistry (CELTIC) at Cardiff University School of Earth and Environmental Sciences. Titanium is separated from the sample matrix using Eichrom DGA resin. The procedure adopted in this

thesis is based on the method initially developed by Zhang et al. (2011) and later modified by Millet and Dauphas (2014). The method used by Millet and Dauphas (2014) is outlined in Table 2.1. This study used a double pass of Step 1 only. Following purification, Ti fractions are treated repeatedly with a 1:1 mixture of concentrated HNO_3 and 30% H_2O_2 to remove any organic material.

Table 2.1 Two-step cation exchange chromatography procedure for Ti purification of samples for MC-ICP-MS analysis. For this this thesis Step 1 was repeated twice. Step 2 is only necessary for extra-terrestrial samples (chondrites meteorites) enriched in Mo, which is an interference on Ti (e.g. Zhang et al., 2011)

Step 1 – DGA Resin	**Acid**	**Volume (ml)**
Clean	MQ	20
Clean	3 M HNO_3	10
Condition	12 M HNO_3	10
Introduction	Sample in 12 M HNO_3	5
Wash	12 M HNO_3	20
Collect Ti	12 M HNO_3 + 1 wt% H_2O_2	10
Clean	MQ	20
Clean	3 M HNO_3	10
Step 2 – AG1-X8 resin		
Clean	MQ	5
Condition	4 M HF	6
Load	Sample in 4 M HF	2.5
Wash	4 M HF	10
Collect Ti	9M HCl + 0.01 M HF	5

2.4 Titanium Stable Isotopic Analysis via MC-ICP-MS

2.4.1 Ti Isotope Measurements using a Nu Plasma II MC-ICP-MS

Ti isotope measurements in this study were performed using a Nu Instruments Plasma II MC-ICP-MS at the Cardiff Earth Laboratory for Trace Element and Isotope Chemistry (CELTIC). All results are given relative to the Origins Laboratory Titanium

reference material (OL-Ti). Sample concentrations over the course of this study range from 0.5-1.3 μg/mL. Samples were taken up in 0.3 M HNO_3 + trace HF solution and introduced to the mass spectrometer though an Aridus II desolvating nebuliser used with Ar. The instrument was fitted with nickel (Ni) jet-sampler and Ni (H) skimmer cones. The measurements were performed in medium resolution mode, with a resolution power (5-95% peak definition, ΔM/M) in the range of ~ 4,000 which was sufficient to clearly identify the peak shoulders of the Ti isotopes, and simultaneously to counter the effect of non-resolvable polyatomic interferences such as $^{28}Si^{19}F$ and $^{14}N^{16}O_2H^+$ that can be introduced via the analyte solution (0.3M HNO_3 – 0.005M HF), which give inference on ^{47}Ti. The 'peak shoulder' is used to define an interference-free mass range on the respective mass, as polyatomic interferences are typically heavier than the respective mass. Titanium ion beam intensity ranged from 30-60 V on amplifiers with 10^{11} Ω resistors in their feedback loop. Ca interference on ^{46}Ti and ^{48}Ti was monitored at mass 44 and corrected during data reduction if necessary. Measurements of an individual sample consisted of 50-60 cycles with an integration time of 10 s. To account for small unresolved polyatomic interferences on ^{47}Ti due to the presence of F from the sample solution and Si from the torch ($^{28}Si^{19}F$), samples are bracketed by measurements of the double spiked OL-Ti standard (Millet and Dauphas, 2014; Millet et al., 2016). The cup configuration used on the Nu Plasma II at the CELTIC lab is provided in Table 2.2.

Table 2.2 Cup configurations used on the Nu Instruments Plasma II MC-ICP-MS at the Cardiff Earth Laboratory for Trace Element and Isotope Chemistry (CELTIC) during this study.

	Collectors						
	H10	**H9**	**H7**	**H4**	**Ax**	**L2**	**Integration Time (s)**
Mass	49.008	48.009	47.010	46.011	44.679	44.013	10

2.4.2 Data Reduction

Data reduction was performed offline using the algebraic method of (Millet and Dauphas, 2014), with uncertainty estimates calculated via Monte-Carlo simulation. The code for the data reduction scheme was written in Python using the NumPy (Harris et al., 2020), SciPy (Virtanen et al., 2020), and OpenPyXl (Gazoni and Clark, 2018) packages. Results are reported relative to the OL-Ti standard as $\delta^{49/47}Ti_{OL\text{-}Ti}$ (hereafter abbreviated as $\delta^{49/47}Ti$) in accordance to the definition of Coplen (2011). To assess the long-term reproducibility of $\delta^{49/47}Ti$ measurements conducted over the duration of this study, a compilation of the $\delta^{49/47}Ti$ compositions of individual measurements of the OL-Ti standard from all measurement sessions at Cardiff from October 2018 to June 2021 are given in Fig. 2.3. This yielded a mean OL-Ti $\delta^{49/47}Ti$ value of -0.001 ± 0.029 ‰ (2s, n=104, Fig. 2.3).

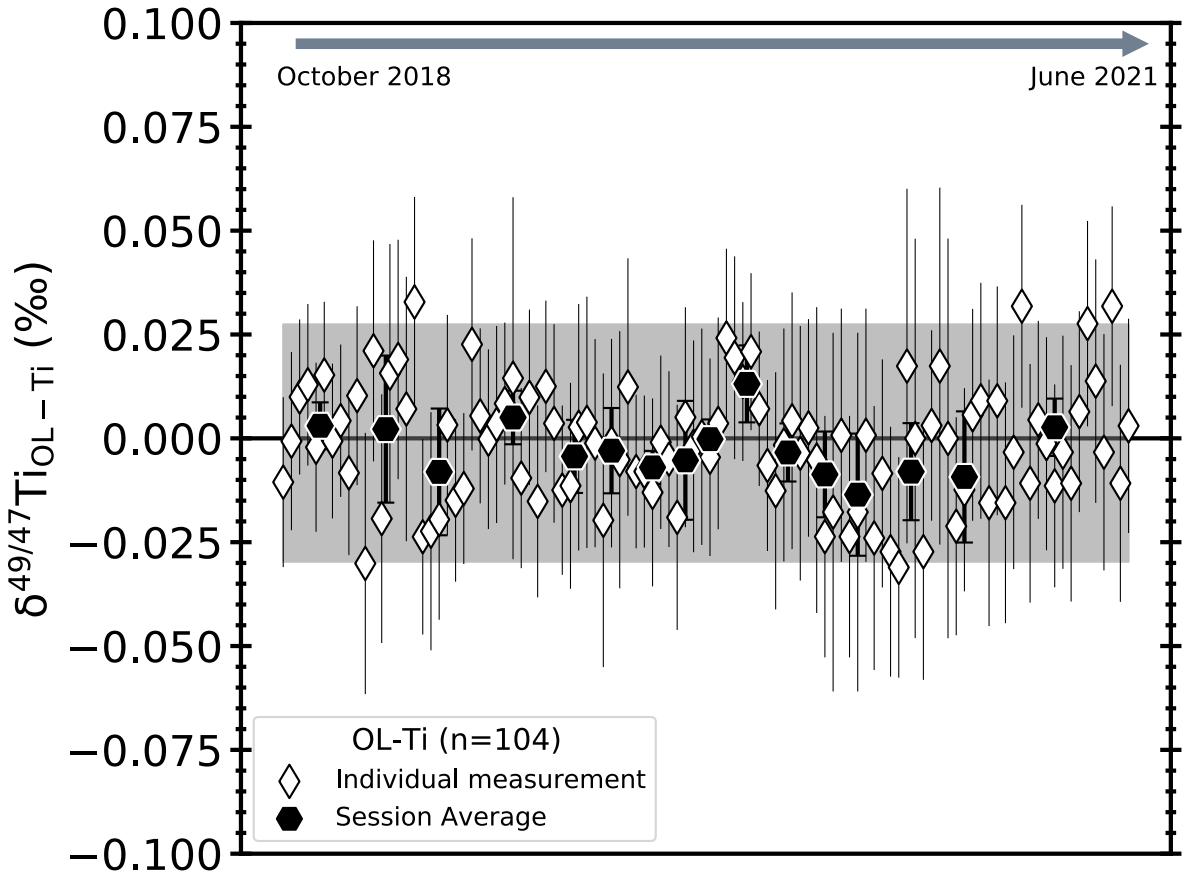

Fig. 2.3 Compilation of $\delta^{49/47}Ti$ compositions of OL-Ti measured over the duration of this study showing the long-term reproducibility. Open diamonds represent individual measurements, whereas the black hexagons give the mean of a whole measurement session (error bars represent the 95% confidence

interval). The shaded grey area represents the overall mean OL-Ti $\delta^{49/47}$Ti value of -0.007 ± 0.032 ‰ (2s, n=107). All data is provided in Appendix E1.

Repeated measurements of Geological (BCR-2, BHVO-2, JB-2, and RGM-2) and Ti solution (Alfa Aesar Ti-wire and Ti solution) reference materials measured over the duration of this study are in excellent agreement with previously published values as shown in Fig. 2.4. Data for all reference materials are provided in Appendix E1.

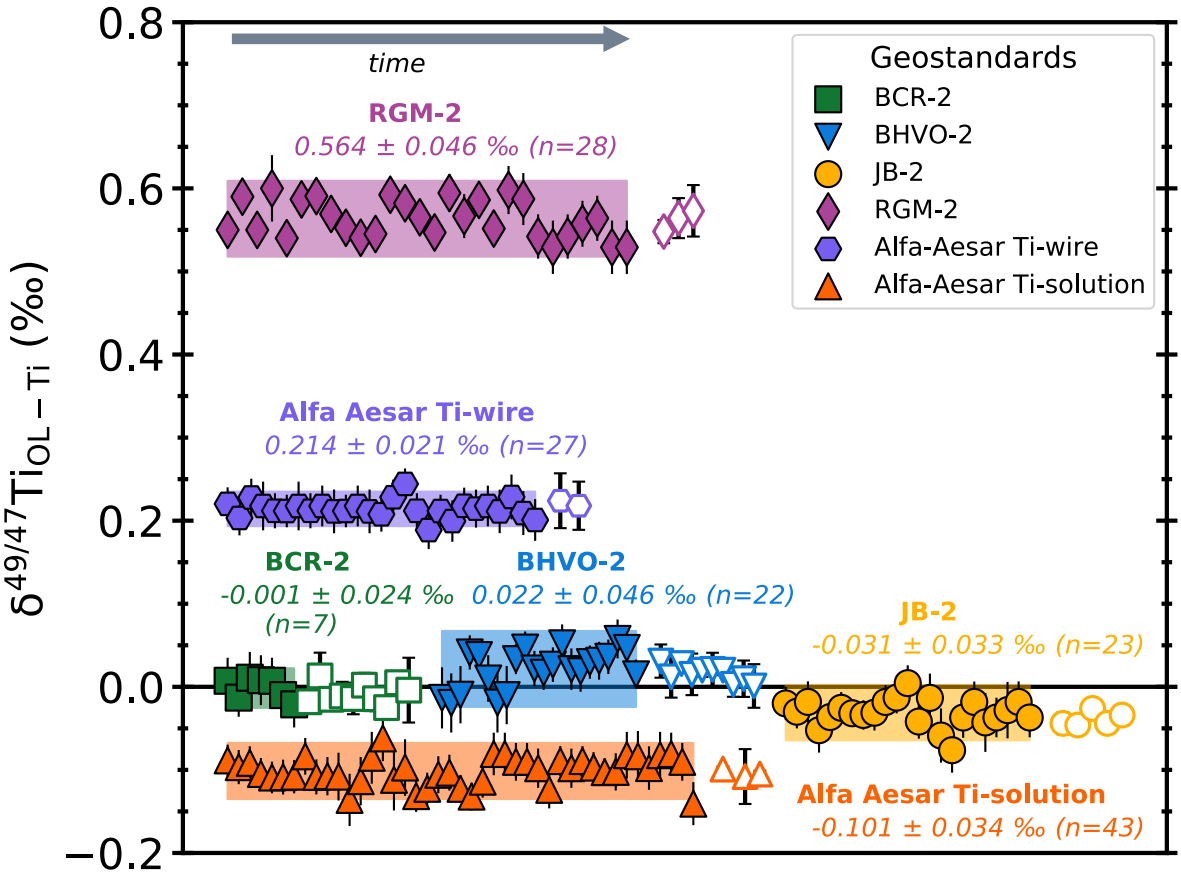

Fig. 2.4 $\delta^{49/47}$Ti compositions of reference geo-standards and Ti solution reference materials measured over the duration of this study; literature values (open symbols) are shown for comparison (Millet and Dauphas, 2014; Williams, 2015; Millet et al., 2016; Greber et al., 2017b; Greber et al., 2017a; Deng et al., 2018; Deng et al., 2019; Johnson et al., 2019; Aarons et al., 2020; Kommescher et al., 2020; Klaver et al., 2021; Williams et al., 2021). All data is provided in Appendix E1.

2.5 Quantitative Petrographic Methods

2.5.1 Scanning Electron Microscopy

A thorough petrographic assessment of the samples in this study was undertaken by obtaining back-scatter electron (BSE) and element maps of Fe-Ti oxide grains in polished ~2.5 cm diameter thick sections targeted as candidates for Ti isotope

analyses. BSE images were acquired at 1024-pixel resolution using a Zeiss Sigma HD Field Emission Gun SEM at the School of Earth and Environmental Sciences, Cardiff University at 15 kV using a 60 μm diameter final aperture. Element maps were acquired using two Oxford Instruments 150 mm^2 Energy Dispersive X-ray Spectrometry (EDS) silicon drift detectors on the same SEM. Operating conditions for element maps were set at 20 kV with a 120 μm aperture and a working distance of 8.9 mm, resulting in a nominal beam current of 4 nA. BSE images and element maps were acquired using Oxford Instruments Aztec software version 5.0. Individual grains were mapped at image resolutions of 512 by 384 or 1024 by 768 pixels. A process time of 0.5 μs was used for EDS with a pixel dwell time of 2250-4500 μs. The resulting element maps were processed using the Aztec software to perform background correction and element overlap deconvolution.

2.5.2 Major Element Mineral Chemistry

Major element chemistry of Fe-Ti oxides (Appendix E3) was acquired using the same SEM instrument described in Section 2.5.1. Major element analyses were performed at 20 kV with a final aperture size of 60 μm and a 2 μs process time with a dead time around 50%, resulting in output count rates of 135,000 cps. A live time of ten seconds was used for each analysis. Checks for beam stability and analytical drift were conducted at 30-minute intervals throughout each session using a Co reference standard. A live time of ten seconds was used for each analysis. Measurements were calibrated using a suite of reference materials (Fe on ASTIMEX magnetite, Ti on Smithsonian ilmenite) and data accuracy was monitored by measuring Smithsonian magnetite and ASTIMEX rutile, and Smithsonian ilmenite as secondary standards. The precision and accuracy of mineral secondary standard measurements are reported in Appendix E3. Analytical procedures for the major element concentrations obtained for rutile and glass from the rutile-melt experimental run products (MHD15_1 and HD4_4) are reported in Klemme et al. (2005).

2.6 Micro-milling and In-situ Sampling

Individual Fe-Ti oxide crystals (ilmenite, titanomagnetite and rutile) and groundmass (or silicate glass in the case of the rutile-melt experimental run products) were micro-sampled at the School of Earth and Environmental Sciences, Cardiff University, using a NewWave Micro-Mill that was operated within a laminar flow hood using Horico tungsten carbide drill bits with a diameter of ~100 μm. The methodology utilised in this study is adapted from Jansen et al. (2018), with similar techniques having been utilised successfully in previous studies (e.g. Charlier et al., 2006). Fe-Ti oxide grains were targeted based on certain criteria which included a lack of chemical zoning and the possession of subhedral to euhedral crystal habits, booth oof which were assessed using the scanning electron microscope (see section 2.5 and chapter 4). Prior to drilling, drill bits were cleaned by submerging them in a clean glass beaker with Milli-Q water and washing them in an ultrasonic bath filled with Milli-Q for 15 minutes. A grid of spots was placed on targeted crystals to maximise the surface area drilled. A drop of Milli-Q was placed on the target prior to engaging the drill to capture the drilled material in suspension. At regular intervals, the Milli-Q containing the drilled material was pipetted into pre-cleaned 7 ml PFA beakers, and new drops of Milli-Q were added to ensure maximum recovery of drilled sample during drilling. Drilling speed was set at 65%, with 75-100 μm/s scan- and drill plunge speeds during drilling. For Fe-Ti oxide grains a drill depth of 75 μm was chosen which produces a hole of approximately 250 μm in diameter. A larger drill depth of 100 μm was used for groundmass targets, resulting in holes approximately 400 μm in diameter. The duration of micro-milling varied from 5-30 minutes per target, depending on the size and TiO_2 concentration of the target. To avoid sampling bias, a range of grain sizes from 250 to 600 were targeted μm, with titanomagnetite grains in Heard Island typically being smaller than ilmenite. As multiple crystals were drilled from the same sample, the sample surface was cleaned with Milli-Q and ethanol before drilling the next crystal. For each sample the phase with the lowest TiO_2 contents (i.e., groundmass or glass) was drilled first to limit the risk of contamination from drilling of TiO_2 rich

phases in the same sample. The acicular habit of rutile in the experimental run products of Klemme et al. (2005) presented a challenge for precise micro-milling of pure phases as many possess a diameter of <100 μm. To circumvent this problem, I specifically targeted rutile-glass mixtures in different proportions (in addition to milling as close to the pure end member phases as possible) which I later utilise to calculate compositions via endmember unmixing (see Chapter 4 for details).

Chapter 3: Controls on Ti isotope Fractionation During Magmatic Differentiation

3.1 Abstract

Titanium offers a burgeoning isotope system that has shown significant promise as a tracer of magmatic processes. Recent studies have shown that Ti displays significant mass-dependent variations linked to the crystallisation of Fe-Ti oxides during magma differentiation. This chapter presents a comprehensive set of Ti isotope data for a range of differentiation suites from alkaline (Ascension Island, Afar and Heard Island), calc-alkaline (Santorini) and tholeiitic (Monowai seamount and Alarcon Rise) magma series to further explore the mechanics of Ti isotope fractionation in magmas. Whilst all suites display an increase in $\delta^{49/47}$Ti (deviation in ^{49}Ti/^{47}Ti of a sample relative to the OL-Ti reference material) during magma differentiation relative to indices such as increasing SiO_2 and decreasing Mg#, the data reveal that each of the three-magma series have contrasting $\delta^{49/47}$Ti fractionation patterns over comparable ranges of SiO_2 and Mg#. Alkaline differentiation suites from intraplate settings display the most substantial range of variation ($\delta^{49/47}$Ti = +0.01 to +2.32‰), followed by tholeiites (-0.01 to +1.06‰) and calc-alkaline magmas (+0.06 to +0.64‰). Alkaline magmas possess high initial melt TiO_2 contents which enables early saturation of ilmenite + titanomagnetite and a substantial degree of oxide crystallisation, whereas tholeiitic and calc-alkaline suites crystallise less oxide and have titanomagnetite as the dominant oxide phase. Positive slopes of FeO*/TiO_2 vs. SiO_2 during magma differentiation are related to high degrees of crystallisation of Ti-rich oxides (i.e., ilmenite). Bulk solid-melt Ti isotope fractionation factors co-vary with the magnitude of the slope of FeO*/TiO_2 vs. SiO_2 during magma differentiation, this indicates that the modal abundance and composition of the Fe-Ti oxide phase assemblage, itself controlled by melt composition, governs Ti isotope fractionation during magma evolution. In addition to this overall control, hydrous, oxidised calc-alkaline suites display a resolvable increase in $\delta^{49/47}$Ti at higher Mg# relative to drier

and more reduced tholeiitic arc suites. These subparallel Ti isotope fractionation patterns are best explained by the earlier onset of oxide segregation in arc magmas with a higher oxidation state and H_2O content. This indicates the potential of Ti isotopes to be utilised as proxies for geodynamic settings of magma generation.

3.2 Introduction

As a result of recent advances in mass spectrometry a growing arsenal of non-traditional mass-dependent isotope systems have been applied to investigate the evolution of the Earth and other terrestrial bodies in the solar system, such as Mg (Teng et al., 2010; Hin et al., 2017), Ca (Simon and DePaolo, 2010; Chen et al., 2019), Fe (Craddock and Dauphas, 2011; Debret et al., 2016), Cr (Bonnand et al., 2016; Schoenberg et al., 2016), V (Prytulak et al., 2013; Prytulak et al., 2016; Sossi et al., 2018) and Ni (Klaver et al., 2020). In particular, analytical advances have enabled increasing application of non-traditional isotopes to study high temperature processes, such as magmatic differentiation, where magnitudes of equilibrium isotope fractionation were generally inferred to be too small to resolve prior to the advent of high-resolution MC-ICP-MS (Zhang et al., 2011; Millet et al., 2012; Millet and Dauphas, 2014; Teng et al., 2015; Willbold et al., 2016; McCoy-West et al., 2017; Nanne et al., 2017). Titanium is a refractory lithophile element that is highly fluid-immobile and abundant in igneous rocks. It has been used extensively within igneous geochemistry to trace magmatic processes and mantle source composition, including delineating island arc signatures in the geologic record (Pearce and Cann, 1973; Shervais, 1982), and more recently, enriched mantle sources in ocean islands (Prytulak and Elliott, 2007). In stark contrast to the use of Ti concentrations, the mass-dependent isotopic composition of Ti has only recently been investigated and applied as a novel isotopic tool to study magmatic processes (Millet et al., 2016; Greber et al., 2017b; Greber et al., 2017a; Deng et al., 2018; Deng et al., 2019; Johnson et al., 2019)

Titanium is present in several co-ordination states within magmatic systems: it predominantly exists in 5-fold co-ordination in silicate melts but can also occupy 4-

fold and 6-fold co-ordination in silicic and mafic melts respectively (e.g. Farges et al., 1996; Farges and Brown, 1997). Mass-dependent isotope fractionation theory dictates that equilibrium mass-dependent isotope fractionation is driven by contrasts in co-ordination number, which by extension control bond strength, with heavy isotopes preferring stronger bonds and vice versa (e.g. Schauble, 2004; Young et al., 2015). As the Ti budget of igneous rocks is controlled by Fe-Ti oxides, such as titanomagnetite ($Fe^{2+}[Fe^{3+},Ti]_2O_4$) and ilmenite ($FeTiO_3$), in which Ti is predominantly hosted in 6-fold sites, the crystallisation of Fe-Ti oxides should consequentially be the main driver of Ti isotope fractionation in magmatic systems, with $\delta^{49/47}Ti$ progressively increasing from basaltic to rhyolitic compositions (Millet et al., 2016; Deng et al., 2019; Johnson et al., 2019). Because Fe-Ti oxide saturation in magmatic systems is controlled in part by the intimate link between magma redox state and water content, this suggests that Ti isotopes have the potential to provide insights into the oxidation state and water content of mantle melts. This property holds promise because, in contrast to other redox sensitive elements such as Fe (Sossi et al., 2012; Dauphas et al., 2014b) and V (Prytulak et al., 2016; Sossi et al., 2018), Ti only exists in one valence state in terrestrial magmatic environments as Ti^{4+} (Millet et al., 2016). This removes the additional complexity of mass-dependent isotope fractionation between different redox states e.g., Fe^{2+} and Fe^{3+} (Williams et al., 2004; Sossi et al., 2012; Dauphas et al., 2014b).

Previous work (Millet et al., 2016; Deng et al., 2019; Johnson et al., 2019) has demonstrated the utility of Ti isotopes as tracers of oxide-melt equilibrium. These studies report magmatic samples exhibiting a progressive increase in $\delta^{49/47}Ti_{OL\text{-}Ti}$ (deviation in $^{49}Ti/^{47}Ti$ in a sample relative to the OL-Ti reference material; hereafter written as $\delta^{49/47}Ti$) with increasing SiO_2 (wt%). This was attributed to the crystallisation of Fe-Ti oxides, in which isotopically light Ti is preferentially incorporated, thus enriching the remaining melt in heavy Ti isotopes. Greber et al. (2017) recently utilised this relationship to constrain the composition of continental crust through time, identifying Ti isotope signatures in Archean shales that indicate that they were likely derived from a felsic protolith. However, Deng et al. (2019) observed a greater range

of fractionation in differentiated samples from sub-alkaline intraplate lavas from the Afar rift and Hekla in Iceland ($\delta^{49/47}$Ti of -0.005 to +2.012‰) compared to that of the calc-alkaline Agung suite ($\delta^{49/47}$Ti of +0.054 to +0.259‰) measured by Millet et al. (2016) and argued for an auxiliary role of melt structure linked to the propensity of more silicic melts to contain a higher proportion of Ti in 4-fold co-ordination (e.g. Farges et al., 1996; Farges and Brown, 1997). The current data set of mass-dependent Ti isotope data for differentiated samples is limited; hence, it is difficult to ascertain if other controls beside Fe-Ti oxide crystallisation exist. The main objective of this contribution is to present high-precision $\delta^{49/47}$Ti measurements of complete differentiation suites in order to: (i) better quantify the fractionation behaviour of Ti isotopes during magmatic differentiation in different magmatic series (alkaline, calc-alkaline and tholeiitic); (ii) determine the presence of auxiliary controls to oxide-melt equilibrium that can either serve to help or hinder Ti isotope fractionation, such as discerning the significance of ilmenite versus titanomagnetite crystallisation as these phases have different Ti bonding environments and thus potentially different fractionation factors (e.g. Leitzke et al., 2018; Wang et al., 2020); and (iii) investigate the potential of Ti isotopes to serve as proxy for the conditions of magma evolution such as redox and melt H_2O content.

3.3 Sample Context and Background

In order to investigate the behaviour of Ti isotopes during magmatic differentiation, a diverse range of predominantly basalt to rhyolite differentiation suites from different geodynamic settings with distinct differentiation trends; alkaline, calc-alkaline and tholeiitic were selected. Whole rock major element variation diagrams and discrimination diagrams for these suites reveal distinct evolution patterns for each of the three magma series investigated here (Fig. 3.1; Table 3.1). This is particularly evident in K_2O and total alkalis, Mg#, and TiO_2 (Fig. 3.1). Alkaline intraplate and tholeiitic lavas typically have low H_2O contents and are relatively reduced (Moore, 1970; Canil, 1999; Campbell, 2001; Dixon and Clague, 2001; Lee et al., 2005). In contrast, calc-alkaline arc magmas are H_2O-rich and oxidised, and hence

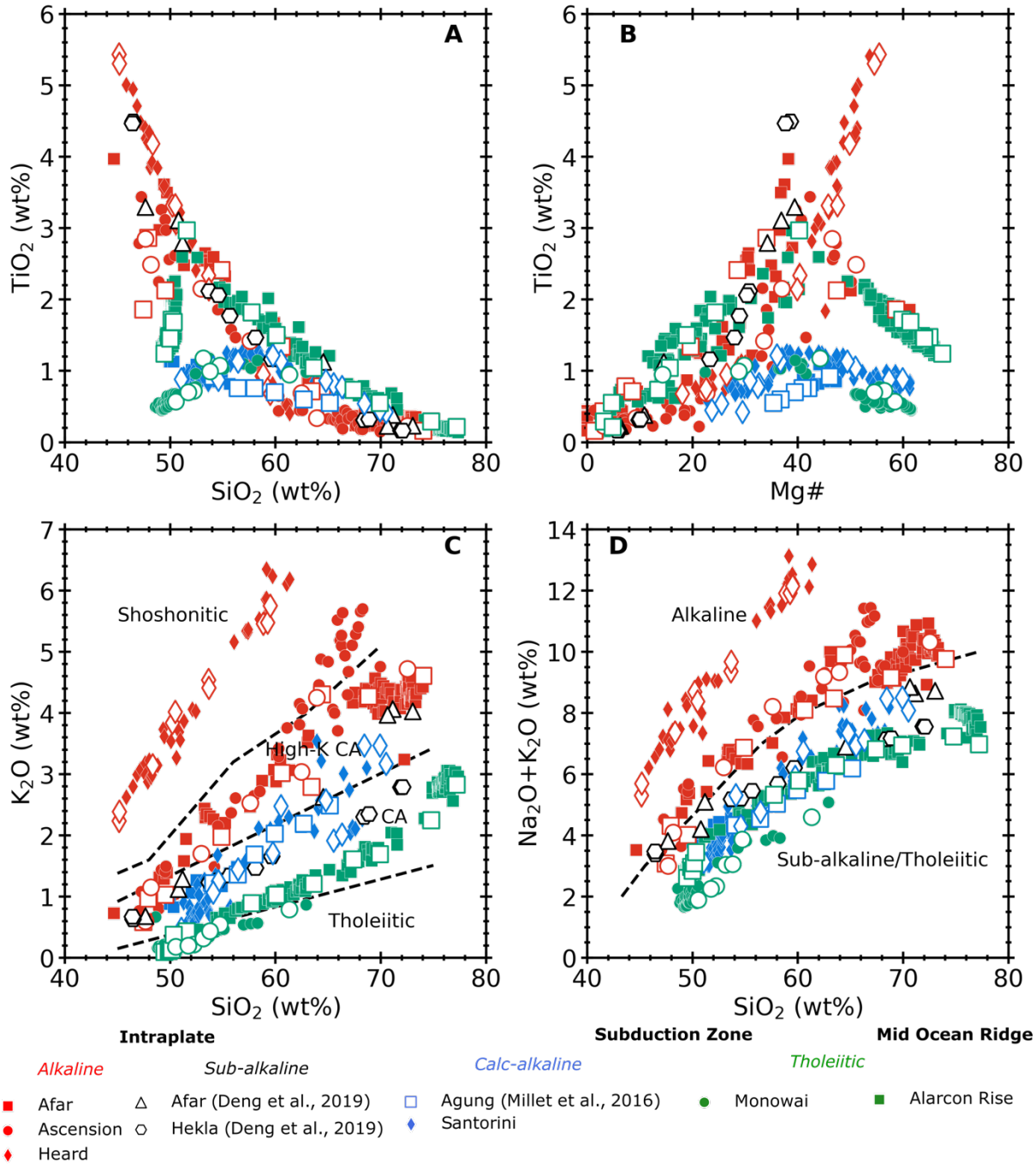

Fig. 3.1 Whole rock major element variation and discrimination diagrams (a) TiO_2 vs SiO_2; (b) TiO_2 vs Mg#; (c) K_2O vs SiO_2 (Peccerillo and Taylor, 1976); (d) Total Alkalis vs. SiO_2 (Bas Le et al., 1986); for the differentiation suites measured in this study (see Appendix E2 and references therein) exhibiting the distinct major element fractional crystallisation paths characteristic of each suite; Alkaline (red), calc-alkaline (blue) and tholeiitic (green). Samples measured for Ti isotopic compositions are denoted by the larger empty symbols. Samples from Deng et al. (2019) are included for comparison. Boundary lines for K_2O vs SiO_2 and Total Alkalis vs. SiO_2 diagrams were taken from Rickwood (1989).

would display earlier onset of Fe-Ti oxide saturation during magma differentiation (Toplis and Carroll, 1995; Howarth and Prevec, 2013; MacLeod et al., 2013; Nandedkar et al., 2014). Importantly, upon oxide saturation, oxidised magmas crystallise Fe-Ti

oxides with lower Ti content than more reduced magmas (Toplis and Carroll, 1995; Berndt et al., 2005; Feig et al., 2010). Calc-alkaline lavas are dominated by titanomagnetite, with ilmenite only appearing in the late stages of differentiation, whereas in reduced magmas ilmenite tends to saturate earlier (Berndt et al., 2005; Feig et al., 2010). Since the pioneering work of Harker and Daly in the early 20th century e.g. (Harker, 1909; Daly, 1914) it has been established that tholeiitic magmas are characterised by enrichments in TiO_2 and FeO during early stages of magma differentiation, that is less pronounced in calc-alkaline magmas due to earlier crystallisation of clinopyroxene and Fe-Ti oxides. Alkaline differentiation suites from intraplate settings display the largest enrichments in TiO_2 compared with both tholeiitic and calc-alkaline suites due to their origin as small melt fractions derived from enriched sources (Prytulak and Elliott, 2007; Fig. 3.1 a and b). The salience of this origin is that their elevated TiO_2 contents enables them to stabilise both titanomagnetite and ilmenite during the early stages of magmatic differentiation (Toplis and Carroll, 1995). Additionally, these intraplate magmas tend to have an intermediate oxygen fugacity between that of mid-ocean ridge tholeiites and calc-alkaline arcs (Kress and Carmichael, 1991).

The suites measured in this study were selected based on the criteria that they are the product of magma differentiation by fractional crystallisation with very limited modification by magma mixing or hybridisation. Evidence for the general absence of magma mixing in the studied suites comes from the scarcity of reverse zoning and disequilibrium textures e.g. Ascension Island (Chamberlain et al., 2016; Chamberlain et al., 2019) and Santorini (Klaver, 2016), lack of radiogenic isotope variation in Agung (Dempsey, 2013), Heard Island (Barling and Goldstein, 1990; Barling et al., 1994; Barling, 1994), and Monowai (Timm et al., 2011), or the preservation of the FeO*, TiO_2, and incompatible trace element enrichment along a single liquid line of descent in magmas recording the early stages of magma differentiation in Alarcon Rise (Clague et al., 2018), Monowai (Kemner et al., 2015) and the Afar Rift (Field et al., 2013). Whilst magma mixing is often invoked as the main

mechanism of generation of intermediate arc magmas e.g. (Reubi and Blundy, 2009; Laumonier et al., 2014; Millet et al., 2014), Santorini is unusual as its eruptive products are the result of low-pressure fractional crystallisation without significant magma mixing as indicated by patterns of major and trace element variation (Nicholls, 1971; Barton and Huijsmans, 1986; Huijsmans et al., 1988; Huijsmans and Barton, 1989; Michaud et al., 2000; Zellmer et al., 2000). Volcanic units on Santorini that do show geochemical evidence for magma mixing, such as the Therasia dome complex and Cape Riva Tuff (Fabbro et al., 2013), are excluded from this study.

Table 3.1 Summary of intensive variables of magmatic differentiation and oxide petrography for Afar (Field et al., 2013); Ascension Island (Chamberlain et al., 2019), Heard Island (Barling, 1990); Santorini (Andujar et al., 2015,2016); Alarcon Rise (Clague et al., 2018) and Monowai (Kemner et al., 2015) differentiation suites measured for their Ti isotopic composition in this study. * indicates intensive variables and Fe-Ti oxide compositions that are derived from Rhyolite MELTS (Gualda et al., 2012). H2O (wt%) is based on estimates for the parental magma of each differentiation suite. Ti-mag = titanomagnetite, Ilm = ilmenite. TiO_2 (wt%) contents for titanomagnetite and ilmenite are average compositions taken from representative datasets from the cited literature and GEOROC (http://georoc.mpch-mainz.gwdg.de/georoc/) in the case of Santorini

Suite	Stage	T (˚C)	P (MPa)	H_2O (wt%)	fO_2	Ti-mag	TiO_2 (wt%)	Ilm	TiO_2 (wt%)
Afar	1	1205 - 848	430 - 100	~0.4	QFM +0.5 -3.6	✓	22.7	✓	50.4
	2	1085 - 800				✓	18.1	✓	51.0
Ascension Island	1	1174 - 932	330 - 250	~0.5	NNO +0.5 - 2.3	✓	22.2	✓	45.7
	2	1034 - 772				✓	20.9	✓	50.1
Heard Island*	1	1216 - 1076	≤ 350	~0.6	~ QFM	✓	19.3	✓	47.3
	2	1070 - 916				✓	15.0	✓	41.9
Santorini	1	1070 - 1000	400 - 200	~3-5	QFM+0.5-NNO +1.5	minor	7.9	×	-
	2	1000 - 900				✓	11.6	rare	47.5
Alarcon Rise*	1	1210 - 1100	100 - 20	~0.2	~ QFM-1	×	-	×	-
	2	1090 - 895				✓	22.5	minor	49.9
Monowai	1	1200 - 1100	≤ 300	< 1.1	n.a.	×	-	×	-
	2	1100 - 1080				✓	10.8	×	-

A summary of both the intensive variables for each differentiation suite and Fe-Ti oxide petrography and composition is provided in Table 3.1. A brief summary of the geologic context of each sample suite is also provided in Table 3.1.

3.3.1 Alkaline differentiation suites

3.3.1.1 Dabbahu, Afar Rift, Ethiopia

The Afar samples were collected from Dabbahu composite volcano in the Manda-Hararo segment of the Afar Rift, Ethiopia in East Africa which has been active for over 67 ka (Field et al., 2013) and cover a compositional range from alkali basalt through trachyandesite to peralkaline rhyolite produced via closed system fractionation (Field et al., 2013). Samples in this study encompass a SiO_2 range of 47 to 75 and 8.5 wt% to 0.02 wt% in MgO, while TiO_2 contents of the Afar lavas range from 0.16 to 2.9 wt%, with the peak in TiO_2 occurring at a Mg# of 34. It is important to note that the Afar samples measured by Deng et al. (2019) are taken from the study of Pik et al. (2006), which were sampled from a different part of the East African rift (Stratoid Series) than those measured in this study and differ slightly in their bulk geochemistry. The Dabbahu sample set has a higher peak TiO_2 content, larger range of Mg# (Fig. 3.1, Appendix E2) and is moderately richer in alkalis (Fig. 3.1). Both titanomagnetite and ilmenite are present as crystallising phases during the entirety of magma differentiation in Afar samples (Table 3.1.), with the tendency for the modal proportion of ilmenite to increase in more evolved lavas (Field et al., 2013).

3.3.1.2 Ascension Island

Ascension Island is located in the southern Atlantic Ocean, 90 km west of the Mid-Atlantic Ridge. The onset of volcanism occurred 5-6 Ma ago, with subaerial volcanism occurring from ~ 1 Ma to present (Jicha et al., 2013; Preece et al., 2018). The samples are products of alkaline magmatism and fractional crystallisation (Chamberlain et al., 2016; Chamberlain et al., 2019) and cover a similar compositional range to that of the Afar samples. SiO_2 contents range from 48 to 72.3 wt%, MgO contents from 6.1 to 0.1 wt%, and the TiO_2 contents from 0.23 to 2.9 wt% and the

maximum in TiO_2 contents occurs at Mg# of 46.5 (Fig. 3.1). Similar to the Afar Rift, both mafic and felsic lavas have titanomagnetite and ilmenite in their crystal cargo, with the relative proportion of ilmenite versus titanomagnetite tending to increase in more intermediate and evolved lavas based on major and trace element modelling (Chamberlain et al., 2019).

3.3.1.3 Heard Island

The Heard Island samples were collected from the Laurens Peninsula Series on the Mt. Dixon volcanic cone (≤1 Ma; Clarke et al., 1983) from Heard Island in the southern Indian Ocean (Barling, 1990; Barling and Goldstein, 1990; Barling et al., 1994; Barling, 1994). The lavas of the Laurens Peninsula Series display a unique chemistry compared to other ocean island suites with extreme enrichments in TiO_2, encompassing a range of 0.7 to 5.4 wt% (Barling, 1994) with the peak occurring at Mg# ~ 55. The lavas are also highly enriched in alkalis, being shoshonitic, and cover a compositional range of basanite to trachyandesite. The samples span a range in SiO_2 from 45. to 60 wt% and MgO contents range from 7.4 to 0.6 wt%. A striking petrologic feature of the Heard Island lavas in the unusually high modal abundance of Fe-Ti oxides (~17.5 - 20% of phenocrysts; titanomagnetite + ilmenite) in basanitic lavas (Table 3.1.) which is reflective of their high initial TiO_2 contents (Barling, 1994; Barling et al., 1994). Silicic lavas are less phyric but titanomagnetite and ilmenite are still dominant phenocryst phases (~5-15%; Barling, 1990).

3.3.2 Calc-alkaline differentiation suites

3.3.2.1 Santorini

Eight samples were measured from Santorini volcano in the South Aegean Volcanic Arc, Greece (Klaver et al., 2016b; Klaver et al., 2016a). The Santorini samples (all <500 ka) form a complete medium to high-K calc-alkaline fractionation trend from basalt to rhyodacite. Santorini is the most hydrous differentiation suite sampled in this work with estimates of the initial H_2O contents in primitive lavas ranging from 3-5 wt% (Andújar et al., 2015). SiO_2 contents of the samples ranges from 51 to 71.5 wt%,

6.9 to 0.70 wt% for MgO, and TiO_2 contents ranging from 0.43 to 1.22 wt%, reaching a peak at Mg# of 44. On the basis of patterns of major and trace element variation the studied Santorini samples were generated mainly as a result of low-pressure fractional crystallisation under hydrous conditions (Nicholls, 1971; Barton and Huijsmans, 1986; Huijsmans et al., 1988; Huijsmans and Barton, 1989; Michaud et al., 2000; Zellmer et al., 2000; Andújar et al., 2015; Andújar et al., 2016). Primitive lavas in Santorini contain minor amounts of titanomagnetite (Nicholls, 1971), with the appearance of more Ti-rich titanomagnetites in andesitic and dacitic lavas, accompanied by minor ilmenite (Table 3.1.; Nicholls, 1971).

3.3.3 Tholeiitic differentiation suites

3.3.3.1 Monowai seamount

The Monowai seamount is situated in the Tonga-Kermadec arc (Timm et al., 2011). The lavas range from tholeiitic basalts through to andesite, with their geochemical variation being consistent with fractional crystallisation under relatively anhydrous conditions (<1.1 wt% H_2O) acting as the major process based on petrography and patterns of major and trace element variation (Timm et al., 2011; Kemner et al., 2015). The SiO_2 contents of these samples range from 51 to 61 wt%, 6.9 to 1.0 wt% for MgO, with TiO_2 contents encompassing a range of 0.57 to 1.17 wt%, reaching a peak in TiO_2 contents at Mg# of 44.20. Petrography indicates the onset of titanomagnetite crystallisation at ~ 4 wt % MgO (Timm et al., 2011; Kemner et al., 2015). Magnetite is present in basaltic and basaltic andesite lavas as a groundmass phase, but major element variation and least squares modelling suggest it is Ti-poor (Kemner et al., 2015).

3.3.3.2 Alarcon Rise

Situated adjacent to the southeastern tip of Baja California (Mexico), Alarcon Rise forms part of the northernmost segment of the East Pacific Rise. It is a unique MORB differentiation suite spanning a compositional range from basalt through to andesite and rhyolite with up to 77 wt% SiO_2 (Clague et al., 2018; Portner et al., 2021). Alarcon

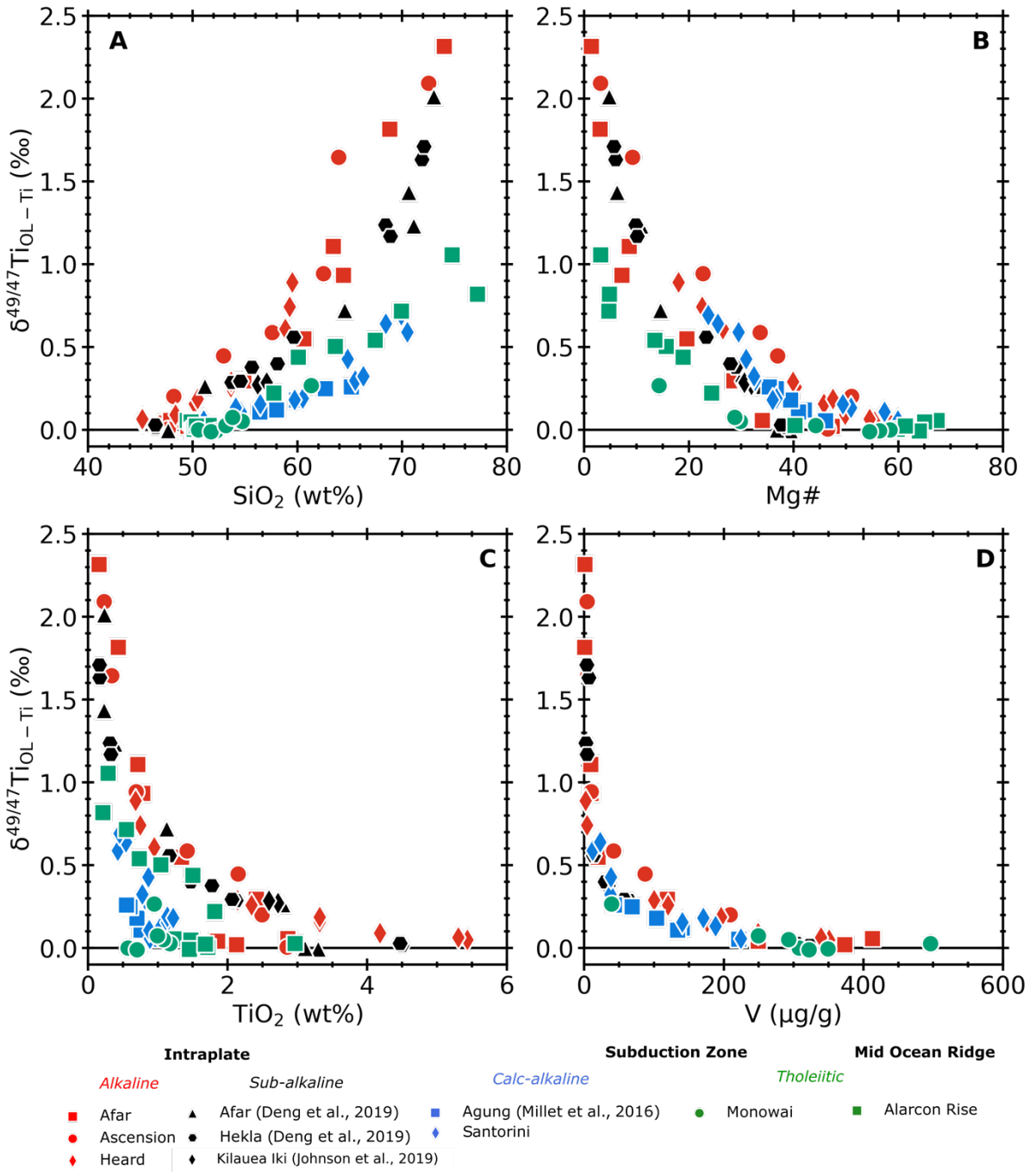

Fig. 3.2 Variations of $\delta^{49/47}$Ti (‰) versus (a) SiO_2 content, (b) Mg#, (c) TiO_2 and (d) V contents (where data is available). Uncertainties for $\delta^{49/47}$Ti (95% confidence interval measurement precision) are smaller than the size of the symbols.

rise contains the first known rhyolites to have originated from a mid ocean ridge setting, with their geochemistry being consistent with petrogenesis via fractional crystallisation (Clague et al., 2018; Portner et al., 2021). The SiO_2 contents of samples selected for this study range from 49 to 77 wt%, 8.9 to 0.1 wt% for MgO. The peak TiO_2 contents of the suite ranges from 0.17 to 3.0 wt% with the peak coinciding with an Mg#

of ~40. Fe-Ti oxide saturation in Alarcon Rise occurs at approximately ~4.5 wt% MgO, with titanomagnetite appearing first in the crystallising assemblage with minor ilmenite occurring in the more evolved lavas (Clague et al., 2018; Portner et al., 2021).

3.4 Results

Mass-dependent Ti isotopic compositions for all reference materials and samples measured in this study are provided in Appendix E2 and illustrated in Fig. 3.2. Data from previous studies (Millet et al., 2016; Deng et al., 2019; Johnson et al., 2019) are included for comparison. Samples of all three magma series define broadly similar trends of increasing $\delta^{49/47}$Ti values with increasing SiO_2 (Fig. 3.2a), consistent with previous studies (Millet et al., 2016; Deng et al., 2019; Johnson et al., 2019), and decreasing Mg# (Fig. 3.2b), TiO_2 (Fig. 3.2c) and V contents (Fig. 3.2d). As first reported by Millet et al. (2016), no significant variation is exhibited across primitive basaltic samples from MORB (tholeiitic), OIB (alkaline) or arc settings (calc-alkaline/tholeiitic), which fall within analytical uncertainty and define the BSE value. Fractionation pathways are offset between the different magma series across a given SiO_2 or Mg# range yet are internally consistent within each magma series (Fig. 3.2). The following section outlines the $\delta^{49/47}$Ti isotopic variation within each magma series.

3.4.1 Alkaline differentiation suites

Alkaline samples measured in this study define a range from +0.01 ± 0.03 ‰ to +2.32 ± 0.03 ‰ (Fig. 3.2). The Afar suite spans the greatest compositional range ($\delta^{49/47}$Ti = +0.03 to +2.32 ‰), in comparison to Ascension (+0.01 to +2.09 ‰) and Heard (+0.05 to +0.89). The range of $\delta^{49/47}$Ti compositions observed in alkaline intraplate lavas is comparable to that recently observed in intraplate lavas measured by Deng et al. (2019; Hekla and Afar) and Johnson et al. (2019; Kilaeua Iki). At a given SiO_2 content, alkaline suites display a greater increase in $\delta^{49/47}$Ti relative to calc-alkaline and tholeiitic magma series, particularly at more silicic compositions (>65 wt% SiO_2; Fig. 3.2). Fig. 3.2 shows that all three alkaline suites exhibit consistent patterns of $\delta^{49/47}$Ti variation with respect to both increasing SiO_2 and decreasing Mg#.

3.4.2 Calc-alkaline differentiation suites

The $\delta^{49/47}$Ti values of all calc-alkaline differentiation suites included in this study vary between +0.05 ± 0.03 ‰ and +0.64 ± 0.02 ‰. The Santorini suite displays a greater range of variation (+0.06 ‰ to +0.64 ‰) compared to Agung (+0.05 ‰ to +0.26 ‰; Fig. 3.2) which essentially encapsulates the entire range of $\delta^{49/47}$Ti variation observed thus far in calc-alkaline arc suites. Calc-alkaline suites display the least fractionation at a given SiO_2 content (Fig. 3.2a), yet conversely display a larger increase in $\delta^{49/47}$Ti values at a higher Mg# in comparison to the tholeiitic differentiation suites of Monowai (tholeiitic island arc) and Alarcon Rise (MOR; Fig. 3.2b). Interestingly, whilst Santorini lavas exhibit a mild TiO_2 enrichment trend at high Mg# (Fig. 3.1b), they also exhibit a resolvable increase in $\delta^{49/47}$Ti over this Mg# range (Fig. 3.2b).

3.4.3 Tholeiitic differentiation suites

The $\delta^{49/47}$Ti composition of samples from the Monowai tholeiitic island arc suite ranges from -0.01 to +0.27, the smallest magnitude of fractionation of any suite measured in this study, whereas the mid-ocean ridge tholeiites from Alarcon Rise range from -0.01 to +1.06 (Fig. 3.2). When plotted against SiO_2, the $\delta^{49/47}$Ti values of the tholeiitic suites occupy a region between the alkaline and calc-alkaline suites (Fig. 3.2a). However, at a given Mg#, tholeiitic suites display lighter $\delta^{49/47}$Ti values compared to both calc-alkaline and alkaline magma series (Fig. 3.2b).

3.5 Discussion - Controls on the Behaviour of Titanium Isotopes during Magmatic Differentiation

3.5.1 Titanium isotope fractionation during magmatic differentiation in different settings

The mass-dependent Ti isotopic composition of samples from alkaline, calc-alkaline, and tholeiitic differentiation suites reveals increases in $\delta^{49/47}$Ti that are correlated with indices of magmatic differentiation such as increasing SiO_2 content and decreasing Mg# (Fig. 3.2 a and b). These results are congruous with and complimentary to earlier work (Millet et al., 2016; Deng et al., 2019). The onset of

resolvable Ti isotope fractionation coincides with a decrease in TiO_2 contents in all suites apart from Santorini (Fig. 3.2c), and in V (Fig. 3.2d). This reinforces the postulation that these trends are the manifestation of fractional crystallisation of Fe-Ti oxides, namely titanomagnetite and ilmenite (Millet et al., 2016; Johnson et al., 2019). Thus, the main driver of Ti isotope fractionation is the proclivity for Fe-Ti oxides to extract light Ti isotopes from the melt, due to the co-ordination number contrast between Fe-Ti oxides (predominantly 6-fold) and melt (dominantly 5-fold with minor 6-fold; see Farges et al., 1996, and Farges and Brown, 1997).

A recent study by Deng et al. (2019), based on measurements of samples from the Afar rift (Pik et al., 2006) and Hekla (Savage et al., 2011), observed that sub-alkaline lavas from intraplate settings are more fractionated than differentiated lavas from other settings at a given SiO_2 content. The data reveal that each of the three-magma series, alkaline, calc-alkaline, and tholeiitic display distinct $\delta^{49/47}Ti$ fractionation patterns across multiple indices of magmatic differentiation (Fig. 3.2). Importantly, the majority of $\delta^{49/47}Ti$ data in the literature have been reported with SiO_2 contents as the sole differentiation index. In this compositional space, alkaline suites display greater Ti isotope fractionation at a given SiO_2 content relative to tholeiitic and calc-alkaline suites respectively (Fig. 3.2a). The offset in Ti isotopic compositions between the three-magma series is particularly apparent at the more evolved end of the fractionation paths (>65 wt% SiO_2), with samples from alkaline suites surpassing the range recorded in the other suites by >1 ‰ (Fig. 3.2). It is noteworthy that the evolved lavas of intraplate settings are depleted in TiO_2 (0.2-0.4 wt% for samples with SiO_2 >65 wt%) relative to those of arc settings (0.3 – 1.0 wt% for samples with SiO_2 >65 wt%). This is consistent with i) large amounts of Fe-Ti oxide crystallisation (e.g. Barling, 1994) and ii) evolved lavas from intraplate settings being the products of high degrees (>80%) of fractional crystallisation (e.g., Chamberlain et al., 2019), hence the fraction of Ti remaining in the melt is lower and in accordance with the lever rule the Ti isotopic variation between primitive and evolved melts is enhanced (Fig. 3.2c). Contrasting patterns of fractionation emerge depending on the differentiation index used (i.e., SiO_2

content or Mg#), which can be utilised to better constrain the mechanisms of Ti isotope fractionation in magmas. In $\delta^{49/47}$Ti-Mg# space, calc-alkaline suites display higher $\delta^{49/47}$Ti values relative to tholeiitic suites at a given Mg# (Fig. 3.2b), with tholeiitic series exhibiting the smallest increase in $\delta^{49/47}$Ti at a given Mg# (Fig. 3.2b). These observations (compared to SiO_2) can be accounted for by the more oxidised and H_2O-rich nature of calc-alkaline magmas, which serves to supress the onset of plagioclase fractionation and enable the earlier crystallisation of clinopyroxene and Fe-Ti oxides during magma evolution (Gaetani et al., 1993; Sisson and Grove, 1993; Grove et al., 2003; Berndt et al., 2005; Feig et al., 2006; Feig et al., 2010; Parman et al., 2011). This effect promotes a faster increase in SiO_2 relative to a slower decrease in Mg# during differentiation of oxidised magmas, thus leading to different trajectories during magma evolution observed between Fig. 3.2 a and b.

The data also show a systematic offset between alkaline and tholeiitic magma suites, with alkaline suites always displaying higher $\delta^{49/47}$Ti relative to tholeiitic suites at a given SiO_2 or Mg#. This might be related to the generally higher TiO_2 content of alkaline lavas, which controls the composition of the oxide phase(s) at equilibrium (Toplis and Carroll, 1995). The effect of melt chemistry on the composition of the oxide phase is best seen in Fig. 3.3, in which the evolution of TiO_2 concentration and FeO^*/TiO_2, which are both strongly controlled by the composition of the oxide phase (e.g. Shellnutt et al., 2009), is shown with respect to SiO_2. The evolution of FeO^*/TiO_2 with respect to SiO_2 can be divided into two distinct stages (stage 1 and stage 2) for each differentiation suite (Fig. 3.3). Each of the three magma series displays a sharp contrast in slope (i.e. $d(FeO^*/TiO_2)/dSiO_2$ and $dTiO_2/dSiO_2$) between the two stages (Fig. 3.3). The slope $d(FeO^*/TiO_2)/dSiO_2$ ranges from negative in stage 1 of tholeiitic suites to positive in alkaline suites. The $d(FeO^*/TiO_2)/dSiO_2$ slopes of stage 2 are consistently more positive than their stage 1 counterparts in each differentiation suite (Fig. 3.3).

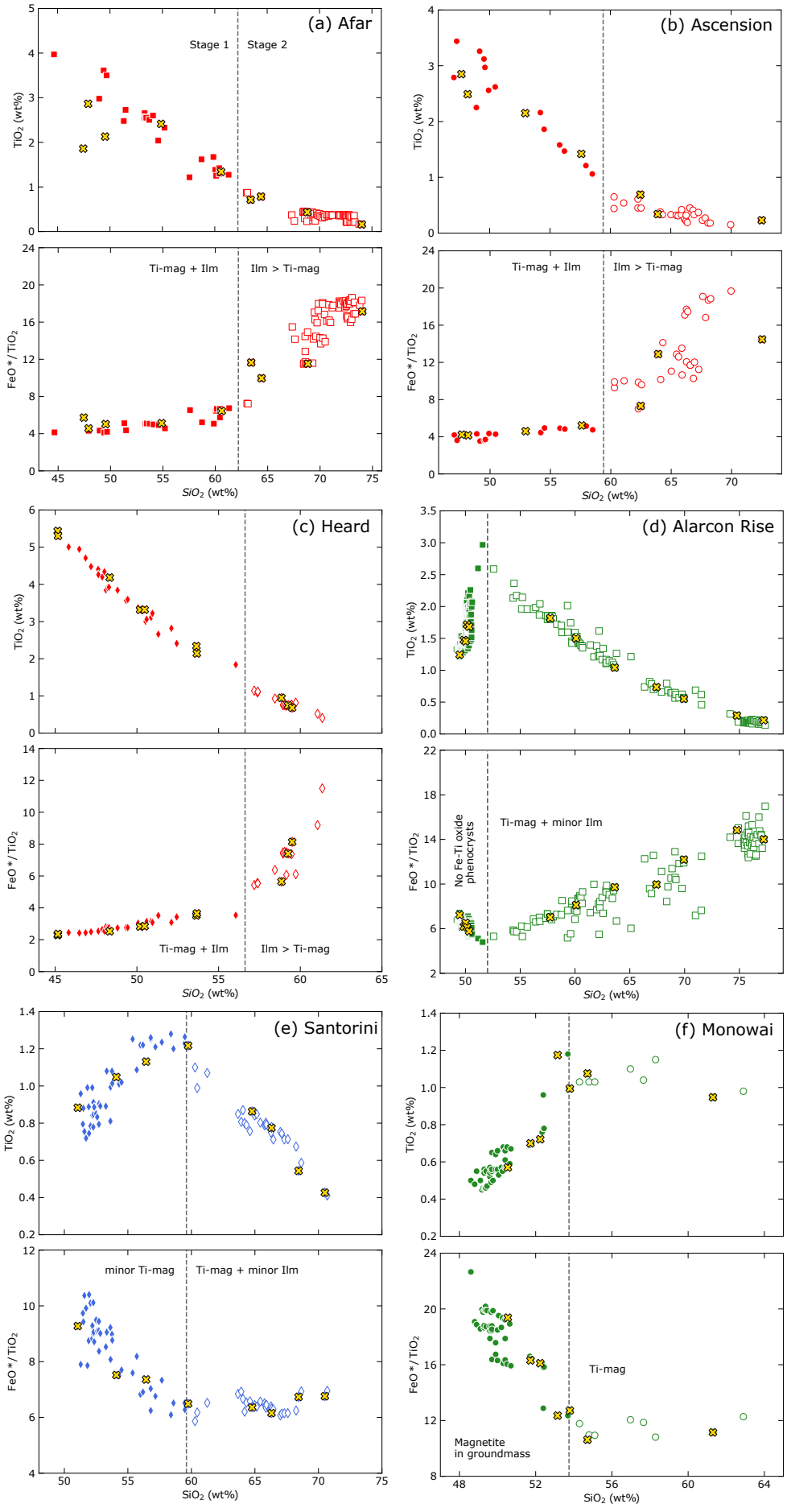
(a) Afar
Stage 1
Stage 2
TiO2 (wt%)
Ti-mag + Ilm
Ilm > Ti-mag
FeO*/TiO2
SiO2 (wt%)
(b) Ascension
TiO2 (wt%)
Ti-mag + Ilm
Ilm > Ti-mag
FeO*/TiO2
SiO2 (wt%)
(c) Heard
TiO2 (wt%)
Ti-mag + Ilm
Ilm > Ti-mag
FeO*/TiO2
SiO2 (wt%)
(d) Alarcon Rise
TiO2 (wt%)
No Fe-Ti oxide phenocrysts
Ti-mag + minor Ilm
FeO*/TiO2
SiO2 (wt%)
(e) Santorini
TiO2 (wt%)
minor Ti-mag
Ti-mag + minor Ilm
FeO*/TiO2
SiO2 (wt%)
(f) Monowai
TiO2 (wt%)
Ti-mag
Magnetite in groundmass
FeO*/TiO2
SiO2 (wt%)

Fig. 3.3 Whole rock TiO_2 vs. SiO_2 and FeO^*/TiO_2 vs. SiO_2 diagrams of the differentiation suites measured in this study. Samples measured for Ti isotopic compositions are marked as gold crosses. Data are reported in Appendix E2. Inflections in both FeO^*/TiO_2 vs. SiO_2 and TiO_2 vs. SiO_2 compositional space, indicated by the dashed lines, define two stages (stage 1 and stage 2) of evolution of each of the suites. These inflections mark either the appearance or change in the modal abundance and composition of Fe-Ti oxides (see section 3.5.2 for details).

The range of $d(FeO^*/TiO_2)/dSiO_2$ displayed in the sample suites is best explained by the crystallisation of oxides of varying compositions, from Ti-poor (negative slopes) to Ti-rich (positive slopes). This is corroborated by petrographic evidence indicating that slope inflections in Fig. 3.3 are the manifestation of changes in the crystallising oxide phase during magmatic differentiation. Indeed, samples that fall within stage 1 of alkaline suites contain high-Ti titanomagnetite (>19 wt% TiO_2) and a minor amount of ilmenite (>48 wt% TiO_2; Table 3.1.), whereas both calc-alkaline and tholeiitic suites lack ilmenite in stage 1. Calc-alkaline suites (Santorini) crystallise minor amounts of titanomagnetite and display a weak negative slope. All tholeiitic suites lack Fe-Ti oxide phenocrysts during stage 1 and display strong negative slopes. The onset of stage 2 in alkaline suites corresponds to the increase in the modal proportion of ilmenite relative to Ti-magnetite (Table 3.1.). In contrast for both calc-alkaline and tholeiitic suites, titanomagnetite becomes dominant and more Ti-rich than in stage 1. This results in $d(FeO^*/TiO_2)/dSiO_2$ that is more positive in stage 2 relative to stage 1 yet less positive than in alkaline suite due to the absence of significant amount of ilmenite.

3.5.2 Modelling Ti isotope fractionation during magmatic differentiation

As noted by Deng et al. (2019) the Ti concentration of silicic melts (>65 wt% SiO_2) from different magmatic series are roughly comparable, yet their $\delta^{49/47}Ti$ compositions differ considerably (Fig. 3.2). This suggests that differences in the crystal phases segregated and/or the total amount of crystallisation during magma evolution in different magma series control the Ti elemental and isotopic budget of magmas. Here, these contrasts are investigated using linear regressions (Fig. 3.4).

The fraction of Ti in a melt (expressed as –ln *f*Ti in order to linearise fractionation relationships, see below) is derived using the relative differences in concentrations of TiO_2 and the average of two highly incompatible trace elements (for which the bulk K_d is <<1 and can effectively be assumed to be 0) that show consistent enrichment patterns with increasing differentiation (Rb and Th, Rb and Ba, Rb and La, and Ba or La where appropriate, see Appendix E2) between any sample and the most primitive sample of each suite as a proxy for the fraction of remaining melt.

Bulk solid-melt fractionation factors ($\alpha_{\text{solid-melt}}$) were derived empirically by taking a weighted least squares linear regression between the fraction of Ti remaining in the melt and the isotopic composition for each differentiation suite. Rearranging the conventional isotopic Rayleigh distillation equation for fractional crystallisation gives:

Eq. 3-1

$$\ln\left(f\mathrm{Ti}\frac{R_A}{R_0}\right) = \alpha \ln f\mathrm{Ti}$$

Where *f*Ti is the fraction of Ti remaining in the melt, R_A/R_0 is the $^{49}Ti/^{47}Ti$ of a sample (A) relative to the most primitive sample (0) and α is the bulk solid-melt fractionation factor. The value of α, and related uncertainties, for a set of samples can then be obtained by weighted least squares linear regression, which one was done for both stages of each sample suite (Fig. 3.4). As there are currently no published trace element data for the Alarcon Rise samples, the fractional crystallisation of this suite was modelled using the Rhyolite MELTS software (Gualda et al., 2012; Fig. 3.5). Using D395-R11 as a staring composition (Appendix E2) crystallisation occurs under parameters similar to those specified by Clague et al. (2018), with 0.2 wt % H_2O, a pressure of 800 bar and oxidation state of QFM-1 (Fig. 3.5). Following the approach of Millet et al. (2016), the Ti isotope evolution of the melt is then calculated using a Rayleigh distillation law and an isotope fractionation factor between Fe-Ti oxides and

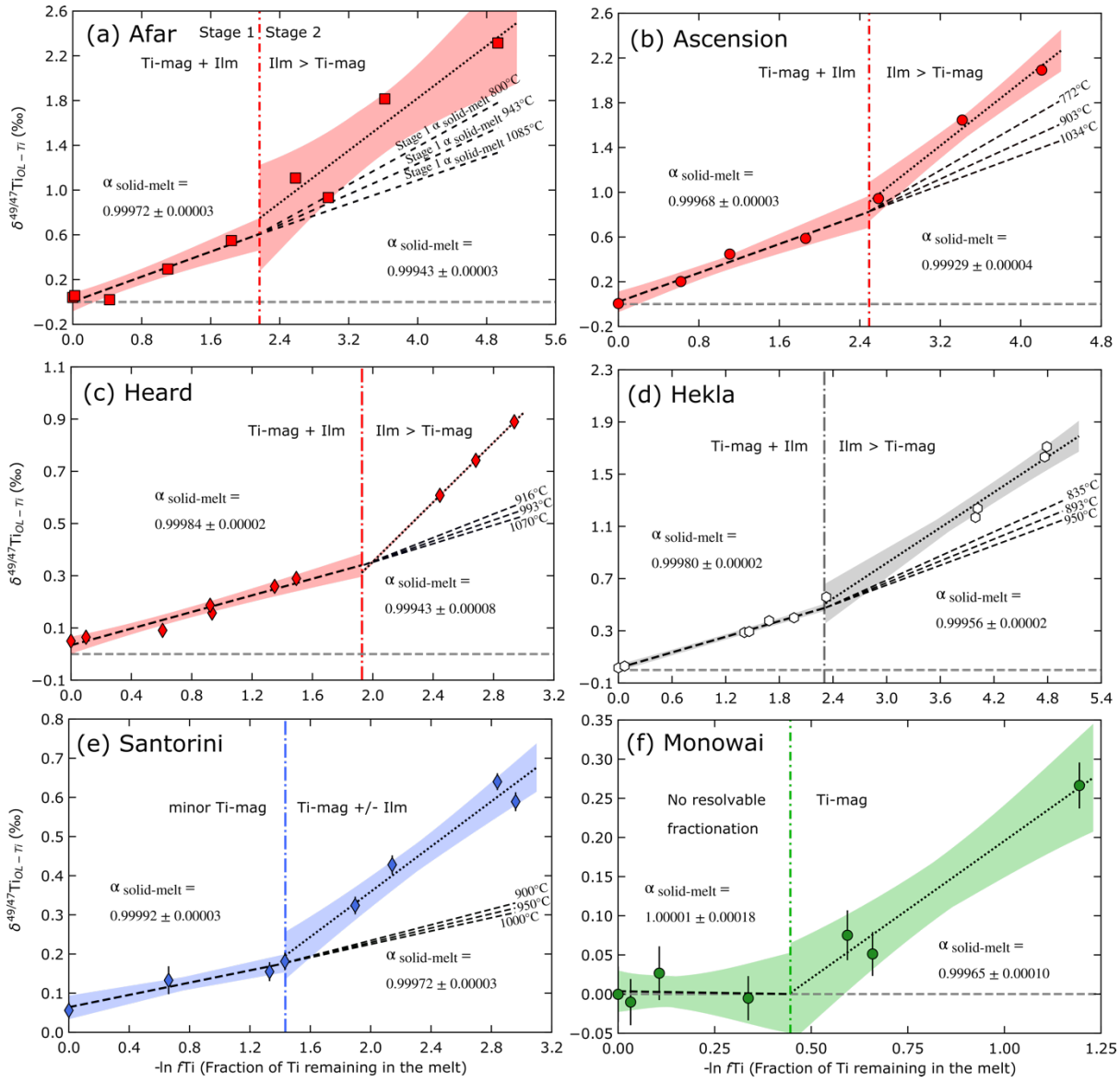

Fig. 3.4 Ordinary least squares linear regressions of the Ti isotopic evolution of differentiation suites from each of the three magma series; (a) Afar (alkaline), (b) Ascension (alkaline), (c) Heard (alkaline), (d) Hekla (data from Deng et al., 2019; sub-alkaline), (e) Santorini (calc-alkaline) and (f) Monowai (tholeiitic). The fraction of Ti remaining in the melt (-ln*f*Ti) was calculated using incompatible trace elements (see Appendix E2). The Afar suite from Deng et al. (2019) could not be considered due to lack of available major and trace element data. Ordinary least regressions were performed for each of the two stages of melt evolution as defined by the major element relationships (Fig. 3.3), with the stage boundaries demarcated by the coloured dashed lines. Bulk $\alpha_{\text{solid-melt}}$ fractionation factors derived from weighted least squares regression (see section 3.5.2 for details). Bulk $\alpha_{\text{solid-melt}}$ values are labelled for each stage and are shown as dashed black lines. Shaded areas denote the 2s error envelope of the ordinary least squares linear regression. Stage 1 $\alpha_{\text{solid-melt}}$ values re-calculated at the recorded temperature ranges for stage 2 (see Table 3.1., temperature ranges for stage 1 and 2 of Hekla were sourced from Höskuldsson et al., 2007; Lucic et al., 2016; Weber and Castro, 2017) are plotted as dashed black lines and show that the temperature decrease during magma differentiation cannot account for the observed range of Ti isotope fractionation (see section 3.5.3 for details).

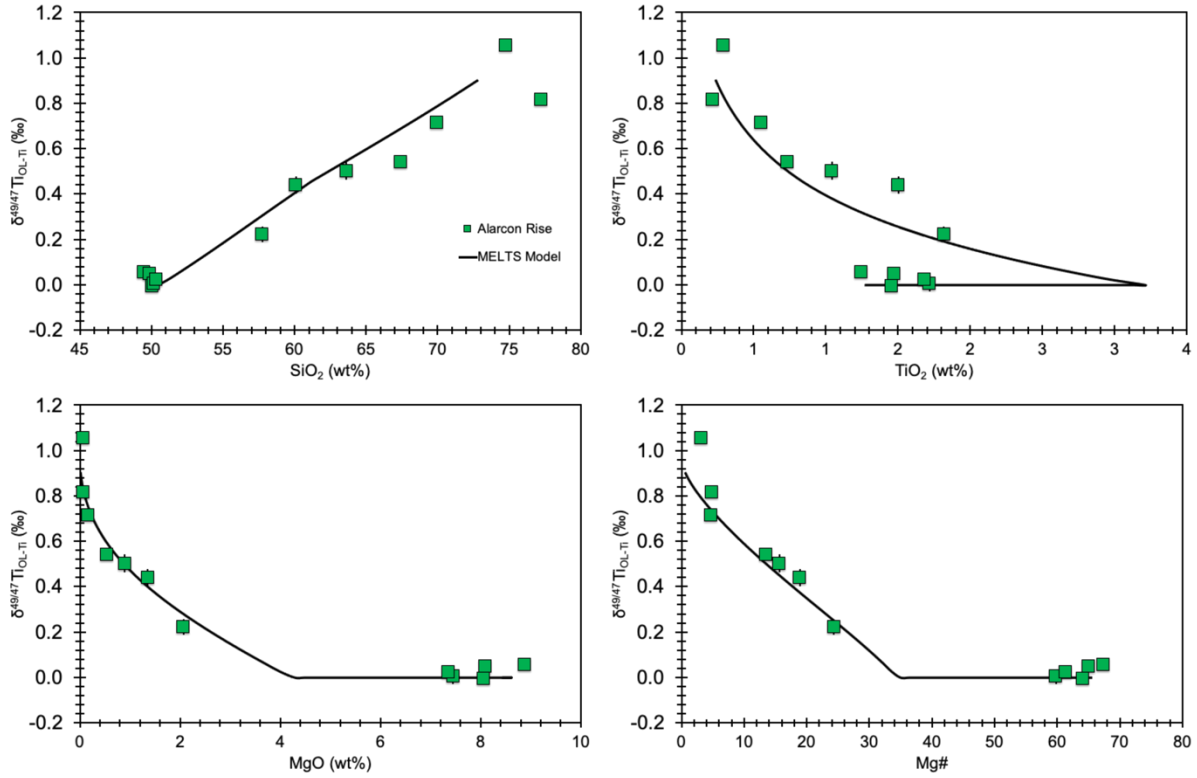

Fig. 3.5 Evolution of Alarcon $\delta^{49/47}$Ti values with respect to a) SiO_2, b) MgO, c) Mg# and, d) TiO_2. The black dashed line represents a fractional crystallisation model produced using Rhyolite-MELTS (Gualda et al., 2012) assigned to fit the Alarcon Rise differentiation suite. Sample D395-R11 was used as a starting composition (see Appendix E2). Crystallisation occurs conditions similar to those specified in Clague et al. (2018); 0.2 wt.% H_2O, an oxidation state of QFM-1 and 800 kbar. Best fit for the data was obtained using a Ti stable isotope fractionation factor between oxides and melt of $\Delta^{49/47}$Ti oxide-melt = $-0.38 \times 10^6/T^2$ (with T in K).

melt ($\Delta^{49/47}Ti_{oxide\text{-}melt}$) weighted according to the proportion of Ti sequestered by Fe-Ti oxides at each step of the model. The best fit for the Alarcon Rise data was achieved using an empirical value of $\Delta^{49/47}Ti_{oxide\text{-}melt} = -0.38‰ \times 10^6/T^2$ (with T in K).

Titanium isotopic fractionation models reveal that no single fractionation factor can account for: (i) the full Ti isotopic evolution of all magma series; and (ii) the range of variation within individual differentiation suites. In all suites where a large range of magma differentiation is captured (i.e., from mafic to silicic magmas), the bulk solid-melt fractionation factors for stage 1 and 2 are significantly distinct (Fig. 3.4). The point at which each linear regression intersects the stage 1/stage 2 boundary from Fig. 3 are consistently within error (Fig. 3.4). Because both stages of magma evolution occur at different temperatures (Table 3.1.), the effect of temperature on the magnitude

of Ti isotope fractionation in stage 1 and 2 within each suite must be examined (Fig. 3.4).

3.5.3 The effect of temperature on Ti isotope fractionation

It has been well established that isotope fractionation factors (expressed as lnα) are proportional to $1/T^2$ (where T is the absolute temperature in Kelvin, e.g., Urey, 1947; Bigeleisen and Mayer, 1947; Schauble, 2004). As such, differences in observed fractionation factors between sample suites could be linked to difference in the temperature of magmatic differentiation between geodynamic settings and/or in magma storage conditions. However, two lines of argument indicate that temperature does not play a major role in the observed Ti isotope fractionation observed in the sample suites.

First, the decrease in temperature from stage 1 to stage 2 for all magma suites could be consistent with the decrease in the bulk $\alpha_{\text{solid-melt}}$. The effect of temperature on modelled bulk crystal-melt fractionation factors was tested by recalculating minimum and maximum $\alpha_{\text{solid-melt}}$ values for stage 1 over the published temperature range of stage 2 for each suite (Fig. 3.4). Temperatures ranges were derived using multiple techniques such as Fe-Ti oxide thermometry and various silicate-liquid thermometers including olivine, plagioclase and clinopyroxene (see Table 3.1. and references therein). The temperature-dependent models reveal that across all three magma series, temperature only has a minor influence on the fractionation patterns, as all models demonstrate that simply decreasing the temperature is not sufficient to alter the stage 1 $\alpha_{\text{solid-melt}}$ in order to reach the increased $\delta^{49/47}$Ti values observed in stage 2 (Fig. 3.4).

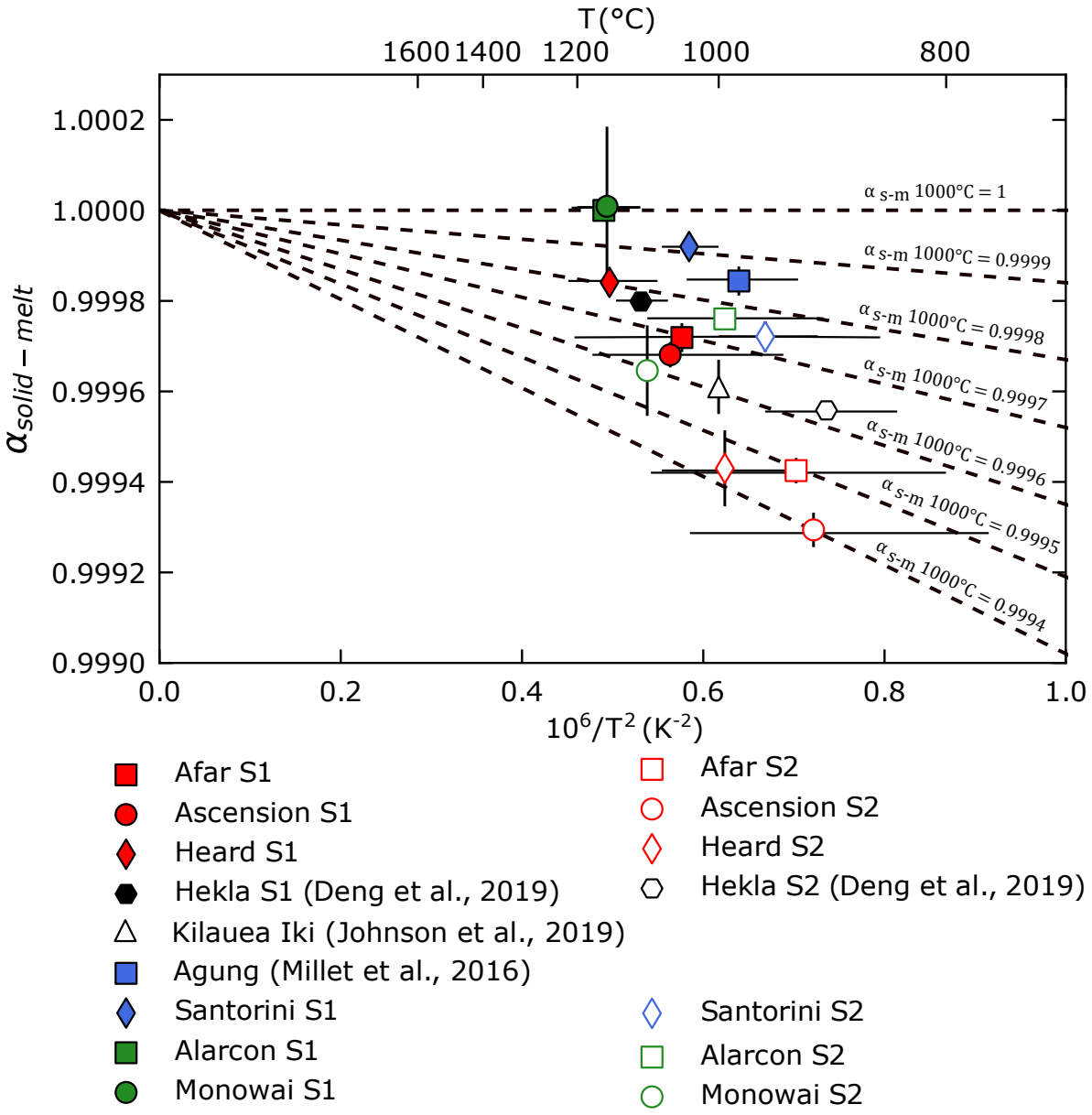

Fig. 3.6 Bulk solid-melt fractionation factors ($\alpha_{solid-melt}$) plotted as a function of $1/T^2$ (K^{-2}). X axis error bars indicate the range of temperature taken from Table 3.1. for stage 1 and 2 (temperature ranges for stage 1 and 2 of Hekla were sourced from Höskuldsson et al., 2007; Lucic et al., 2016; and Weber and Castro, 2017). Dashed black lines indicate linear functions of $\alpha_{solid-melt}$ versus$1/T^2$ (K^{-2}).

Second, the $\alpha_{solid-melt}$ values for both stage 1 and 2 do not follow a simple linear relationship with $1/T^2$ (Fig. 3.6) but instead $\alpha_{solid-melt}$ across all three magma series displays a large variation at a given temperature (Fig. 3.6). Both calc-alkaline and tholeiitic suites consistently display significantly smaller fractionation factors with decreasing temperature (increasing $1/T^2$) compared to alkaline suites (Fig. 3.6) Consequently, temperature only has a secondary control on Ti isotope fractionation

during magma evolution and other factors such as melt chemistry and/or structure govern Ti isotope fractionation during magma differentiation.

3.5.4 Linking contrasting magnitudes of titanium isotope fractionation to melt composition

Titanium-bearing oxides host Ti in 6-fold co-ordinated sites, whereas Ti is dominantly present in 5-fold coordination in silicate melts relative to 6-fold co-ordinated Ti, with 4-fold co-ordinated Ti found in minor amounts only in silicic melts (Farges et al., 1996). Therefore, the appearance of 4-fold co-ordinated Ti during magma differentiation may lead to distinct fractionation patterns and increased isotope fractionation factors in silicic melts relative to mafic melts. The lack of detailed melt structure data for Ti makes it difficult to estimate how melt composition affects the Ti coordination as well as over what range of silica content 4-fold co-ordinated titanium appears and whether it coincides with the boundary between stage 1 and 2 (Fig. 3.3; Fig. 3.4). Nevertheless, the coordination environment in silicate melts can be qualitatively evaluated using an estimate of melt polymerisation such as NBO/T (i.e., the ratio between non-bridging oxygen and tetrahedrally co-ordinated cations; Mills, 1993). Across all the sample suites investigate in this study, it is notable that i) the decrease in NBO/T is monotonic over the entire SiO_2 range and ii) all suites broadly align on the same overall trend, thus indicating no major differences in their respective coordination environment (Fig. 3.7). Therefore, while more detailed studies of Ti coordination in silicate melts are warranted, it appears unlikely that melt structure plays a dominant role in controlling mass dependent Ti isotope variations in magmatic systems. In contrast, the data suggest that Ti isotope fractionation in magmas is controlled by the abundance and composition of oxides in the segregating crystal fraction, which itself is controlled by melt chemistry, especially melt FeO and TiO_2 content (e.g., Toplis and Carroll, 1995). The boundary between stage 1 and stage 2 does not occur at the same proportion of Ti remaining in the melt ($-\ln f$Ti) in all suites, yet it is broadly consistent between suites of the same magma series and corresponds to major inflections in FeO^*/TiO_2 vs. SiO_2. Importantly, the least fractionated suites

also have the most Ti remaining in the melt after stage 1 (c. 50% for tholeiitic series), followed by calc-alkaline (c. 25%) and alkaline (c. 15%). This reflects the amount of Ti partitioning into the oxide phase, which increases from tholeiites to calc-alkaline and alkaline magmas.

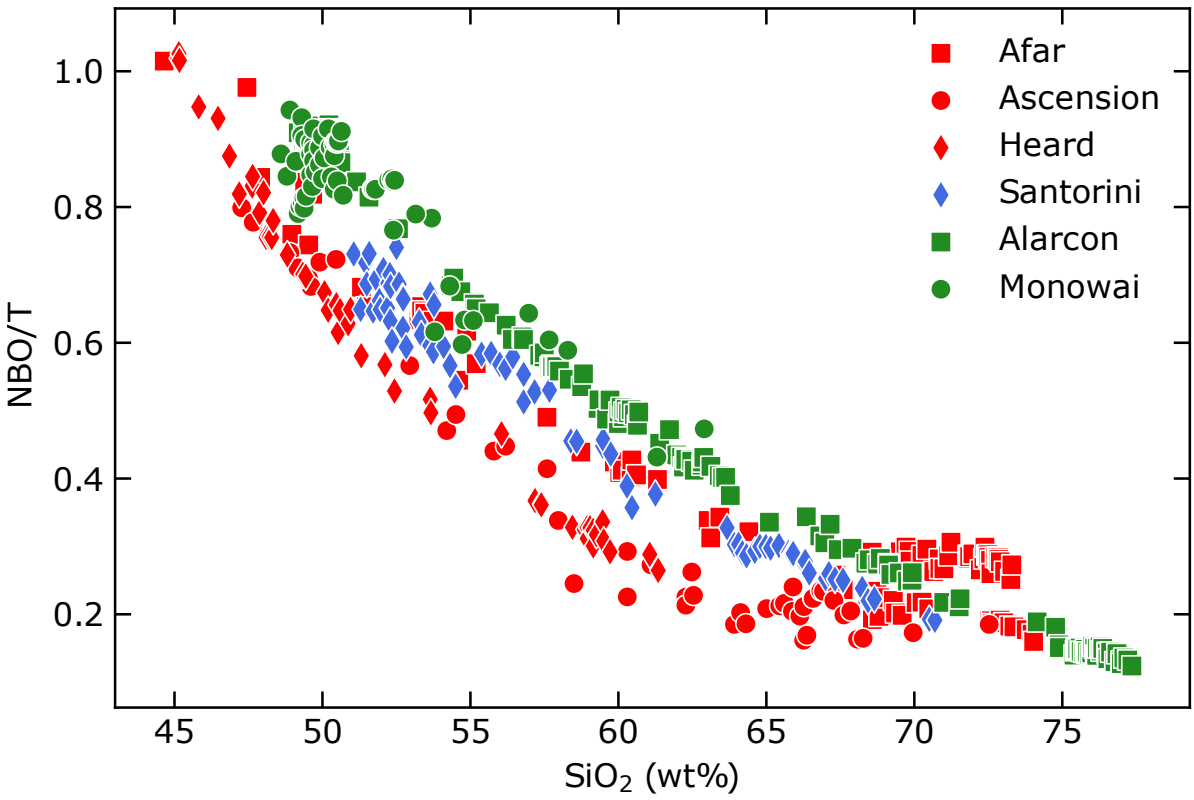

Fig. 3.7 Variation of NBO/T (ratio of Non-Bridging Oxygen and Tetrahedrally co-ordinated cations; Mills, 1993) vs. SiO_2 for all differentiation suites (Alkaline, Calc-alkaline, and Tholeiitic) measured for their Ti isotopic composition in this study.

The melt chemistry control on Ti isotope fractionation in magma is further indicated by a robust covariation between calculated solid-melt fractionation factors and $d(FeO^*/TiO_2)/dSiO_2$ (Fig. 3.8). This correlation holds for all stages and all suites (including those measured by Deng et al., 2019 and Johnson et al., 2019) apart from stage 1 of tholeiitic suites, in which there is no resolvable fractionation (Fig. 3.8). All fractionation factors are recalculated to a common temperature of 1000˚C (Fig. 3.8). The relationship in Fig. 3.8 can be described using a least squares regression as follows:

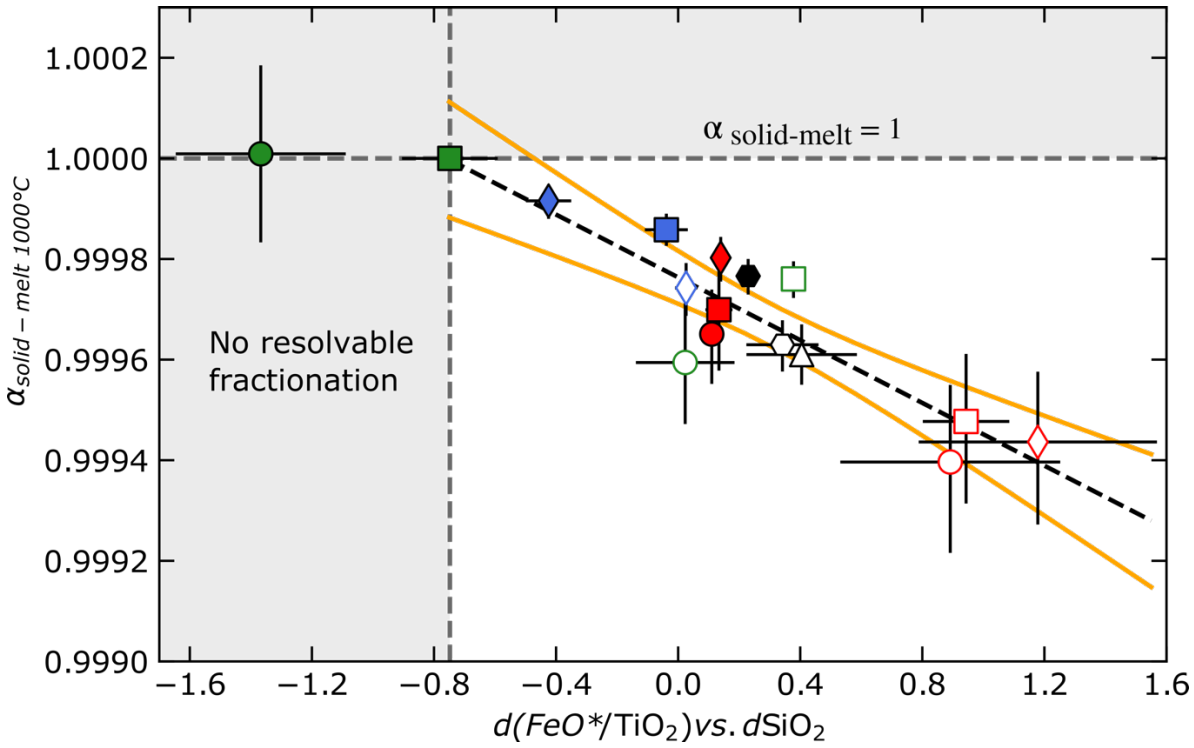

Fig. 3.8 (a) Bulk solid-melt fractionation factors (αsolid-melt) derived from weighted least squares regressions calculated at 1000˚C (Fig. 4) shown as a function of (dFeO*/TiO2)/dSiO2 values taken from Figure 3.3. Error bars display the 2s uncertainty on the data points. Error related to temperature ranges for each stage has been propagated. The black line indicates the least squares regression of the data, with the orange lines indicating the 2s uncertainty of the regression. Data from stage 1 of Tholeiitic suites are excluded from the regression as they display no resolvable fractionation. A co-variation trend (R2=0.75) can be observed between decreasing αsolid-melt and increasing FeO*/TiO2 slope. The (dFeO*/TiO2)/dSiO2 of Hekla is based on a representative dataset sourced from GEOROC (http://georoc.mpch-mainz.gwdg.de/georoc/), which includes all samples from Savage et al. (2011). For Kilauea Iki, (dFeO*/TiO2)/dSiO2 is based on selected whole rock and glass data from Helz et al. (1994) and Greaney et al. (2017) respectively; picrites and olivine basalts have undergone significant accumulation of olivine phenocrysts (Helz, 1987) and were therefore excluded. The value of -0.39 ± 0.06‰ (αsolid-melt = 0.99961, white triangle) produced by Johnson et al. (2019) plotted for comparison and is in good agreement with the co-variation shown in Fig. 3.8. Figure symbols are identical to those shown in Fig. 3.6.

Eq. 3-2

$$For\ \frac{d\left(\frac{FeO^*}{TiO_2}\right)}{dSiO_2} < -0.75\ \propto_{solid-melt} = 1$$

$$For -0.75 < \frac{d\left(\frac{FeO^*}{TiO_2}\right)}{dSiO_2} \leq +1.6:$$

Eq. 3-3

$$\propto_{solid-melt} = -3.1E^{-4}\ (\pm 5E^{-5}) \times \frac{d\left(\frac{FeO^*}{TiO_2}\right)}{dSiO_2} + 0.9998\ (\pm 3E^{-5})$$

This correlation suggests that the Ti content of Fe-Ti oxides plays an important role in controlling Ti isotope fractionation during magmatic differentiation, with Ti-rich oxides having a stronger affinity for light isotopes of Ti than Ti-poor oxides, which is consistent with the results of a recent ab-initio study of inter-mineral Ti isotope fractionation by Wang et al. (2020), with rutile (TiO_2) possessing a greater fractionation factor than that of ilmenite and geikielite ($MgTiO_3$). Wang et al. (2020) did not perform ab-initio calculations for titanomagnetite but postulated that variations in its Ti contents would also likely affect its fractionation factor. This observation is also consistent with studies of other isotope systems, namely Fe isotopes, in which spinel solid-solution plays an important role in controlling equilibrium Fe isotope fractionation factors (e.g. Roskosz et al., 2015). Studies of the crystal structure of Ti-bearing oxides indicate that while the Ti-O bonds in titanomagnetite (0.205-0.206 nm) are longer than in ilmenite (0.197-0.199 nm; Wechsler et al., 1984; Wechsler and Prewitt, 1984) they also display different crystal structure. Titanomagnetite has an inverse spinel structure with a Fd3m space group (Bragg, 1915; Nishikawa, 1915; Barth and Posnjak, 1932) which contains one IV-co-ordinated cation and two VI-co-ordinated cations per four oxygens. At high temperature (>850˚C), Fe and Ti can become randomly distributed between these sites, implying that some Ti in titanomagnetite may be hosted in 4-folded coordination (Wu and Mason, 1981; O'Neill and Navrotsky, 1983; Wechsler and Prewitt, 1984). No such disorder could be observed in the R3 space group of ilmenites up to a temperature of 1050˚C (Wechsler and Prewitt, 1984), where all $Ti^{4+}$is hosted in 6-fold coordination. Thus, the crystal structure of titanomagnetite provides a potential mechanism by which it does not fractionate Ti isotopes as much as ilmenite. In addition, such a mechanism would also imply that the Ti isotope fractionation factor between titanomagnetite and melt should be linked to its Ti content for a given temperature.

3.5.5 Implications of redox conditions and water content on titanium isotope fractionation

The data establishes that at, a given Mg#, calc-alkaline arc suites have a heavier Ti isotopic composition than tholeiitic suites (Fig. 3.2). However, when the three individual arc suites are examined in isolation, they define distinct Ti isotopic fractionation paths (Fig. 3.9). Primitive Santorini samples display an early increase in $\delta^{49/47}$Ti at high Mg#, compared to Agung, which in turn, is heavier than Monowai (Fig. 8). The resolvable Ti isotopic fractionation in basalts and basaltic andesites is a result of the early onset of Fe-Ti oxide crystallisation (Fig. 3.9). Basaltic magmas at Santorini have an estimated initial H_2O content of 3-5 wt% and fO_2 ~ QFM +0.5 (Andújar et al., 2015; Andújar et al., 2016). Based on the methodology of Parman et al. (2010), which utilises Al_2O_3 vs. MgO fractionation paths as a proxy for the suppression of plagioclase to infer pre-eruptive H_2O contents, Dempsey (2013) derived initial H_2O contents of 2-3 wt% for the Agung suite. Based on major element trends and thermobarometry of basaltic glasses, Kemner et al. (2015) concluded that Monowai parental basalts contain between ~0.5-1.1 wt% H_2O and follow a typical tholeiitic and hence a reduced fractionation path.

The onset of Fe-Ti oxide crystallisation is dependent on the interplay between initial melt H_2O contents and fO_2.. Toplis and Carroll (1995; 1996) demonstrated that the saturation temperatures of Fe-Ti oxides are dependent on fO_2, with oxidising conditions in calc-alkaline suites being favourable to the early saturation of titanomagnetite. Increasing the H_2O content in a melt depresses the temperature of when both Fe-Mg silicates and plagioclase appears on the liquidus, whereas magnetite crystallisation is independent of H_2O contents (Sisson and Grove, 1993; Berndt et al., 2005; Feig et al., 2006; Feig et al., 2010). Experimental studies have examined the differentiation pathways of tholeiitic basalts (e.g., Berndt et al., 2005; Feig et al., 2006; Feig et al., 2010) and arc basalts (Sisson and Grove, 1993; Tatsumi and Suzuki, 2009; Andújar et al., 2015; Melekhova et al., 2015) under differing initial H_2O contents and fO_2 conditions. Hydrous experiments on arc basalt starting compositions produced

both a higher modal abundance of Fe-Ti oxides and greater depletions in TiO_2 with increasing H_2O (Tatsumi and Suzuki, 2009; Andújar et al., 2015; Melekhova et al., 2015).

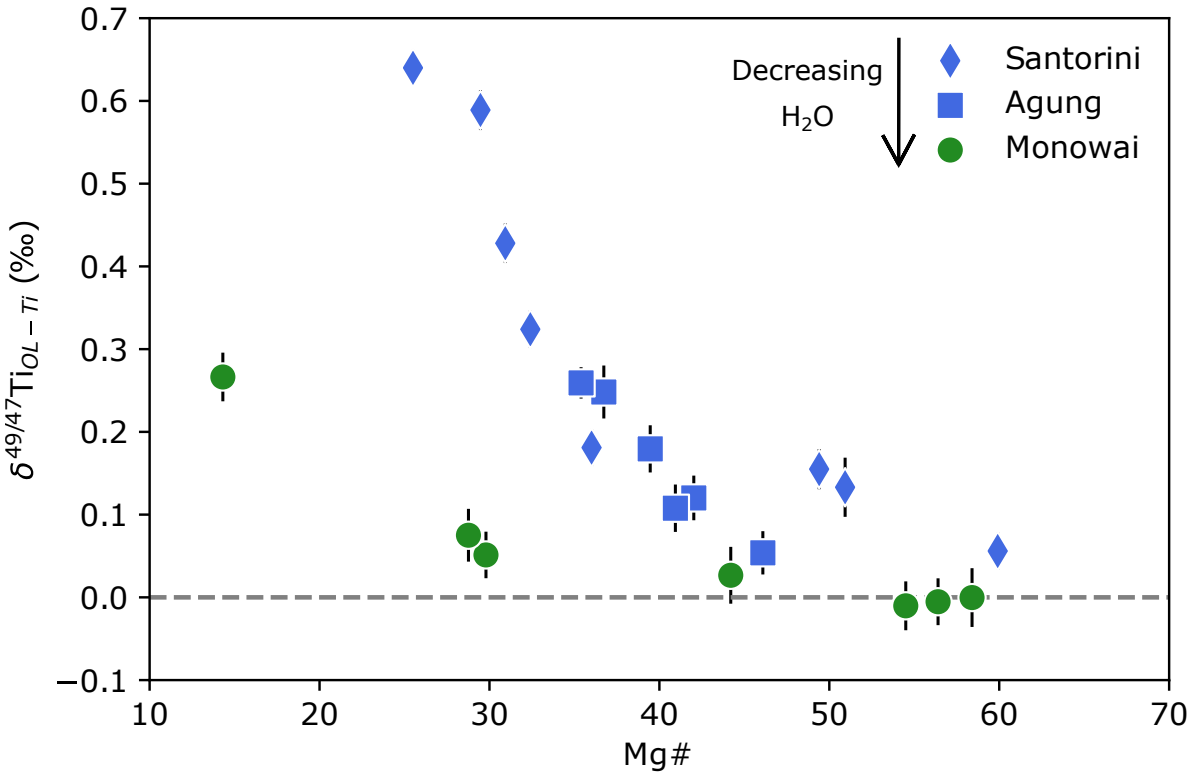

Fig. 3.9 Variations of δ49/47Ti versus Mg# for arc differentiation suites. Distinct fractionation patterns are observed for the different suites, with suites deriving from wetter and more oxidised parental magmas displaying earlier onset of Ti isotope fractionation linked to earlier onset of oxide saturation (see section 3.5.5 for details).

Therefore, the pattern of Ti isotope fractionation observed in the arc differentiation suites is consistent with earlier oxide saturation, specifically titanomagnetite, in more hydrous and oxidised magmas (Gaetani et al., 1993; Sisson and Grove, 1993; Grove et al., 2003), such as Santorini and Agung. The latter have significantly higher initial H_2O contents than Monowai which sets differentiating magmas under different fO_2 conditions on distinct but subparallel trends in $\delta^{49/47}Ti$ versus Mg# space (Fig. 3.9). These results indicate that variation of Ti isotope fractionation between different arc differentiation suites is in part a function of contrasting magma water content and hence redox conditions. Measurements of Ti isotopic variations in other arc differentiation suites that have well-constrained redox

and H_2O information, will allow the calibration of Ti isotopes as a novel isotopic proxy for H_2O contents and fO_2 conditions in arc magmas.

3.6 Conclusions

This study presents a comprehensive investigation of the behaviour of mass dependent Ti isotope variations in terrestrial magmatic systems to deduce the controls on its isotopic fractionation. The main conclusions of this study are as follows:

i. There are contrasting patterns of Ti isotope fractionation during magmatic differentiation between different magmatic environments related to the fractional crystallisation of isotopically light Fe-Ti oxides. Of the investigated magma series, alkaline differentiation suites from intraplate settings display the most substantial variation in their Ti isotopic composition ($\delta^{49/47}Ti$ = +0.01 to +2.32‰), followed by tholeiites (-0.01 to +1.06‰) and calc-alkaline suites (+0.06 to +0.64‰).

ii. The co-evolution of FeO^*/TiO_2 and $\delta^{49/47}Ti$ in differentiating magmas indicates that magnitude of Ti isotopic fractionation is dominantly controlled by the composition and abundance of Fe-Ti oxides. This, in turn, is linked to the Fe-Ti contents of primitive magmas. Alkaline suites have a much higher FeO^* and TiO_2 melt content which enables the early crystallisation of titanomagnetite and ilmenite, and a higher modal abundance of Fe-Ti oxides in general. In contrast, titanomagnetite serves as the dominant control of the Ti budget in the other suites.

iii. Arc suites show different Ti isotope fractionation paths that scale with the redox state and H_2O content of parental magmas. Hydrous, oxidised calc-alkaline suites like Santorini and Agung display an enrichment in heavier Ti isotopes at a given Mg# relative to drier and more reduced arc tholeiitic suites such as Monowai.

Chapter 4: Empirical and Experimental Constraints on Fe-Ti Oxide-Melt Titanium Isotope Fractionation Factors

4.1 Abstract

Studies of the titanium (Ti) isotope composition of terrestrial igneous rocks have revealed significant mass-dependent variations, with i) felsic rocks exhibiting isotopically heavier compositions in comparison to mafic rocks; and ii) alkaline magmas displaying heavier Ti isotope compositions than tholeiitic and calc-alkaline magmas at similar SiO_2 content. This fractionation pattern is the manifestation of Fe-Ti oxide-melt equilibria, with light Ti isotopes preferentially sequestered by Fe-Ti oxides, which results in a progressive enrichment of heavy isotopes in co-existing melt during magmatic differentiation. Quantitative constraints on equilibrium Ti isotope fractionation between different species of Fe-Ti oxides (titanomagnetite, ilmenite and rutile) and silicate melts are, however, still lacking. To address this, I have measured the Ti isotope composition of co-existing Fe-Ti oxides and groundmass or silicate melt in both natural lavas from contrasting tectonic settings (Heard Island and Santorini), and experimental run products (rutile-melt). All Fe-Ti oxide phases analysed were consistently isotopically lighter than their host groundmass or silicate melt. Ilmenite and rutile possess relatively homogeneous $\Delta^{49/47}Ti$ values. The observed difference in Ti isotope composition between these phases and melt is primarily reflective of small differences in their Ti-O bond length, with ilmenite being isotopically lighter ($\Delta^{49/47}Ti_{ilmenite\text{-}melt}$ at 1000 K = -0.59±0.04‰) compared to rutile ($\Delta^{49/47}Ti_{rutile\text{-}melt}$ at 1000 K = -0.41±0.09) due to slightly longer Ti-O bonds in ilmenite. In contrast, the variation in $\Delta^{49/47}Ti$ observed between titanomagnetite and groundmass increases as a function of TiO_2 contents with $\Delta^{49/47}Ti_{titanomagnetite\text{-}melt}$ values at 1000 K ranging up to -1.12‰ in Ti-rich titanomagnetite (~23 wt.% TiO_2) from Heard Island compared to -0.64‰ in Santorini (~13 wt.% TiO_2), which could be interpreted as resulting from a weaker crystal lattice due to strain from exchange of smaller Fe^{3+} ions with larger Fe^{2+} and Ti^{4+} ions during magnetite-ulvöspinel solid solution. These results are consistent with

fractionation factors inferred from Ti isotopic analyses of mineral separates and ab-initio calculations. Finally, these fractionation factors, in combination with Ti isotope fractionation factors for silicate minerals proposed by previous studies to successfully model the behaviour of Ti isotopes during partial melting of Earth's mantle as well as fractional crystallisation of magmas from distinct magma series.

4.2 Introduction

Studies investigating the mass-dependent titanium (Ti) isotope variation have recently gained momentum, with Ti isotopes displaying great potential as a novel tool to trace terrestrial magmatic and sedimentary processes (Millet et al., 2016; Greber et al., 2017a; Greber et al., 2017b; Johnson et al., 2019; Hoare et al., 2020; Zhao et al., 2020; Klaver et al., 2021) as well as lunar and other extra-terrestrial magmatism (Millet et al., 2016; Greber et al., 2017b; Kommescher et al., 2020; Rzehak et al., 2021; Williams et al., 2021). Several of these studies have previously demonstrated the potency of Ti isotope variations as a tracer of Fe-Ti oxide-melt equilibria. Evolved melts invariably display higher $\delta^{49/47}$Ti relative to primitive melts, which is likely driven by the fractional crystallisation of isotopically light Fe-Ti oxides, thereby progressively enriching the melt with heavy isotopes during fractional crystallisation (Millet et al., 2016; Deng et al., 2019; Johnson et al., 2019; Hoare et al., 2020). The empirical evidence that Fe-Ti oxides appear to prefer the lighter isotopes of Ti is bolstered by the difference in coordination of Ti between oxides and silicate; Ti primarily occupies a 5-fold coordination in silicate melts and 6-fold coordination in Fe-Ti oxides (Farges et al., 1996a; Farges et al., 1996b; Farges and Brown, 1997). This coordination contrast serves as the main mechanism driving Ti isotope fractionation in accordance with stable isotope theory (Bigeleisen and Mayer, 1947; Urey, 1947; Schauble, 2004). Contrasts in the magnitude of $\delta^{49/47}$Ti variation have also been documented among magmas from different tectonic settings with evolved melts from Ti-rich alkaline intraplate magmas exhibiting significantly greater Ti isotope variation compared to those from tholeiitic and calc-alkaline magmas (Deng et al., 2019; Hoare et al., 2020;

Zhao et al., 2020). Hence, the magnitude of Ti isotope fractionation observed during magmatic differentiation is controlled additionally by melt TiO_2 content and redox conditions, both of which influence the timing of Fe-Ti oxide crystallisation, modal abundance and composition of Fe-Ti oxides that crystallise (Toplis and Carroll, 1995; Hoare et al., 2020). As such, Ti isotopes have the potential be to utilised as a proxy for the geodynamic origins of magmas throughout geologic history (Greber et al., 2017a; Aarons et al., 2020; Hoare et al., 2020).

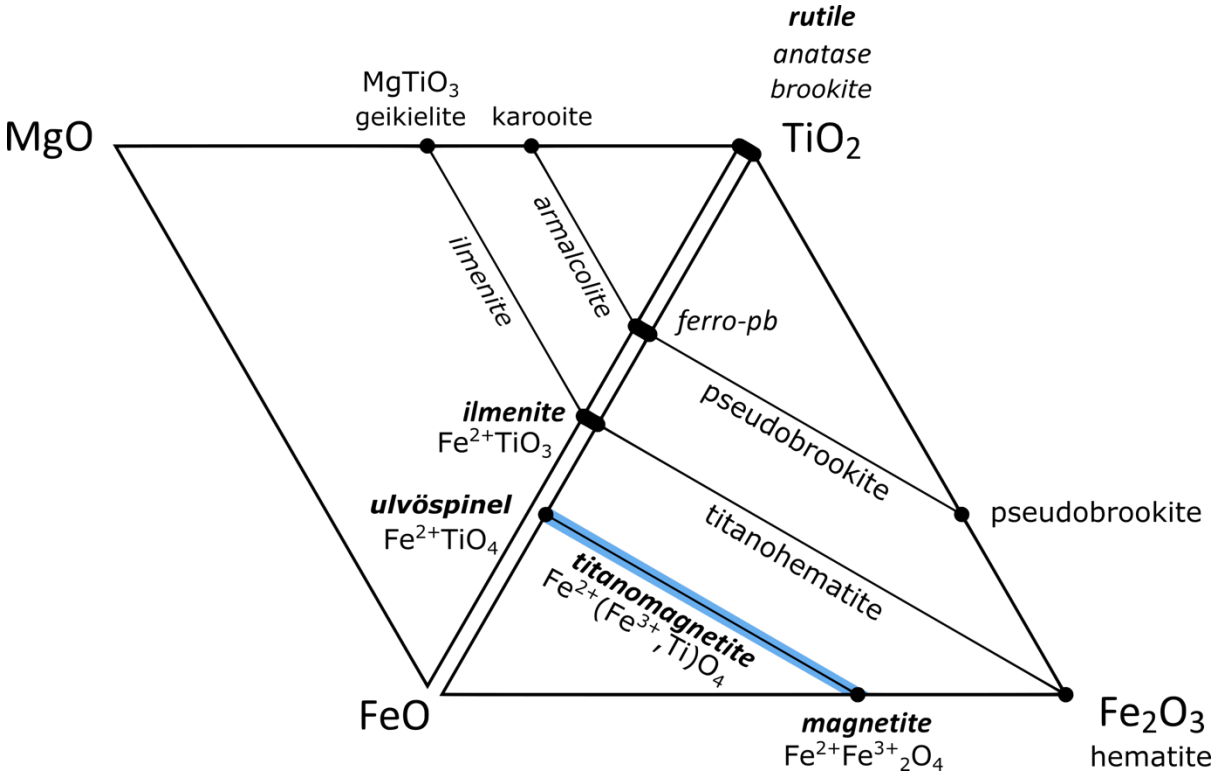

Fig. 4.1 TiO_2-FeO-Fe_2O_3 and TiO_2-MgO-FeO ternary diagrams showing the compositional diversity of different Fe-Ti oxide species. The lines denote high temperature solid solutions (ulvöspinel-magnetite, hematite-ilmenite, pseudobrookite-ferropseudobrookite, geikielite-ilmenite, and karooite-armalcolite). The boldened mineral species and highlighted solid solutions are the focus of this study.

Measurements of bulk Fe-Ti oxides separates have confirmed they are isotopically lighter in comparison to co-existing melt, groundmass, and silicates minerals (Johnson et al., 2019; Mandl, 2019; Greber et al., 2021; Nie et al., 2021; Rzehak et al., 2021). However, studies of bulk mineral separates, while useful, are limited by the inability to separate different co-existing oxides for analysis (e.g., titanomagnetite+ilmenite) as well as by the lack of critical petrographic information pertaining to mineral-melt equilibrium. Hence, even though quantification of Fe-Ti

oxide–melt Ti isotope fractionation factors is key to fully develop Ti isotopes into a mature petrological tool, such quantitative fractionation factors are currently lacking. Important aspects that require attention are the effects of mineral composition (e.g., the magnetite-ulvöspinel solid-solution; Fig. 4.1) and the full range of Ti isotope variation in other Fe-Ti oxide phases such as ilmenite and rutile (Fig. 4.1), which remain unconstrained.

In this chapter I present measurements of the Ti isotope composition of individual Fe-Ti oxide phenocrysts (titanomagnetite, ilmenite, and rutile) and their co-existing silicate melt or microcrystalline groundmass. Using micro-milling, I sampled two experimental run products (rutile-melt; Klemme et al., 2005), and six lavas (three per suite) from Heard Island (alkaline, intraplate) and Santorini (calc-alkaline, subduction zone). Measurement of individual Fe-Ti oxides from contrasting melt compositions (intraplate vs. subduction zone) enables us to further explore the controls of both melt and Fe-Ti oxide composition on the magnitude of Ti isotope fractionation during magmatic differentiation. Once the mechanics of Ti isotope fractionation are better constrained these fractionation factors are then be applied to forward modelling of igneous processes such as mantle melting and magmatic differentiation.

4.3 Sample Petrography

A petrographic summary and modal phase assemblages for all samples used in this study are provided in Table 4.1. Fe-Ti oxide compositions are given in Appendix E3. A brief petrographic description of the natural sample sets (Heard Island and Santorini) and the rutile-melt experiments is provided in the following section.

4.3.1 Santorini

The island of Santorini is located in the Aegean sea (Greece) and forms part of the South Aegean Volcanic Arc (e.g., Druitt et al., 1999). The three samples (Table 4.1) selected for use in this study are <500 ka and form part of a low pressure, medium-K

Table 4.1 Modal abundances (modal %) of the main phases within Heard Island and Santorini samples selected for micro-milling. Mineral abbreviations are from Whitney and Evans (2010).

Suite	Sample	Modes		% Phenocrysts						
		Matrix	Crystals	Mag	Ilm	Ol	Cpx	Opx	Pl	Amp
Heard Is.	HB24	39	61	3	9	22	63	-	3	-
	65054	89	11	3	5	21	58	-	13	-
	65019	84	16	2	1	11	24	-	44	18
Santorini	AAS-021	70	30	6	-	-	39	≤1	54	-
	AAS-027	65	35	2	-	-	17	≤1	81	-
	AAS-028	72	28	4	-	-	17	≤1	78	-

calc alkaline differentiation sequence (Nicholls, 1971; Huijsmans et al., 1988; Huijsmans and Barton, 1989; Andújar et al., 2015; Andújar et al., 2016). Sample AAS-021 is an andesite from Mt. Mikro Profitis Ilias, whereas AAS-027 and -028 are samples from the 1940–1941 and 1866 dacitic lava flows of Nea Kameni, respectively (Klaver et al., 2016a; Klaver et al., 2016b). The samples contain variable proportions of euhedral to subhedral phenocrysts (50-500 μm) of clinopyroxene, plagioclase, and magnetite, with minor orthopyroxene and apatite, set within a microcrystalline groundmass (Fig. 4.2a). Titanomagnetites are predominantly euhedral and possess relatively homogeneous compositions across the three samples (13-15 wt.% TiO_2; Appendix E3), with no compositional zoning observed in individual phenocrysts (Fig. 4.2a, b), which indicates titanomagnetite and the melt are in equilibrium. However, some titanomagnetite crystals were observed with fine exsolution lamellae of slightly higher TiO_2 contents (19-21 wt.%), which is typically the result of sub-solidus cooling. Of the targeted crystals, only one (AAS-021 G3-M1) exhibited these fine Ti-rich lamellae.

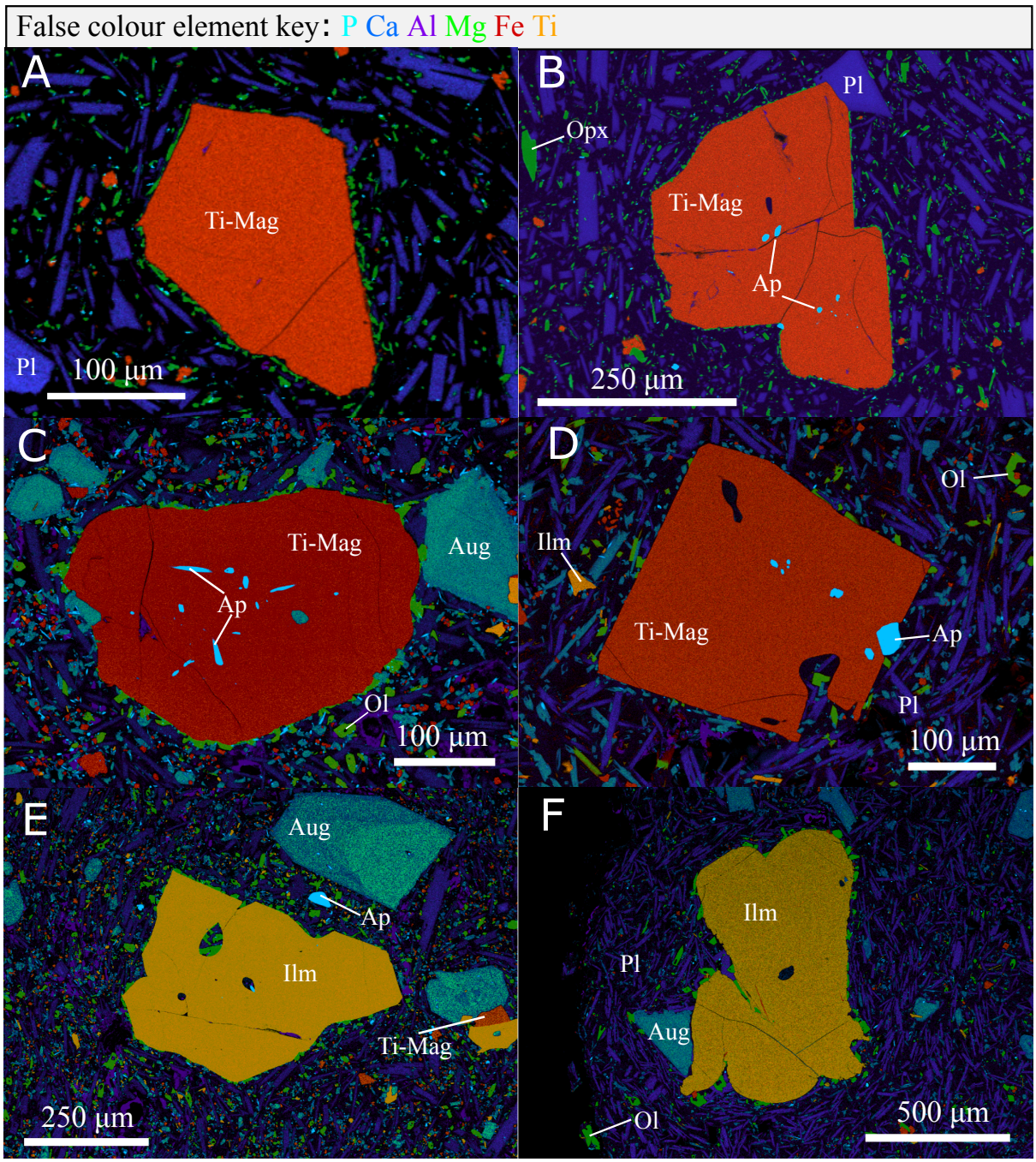

Fig. 4.2 False colour element maps of Fe-Ti oxides from Santorini and Heard Island samples. Mineral abbreviations shown in the figure are in accordance with those defined by Whitney and Evans (2010). a) Titanomagnetite phenocryst (LH 010) in rhyodacite AAS-028 from Santorini. b) Titanomagnetite phenocryst (LH 005) in rhyodacite AAS-027 from Santorini. Note the presence of minor apatite inclusions (bright blue). The groundmass includes small crystals of orthopyroxene (green) and small laths of plagioclase (purple). c) Titanomagnetite (LH 012) in basanite HB24 (Heard Island). The groundmass includes olivine (green), zoned titan-augite (pale blue to blue-green), small laths of plagioclase (purple) and small crystals of titanomagnetite (red/orange) and ilmenite (yellow/light orange). d) Titanomagnetite (LH 016) phenocryst in basaltic trachyandesite 65054 (Heard Island). e) Ilmenite phenocryst in HB24 (LH 019). f) Ilmenite (LH 012) phenocryst in 65054. Note that all the Fe-Ti oxides are compositionally un-zoned.

4.3.2 Heard Island

Heard Island is located on the Kerguelen Plateau in the southern Indian Ocean. The lavas included in this study are from the ≤1 Ma Mt. Dixon volcanic cone and belong to the Laurens Peninsula series (LPS) (Clarke et al., 1983; Fox et al., 2021). The samples have previously been measured for major- and trace elements contents as well as radiogenic isotopes (Barling, 1990; Barling and Goldstein, 1990; Barling, 1994; Barling et al., 1994). Whole rock $\delta^{49/47}$Ti measurements are reported in Hoare et al. (2020). The three Heard Island samples (Table 4.1) selected for micro-milling are HB24 (basanite), 65054 (basaltic trachyandesite), and 65019 (trachyandesite) that fall on the liquid line of descent observed in the LPS (Barling, 1990; Barling, 1994; Hoare et al., 2020). A common feature present across all LPS lavas is the high modal abundance of Fe-Ti oxides (ilmenite and titanomagnetite), which is reflective of the high TiO_2 contents (> 5 wt.%) of their parental magma (Barling, 1994; Hoare et al., 2020). Sample HB24 is a porphyritic basanite with ~30% phenocrysts hosted within a microcrystalline groundmass comprised of olivine, augite, plagioclase, ilmenite and titanomagnetite (Fig. 4.2c, e). Minor amounts of apatite and sulfide are also present. The phenocryst assemblage is identical to that of the groundmass. Phenocrysts are euhedral to subhedral and range from 0.1 to 1 mm in size. Some phenocrysts also contain minor inclusions of apatite (Fig. 4.2 c, e). Sample 65054 is a basaltic trachyandesite with ~10-15% phenocrysts within a vesicular microcrystalline groundmass. The mineral assemblage of 65054 is like HB24, with phenocrysts of olivine, augite, plagioclase, ilmenite and titanomagnetite (Fig. 4.2d, f). Sample 65019 is a trachyandesite with ~5-10% phenocrysts in a vesicular microcrystalline groundmass. The phenocryst assemblage of 65019 is comprised of augite, plagioclase, ilmenite, titanomagnetite, kaersutitic amphibole, and minor amounts of biotite. Samples 65054 and 65019 are noticeably less phyric than HB24 (Fig. 4.2); in both samples, phenocrysts are euhedral to subhedral and range from 0.1 to 0.5 mm in size. Fe-Ti oxide compositions are relatively homogenous across all three samples, exhibiting a narrow range of variation in TiO_2 contents from 21-23

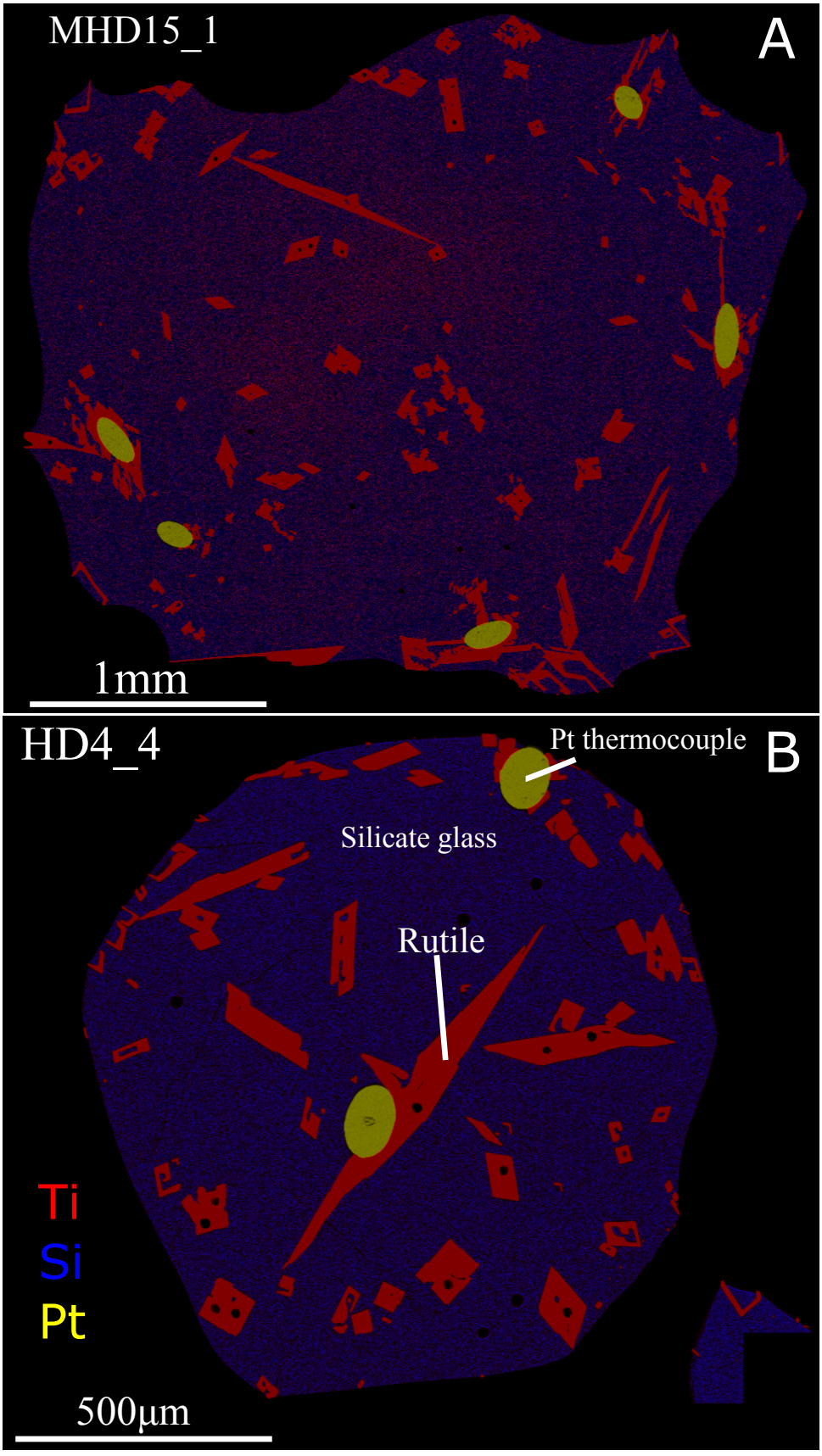

Fig. 4.3 False colour element maps of rutile-melt experimental run products; a) MHD15_1, and b) HD4_4. Rutile (red), either appear as acicular needles or tabular euhedral crystals, surrounded by silicate glass (blue). The platinum thermocouple is also shown (yellow).

wt.% in titanomagnetite and 47-49 wt.% in ilmenite (Appendix E3). In addition to Fe-Ti oxides, sample 65019 also possesses other Ti-bearing phases, mainly kaersutite (~6-8 wt.% TiO_2) and minor amounts of biotite (~8-10 wt.% TiO_2) (Barling, 1994). The predominantly euhedral habit and lack of compositional zoning in Fe-Ti oxides in these Heard Island samples indicate they are in equilibrium with their host melt.

4.3.3 Rutile-melt experiments

The rutile-melt experimental run products MHD15_1 and HD4_4 used in this study are from Klemme et al. (2005) and are comprised entirely of rutile crystals and quenched silicate glass (Fig. 4.3). In both experiments, rutile crystal size ranges from ~50-600 μm (Fig. 4.3) and exhibit no evidence of zoning or the presence of mineral inclusions (Fig. 4.3), indicating they are equilibrium with the melt. The experimental procedure and starting composition for these runs are given in Klemme et al. (2005), and only a short description is provided here: both experiments analysed in this study were conducted using an andesitic starting composition (SKHDAN1) in a 1 atm. furnace and were run at a final run temperature of 1250°C, redox conditions (in units of log fO_2) were set at -0.96 and -4.0, with run duration times of 57 and 49 hours for MDH15_1 and HD4_4 respectively.

4.4 Results

4.4.1 Fe-Ti Oxide Oxide Geothermometry and Oxygen-Barometry

Coexisting touching Fe-Ti oxide pairs (ilmenite and magnetite) were found in all three Heard Island samples. The ILMAT program (Lepage, 2003) was used to calculate FeO/Fe_2O_3 utilising the method of Carmichael (1966), and also to check the stoichiometry. Providing the Fe-Ti oxide pairs showed no compositional zoning and passed the Mg/Mn equilibrium test of Bacon and Hirschmann (1988), the Fe-Ti oxide geothermometer and oxygen barometer of Ghiorso and Evans (2008) was applied using the ENKI Cloud app front end (Ghiorso and Prissel, 2020) to determine the temperature and oxygen fugacity (relative to the Nickel-Nickel oxide; NNO buffer). For samples 65054 and 65019, coexisting touching pairs were less common than in

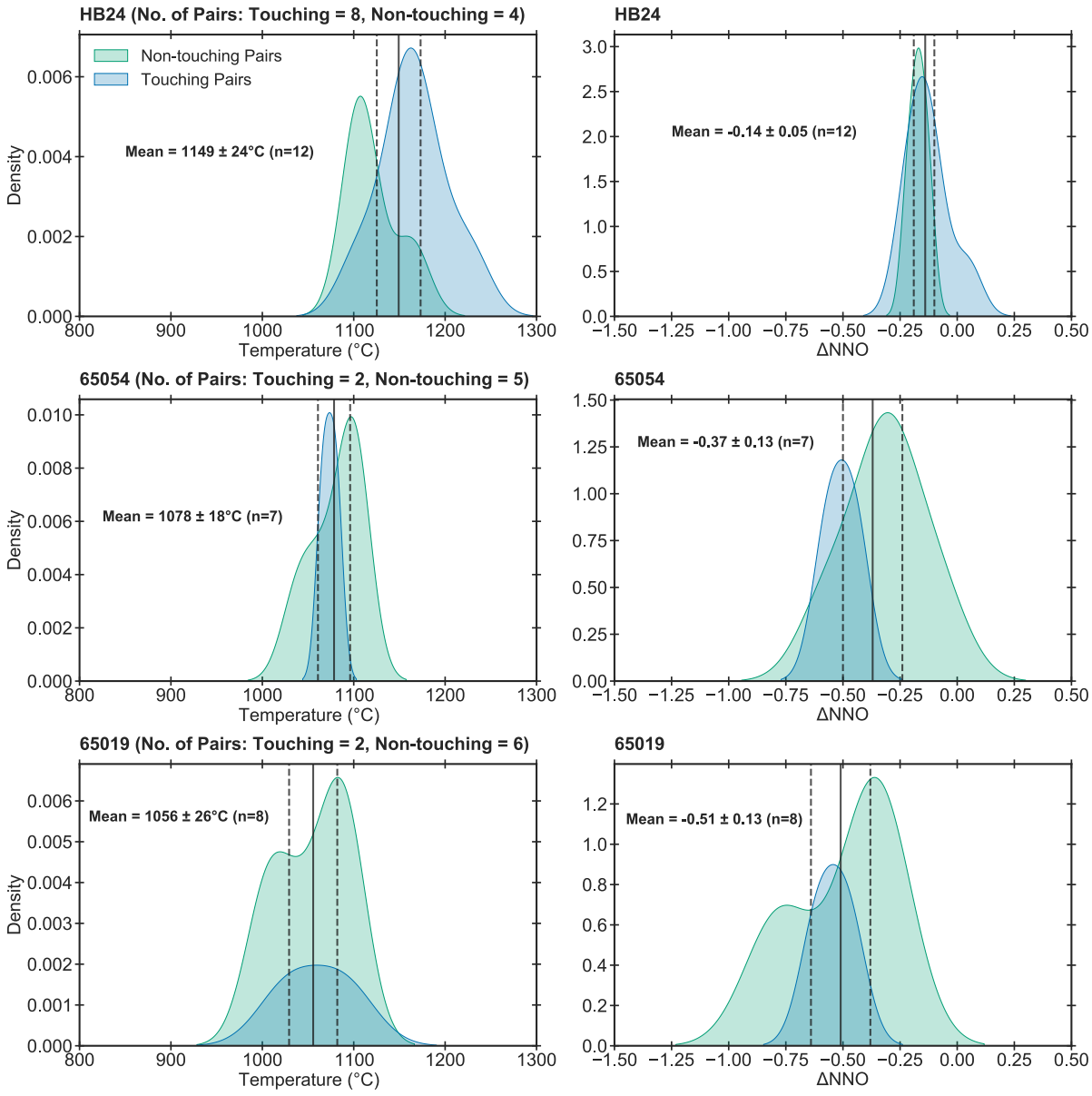

Fig. 4.4 Kernel density estimates (KDE) of temperature and fugacity values derived from non-touching (green) and touching Fe-Ti oxide pairs (ilmenite and titanomagnetite). Uncertainties (dashed lines) on the mean values (solid lines) are reported as 2se.

HB24 and thus adjacent non-touching Fe-Ti oxides were selected using the same criteria as for touching pairs to supplement the touching pairs. The temperature and fO_2 values derived from both touching and non-touching pairs overlap and are in general agreement (Fig. 4.4 and Fig. 4.5). Temperatures based on the Fe-Ti oxide thermometer range from 1103 to 1227 ºC (n=11) for HB24, 1039 to 1103 ºC (n=7) for 65054, and 1003 to 1092 ºC (n=8) for 65019 (Fig. 4.4 and Fig. 4.5). Oxygen fugacity (fO_2,

expressed as ΔNNO) ranges from +0.05 to -0.22 for HB24, -0.08 to -0.56 for 65054, and -0.33 to -0.78 for 65019 (Fig. 4.4 and Fig. 4.5).

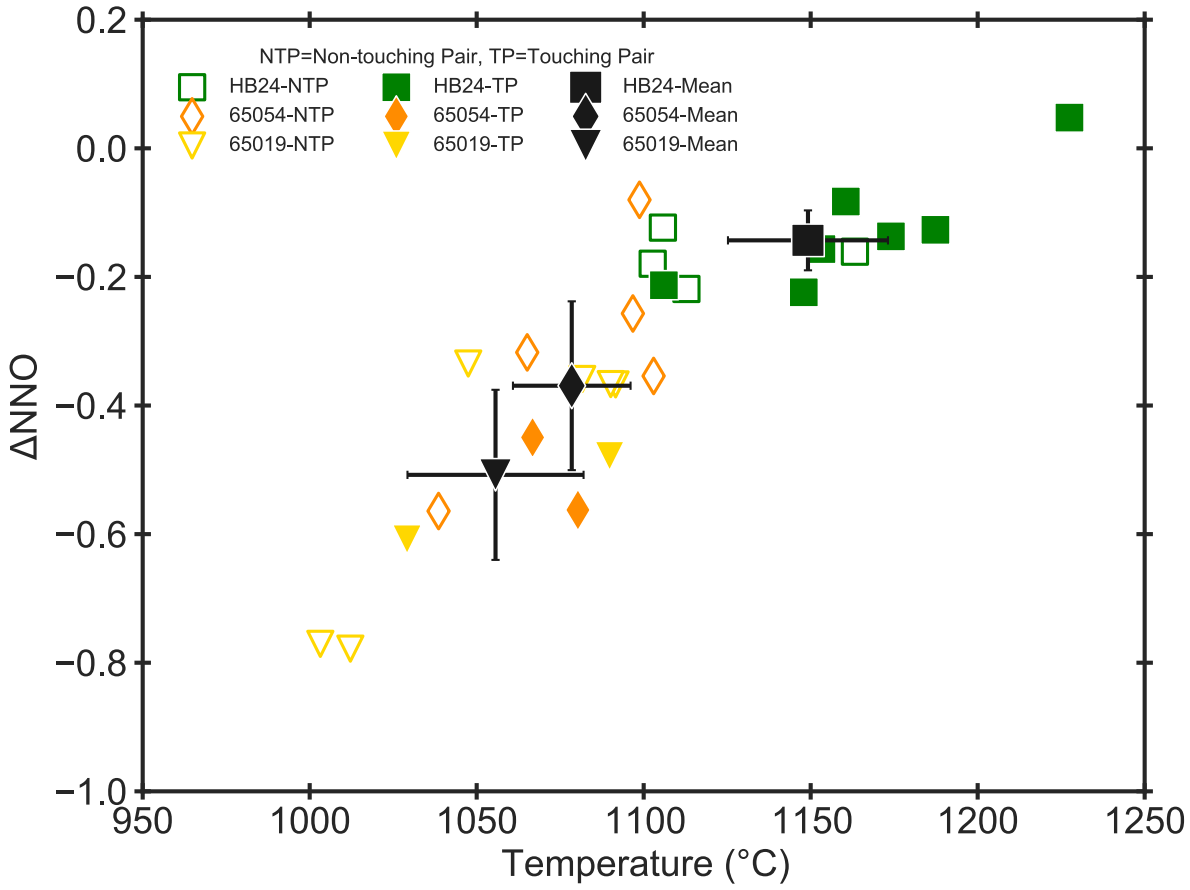

Fig. 4.5 Oxygen fugacity relative to NNO (nickel-nickel oxide) versus temperature values derived from Fe-Ti oxide pairs calculated using the method of Ghiorso and Evans (2008). Open symbols represent non-touching oxide pairs, filled symbols represent touching oxide pairs. The error bars represent the 2se of the mean values (black symbols).

It is common for equilibrium Fe-Ti oxide pairs from a single sample to show a range of temperature and fO_2 values which reflects temporal evolution in the magmatic system (Blundy and Cashman, 2008). To provide temperature estimates that can be tied to Ti isotope fractionation factors for Heard Island Fe-Ti oxides, the data from the equilibrium pairs for each sample was used to calculate a mean temperature (Fig. 4.4 and Fig. 4.5; 1149 ± 24 ºC for HB24, 1078 ± 18 ºC for 65054, and 1056 ± 26 ºC for 65019. Errors are reported as 2se). The 2s uncertainty on the temperature is propagated when fractionation factors are normalised to a common temperature.

4.4.2 Ti isotope compositions of natural samples

The $\delta^{49/47}$Ti data for the groundmass (for natural samples), silicate glass (for experimental run products), and all Fe-Ti oxide phases are given in Appendix E3 and shown in Fig. 4.6. Groundmass $\delta^{49/47}$Ti ranges from +0.245 to +0.526 ‰ for Heard

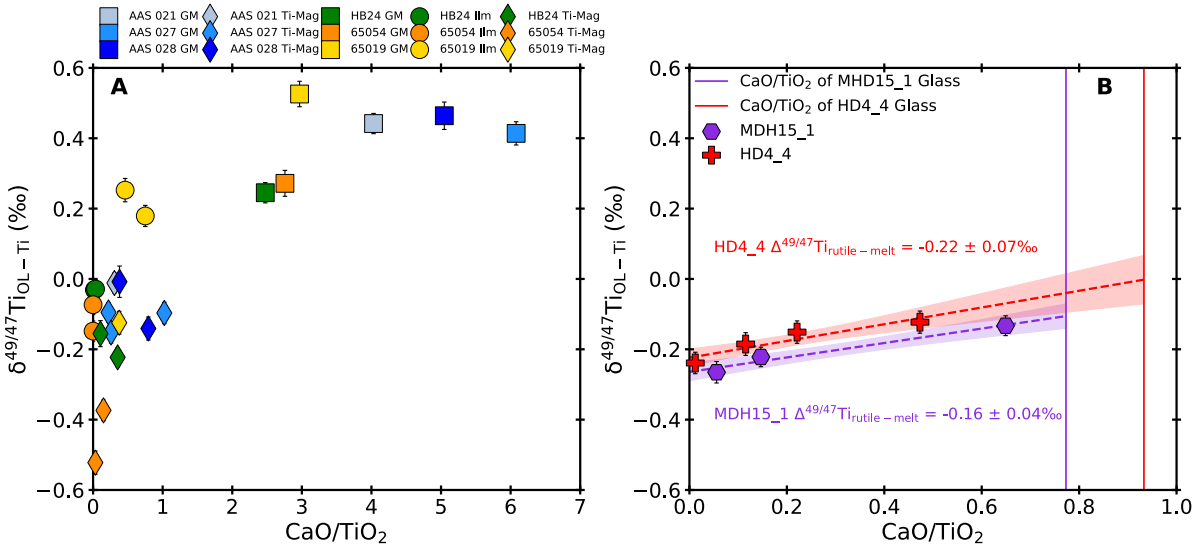

Fig. 4.6 a) $\delta^{49/47}$Ti versus CaO/TiO_2 for micro-milled Fe-Ti oxides (titanomagnetite and ilmenite) and groundmass from Heard Island and Santorini samples. b) $\delta^{49/47}$Ti versus CaO/TiO_2 for micro-milled rutile and silicate glass mixtures from rutile-melt experimental run products (MHD15_1 and HD4_4). Vertical coloured lines indicate the CaO/TiO_2 value of pure glass from Klemme et al. (2005). Dashed lines represent two component mixing lines from a york regression used to calculate the $\delta^{49/47}$Ti of pure rutile and glass. The shaded area represents the 2s of the regression.

Island samples, and from +0.414 to +0.464 ‰ for Santorini samples. Ilmenite from Heard Island samples has $\delta^{49/47}$Ti ranging from -0.148 to +0.253 ‰, with ilmenites consistently displaying isotopically lighter compositions compared to their corresponding groundmass (Fig. 4.6a). Titanomagnetite from Heard Island samples possesses $\delta^{49/47}$Ti = -0.522 to -0.124 ‰ and is isotopically lighter with respect to both groundmass and ilmenite within the same sample (Fig. 4.6a). In Santorini samples, titanomagnetite is also isotopically lighter with respect to groundmass but displays a narrower range of $\delta^{49/47}$Ti (-0.141 to -0.008 ‰) compared to Heard Island (Fig. 4.6a).

All measured Ti isotope fractionation between micro-milled Fe-Ti oxides and groundmass (or silicate glass) was calculated using the following equation and is shown in Fig. 4.7 and provided in Appendix E3:

Eq. 4-1

$$\Delta^{49/47}Ti_{oxide-melt} = \delta^{49/47}Ti_{oxide} - \delta^{49/47}Ti_{groundmass}$$

Individual $\Delta^{49/47}Ti_{oxide\text{-}melt}$ values for titanomagnetite, ilmenite and rutile are provided in Appendix E3. $\Delta^{49/47}Ti_{magnetite\text{-}melt}$ values exhibited by Santorini samples define a relatively narrow range of -0.453 to -0.605‰, in comparison to the larger variation observed in Heard Island of -0.401 to -0.794‰ (Fig. 4.7 and Appendix E3). Ilmenite-melt Ti isotope fractionation ($\Delta^{49/47}Ti_{ilmenite\text{-}melt}$) calculated for Heard Island samples ranges from -0.420 to -0.273‰ (Appendix E3). Values of $\Delta^{49/47}$Ti obtained from mineral separates by Mandl (2019) from the Kneeling Nun Tuff (KNT) are also included for comparison (Fig. 4.7a). The $\Delta^{49/47}$Ti value of KNT ilmenite is in good agreement with those observed in Heard Island and the $\Delta^{49/47}$Ti value of KNT titanomagnetite is comparable to those of Santorini (Fig. 4.7a).

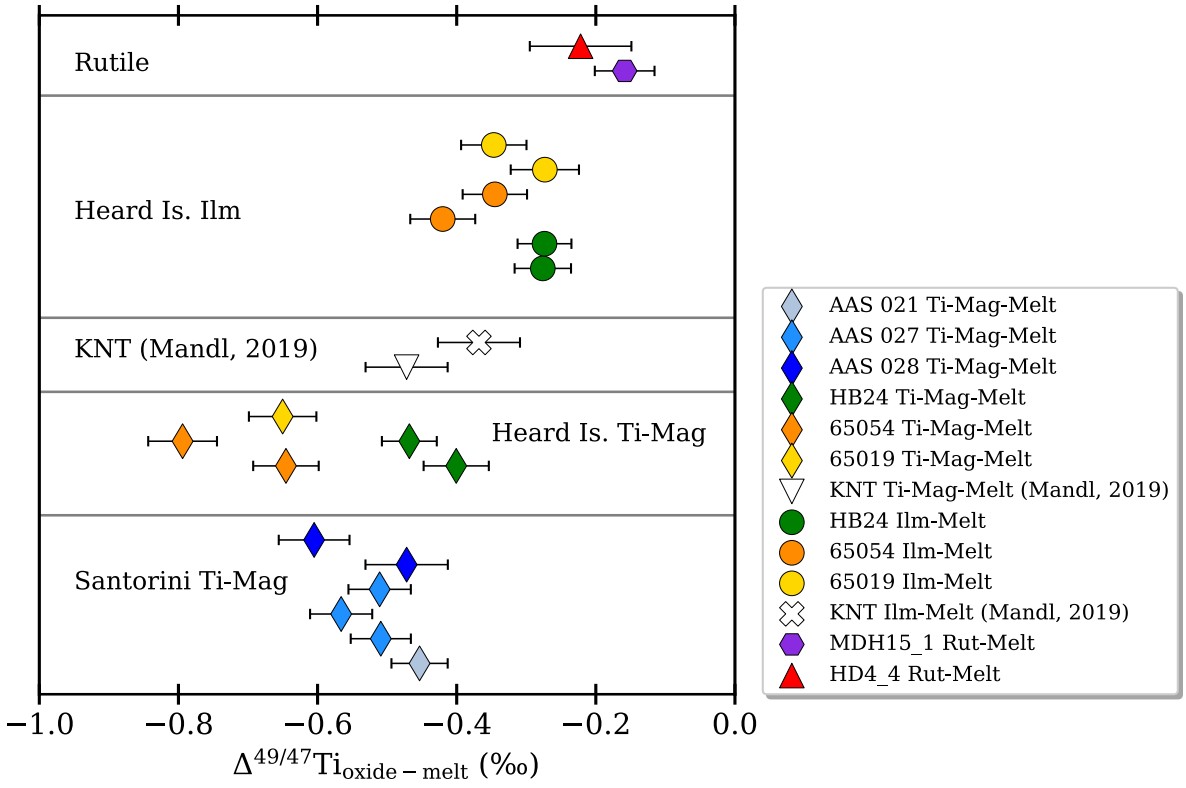

Fig. 4.7 a) $\Delta^{49/47}$Ti values for rutile-melt, titanomagnetite-melt and ilmenite-melt as reported in this study. Fractionation factors derived from mineral separates from the Kneeling Nun Tuff (KNT; Mandl, 2019) are shown for comparison. Error bars report 2s errors.

4.4.3 Ti isotope compositions of experimental samples

The $\delta^{49/47}$Ti values for micro-milled samples in the rutile-melt experiments range from -0.265 to -0.123 ‰ and are positively correlated with CaO/TiO_2 (Fig. 4.6b). Mixing lines on $\delta^{49/47}$Ti vs. CaO/TiO_2 were utilised to calculate the $\delta^{49/47}$Ti value for pure rutile and silicate glass in each experimental run product. This was performed using a York regression for the linear relationship between $\delta^{49/47}$Ti and CaO/TiO_2 of the micro-milled samples (Fig. 4.6b) and extrapolating the regression to the CaO/TiO_2 of rutile (assumed to be 0) and the composition of the silicate glass reported in Klemme et al., (2005). The $\delta^{49/47}$Ti values calculated for pure rutile ($CaO/TiO_2 = 0$) are -0.264 ± 0.025‰ and -0.224 ± 0.024‰ for MDH15_1 and HD4_4 respectively. The $\delta^{49/47}$Ti values calculated for pure silicate glass are -0.106 ± 0.035‰ and -0.002± 0.069‰ for MDH15_1 and HD4_4 respectively (see Appendix E3). These values were then used to quantify rutile-melt Ti isotope fractionation following Eqn.1. The values of $\Delta^{49/47}Ti_{rutile\text{-}melt}$ are -0.159 ± 0.043‰ and -0.222 ± 0.073‰ for MDH15_1 and HD4_4 respectively (see Appendix E3); the fractionation factors observed in both experiments are within error of each other.

4.4.4 Fe-Ti oxide-melt Ti isotope fractionation factors

At magmatic temperatures, isotopic fractionation factors (expressed as $\ln\alpha$ where α is the ratio of the isotopic composition of two phases; cf. Young et al., 2015) are proportional to the inverse square of the absolute temperature. To quantify Ti isotope oxide-melt fractionation factors, the data was regresed versus temperature (as $10^6/T^2$ with T in K) and, in the case of titanomagnetite, its TiO_2 content (Fig. 4.8).

Temperature values for Heard Island samples are the mean values obtained from Fe-Ti oxide geothermometry (see section 4.1). Temperature estimates for Santorini samples were taken from a compilation of literature data including two-pyroxene thermometry (Barton and Huijsmans, 1986); Fe-Ti oxide thermometry (Gertisser et al., 2009; Druitt, 2014); and melt inclusion analyses (Gardner et al., 1996; Michaud et al., 2000). This data gave a mean temperature estimate of 921 ± 31 ºC (n=9).

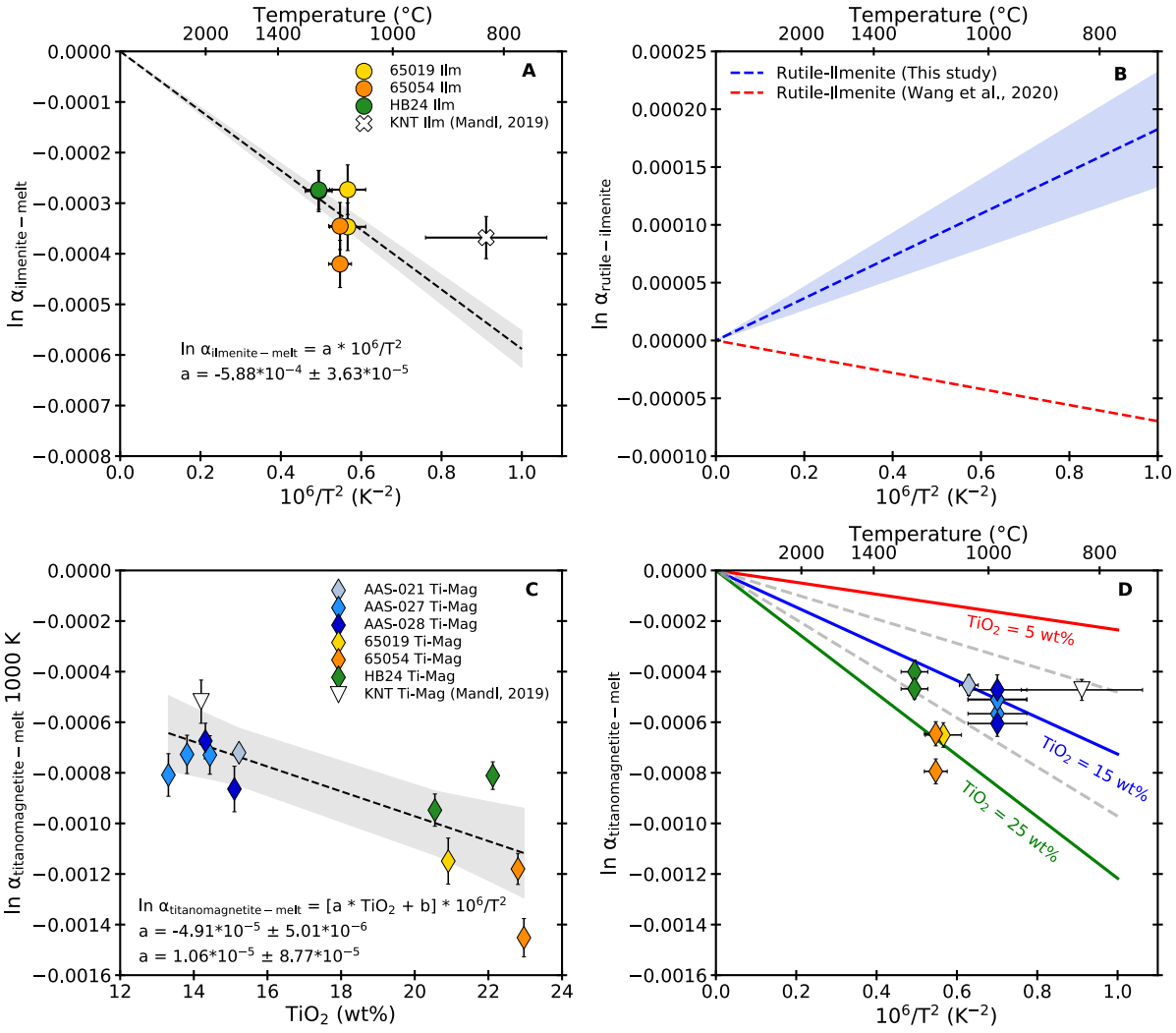

Fig. 4.8 Regression of Fe-Ti oxide-melt Ti isotope fractionation factors (expressed as $\ln\alpha_{\text{oxide-melt}}$). a) $\ln\alpha_{\text{ilmenite-melt}}$ as function of temperature (expressed as $10^6/T^2$ in units of Kelvin and degrees Celsius). b) $\ln\alpha_{\text{rutile-ilmenite}}$ as function of temperature calculated by Wang et al. (2020) (red) and this study (blue). The shaded areas represent the 2s uncertainty accounting for the propagation of uncertainty on the linear regression for both $\ln\alpha_{\text{ilmenite-melt}}$ and $\ln\alpha_{\text{rutile-rutile}}$. c) $\ln\alpha_{\text{titanomagnetite-melt}}$ normalised to 1000K versus TiO_2 (wt.%). d) Results of regressions of $\ln\alpha_{\text{titanomagnetite-melt}}$ for varying TiO_2 content (5, 15, and 20 wt.%; solid lines, 10 and 20 wt.%; dashed grey lines). $\ln\alpha_{\text{titanomagnetite-melt}}$ values for Santorini, Heard Island and KNT (Mandl, 2019) are also plotted at their respective temperature values. The 2s uncertainty of the regressions is indicated by the shaded areas.

for the dacites (AAS-027 and 28) and 987 ± 12 ºC (n=11) for the andesitic sample AAS-021. These temperature estimates are in good agreement with optical pyrometer measurements conducted during the 1925-1926 eruption on Nea Kameni (Washington, 1926; Reck et al., 1936). For the ilmenite and titanomagnetite data reported by Mandl (2019) for the Kneeling Nun Tuff, temperature constraints from

Szymanowski (2019) were used that suggest a mean crystallisation temperature of 775 ± 43 ºC based on plagioclase, amphibole, zircon and titanite thermometers.

A weighted linear regression of $\ln\alpha_{\text{ilmenite-melt}}$ was performed against $10^6/T^2$ (K^{-2}) using the data from this study and Mandl (2019) (Fig. 4.8a), which obtained the following linear relationship for $\ln\alpha_{\text{ilmenite-melt}}$ as a function of temperature, where $\ln\alpha_{\text{ilmenite-melt}} = 0$ when $10^6/T^2 = 0$:

Eq. 4-2

$$lna_{ilmenite-melt} = -5.88 * 10^{-4}(\pm 3.63 * 10^{-5}) * {}^{10^6}/_{T^2}$$

The 2s uncertainty is given in brackets. The rutile-melt experiments measured in this study yielded the following relationship with respect to temperature ($10^6/T^2$), anchored to $\ln\alpha_{\text{rutile-melt}} = 0$ when $10^6/T^2 = 0$:

Eq. 4-3

$$lna_{rutile-melt} = -4.06 * 10^{-4}(\pm 8.59 * 10^{-5}) * {}^{10^6}/_{T^2}$$

The 2s uncertainty is given in brackets. These two expressions derive a $\ln\alpha_{\text{rutile–ilmenite}}$ of 0.00018 ± 0.00009 at 1000 K, which is slightly larger than that predicted by density functional theory (DFT) models reported by Wang et al. (2020; see Fig. 4.8b), due to the observation that the $\ln\alpha_{\text{ilmenite-melt}}$ is greater than that of $\ln\alpha_{\text{rutile-melt}}$ at a given temperature (Fig. 4.8).

Due to the broad range of TiO_2 content between titanomagnetite in Santorini and Heard Island (Fig. 4.8, Appendix E3), all $\ln\alpha_{\text{titanomagnetite-melt}}$ were normalised to a common temperature of 1000 K (where $10^6/1000^2 = 1$; Fig. 4.8c), and regressed as a function of titanomagnetite TiO_2 content at a given temperature ($10^6/T^2$) to yield:

Eq. 4-4

$$lna_{titanomagnetite-melt} =$$
$$[-4.91(\pm 5.01 * 10^{-6}) * TiO_2 + 1.06 * 10^{-5}(\pm 8.77 * 10^{-5})] * {}^{10^6}/_{T^2}$$

The 2s uncertainties are given in brackets. The results of the regression for $\ln\alpha_{\text{titanomagnetite-melt}}$ using different TiO_2 contents as a function of temperature is shown in

Fig. 4.8d, along with $\ln\alpha_{\text{titanomagnetite-melt}}$ values from Heard Island, Santorini and Kneeling Nun Tuff (KNT; Mandl, 2019), the values $\ln\alpha_{\text{titanomagnetite-melt}}$ calculated from the regression are in good agreement with those observed in the natural samples (Fig. 4.8d).

4.5 Discussion

The data presented in this study provide conclusive evidence that Fe-Ti oxides have a notably lighter Ti isotope composition than co-existing silicate melt, consistent with previous studies (Johnson et al., 2019; Mandl, 2019; Greber et al., 2021; Nie et al., 2021; Rzehak et al., 2021) but, in contrast to those studies, this study is the first to quantify oxide-melt fractionation factors. Additionally, it shows that titanomagnetite and ilmenite, the main hosts of Ti in magmatic systems, display mutually distinct affinity for Ti isotopes as hypothesised by Hoare et al. (2020) from whole rock data. The following sections consider what controls the magnitude of Ti isotope fractionation for different Fe-Ti oxides and examine applications of these fractionation factors to model magmatic processes.

4.5.1 Controls on the magnitude of Fe-Ti oxide–melt Ti isotope fractionation factors

4.5.1.1 The role of Ti-O bond length

Stable isotope theory asserts that heavier isotopes prefer shorter bonds, which are stronger due to elevated vibrational frequencies (Bigeleisen and Mayer, 1947; Urey, 1947; Schauble, 2004). The effect of bond length on the magnitude of mass-dependent isotope fractionation factors has previously been documented for some isotope systems such as Fe (e.g. Hill and Schauble, 2008; Sossi and O'Neill, 2017), where the magnitude of Fe isotope fractionation factors were found to be inversely proportional to Fe-O bond length (Sossi and O'Neill, 2017). The ab-initio study of Wang et al. (2020) demonstrated that the reduced partition function ratio ($10^3\ln\beta$) of $^{49}Ti/^{47}Ti$ calculated for silicates, ilmenite, and rutile were generally negatively correlated with the average Ti-O bond lengths. Available published data on the crystal

structure of Fe-Ti oxide minerals indicates that titanomagnetite has longer average Ti-O bonds (0.204±0.001 nm) compared to ilmenite (0.198±0.001 nm; Wechsler et al., 1984; Wechsler and Prewitt, 1984). Rutile possesses a slightly shorter average Ti-O bond length (0.196±0.001 nm) compared to ilmenite (Samat et al., 2016 and references therein). Thus, on the inference from Ti-O bond lengths titanomagnetite would be predicted to possess the greatest affinity for lighter isotopes. Fig. 4.9 shows that Ti-O bond length only has a limited effect on the magnitude of $\ln\alpha_{\text{oxide-melt}}$ which slightly decreases from rutile to titanomagnetite at 1000 K. However, there are inconsistencies in the relationship observed in the data compared to that of Wang et al. (2020). In the ab-initio modelling done by Wang et al. (2020) $10^3\ln\beta$ of $^{49}Ti/^{47}Ti$ for rutile is lower than that of ilmenite-geikielite solid solution despite the longer Ti-O bond length of ilmenite-geikielite. Whilst Ti-O bond length can account for the small difference between $\ln\alpha_{\text{rutile-melt}}$ and $\ln\alpha_{\text{ilmenite-melt}}$, the resolvable variation observed for $\ln\alpha_{\text{titanomagnetite-melt}}$ between 13-23 wt.% TiO_2 (the entire range of TiO_2 contents for measured samples) indicates that composition rather than bond length acts as the main control on $\ln\alpha_{\text{titanomagnetite-melt}}$ (Fig. 4.8 c, d)

4.5.1.2 The role of melt and Fe-Ti oxide composition

Elevated TiO_2 contents in parental magmas enable early saturation and high modal abundance of both ilmenite and Ti-rich titanomagnetite (e.g. Toplis and Carroll, 1995), which enhances Ti isotope fractionation during magmatic differentiation in intraplate magmas due to the dominance of ilmenite+titanomagnetite on the elemental and isotopic budget of Ti throughout magma evolution (Hoare et al., 2020). Titanomagnetites in Heard Island lavas are Ti-rich (20-23 wt.% TiO_2) and display larger variation in $\ln\alpha_{\text{titanomagnetite-melt}}$ compared to Santorini titanomagnetites that have lower TiO_2 contents (Fig. 4.8c). The variation in the value of $\ln\alpha_{\text{titanomagnetite-melt}}$ could be dependent on TiO_2 contents. This could be related to changes in crystal structure and Ti-O bond length as a function of TiO_2 content in the ulvöspinel-magnetite solid (Fig. 4.1).

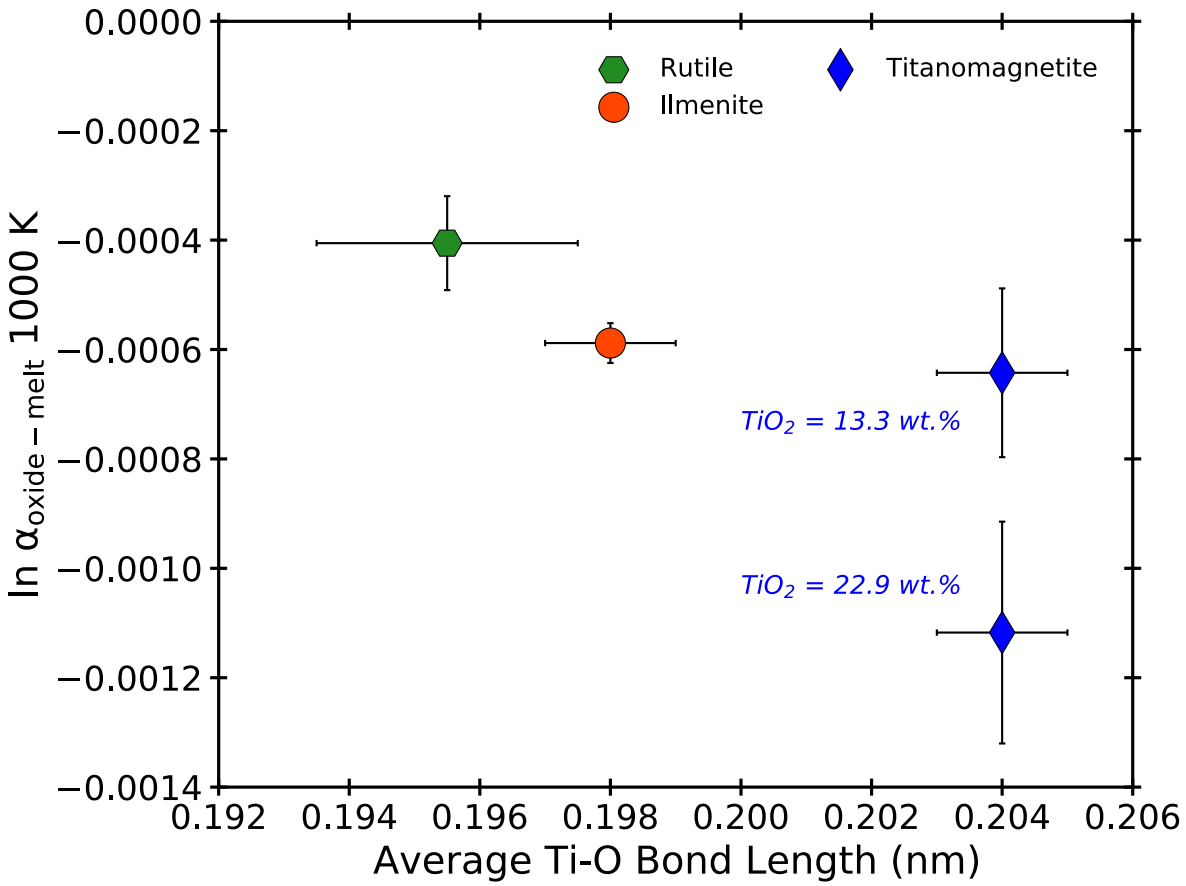

Fig. 4.9 lnα for rutile-, titanomagnetite- and ilmenite-melt at 1000 K versus average Ti-O bond length (in nanometres). $\Delta^{49/47}$Ti values were calculated from the regression of ln$\alpha_{oxide-melt}$ shown in Fig. 4.8 and errors shown are 2s. Selected TiO_2 contents for titanomagnetite represent the minimum and maximum values observed across Santorini and Heard Island samples. X-axis error bars on Ti-O represent the range of bond lengths reported in the literature.

It has been well documented that the chemical composition of a mineral affects its crystal structure and consequently also elemental partitioning between minerals and their host melt (Lundstrom et al., 1998; Hill et al., 2000). More recently, studies have begun to consider the implications for mass-dependent isotope fractionation (e.g. Huang et al., 2010; Feng et al., 2014; Roskosz et al., 2015; Wang et al., 2017; Wu et al., 2017). Using first principles calculations, Feng et al. (2014) observed that mass-dependent Ca isotope fractionation between orthopyroxene (opx) and clinopyroxene (cpx) was not solely controlled by temperature, but also a function of Ca contents as the average Ca-O bond length in orthopyroxene is strongly affected by its Ca content. Feng et al. (2014) observed that 10^3ln$\alpha_{opx-cpx}$ increased substantially with decreasing Ca

content in orthopyroxene, (Huang et al., 2010; Wang et al., 2017). Titanomagnetite ($Fe_{(3-x)}Ti_xO_4$) is a solid solution (Fig. 4.1) between magnetite ($Fe^{3+}[Fe^{2+}\ Fe^{3+}]O_4$) and ulvöspinel ($Fe^{3+}[Fe^{2+}\ Ti^{4+}]O_4$; see Fig. 4.1), which possess an 'inverse' spinel structure with an *Fd3m* space group (Barth and Posnjak, 1932). Titanium (as Ti^{4+}) is thought to almost exclusively occupy the octahedral site (Fujino, 1974; Wechsler et al., 1984), although some studies have postulated that minor Ti^{4+} also exists in the tetrahedral site (Stout and Bayliss, 1980; Sedler et al., 1994). Generally, as the Ti content of titanomagnetite increases, the proportion of the ulvöspinel endmember increases which results in a higher proportion of Ti^{4+} in the octahedral site at the expense of Fe^{3+}, and a concurrent increase in Fe^{2+} in both the tetrahedral and octahedral sites to maintain charge balance (Akimoto et al., 1957; Bosi et al., 2009; Pearce et al., 2010; Okube et al., 2018). The ionic radii of Ti^{4+} and Fe^{3+} occupying VI-fold coordination are relatively similar, at 0.0605 and 0.0645 nm (high-spin) respectively (Shannon, 1976). However, ferrous iron (Fe^{2+}) has a larger ionic radius, both in VI and IV-fold coordination, at 0.0780 and 0.0630 nm respectively (Shannon, 1976). Therefore, as the proportion of the ulvöspinel endmember (and hence the TiO_2 content) increases so does the proportion of Fe^{2+} in both the VI and IV sites with smaller ions (Fe^{3+}) being replaced. This has the potential to impose strain on the crystal lattice and possibly weaken the bonding environment which could consequently influence isotope fractionation. This is supported via crystallographic evidence of the positive correlation between increasing Ti content and the size of the unit cell parameter of titanomagnetite (Bosi et al., 2009; Pearce et al., 2010). These observations are concomitant with an increase in the structural instability of titanomagnetite, with Bosi et al. (2009) noting that the global instability index (*GII*, see Salinas-Sanchez et al., 1992; Brown, 2016) increases as function of increasing Ti contents. Hence, these conditions would make Ti-rich titanomagnetite favour lighter isotopes which is consistent with the observation that when normalised to a common temperature, Ti-rich titanomagnetite from Heard Island consistently display more negative $\ln\alpha_{titanomagnetite\text{-}melt}$ values than those from Santorini (Fig. 4.8c).

4.5.2 Geologic applications of Ti isotope fractionation factors

The Ti isotope fractionation factors derived in this study provide new opportunities to utilise and develop Ti isotopes as a geochemical tool which can be applied to a variety of geologic processes. In this section the robustness of these new fractionation factors is tested using forward modelling of terrestrial mantle melting and magmatic differentiation.

4.5.2.1 Estimating silicate-melt Ti isotope fractionation factors

Whilst the elemental and hence isotopic budget of Ti in magmatic rocks is predominantly controlled by Fe-Ti oxides, silicates could influence Ti isotopes in magmatic systems where Fe-Ti oxides are largely absent such as in un-metasomatized peridotites or in certain magmas where silicate phases such as amphibole, biotite, and titanite contain non-trivial amounts of Ti. Titanium isotope analyses of silicates are thus far limited. Mandl (2019) reported Ti isotope compositions for amphibole, biotite, and titanite mineral separates from the Kneeling Nun Tuff and observed that they were isotopically lighter with respect to their host groundmass. This is consistent with Ti occupying a higher coordination state in all these phases compared to silicate melt.

Analyses of orthopyroxene-melt experimental run products by (Rzehak et al., 2021) revealed $\Delta^{49/47}Ti_{orthopyroxene\text{-}melt}$ displays relatively limited fractionation at -0.002 ± 0.017‰ to +0.050 ± 0.025‰ at conditions relevant to terrestrial magmatism (Air to FMQ-2; where Ti^{3+} is absent). The coordination state of Ti in silicates is difficult to constrain and often non-uniform, ranging from IV-fold in quartz (Sandstrom et al., 1980) and plagioclase (Oberti et al., 1992), to variable proportions of IV-fold and VI-fold in olivine and clinopyroxene (Leitzke et al., 2018), with clinopyroxene being the main host of Ti in oxide-free mafic melts. Quartz, plagioclase and olivine have negligible influence on the Ti budget of igneous rocks. For Ti-rich biotite (8-14 wt.% TiO_2), it has been suggested that up to 90% Ti occupies a site with VI-fold coordination (Henderson and Foland, 1996). Phases that control the Ti budget of typical of terrestrial mantle lithologies, like pyroxene, garnet and spinel, appear to host Ti

predominantly in VI-fold coordination (O'Neill and Navrotsky, 1983; Waychunas, 1987).Variations of the coordination state of Ti in silicate phases have important ramifications for Ti isotopes in magmatic systems as a higher proportion of IV-fold coordinated Ti will drive silicates to heavier isotopic compositions relative to melt.

To provide estimates on the magnitude of various silicate-melt Ti isotope fractionation factors (Fig. 4.10), the new rutile-melt fractionation factor (Eq. 4-4) is combined with the mineral-mineral fractionation factors for rutile and Ti-bearing silicates that are derived from the *ab initio* density functional theory calculations as reported by Leitzke et al. (2018) and Wang et al. (2020). The rutile-melt fractionation factor was chosen as opposed to ilmenite due the relative simplicity of its structure and limited compositional variability in comparison to ilmenite ($\ln\alpha$ values for silicates when anchored to ilmenite-melt are provided in Appendix E3 and shown in Fig. 4.11). Resulting mineral-melt fractionation factors for silicate minerals at 1000 K are listed in Appendix E3 and shown in Fig. 4.10 alongside empirical data from the literature (Mandl, 2019; Rzehak et al., 2021) and the complete set of Fe-Ti oxide fractionation factors from this study. The *ab initio* models from Leitzke et al. (2018) and Wang et al. (2020) indicate that if Ti is exclusively present in IV-fold coordination, pyroxene and garnet are isotopically heavier than coexisting melt, consistent with stable isotope theory (Fig. 4.10).

Conversely, if Ti is exclusively hosted in an octahedral site (VI-fold coordinated), pyroxene and garnet show minimal fractionation (Fig. 4.10). The amphibole, biotite and titanite Ti isotope fractionation factors reported by Mandl (2019) for natural samples are smaller than those derived *ab initio* for clinopyroxene and garnet with Ti in VI-fold coordination (Fig. 4.10). This is consistent with the presence of longer Ti-O bonds in these phases (Farges et al., 1996b; Henderson and Foland, 1996; Tiepolo et al., 2007). The values for orthopyroxene-melt fractionation from Rzehak et al. (2021) show a narrow range of variation, and are within error of the clinopyroxene-melt and garnet-melt fractionation factors calculated from the *ab initio* studies of Leitzke et al.

(2018) and Wang et al. (2020) assuming Ti is exclusively in VI-fold coordination (Fig. 4.10).

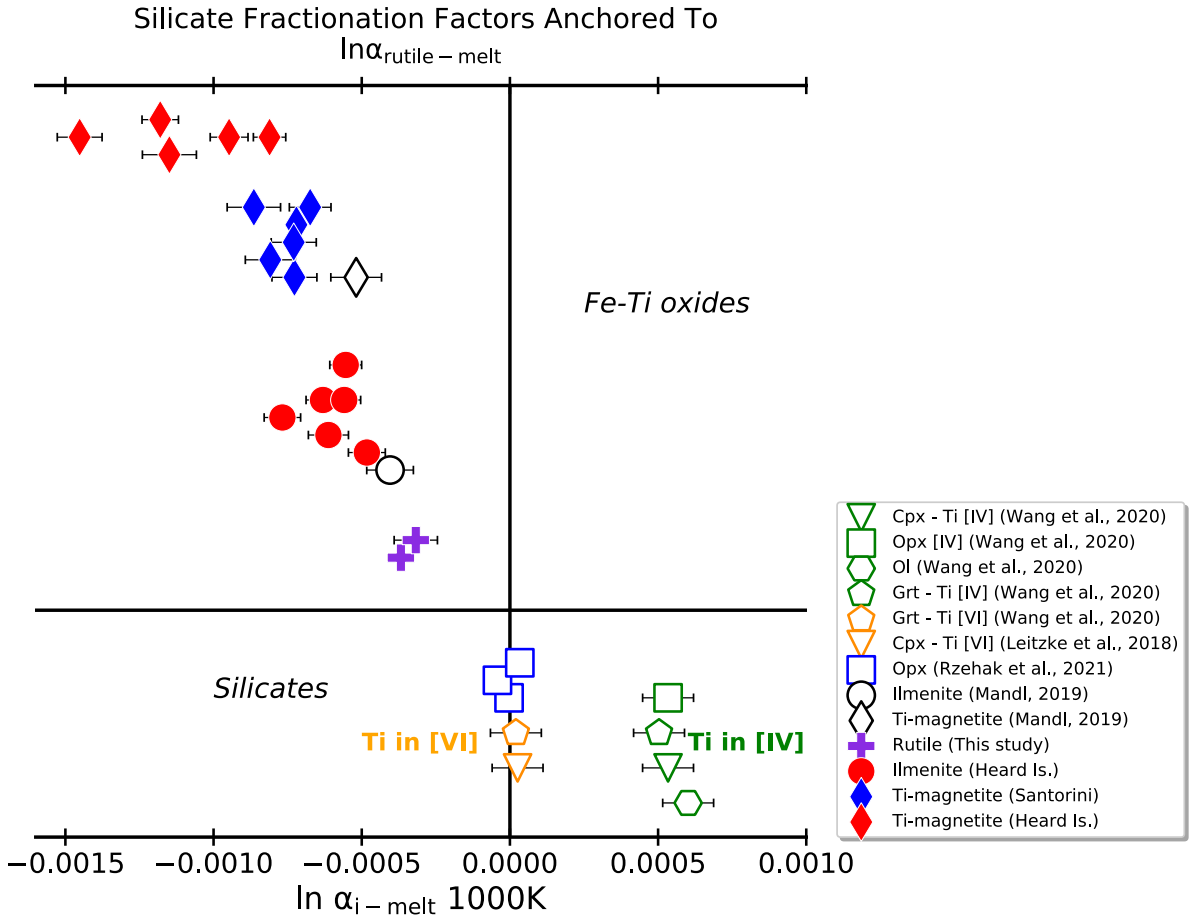

Fig. 4.10 lnα between a phase i and melt at 1000 K when lnα rutile-melt is used as the anchor for the value of β melt. Mineral-mineral fractionation factors are from the first principles as reported in Wang et al. (2020). 2s error bars on Ti isotope fractionation factors calculated from the Wang et al. (2020) data represent the propagated uncertainty on the lnα rutile-melt regression as a function of temperature (expressed as $10^6/T^2$ in units of Kelvin).

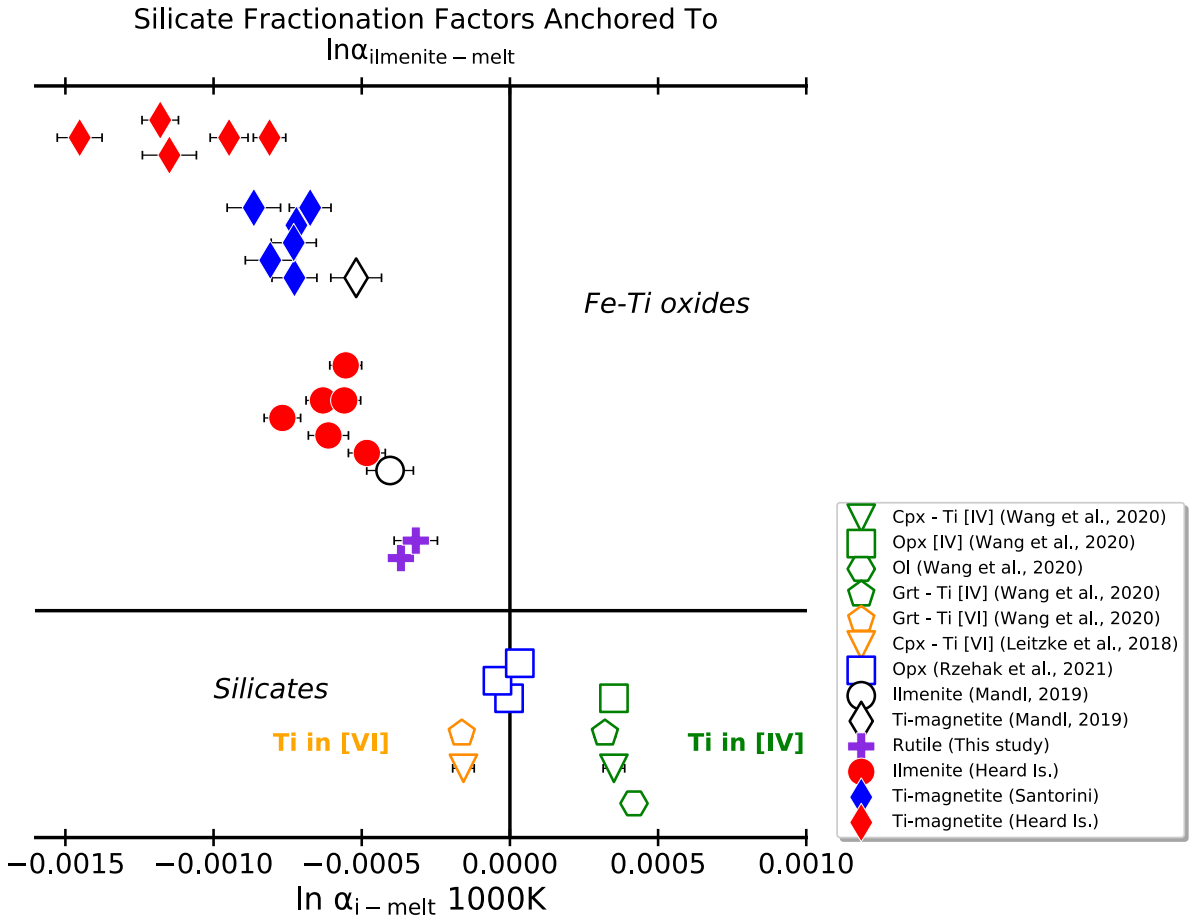

Fig. 4.11 lnα between phase i and melt when lnα ilmenite-melt is used as the anchor for the value of β melt. Mineral-mineral fractionation factors are from the first principles as reported in Wang et al. (2020). 2s error bars on Ti isotope fractionation factors calculated from the Wang et al. (2020) data represent the propagated uncertainty on the lnα ilmenite-melt regression as a function of temperature (expressed as $10^6/T^2$ in units of Kelvin).

4.5.2.2 Ti isotope modelling during magmatic differentiation

To evaluate the robustness of the empirical and calculated Ti isotope fractionation factors, forward modelling was used to simulate the Ti isotope evolution during fractional crystallisation for the differentiation suites from Hoare et al., (2020). Least squares major element models (see Appendix E3) were used to estimate modal proportions of fractionating phases and thus the bulk solid-melt Ti isotope fractionation factor. The mineral modes, compositions, and bulk solid-melt Ti isotope fractionation factors are given in Appendix E3. The Ti isotope evolution of each suite was modelled via a Rayleigh fractionation process using the $\delta^{49/47}$Ti of the most primitive sample as the starting point. The uncertainties in temperature and the

fractionation factors are propagated into the calculation of the bulk solid-melt Ti isotope fractionation factor.

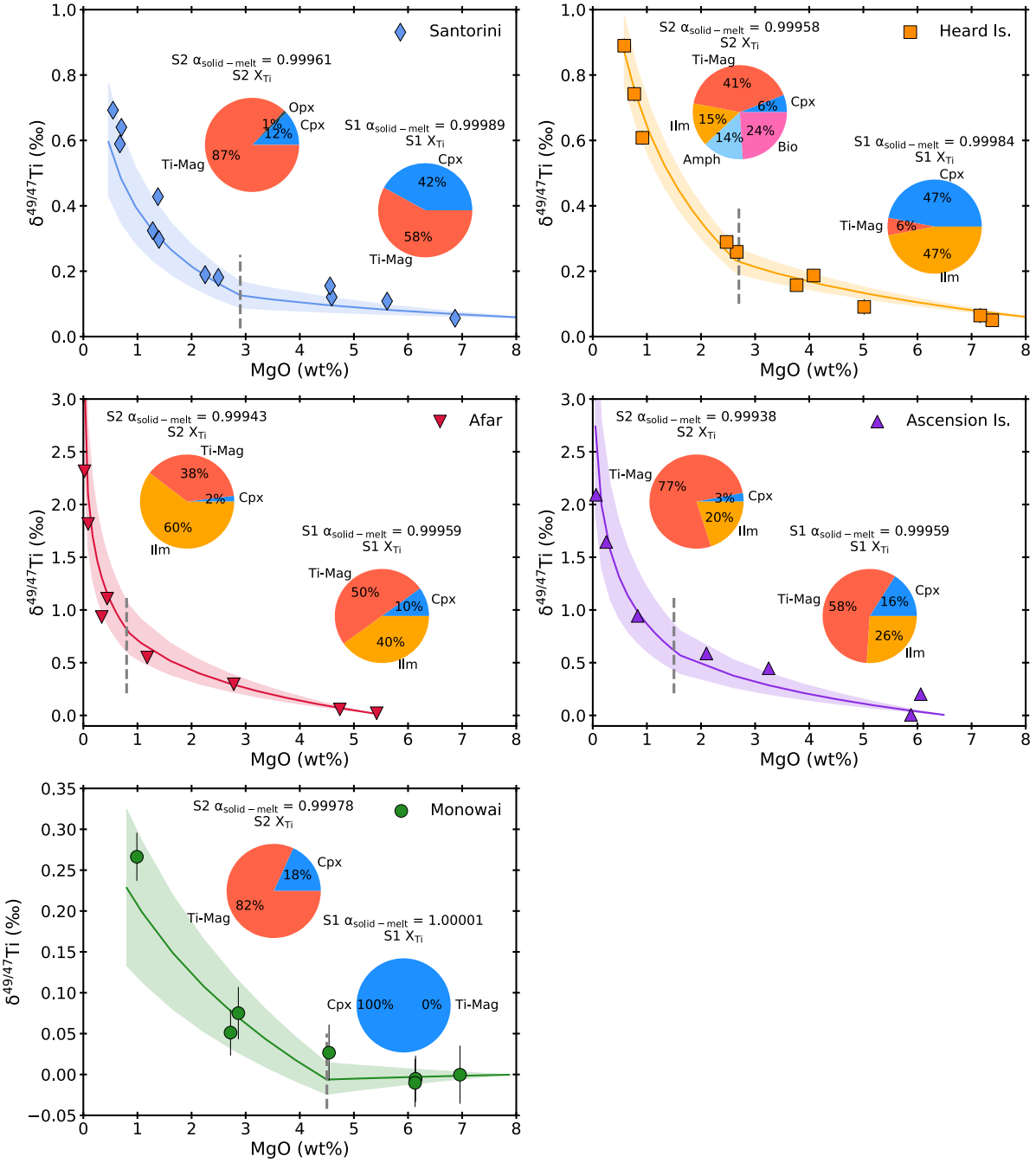

Fig. 4.12 $\delta^{49/47}$Ti compositions of magmatic differentiation suites (solid symbols) from Hoare et al. (2020) plotted against MgO contents. IgPet (Carr and Gazel, 2017) was used to model the fractional crystallisation of these differentiation suites via least-squares mass balance modelling (e.g. Bryan et al., 1969) using mineral compositions taken from the literature (see Appendix E3). The $\delta^{49/47}$Ti evolution was modelled using a Rayleigh fractionation law and a bulk $\alpha_{solid\text{-}melt}$ weighted on the proportion of Ti in each crystallising phase. Modelling was performed into two steps (S1 and S2; demarcated by the vertical grey dashed lines) from the most primitive lava to a representative intermediate composition, then from the intermediate to most evolved composition. The results of the model are shown by the solid-coloured lines. The shaded error represents the 2s uncertainty on bulk $\alpha_{solid\text{-}melt}$ with propagated

uncertainty from the temperature variation at each stage of the model and the various lnα regressions used to calculate the Ti isotope fractionation factors. The pie charts display the proportion on Ti in each phase in each step of the model (S1 and S2) along with the value of bulk $\alpha_{\text{solid-melt}}$ represented by the solid-coloured lines.

The Rayleigh fractionation model results are shown in Fig. 4.12, which displays $\delta^{49/47}$Ti values relative to MgO contents. For each of the differentiation suites, the modelled melt value calculated using the bulk solid-melt Ti isotope fractionation factor is in good agreement with the $\delta^{49/47}$Ti variation observed with respect to decreasing MgO contents of samples from Hoare et al., (2020; Fig. 4.12). It is also clear from Fig. 4.11 that major changes in the trajectory of $\delta^{49/47}$Ti variation during magmatic differentiation correspond to changes in the modal abundance and composition of Ti-rich phases, primarily titanomagnetite and ilmenite (Hoare et al., 2020). During the first step of the differentiation of the Monowai samples, clinopyroxene is the only Ti-bearing phase present (Fig. 4.12; Timm et al., 2011; Kemner et al., 2015). The lack of resolvable fractionation observed in this step is consistent with the mantle melting models where Ti is hosted in the octahedral site of clinopyroxene (see section 5.2.3; Fig. 4.12a). The results presented here provide further evidence that the modal proportions of Ti-bearing phases in the crystallising mineral assemblage exert the main control on the magnitude of variation of $\delta^{49/47}$Ti values observed between magmas of different tectonic settings (Hoare et al., 2020). High melt TiO_2 contents enables the crystallisation of Ti-rich titanomagnetite and ilmenite in high modal abundance (e.g. Toplis and Carroll, 1995), which serves to drive bulk $\Delta^{49/47}Ti_{\text{solid-melt}}$ to significantly lighter values than magmas that possess fewer Fe-Ti oxides with lower TiO_2 contents as is the case for tholeiitic and calc-alkaline arc magmas.

4.5.2.3 Ti isotope modelling of mantle melting

During melting of either spinel- or garnet-facies peridotite, Ti behaves as a moderately incompatible element which facilitates its efficient extraction from the mantle during basalt petrogenesis (Prytulak and Elliott, 2007; Gale et al., 2013). Consequently, previous studies have proposed that the $\delta^{49/47}$Ti compositions of basalts is reflective of their mantle source, and hence that partial melting of the mantle

produces no resolvable Ti isotope fractionation (Millet et al., 2016). This is supported by the indistinguishable $\delta^{49/47}$Ti compositions of primitive basalts and mantle lithologies (Millet et al., 2016). However, Deng et al. (2018) observed a subtle offset between the $\delta^{49/47}$Ti composition of N-MORB and E-MORB, arguing that the former is isotopically lighter due to mantle depletion during the generation of continental crust in the Archean.

The batch melting of primitive mantle is modelled from 6 to 1 GPa to test the effect of mantle mineralogy and the genesis of mid ocean ridge basalts. Two scenarios are considered i) the coordination of all Ti in clinopyroxene and garnet is VI-fold coordination and ii) all Ti is in IV-fold coordination.

Modelling of mantle melting was undertaken using both pMELTS (Ghiorso et al., 2002) for melting of primitive mantle (Palme and O'Neill, 2014) of which $\delta^{49/47}$Ti = 0 at 1 GPa, and using experimental data from Walter (1998) for garnet-peridotite melting at 4 and 6 GPa. The 1 GPa pMELTS models were run in 5°C increments from the liquidus to solidus at fO_2 = FMQ-1. Ti isotope compositions of melt and residue at each increment was calculated from isotopic mass balance. Given that spinel and titanomagnetite share a common crystal structure with VI coordinated Ti (O'Neill and Navrotsky, 1983; Waychunas, 1987), the Ti isotope fractionation factor for spinel-melt is calculated using Eqn. 5 at every temperature step and using spinel TiO_2 contents produced by pMELTS. The results of melting a primitive mantle composition at 1-6 GPa over the batch melting interval of 0-25% are shown in Fig. 4.13 and are plotted relative to the BSE value of +0.005‰ from Millet et al. (2016). The same models using silicate-melt Ti isotope fractionation factors anchored to ilmenite-melt, as opposed to rutile-melt, are shown in Fig.4.14 and Appendix E3.

Fig. 4.13 shows that the coordination state of Ti in typical mantle mineralogies has a significant influence on the resulting Ti isotope composition of partial melts of the mantle. If Ti is in VI-fold in silicates melting of the primitive mantle produces no significant variation in $\delta^{49/47}$Ti that is resolvable at the current limits of analytical

uncertainty (±0.02 ‰), with both melt and residue being close to the BSE value (Fig. 4.13a, Fig.4.14a). However, when Ti in mantle silicates is in IV-fold coordination,

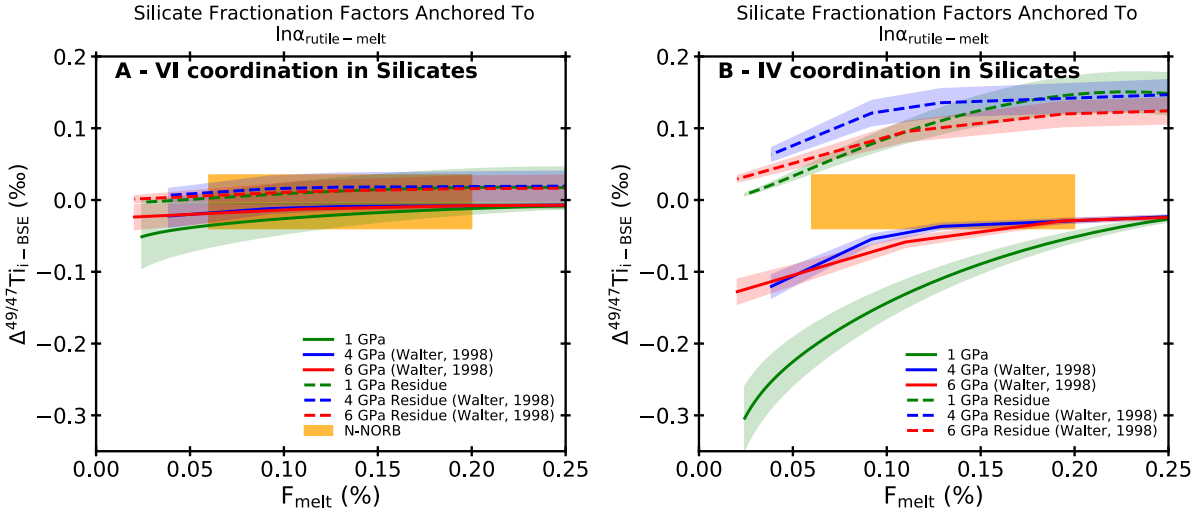

Fig. 4.13 $\Delta^{49/47}$Ti values mantle melting models relative to the BSE for melt (solid lines) and residue (dashed lines) as a function of degree of melting and pressure for; a) pMELTS modelling of a primitive mantle source (PM; Palme and O'Neill, 2014) at 1 GPa and melting of a garnet peridotite (KR4003) at 4 and 6 GPa (Walter, 1998) when Ti in silicates is in VI-fold coordination; b) Same models as panel a) but for a scenario where Ti in silicates is in IV-fold coordination. The orange field represents the mean $\Delta^{49/47}$Ti value of N-MORB relative to the BSE (-0.004 ± 0.039 ‰ (2sd); Millet et al., 2016, Deng et al., 2018; Hoare et al., 2020; Zhao et al., 2020). Shaded areas represent the 2s error on the models. All α values used are anchored to α rutile-melt (see fig 4.10).

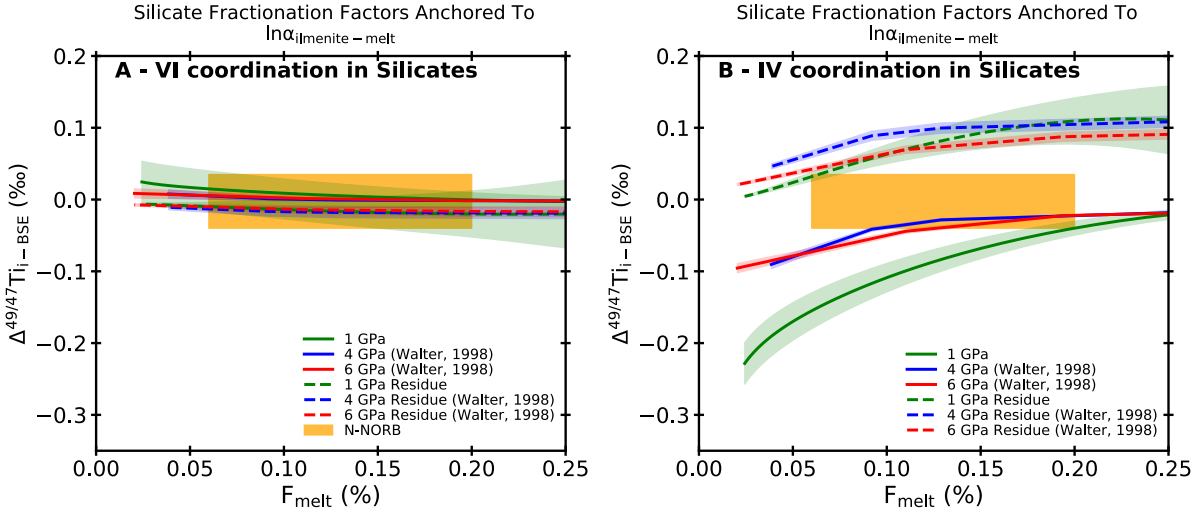

Fig. 4.14 Ti isotope mantle melting models for melt (solid lines) and residue (dashed lines) as a function of degree of melting and pressure for; a) pMELTS modelling of a primitive mantle source (PM; Palme and O'Neill, 2014) at 1 GPa and melting of a garnet peridotite (KR4003) at 4 and 6 GPa (Walter, 1998) when Ti in silicates is in VI-fold coordination; b) Same models as panel a) but for a scenario where Ti in silicates is in IV-fold coordination. The orange field represents the mean $\delta^{49/47}$Ti value of N-MORB (+0.001 ± 0.039 ‰ (2sd); Millet et al., 2016, Deng et al., 2018; Hoare et al., 2020; Zhao et al., 2020). Shaded areas represent the 2s error on the models. All α values used are anchored to α ilmenite-melt (Fig. 4.11).

partial melting produces melts that are significantly isotopically lighter and residua that are isotopically heavier relative to the BSE (Fig. 4.13b, Fig. 4.14b). Previous studies (Greber et al., 2017b; Williams et al., 2021) have shown the $\delta^{49/47}$Ti compositions of chondrites are within error of primitive basalts and mantle samples (Millet et al., 2016). These results can only be reproduced in a partial melting model in which Ti is hosted in 6-fold coordination in mantle clinopyroxenes and garnets. Furthermore, this model reproduces the lack of variation observed between ultramafic-mafic rocks derived from different degrees of mantle melting such as komatiites (Millet et al., 2016; Greber et al., 2017b; Hoare et al., 2020; Zhao et al., 2020).

It is notable however, that Deng et al. (2018) observed an offset between chondrites and komatiites, which was best explained by Ti isotope fractionation during extraction of the continental crust. However, this cannot be reconciled by partial melting of the mantle with Ti in a 4-fold coordination as this generates heavy residues relative to melts, contrary to that particular dataset. While it is beyond the scope of this study to discuss these particular data, the fractionation factors clearly indicate that Ti is hosted in 6-fold coordination in the mantle and this results in limited, within current analytical uncertainty, isotope fractionation during partial melting.

4.6 Conclusions

This chapter presents the $\delta^{49/47}$Ti compositions of micro-milled Fe-Ti oxides and groundmass to derive Fe-Ti oxide-melt Ti fractionation factors. A well-constrained set of Ti isotope fractionation factors are necessary to provide further quantitative constraints on the mechanics of Ti isotope fractionation in magmatic processes and at the mineral scale. The main conclusions of this study are as follows:

i. These results show that titanomagnetite displays the largest mineral/melt $\delta^{49/47}$Ti fractionation factors, followed by ilmenite, and then rutile. This is consistent with stable isotope theory which dictates lighter isotopes prefer

longer bonds, with Ti-O bond length decreasing from magnetite to ilmenite and rutile.

ii. The titanomagnetite-melt fractionation factor increases as a function of titanomagnetite TiO_2 content, with titanomagnetite from Heard Island (>20 wt.% TiO_2) consistently displaying larger fractionation factors compared Santorini (≤15 wt.% TiO_2).

iii. The data enables the calculation of Fe-Ti oxide-melt fractionation factors as a function of temperature, and TiO_2 content in the case of titanomagnetite.

iv. These fractionation factors combined with petrographic constraints, can be applied to successfully model mantle melting and reproduce the $\delta^{49/47}Ti$ evolution of a series of differentiation suites.

Chapter 5: Titanium isotope and trace element insights into the redox evolution of the Oman ophiolite mantle sources and melts

5.1 Abstract

The Oman ophiolite is the best preserved and largest ophiolite complex available for study. Long-standing debate surrounding its geodynamic context of formation hinges on two competing hypotheses: (1) the ophiolite formed at an open-ocean mid-ocean ridge, and thus is a unique, invaluable direct analogue for fast-spreading oceanic crust, or (2) it formed by spreading above a nascent subduction zone. Evidence supporting the latter is provided by the presence of elevated water contents and arc-like geochemical signatures, but this has remained controversial, as some have instead attributed these signatures to other processes such as hydrothermal fluids. This chapter uses a novel combination of trace element ratios and titanium (Ti) isotope compositions of sheeted dikes and lavas to differentiate between these hypotheses, with particular focus on the redox state of melts and mantle sources throughout the magmatic history of the ophiolite. Primitive (MgO > 6 wt.%) lavas and dikes from Oman, filtered from an overall database of >1200 samples, show large variations in concentrations and ratios of redox-sensitive elements. Importantly, the range of variation in these elements and ratios increases both spatially (from S to N) and temporally throughout the ophiolite. Mantle melting models considering varying source redox state indicate that the trace element systematics of the lavas and sheeted dikes can be replicated by melting of a progressively oxidised source. The trace element systematics are complemented by the observation that the Ti isotope evolution of differentiated Oman ophiolite melts mirror hydrous fractionation trends distinct from dry tholeiitic suites typical of MOR settings, suggesting parental melts that are oxidised relative to N-MORB. Overall, the trace element and Ti isotope systematic of Oman ophiolite dikes and lavas suggest the progressive introduction of water in the active melting column under the Oman ophiolite and thus its likely formation in proximity to a nascent subduction zone.

5.2 Introduction: The ophiolite – mid-ocean ridge connection

The growth and accretion of oceanic crust produced at mid ocean-ridges via seafloor spreading is one of the predominant mechanisms driving the physio-chemical evolution of the Earth. Approximately 70% of our planet's surface is generated via mid-ocean ridge magmatism, with mid-ocean ridge basalts (MORB) being the most voluminous igneous rocks on the Earth. The structure of oceanic crust created at fast-spreading ridges is characterised by homogeneous layers mainly composed of mafic cumulate rocks (e.g. Madsen et al., 1990; Lin and Morgan, 1992; Canales et al., 1998; Pablo Canales et al., 2003). At fast spreading ridges the generation of oceanic crust is driven by the ascent, differentiation and crystallisation of MORB magmas which originate from the axial melt lens (AML), situated between a solidified gabbroic layer and an overlying sheeted dike sequence (e.g. Vera et al., 1990; Koepke and Zhang, 2020 and references therein). The role of the AML during crustal formation is actively debated, centred around two competing hypotheses: (i) the AML is the progenitor of the entire lower, gabbroic lower crust, with cumulates crystallising from a suspended crystal mush (e.g. Henstock et al., 1993; Morgan and Chen, 1993; Coogan et al., 2007; Faak et al., 2015) or (ii) significant portions of mafic cumulates are derived from in-situ crystallisation deep in the crust (e.g. Kelemen et al., 1997; Lissenberg et al., 2004; Maclennan et al., 2005; VanTongeren et al., 2008; VanTongeren et al., 2015).

Since pristine outcrops of lower oceanic crust formed at modern fast-spreading mid-ocean ridge systems are notoriously rare and challenging to access it has become necessary to pursue studies of potential analogues within the geologic record. The study of ophiolites, which are fragments of oceanic lithosphere thrusted on land, have played a fundamental role in contributing to our understanding of the geodynamic processes associated with mid-ocean ridges (e.g. Nicolas et al., 2000; Nicolas, 2012), with some regarding them as direct analogues for open-ocean fast-spreading ridge systems (e.g. Coleman, 1981; Nicolas et al., 1988; Boudier et al., 1997). The Oman-United Arab Emirates (UAE; or Semail) ophiolite, the focus of this chapter, has been

pivotal in advancing our conceptual understanding of oceanic lithosphere and other ophiolites on Earth.

5.3 The Oman-UAE ophiolite

5.3.1 Geologic setting

The Oman-EAU ophiolite, the majority of which is located within the Sultanate of Oman (with the northernmost section in the UAE), spans approximately >10,000 km2 (~500 km long and ~150 km wide; Searle and Cox, 1999), and is considered as one the largest and best-preserved portions of oceanic lithosphere on Earth. The ophiolite formed ca 96. Ma (Rioux et al., 2012) at a fast-spreading centre situated above a north-east dipping subduction zone, that resulted in its transport and emplacement onto to the Arabian continent in the late Cretaceous during the closure of the Tethyan ocean (e.g. Lippard, 1986; Ernewein et al., 1988; Searle and Cox, 1999; Rioux et al., 2012). Despite its complex history, the ophiolite is relatively un-deformed and is comprised of 12 fault-bounded blocks (Fig. 5.1) exhibiting a classic "Penrose" structure (Anonymous, 1972) defined by, from the bottom to the top, ultramafic mantle cumulates, layered and high level gabbroic cumulates, a sheeted dike complex (SDC) and associated pillow lavas.

The precise geodynamic setting of the Oman ophiolite is still actively debated, with decades of field studies and geochemical data suggesting a polygenetic origin which could consequently invalidate its use as a direct analogue for oceanic lithosphere formed at a fast-spreading mid-ocean ridge. Initially, the Oman ophiolite was regarded as a perfect representation of crust generated at a mid-ocean ridge (Coleman, 1981), with some making direct comparisons to that of crust formed at the East Pacific Rise (e.g. Boudier et al., 1997; Nicolas, 2012). However, in the northern section of the ophiolite there is a notable increase in the geochemical diversity of volcanic units (Fig. 5.1), ranging from depleted tholeiites (e.g. Pearce et al., 1981; Alabaster et al., 1982; Belgrano and Diamond, 2019) to boninites (e.g. Ishikawa et al., 2002; Goodenough et al., 2013) which are indicative of a depleted and hydrated mantle

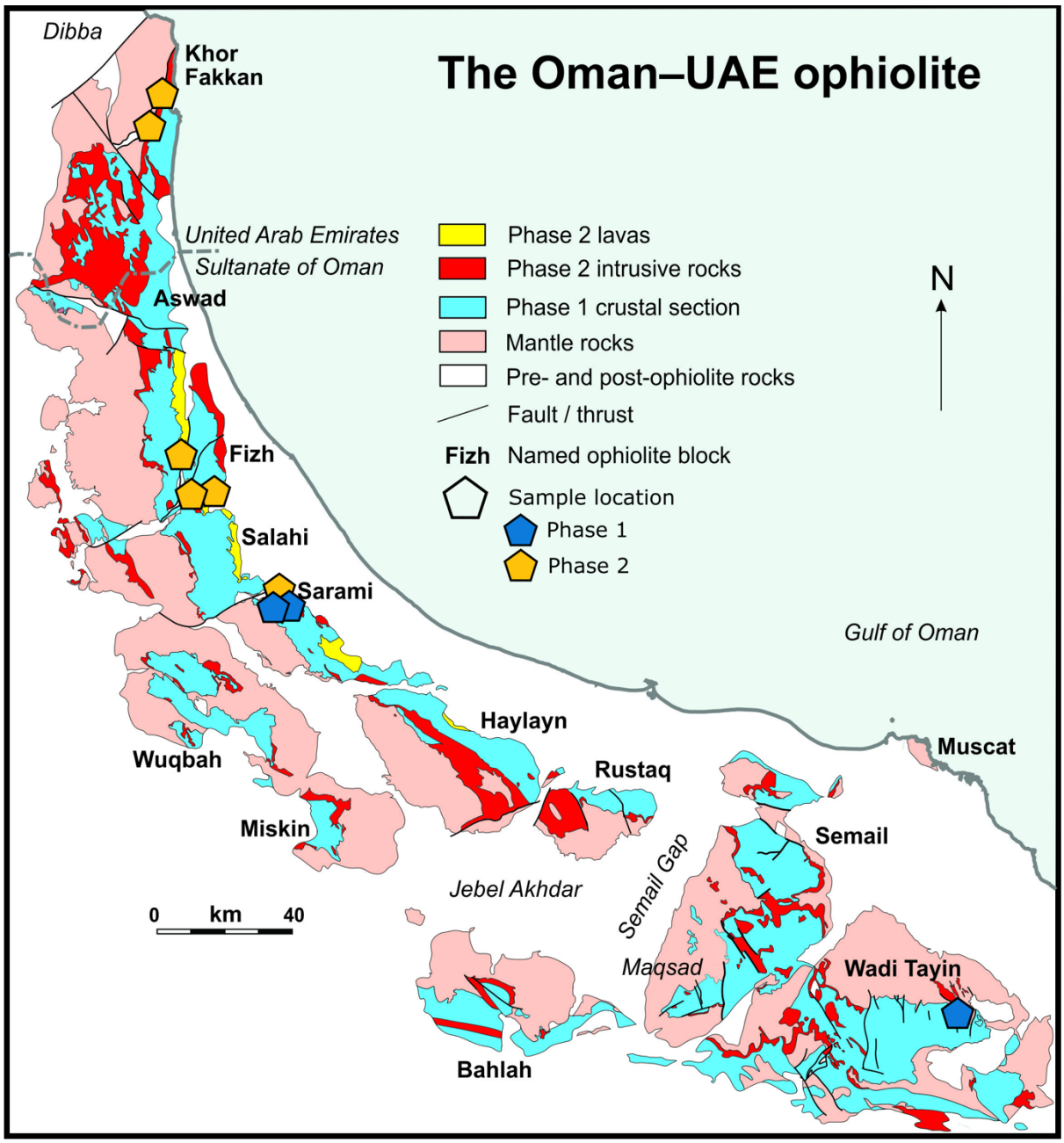

Fig. 5.1 Simplified geologic map of the Oman/UAE ophiolite. Sample locations are represented by pentagons. Maps is adapted from Goodenough et al. (2014) with subsequent modifications from de Graaff et al. (2019). The locations of samples selected for Ti isotope analyses are denoted by the pentagon symbols.

source related to the onset of subduction (e.g. Reagan et al., 2010). Plutonic equivalents of these units have also been found in the south (Fig. 5.1; De Graaff et al., 2019). In addition, more recent studies have observed that the formation of the main gabbro-sheeted dike-pillow lava sequence most akin to oceanic lithosphere required parental melts with water contents far greater than typical MORB magmas (>0.2 – 1 wt. % H_2O;

MacLeod et al., 2013; Müller et al., 2017; Koepke et al., 2021), and thus the subduction signature is ubiquitous throughout the entire ophiolite.

Despite mounting evidence that the Oman ophiolite formed at a subduction zone, others maintain it formed at a true open-ocean mid-ocean ridge and provide alternative hypotheses for the origins of the water in the mantle source from ancient subduction (e.g. Moores and Kellogg, 2000) to hydrothermal fluids (e.g. Benoit et al., 1999; Abily et al., 2011). The aim of this chapter will attempt to resolve the debate by using Ti isotope composition of Oman lavas and dikes as a novel isotopic tool to deduce the geodynamic origin of the ophiolite.

5.3.2 Magmatic history and diversity

Owing to the geochemical diversity observed within the Oman ophiolite, numerous workers have attempted to define the various phases and types of magmatism (e.g. Pearce et al., 1981; Alabaster et al., 1982; Ernewein et al., 1988; Goodenough et al., 2013; Goodenough et al., 2014; Belgrano et al., 2019). This chapter will follow the terminology of Goodenough et al. (2014) who utilised a combination of field data, geochemistry and mineralogy to broadly classify Oman ophiolite magmatism into two distinct groups: Phase 1 and Phase 2.

Phase 1 magmatism encompasses the earliest stages of magmatism which includes upper mantle mafic cumulates, gabbroic cumulates, and the sheeted dike with associated pillow lavas. These units have previously been referred to as the 'Geotimes' (Alabaster et al., 1982) and V1 (Ernewein et al., 1988). The composition of Phase 1 parental magmas is broadly comparable to that of Indian MORB (Fig. 5.2 e.g. Godard et al., 2003; Godard et al., 2006). However, a significant amount of Phase 1 also exhibit trace element characteristics comparable to that of fore-arc basalts and back-arc basalts (Fig. 5.2; Fig. 5.3; MacLeod et al., 2013). Relative to Indian MORB, Phase 1 compositions extend to lower MgO (Fig. 5.2; and higher SiO_2). TiO_2 and Cr also exhibit a more pronounced decrease during magmatic differentiation (i.e., decreasing MgO or increasing Y; Fig. 5.2). However, some Phase 1 lavas and dikes display large

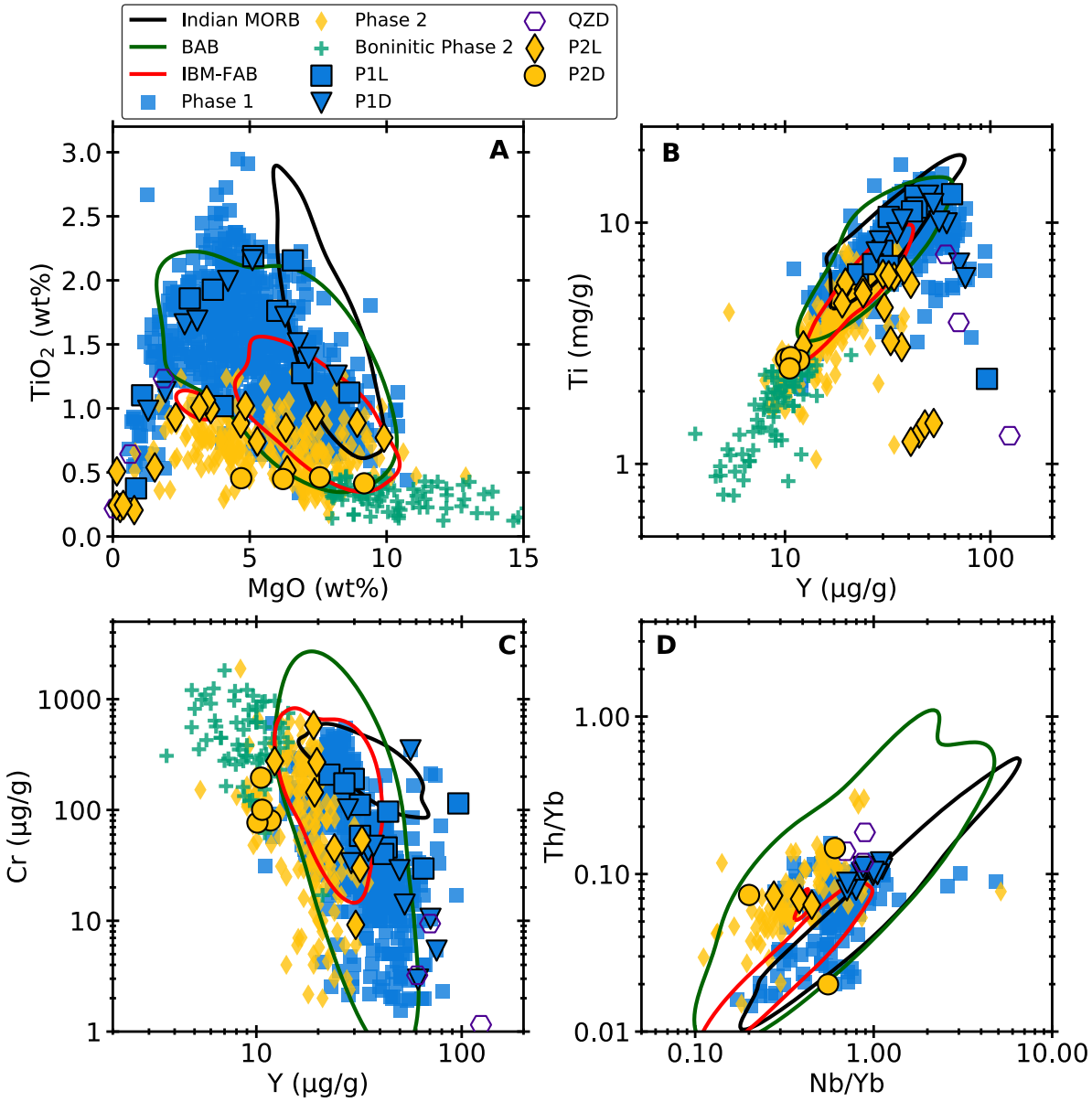

Fig. 5.2 Selected major and trace element variation and discrimination diagrams for Oman Phase 1 (blue squares) and 2 (yellow diamonds) lavas (L) and dikes (D). Quartz diorites (QZD) are from Phase 1 (see text). Larger symbols with black outlines represent samples measured for Ti isotopes. Boninitic Phase 2 (green symbols; classified based on criteria from Todd et al., 2012; and Pearce and Reagan, 2019) is included for comparison but is excluded from further plots and discussion. (A) - TiO_2 v.s. MgO (anhydrous, wt. %). (B) - Ti v.s. an immobile trace element, Y as an alteration resistant differentiation proxy after Pearce et al. (1981) and Alabaster et al. (1982) but with Y replacing Zr. (C) - Cr v.s. Y. (D) - Th/Yb - Nb/Yb diagram for subduction influence after. Oman data are from 'Oman DB' which include >1200 published and unpublished data compiled by Christopher Macleod and used with permission. Indian MORB, Back-arc basin (BAB) and Izu-Bonin-Mariana Fore-arc (FAB) basalt fields are defined by a kernel density contour that contains 95% of the data. Indian MORB and BAB data are taken from the compilation of Gale et al. (2013) and references therein. IBM-FAB data are from Reagan et al. (2010) and Shervais et al. (2019).

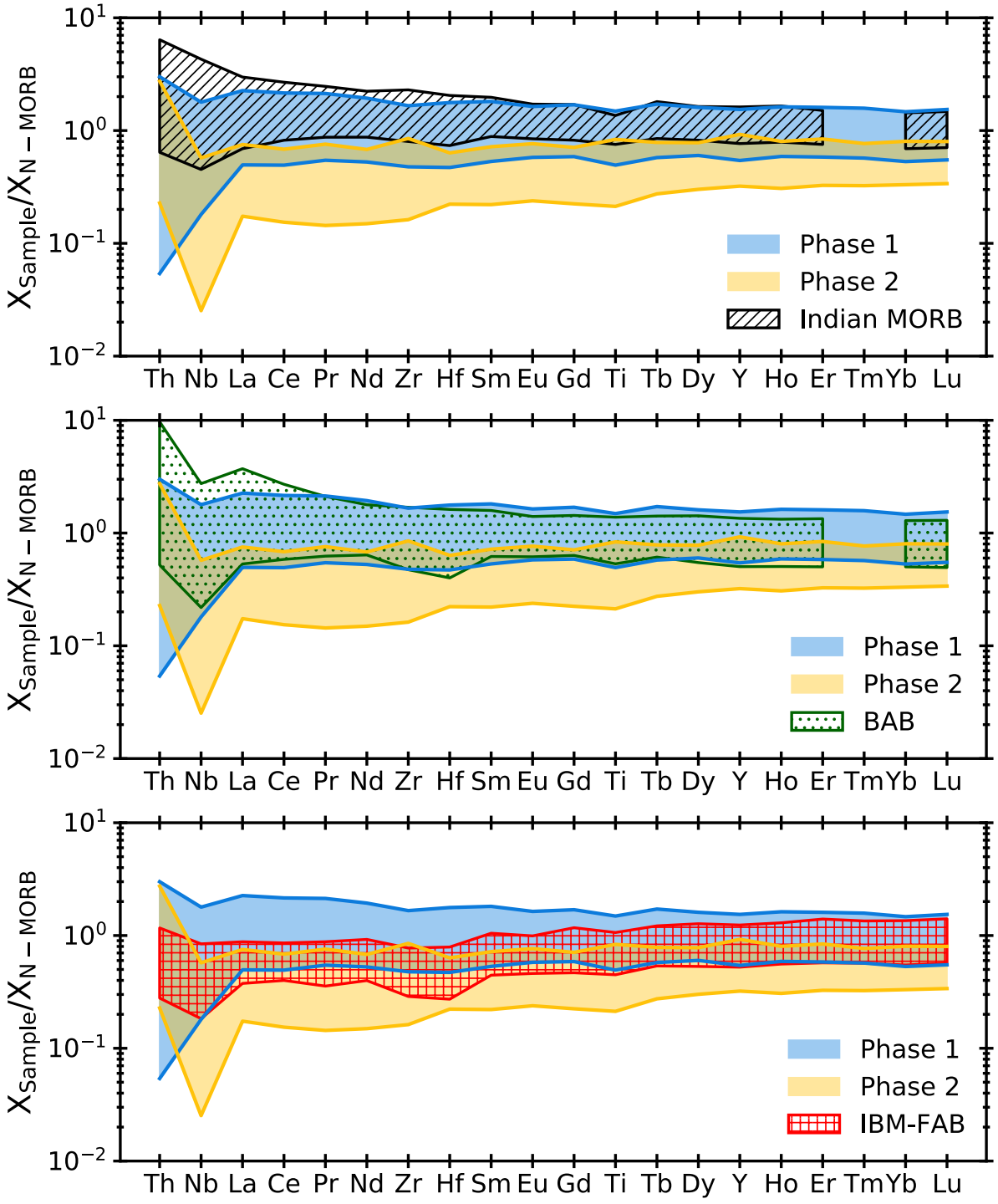

Fig. 5.3 Normal-MORB normalised trace element spider diagrams with fields showing the absolute 2σ range for primitive Oman ophiolite lavas and dikes compared to Indian MORB, back-arc basin (BAB) basalts, and Izu-Bonin-Mariana fore-arc basalts (IBM-FAB). Data sources for all suites are the same as those presented in Fig. 5.2, but filtered for samples with MgO (wt.%) > 6. Normalising values are from Pearce and Parkinson (1993).

variations in Th coupled with subtle depletion in Nb (Fig. 5.3), and elevated Th/Yb (Fig. 5.2) indicative of mild source depletion and/or influence from subduction-

derived fluids (Pearce, 1982; Pearce, 2008), relative to typical MORB. This is complemented by the observation that liquid lines of descent for major and minor elements (notably MgO vs. TiO_2) in Phase 1 resemble hydrous tholeiitic magmas often associated with fore and back arc spreading centres (Fig. 5.2; MacLeod et al., 2013; Müller et al., 2017; De Graaff et al., 2019).

Phase 2 comprises the later stages of magmatism in the Oman ophiolite and is characterised by cross-cutting sequences of plutonic units that include wehrlites, gabbros, tonalites and trondhjemites (e.g. De Graaff et al., 2019), and lavas and dikes that range in composition from basaltic to rhyolitic (e.g. Alabaster et al., 1982; Godard et al., 2006). Relative to Phase 1, Phase 2 magmas are characterised by lower TiO_2 contents (Fig. 5.2) notable depletions in rare earth (REE; e.g. Y, La, Ce, Nd and Sm) and high field strength (HFSE; e.g. Zr, Hf, Nb and Ta) elements (Fig. 5.2; Fig. 5.3). Phase 2 incorporates the Lasail, Alley and clinopyroxene-phyric units of Alabaster et al. (1982), which were later collectively termed 'V2' by (Ernewein et al., 1988) and also units with boninitic affinity (Ishikawa et al., 2002). Whilst there are nuanced compositional differences amongst some of these subdivisions (e.g. clinopyroxene compositions; see Alabaster et al., 1982; Belgrano et al., 2019), the bulk major and trace element systematics of non-boninitic Phase 2 magmas are broadly consistent with origins from the same subduction-related hydrous depleted source (Goodenough et al., 2014; Haase et al., 2016; De Graaff et al., 2019). Phase 2 samples with a boninitic affinity (defined using criteria from Todd et al., 2012; Pearce and Reagan, 2019) are show separately in Fig. 5.2 and are excluded from discussion for the remainder of this chapter due to the complex and often disputed nature of their geodynamic significance and classification (for a detailed review see Pearce and Reagan, 2019 and references therein).

5.3.3 Sample selection

Samples selected for Ti isotope analyses were chosen from both Phase 1 and Phase 2 from several localities to provide comprehensive spatial and temporal

coverage across the entire ophiolite complex (Fig. 5.1), with the aim to utilise Ti isotopes to trace the onset of hydration of Oman ophiolite magmas through time by comparing observed Ti isotope fractionation trends in Oman suites to modern volcanic suites where the water contents of the parental magma is well constrained (see chapter 3 and Hoare et al., 2020).

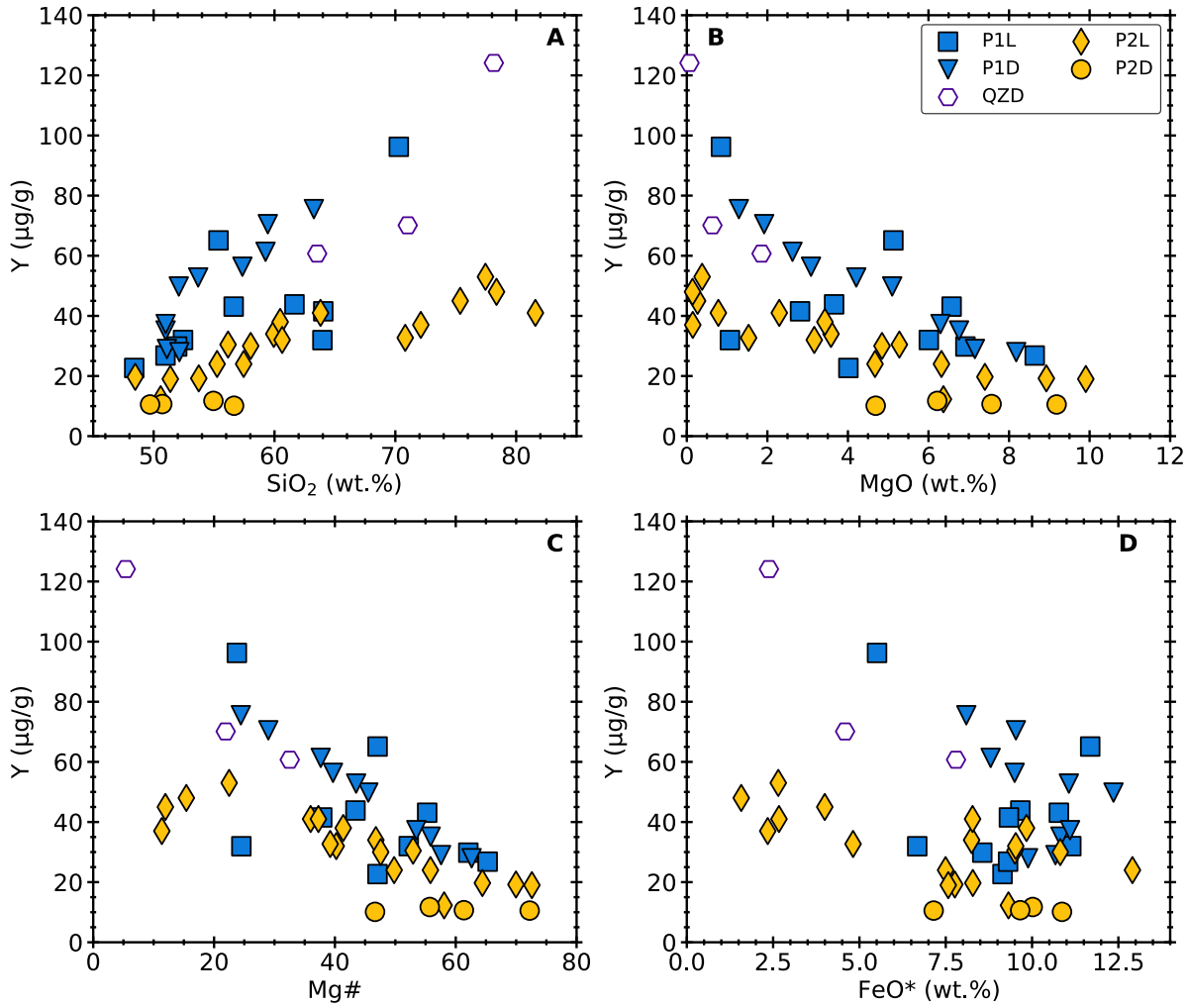

Fig. 5.4 Screening for mobility of conventional major element indices of magmatic differentiation in samples selected for Ti isotope analysis, relative to Y, an immobile, incompatible element based on the methodology of Cann (1970). (A) – Y vs. SiO_2; (B) – Y vs. MgO; (C) – Y vs. Mg#; (D) – Y vs. FeO*. All major elements are in wt.% re-calculated on an anhydrous basis. The systematic covariation observed between selected major elements and Y suggest they likely mirror their original magmatic compositions and thus have not been significantly affected by alteration, apart from some of the P1L samples which display notable scatter.

The bulk compositions of the samples for major, minor and trace elements are provided in Appendix E4 and select elements are shown in Fig. 5.2 and Fig. 5.4 along with the entire dataset from 'OmanDB' (courtesy of Christopher MacLeod).

Phase 1 samples consist of both dikes (P1D) and lavas (P1L). The Phase 1 dikes are sourced from the sheeted dike complex located at Wadi Saq, situated within the north-eastern Ibra valley, Wadi Tayin massif in the southern Oman ophiolite (Fig. 5.1). A detailed petrographic and geochemical description of these samples can be found in Loocke (2016). Wadi Saq sample define a tholeiitic liquid line of descent, typical of Phase 1 (Fig. 5.2). Major and minor element contents (wt.% anhydrous) are as follows SiO_2 contents range from 50.99 to 64.04, MgO contents from 1.29 to 8.18, and TiO_2 contents from 0.98 to 2.16 wt.%. SiO_2 and MgO contents show coherent correlation with variations in TiO_2 and Y (Fig. 5.2; Fig. 5.4) both of which are considered to be immobile during alteration (e.g. Cann, 1970; Staudigel et al., 1996), indicating SiO_2 and MgO contents have been relatively unaffected by alteration. This is also consistent with relative low loss on ignition (LOI) values in Wadi Saq samples (0.88-3.96). Phase 1 lavas are from the Ghuzayn area of the Sarami massif (Fig. 5.1) located in the central part of the ophiolite, collected by Christopher MacLeod in 1989. The Sarami samples exhibit greater LOI values (1.66-4.87) and scatter in co-variations of SiO_2-MgO-TiO_2-Y compared to Wadi Saq (Fig. 5.2; Fig. 5.4), suggesting a higher degree of alteration. Sarami samples cover a larger compositional range; 48.39 to 70.29 wt.% for SiO_2, 8.64 to 0.85 wt.% for MgO, and 0.4 to 2.19 wt.% for TiO_2 relative to Wadi Saq (Fig. 5.2; Fig. 5.4). For both Wadi Saq and Sarami, the peak in TiO_2 contents occurs at ~5 wt.% MgO (Fig. 5.2). In addition, 3 quartz diorites (QZD) from Wadi Saq were also selected which continue the elemental fractionation trends seen in the sheeted dike complex to more evolved compositions (Fig. 5.2; Fig. 5.4), and are interpreted to be co-genetic and the products of extensive fractional crystallisation of the same source (Loocke, 2016).

Phase 2 lava samples are from the Fizh massif (n=15) in the north and the Sarami massif (n=3) in the centre (Fig. 5.1). The bulk major, minor and trace element chemistry for the majority of Fizh Phase 2 lavas is reported in Lippard (1986; n=6) and Pearce et

al. (1981; n=7). The remaining Fizh Phase 2 lavas are from J. Pearce (unpublished). Sarami Phase 2 lavas are from C. MacLeod (1989, unpublished). The selected Phase 2 lavas define a compositional range from basalt to rhyolite. SiO_2 contents from 48.48 to 81.59 wt.%, MgO contents from 0.14 to 9.91, and TiO_2 contents from 0.22 to 1.02 wt.% (Fig. 5.2; Fig. 5.4). LOI values for Phase 2 lavas are generally higher (1.28 to 9.24) relative to Phase 1 suggesting more extensive alteration. However, SiO_2 and MgO show systematic trends relative to variations in TiO_2 and Y (Fig. 5.2; Fig. 5.4), which implies the effects of alteration on Mg and Si are relatively limited. The lavas also exhibit lower Ti and Y contents, and elevated Th/Yb (Fig. 5.2; Fig. 5.4). Phase 2 dike samples are from Goodenough et al. (2013) and were collected from the Khor Fakkan massif located in the northern-most section of the ophiolite in the United Arab Emirates (Fig. 5.1). Units from the Khor Fakkan area exhibit a prominent subduction signature that is interpreted to reflect a highly depleted, hydrous mantle source (Goodenough et al., 2014). Khor Fakkan dikes are characterised by markedly low TiO_2 contents (0.42-0.46 wt.%; Fig. 5.2; Fig. 5.4), significant depletion in REE's such as Y, and elevated Th/Yb (Fig. 5.2; Fig. 5.4). SiO_2 contents for Khor Fakkan dikes range from 49.70 to 56.65 wt.%, with MgO contents from 6.22 to 9.18 (Fig. 5.2; Fig. 5.4). LOI values of 0.53-1.3 suggest the dikes are relatively unaltered.

5.4 MELTS modelling

The effect of water on fractionation trends in Oman ophiolite lavas and dikes, liquid lines of descent were modelled using the 1.1.0 version of Rhyolite MELTS (Ghiorso and Gualda, 2015). An experimental MORB composition from Kinzler and Grove (1993) was used as the parental magma composition but with the TiO_2 contents lowered to 0.7 wt.% to match the inferred parental magma of the Oman ophiolite (Pallister, 1984; MacLeod et al., 2013). The starting water contents of the parental magma was progressively varied between 0 to 1 wt.% (with the inferred range of H_2O contents for Phase 1 magmas being 0.2-1 wt.%; MacLeod et al., 2013; Müller et al., 2017; De Graaff et al., 2019) with the pressure fixed at 200 MPa to simulate shallow

fractionation at intra-crustal depth (De Graaff et al., 2019). The oxygen fugacity (fO_2) was set at quartz-fayalite-magnetite (QFM) buffer. From the liquidus temperature each crystallisation step is defined by a 5°C incremental temperature decrease, with the model stopping at 800°C, at which point ca. 70-80% of the liquid has crystallised.

The Ti isotope evolution of the evolving melt is calculated incrementally at each step using a Rayleigh distillation law (see chapter 3 for details). The bulk fractionation factor is weighted relative proportion of Ti in each phase in the crystallising assemblage. The Ti isotope fractionation for each phase (i.e., titanomagnetite and ilmenite, clino- and orthopyroxene) are calculated using the equations derived from linear regression analysis in chapter 4. Enrichment of Zr and Y in the melt (C_L/C_O) during fractionation crystallisation was also calculated from the Rhyolite MELTS output using a rayleigh fractionation law: $^{C_L}/_{C_o} = F^{(D-1)}$. Partition coefficients ($D_{i\text{-melt}}$) for each phase were calculated using the derived equations from the multiple linear regression analysis of Bédard (2005; 2006; 2007; 2014), which enable D values to change with respect to melt composition. Bulk D values were calculated incrementally using the mineral modal proportions at each step of MELTS model.

5.5 Results

Mass-dependent Ti isotope compositions for all reference materials and Oman samples are provided in Appendix E4 and illustrated in (Fig. 5.5). Samples from both Phase 1 and Phase 2 exhibit trends of increasing $\delta^{49/47}$Ti correlates with increasing SiO_2, decreasing TiO_2 and Mg# consistent with previous studies (Fig. 5.5; Millet et al., 2016; Deng et al., 2019; Johnson et al., 2019; Hoare et al., 2020; Zhao et al., 2020). $\delta^{49/47}$Ti also displays a positive correlation with increasing Y contents (Fig. 5.5). The following section outlines the $\delta^{49/47}$Ti variation within each phase of magmatism.

5.5.1 Phase 1

Phase 1 displays $\delta^{49/47}$Ti values that range from -0.01±0.03‰ to +1.24±0.02‰ for lavas (P1L); +0.00±0.02‰ to +0.60±0.02‰ for sheeted dikes (P1D); and +0.48±0.04‰ to +1.59±0.03‰ for quartz diorites (QZD). At a SiO_2 contents >60 wt.% Phase 1 exhibits a

greater increase in $\delta^{49/47}$Ti relative to Phase 2, with this observation most apparent in Phase 1 dikes (Fig. 5.5). Phase 1 samples define a $\delta^{49/47}$Ti vs. SiO_2 trend that is intermediate between the trends observed in high-Ti intraplate magmas (Fig. 5.5; Deng et al., 2019; Hoare et al., 2020) and those from tholeiitic and calc-alkaline suites (Fig. 5.5; Hoare et al., 2020). Relative to Mg# the majority of Phase 1 show $\delta^{49/47}$Ti values that fall along a similar trend to calc-alkaline magmas (Hoare et al., 2020), notwithstanding some scatter (Fig. 5.5).

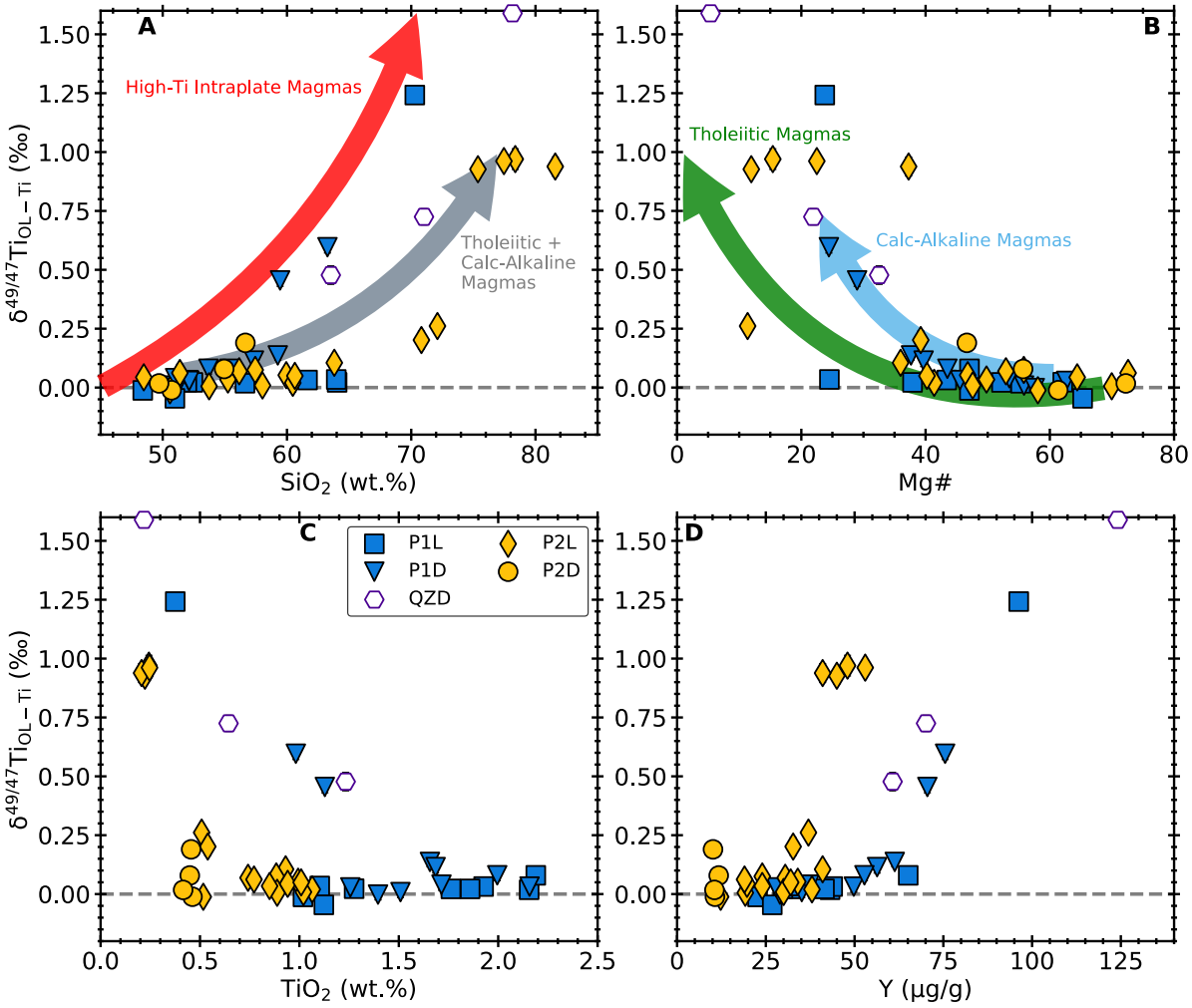

Fig. 5.5 Variations of $\delta^{49/47}$Ti (‰) versus: (A) – SiO_2; (B) – Mg# (100*Mg/Mg+Fe^{2+}); (C) – TiO_2; and (D) – Y contents in microgram per gram (µg/g). SiO_2 and TiO_2 are in weight percent (wt.%; recalculated on an anhydrous basis). Uncertainties for $\delta^{49/47}$Ti (95% confidence intervals) are smaller than the symbol size. The coloured arrows indicate the general evolution pathways for magmatic differentiation suites of varying geodynamic origin compiled from the literature (see Millet et al., 2016; Deng et al., 2019; Johnson et al., 2019; Hoare et al., 2020, and Chapter 3).

5.5.2 Phase 2

$\delta^{49/47}$Ti values for Phase 2 samples vary from range from -0.01±0.02‰ to +0.97±0.04‰ for lavas (P2L) and -0.01±0.02‰ to +0.19±0.02‰ for dikes (P2D). Compared to Phase 1, Phase 2 samples display elevated $\delta^{49/47}$Ti values at lower TiO_2 and Y contents (Fig. 5.5). Phase 2 samples display the least variation in $\delta^{49/47}$Ti at a given SiO_2 (Fig. 5.5), yet conversely exhibit larger variation in $\delta^{49/47}$Ti with decreasing Mg# relative to Phase 1, but with notable scatter at Mg# <40 (Fig. 5.5).

5.6 Discussion: Ti isotope and trace element constraints on the geodynamic setting of the Oman Ophiolite

Whilst the general trace element systematics of units within the Oman ophiolite provide clear evidence for progressive depletion of mantle sources, they fail to provide unambiguous constraints for or against either a polygenetic, supra-subduction setting or a pure mid ocean ridge origin. In this section a novel combination of Ti isotopes, incompatible, immobile, and redox-sensitive trace elements are utilised to probe the redox conditions of differentiated magmas and the mantle source from which they originated.

5.6.1 Pitfalls and Challenges to Finding Robust Indices of Magma Differentiation in Ophiolites

Hydrous and hence oxidised magmas display distinct Ti isotope fractionation trends relative to drier and more reduced tholeiitic magmas (Chapter 3 and Hoare et al., 2020). This is best represented by covariation of $\delta^{49/47}$Ti with respect to Mg#, with hydrous calc-alkaline arc magmas (>2 wt.% H_2O) exhibiting elevated $\delta^{49/47}$Ti at a given Mg# relative to both island-arc (<1 wt.% H_2O) and mid-ocean ridge tholeiites (<0.2 wt.% H_2O). This contrast in $\delta^{49/47}$Ti is a direct manifestation of the earlier onset of Fe-Ti oxide crystallisation in hydrous magmas (Hoare et al., 2020), due to the suppression of the plagioclase liquidus temperature (e.g. Berndt et al., 2005; Feig et al., 2006; Feig et al., 2010; Nandedkar et al., 2014). Additionally, as the terrestrial mantle is homogenous with respect to $\delta^{49/47}$Ti (e.g. Millet et al., 2016; Greber et al., 2017; Zhao et

al., 2020), the $\delta^{49/47}$Ti of parental magmas is unlikely to be modified by source depletion or enrichment processes as evidenced by mantle melting modelling in Chapter 4.

However, there is an additional caveat in that the calc-alkaline and tholeiitic Ti isotope evolution trends are dictated by analyses of differentiated lavas that are geologically young (all < 3 Ma), fresh, well-characterised, and have strong petrographic and geochemical evidence supporting origins as the products of fractional crystallisation (see Chapter 3 for details). Thus, this poses potential problems when attempting to apply such a proxy further back into the geologic record, particularly as ophiolites have often experienced intense alteration (e.g. Pearce, 2008; Pearce, 2014 and references therein). Whilst Ti is an immobile element (e.g. Staudigel et al., 1996), and, as such its isotopic budget is likely unaffected by processes such as weathering and metamorphism, major element proxies for magmatic differentiation such as Si, Mg and Fe can be mobilised to varying degrees (Fig. 5.4; Cann, 1970; Floyd and Winchester, 1978; Pearce, 2014). In the past use of conventional major elements has led to some erroneous classification of altered rocks from ophiolites as evolved calc-alkaline arc lavas (e.g. Miyashiro, 1973; Pearce and Robinson, 2010). Whilst it is apparent from Fig. 5.5 that Oman samples generally exhibit increasing $\delta^{49/47}$Ti with decreasing Mg# likely due to Fe-Ti oxide crystallisation, there is notable scatter that encompasses the range of both calc-alkaline and tholeiitic differentiation pathways. For example, most Phase 1 samples evolve along a trajectory comparable to that of calc-alkaline suites with parental magmas that have initial H_2O contents >2 wt.%, which is at odds with previous H_2O estimates for Phase 1 of 0.2-1 wt.%, and hence their origins from 'moist' MORB magmas. Similarly, $\delta^{49/47}$Ti-Mg# systematics would suggest Phase 2 samples evolved from parental magmas that range from relatively dry tholeiites to hydrous arc magmas (Fig. 5.5). Therefore, it difficult to place precise constraints on the water contents of Oman magmas using Mg# alone, as alteration has to potential to induce modifications to the concentrations of both mobile elements used to calculate this ratio as can be observed Fig. 5.4, where some samples exhibit scatter in both MgO and FeO* relative to Y.

Recently there have also been efforts to apply $\delta^{49/47}$Ti-SiO_2 variations as a geodynamic proxy for Archean rocks (Aarons et al., 2020). However, differentiation trajectories in $\delta^{49/47}$Ti-SiO_2 space are primarily a reflection of the Ti contents of the parental magma (Hoare et al., 2020 and Chapters 2 and 3). Ti-rich intraplate magmas displaying greater variation in $\delta^{49/47}$Ti-SiO_2 space as high melt Ti contents enables crystallisation of both ilmenite and high-Ti titanomagnetite (Hoare et al., 2020; and Chapters 3 and 4). Despite varying parental water contents, Arc magmas and MOR tholeiites define relatively similar trends for $\delta^{49/47}$Ti-SiO_2 (Fig. 5.5; Hoare et al., 2020). The observation that Phase 1 samples that are spatially related display a large range of variation $\delta^{49/47}$Ti-SiO_2 compositional space makes it difficult to derive any meaningful geodynamic information. Hence $\delta^{49/47}$Ti-SiO_2 systematics can only be used to identify Ti-rich intraplate magmas and provides no inference on the redox state of the original parental magma from which the samples evolved.

Immobile and/or incompatible elements such as Ti, Y, Zr, and Nb have previously been utilised to circumvent the effects of alteration and decipher the geodynamic origin of ophiolites (e.g. Pearce and Cann, 1973; Pearce and Norry, 1979; Pearce et al., 1981; Alabaster et al., 1982; Pearce, 2008; Pearce and Robinson, 2010), thus providing the ideal context from which to interpret the $\delta^{49/47}$Ti variations observed in Oman samples. Fig. 5.5 demonstrates that $\delta^{49/47}$Ti variations for Oman samples are best observed relative to their co-variation with Ti and Y, with both Phase 1 and Phase 2 exhibiting coherent trends with greatly reduced scatter compared to when either SiO_2 or Mg# are used as differentiation indices.

5.6.2 Estimation of Parental Magma Compositions

As demonstrated by MacLeod et al. (2013) the magmatic differentiation of Phase 1 lavas and dikes is best explained by fractionation from a hydrous tholeiitic parent magma, and empirically, the major element compositions of Phase 1 have closer affinity to magmas associated with both back-arc and fore-arc settings than the majority of MOR derived magmas. By utilising the same MELTS modelling approach

taken by MacLeod et al. (2013) the influence of water contents on Ti isotope fractionation trends in the Oman samples can be investigated. Details of the MELTS modelling are given in section 5.4.1.

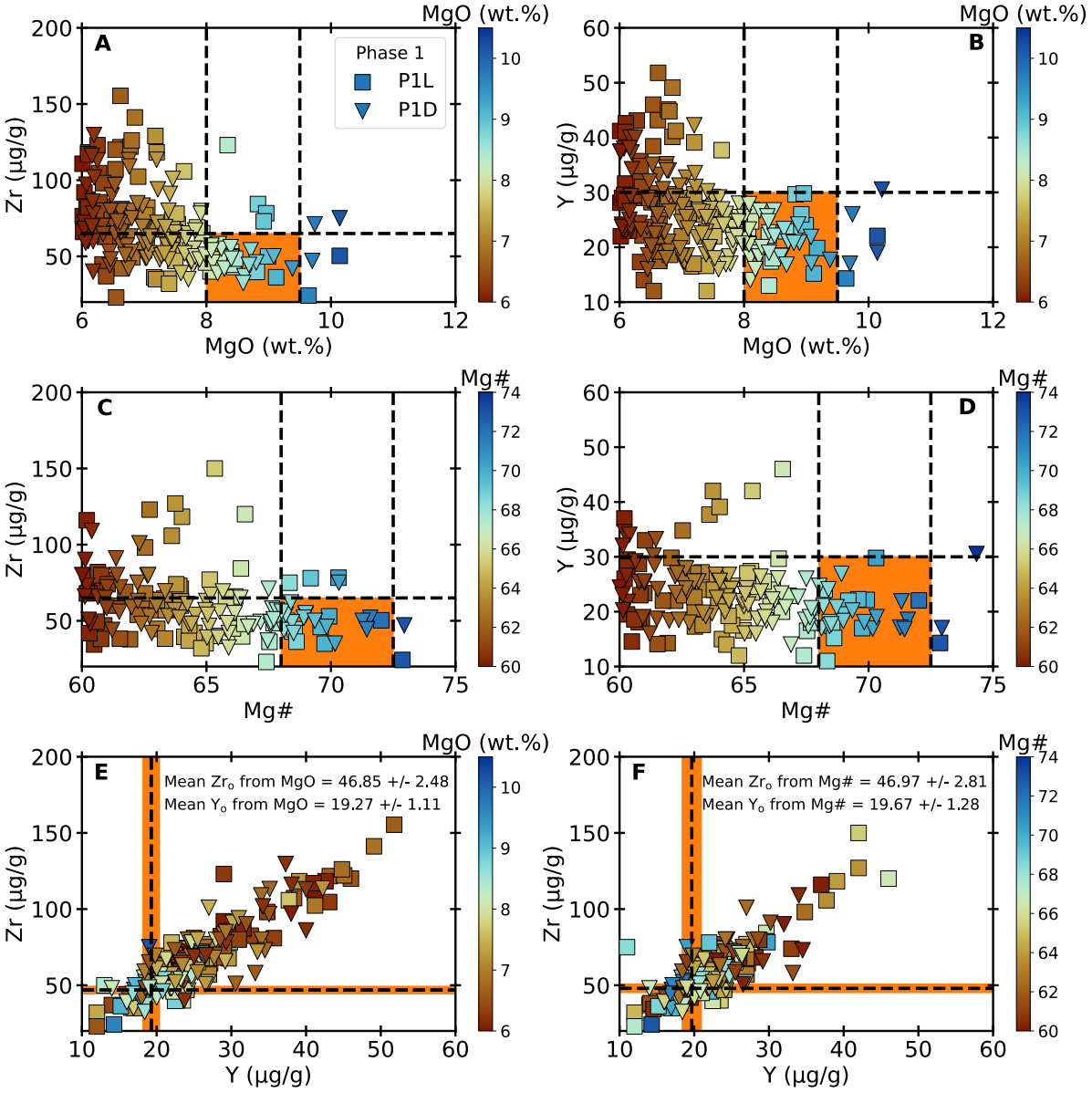

Fig. 5.6 Screening of primitive Phase 1 lavas (P1L) and dikes (P1D) using either MgO > 6 wt.% or Mg# > 60. (A) – Zr vs. MgO. (B) – Y vs. MgO. (C) – Zr vs. Mg#. (D) Y vs. Mg#. (E) Zr vs. Y for samples with MgO > 6 wt.%. (F) Zr vs. Y for samples with Mg# > 60. Colour bars are shown for MgO or Mg values depending on the panel. The shaded orange area in panels A-D indicates the compositional space from which the estimated parental magma Zr and Y contents was derived. The dashed lines indicate the cut-offs imposed for values of MgO, Mg#, Zr and Y were imposed to remove samples that exhibited enrichment in Zr or Y due to fractional crystallisation (MgO < 8; Mg#<68) and outliers. The dashed lines in panels E and F show the mean Zr and Y values derived from using MgO and Mg# respectively. The shaded orange areas in panels E-F indicate the 2-standard error on the mean.

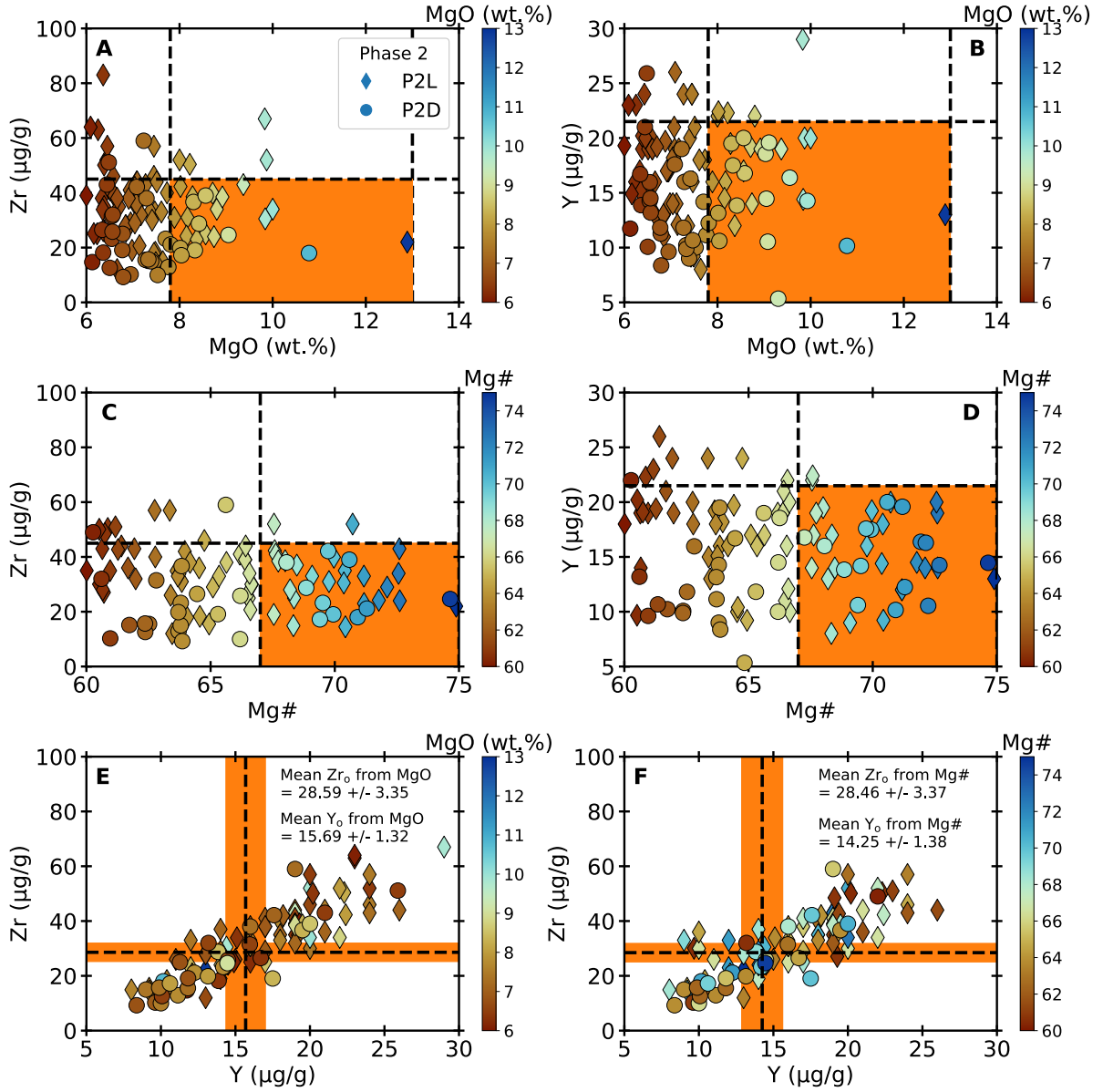

Fig. 5.7 Screening of primitive Phase 2 lavas (P2L) and dikes (P2D) using either MgO > 6 wt.% or Mg# > 60. (A) – Zr vs. MgO. (B) – Y vs. MgO. (C) – Zr vs. Mg#. (D) Y vs. Mg#. (E) Zr vs. Y for samples with MgO > 6 wt.%. (F) Zr vs. Y for samples with Mg# > 60. Colour bars are shown for MgO or Mg values depending on the panel. The shaded orange area in panels A-D indicates the compositional space from which the estimated parental magma Zr and Y contents was derived. The dashed lines indicate the cut-offs imposed for values of MgO, Mg#, Zr and Y were imposed to remove samples that exhibited enrichment in Zr or Y due to fractional crystallisation (MgO < 7.8; Mg#<67) and outliers. The dashed lines in panels E and F show the mean Zr and Y values derived from using MgO and Mg# respectively. The shaded orange areas in panels E-F indicate the 2-standard error on the mean.

As primitive Phase 2 magmas are generally more depleted in elements such as Ti, Zr, and Y relative to Phase 1, this results in an offset in the differentiation trends observed in both Y (or Zr) with respect to either Ti or $\delta^{49/47}$Ti (Fig. 5.2; Fig. 5.5). Therefore, to facilitate direct comparison between the two phases, $\delta^{49/47}$Ti variations

should be evaluated relative to the enrichment factor of Y and Zr in the samples relative to a primitive 'parental magma'. By utilising a 'big data' approach on all available geochemical data for Oman ophiolite (Oman DB; MacLeod et al. unpublished) constraints can be placed on potential parental magma compositions (Fig. 5.6; Fig. 5.7) from which Zr and Y enrichment can be propagated (see captions of Fig. 5.6; Fig. 5.7 for details). Fig. 5.6 and Fig. 5.7 demonstrate the approach taken to estimate the Zr and Y concentration of a representative parental magma for Phase 1 and Phase 2 respectively. The estimates are based on a selection of primitive samples that show little to no increase in Zr or Y, with respect to MgO or Mg# due to fractional crystallisation. This approach was slightly more challenging for Phase 2 than Phase 1 due to the smaller data set and the less apparent positive inflection in Zr or Y with increasing MgO or decreasing Mg# (Fig. 5.7).

5.6.3 Ti isotope hygrometry: Elucidating the water contents of differentiated Oman ophiolite melts

The $\delta^{49/47}$Ti values along with Zr and Y enrichment factors of Oman ophiolite lavas and dikes superimposed onto liquid lines of descent modelled using rhyolite MELTS outputs (for model details see 5.4.1) are show in Fig. 5.8. The TiO_2-MgO systematics of Phase 1 lavas and dikes are best replicated from a parental magma with 0.2-0.5 wt.% H_2O (Fig. 5.8), consistent with previous estimates for Phase 1 (MacLeod et al., 2013). However, when $\delta^{49/47}$Ti evolution is modelled vs. MgO for varying H_2O contents, most samples display trends in excess of 1 wt.% H_2O, with no discernible difference between Phase 1 and Phase 2 magmas (Fig. 5.8). In contrast, when the evolution of $\delta^{49/47}$Ti is compared to the enrichment of Zr and Y, discrete differentiation trends become apparent (Fig. 5.8). The $\delta^{49/47}$Ti evolution Phase 1 lavas and dikes is best reproduced with a parental magma with 0.5 wt.% H_2O, particularly with respect to Y enrichment (Fig. 5.8), whereas Zr enrichment display more scatter potentially due to the accumulation of Zr-rich phases such as zircon (Fig. 5.8). However, most samples are within the 95% confidence interval of the weighted linear regression of the whole data set (Fig. 5.8). Phase 2 samples consistently display elevated $\delta^{49/47}$Ti values with

respect to Zr or Y enrichment than Phase 1, implying their parental magma contained >1wt.% H_2O (Fig. 5.8). As rhyolite MELTS is best suited to modelling

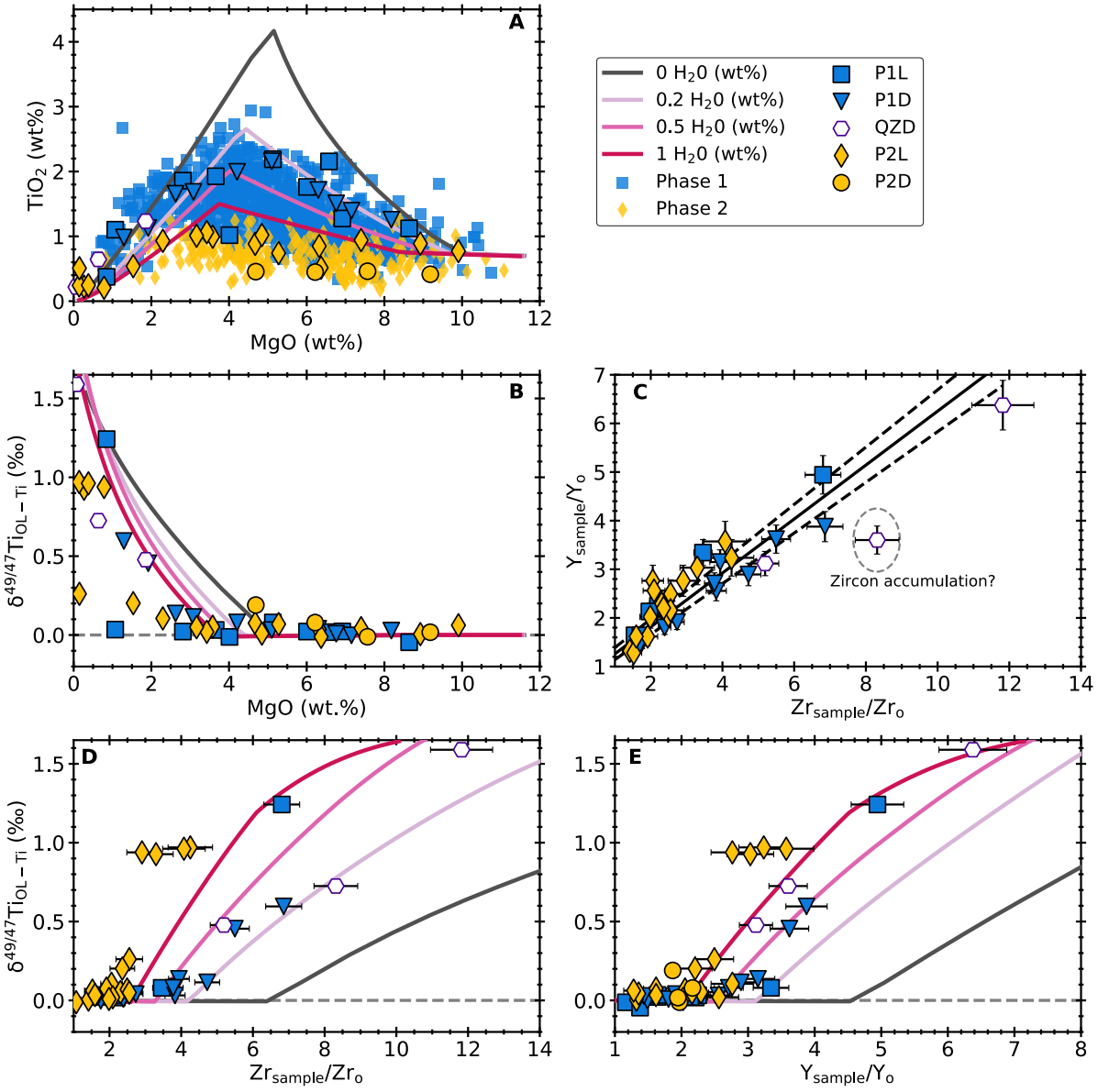

Fig. 5.8 Results of MELTS modelling (A) – TiO_2 vs. MgO and (B) – $\delta^{49/47}Ti$ vs. MgO for Phase 1 and Phase 2. Details of the conditions of the rhyolite MELTS models and the Rayleigh distillation modelling for the $\delta^{49/47}Ti$ compositions of the MELTS output can be found in section 5.4.1. (C) – Co-variation of Y and Zr enrichment factors for Phase 1 and Phase 2 samples, error bars represent error propagated from the uncertainty on the estimated Y or Zr contents of the parental magma from Fig. 5.6 and Fig. 5.7. Solid black line represents a weighted linear regression of all samples, with dashed black lines indicating the 95% confidence interval of the regression. (D) – $\delta^{49/47}Ti$ vs. Zr enrichment factor. (E) – $\delta^{49/47}Ti$ vs. Y enrichment factor. Solid lines represent liquid lines of descent produced by varying the H_2O contents of the starting composition from 0-1 wt.% in rhyolite MELTS.

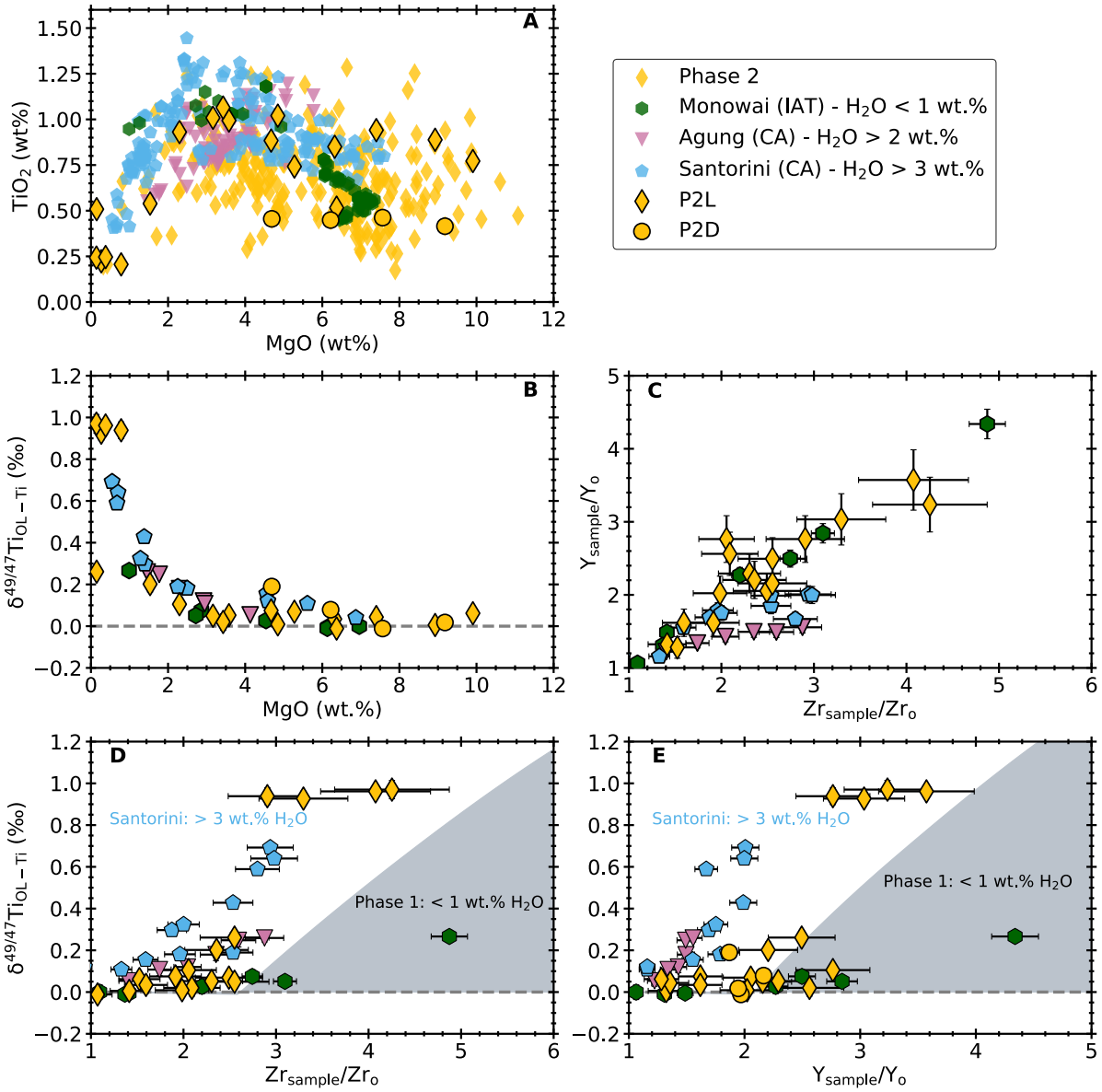

Fig. 5.9 Phase 2 lavas and dikes compared to differentiated arc magmas from Chapter 3 and Hoare et al. (2020) (A) – TiO_2 vs. MgO and (B) – $\delta^{49/47}Ti$ vs. MgO. (C) – Co-variation of Y and Zr enrichment factors for Phase 2 samples and arc suites, error bars represent error propagated from the uncertainty on the estimated Y or Zr contents of the parental magma from Fig. 5.6 and Fig. 5.7. The Zr and Y enrichment factors for arc suites were derived in the same manner as the Oman samples. Arc dataset is provided in Appendix E1 and E2. (D) – $\delta^{49/47}Ti$ vs. Zr enrichment factor. (E) – $\delta^{49/47}Ti$ vs. Y enrichment factor. The shaded grey area in panels D-E represents the maximum extent of the MELTS models from Fig. 5.8, with the edge defined by the 1 wt.% H_2O model.

tholeiitic compositions at a limited range of H_2O contents (<1wt.% H_2O; e.g. Nandedkar et al., 2014), in order to place more precise constraints on the water contents of Phase 2 parental magmas, their compositions were directly compared to suites of differentiated arc magmas where the H_2O contents of the parental magma is well constrained as shown in Fig. 5.9.

Fig. 5.9 demonstrates that not only are the major element systematics of Phase 2 comparable to arc magmas (from both tholeiitic island and calc-alkaline arcs), but they also exhibit similar $\delta^{49/47}$Ti fractionation trends. In general, Phase 2 samples define a trend that is intermediate between hydrous calc-alkaline magmas (>3 wt.% H_2O) and the 1 wt.% H_2O fractionation trend modelled using MELTS (Fig. 5.9). Island arc tholeiites are often used as an analogue for Phase 2, however when compared to the Monowai differentiation suite (<1 wt.% H_2O), Phase 2 consistently displays increased $\delta^{49/47}$Ti values relative to Zr and Y enrichment (Fig. 5.9). When considering both comparisons to natural arc data and MELTS modelling, it is likely that the parental magma of Phase 2 had between 1 and 3 wt.% H_2O (Fig. 5.9). This is consistent with concentrations of H_2O ranging from 1.5 to 2.7 wt.% measured in primitive (>5 wt.% MgO) Phase 2 basaltic glasses (Belgrano et al., 2021).

Overall, the $\delta^{49/47}$Ti compositions of Oman ophiolite lavas and dikes indicate that Phase 1 magmas possess initial water contents ~0.5 wt.% H_2O, which is significantly greater than observed for modern East Pacific Rise MORB (to which Phase 1 is often compared) at ~0.2 wt.% (le Roux et al., 2006; Portner et al., 2021). The observation that Phase 1 samples from the southernmost section of the ophiolite also exhibit a hydrous fractionation trend further corroborates that the 'moist MORB', and hence subduction signature is ubiquitous throughout the entire ophiolite. Whereas Phase 2 have estimated initial H_2O contents ~2 wt.%, comparable to modern arc magmas. This provides further evidence for a transition from moist to wet magmatism during the history of the Oman ophiolite. Given that constraints from geochronology date Phase 1 at 96.5-95.5 Ma, compared to 95.4-95.1 for Phase 2 (Rioux et al., 2012; Rioux et al., 2013), it is clear the increase in the influx of water occurred extremely rapidly (~2 Myr).

5.6.4 The redox state of Oman ophiolite mantle sources

Titanium isotopes provide clear evidence that magmatic differentiation in the Oman ophiolite, both spatially and temporally, occurred under hydrous conditions. Observations from Ti isotopes can be combined with investigations of variations in

redox-sensitive and incompatible elements to provide comprehensive constraints on redox transitions within the ophiolite, whilst also assessing the impact of mantle source depletion.

Elements that possess variable redox states under terrestrial conditions can be utilised to probe the redox state of magmas. Vanadium (V) can possess multiple oxidation states, which influences its partition coefficient ($D_V^{mineral/melt}$) during magmatic processes such as mantle melting. V occurs in both 3+ and 4+ oxidation states (e.g. Gaetani and Grove, 1997; Canil, 1999). V^{3+} is more compatible in igneous minerals (olivine, clino- and orthopyroxene), than V^{4+}, hence $D_V^{mineral/melt}$ decreases as oxygen fugacity (fO_2) increases (e.g. Canil, 1999; Mallmann and O'Neill, 2009; Laubier et al., 2014). Thus, V becomes more incompatible under oxidising conditions. The redox-sensitive partitioning of V has previously been used to estimate the redox state of the mantle source regions of basalts from both mid-ocean ridge and subduction zone settings (Shervais, 1982; Pearce and Parkinson, 1993; Lee et al., 2005; Mallmann and O'Neill, 2009; Laubier et al., 2014). When V is coupled with an incompatible element such as Ti, Y or Yb, the depletion of V relative to these elements is a function of redox state, and hence Ti/V or V/Y can be utilised as a redox proxy (Shervais, 1982; Laubier et al., 2014). It has previously been documented that back arc basin basalts (BABB) show elevated V/Yb relative to MORB, which is interpreted to be the consequence of increased fO_2 and H_2O, due to the influence of subduction derived fluids on mantle source of BABB (Laubier et al., 2014). Therefore, the redox conditions of the Oman ophiolite can be investigated by examining the V-Ti-Y systematics of primitive Oman samples, relative to MORB and subduction-zone influenced basalts.

Following the protocol adopted by Laubier et al. (2014) only samples with MgO ≥ 6 wt. % and Dy/Yb < 2 were selected to avoid the effect of magnetite crystallisation and residual garnet, respectively, on V contents. From a database (OmanDB) of >1200 entries this yielded a dataset of 291 and 117 primitive samples for Phase 1 and Phase 2 respectively. The V-Ti-Y compositions of primitive Oman samples compared to Indian MORB, fore arc basalts and back arc basalts are shown in Fig. 5.10, along with

non-modal fractional melting trends produced by melting a depleted MORB mantle source (DMM) under varying oxygen fugacity (QFM -1 to QFM+1). The parameters used to perform the melting calculations are provided in Table 5.1.

Based on V-Ti-Y systematics, Fig. 5.10 shows that most primitive lavas and dikes from Phase 1 can be produced by melting of a DMM source at QFM ± 0.5 after 0.1-15% melt extraction. The bulk of Phase 1 data exhibit V, Ti and Y contents comparable to Indian MORB (Fig. 5.10). The most recent estimate of the average fO_2 of MOR is QFM +0.1 (Berry and O'Neill, 2021), which is consistent with estimates from Fig. 5.10, notwithstanding some variation.

Table 5.1 Mineral modes, melt modes and partition coefficients used to perform non-modal fractional melting calculations using both a DMM source and a depleted residue. The same parameters were used for the melting calculations for the depleted residue composition. The concentrations of Ti, Y and V remaining in the residue are also provided. V partition coefficients at a given fO_2 were calculated using the calibration curves of Mallmann and O'Neill (2009). 1 – Workman and Hart (2005); 2 – Niu (1997); 3 – Pearce and Parkinson (1993); 4 – Mallmann and O'Neill (2009).

Source: DMM (Salters and Stracke, 2004)						
Mineral			Ol	Opx	Cpx	Sp	Ref.
Mode			57	28	13	2	1
P_i (Melt Mode)			-0.17	0.65	0.47	0.05	2
$D_x^{i\text{-}melt}$	Ti		0.010	0.110	0.350	0.100	3
	Y		0.005	0.080	0.500	0.001	
	V	QFM +1.5	0.020	0.074	0.175	1.062	4
		QFM +1	0.028	0.102	0.253	1.687	
		QFM +0.5	0.041	0.142	0.370	2.674	
		QFM	0.060	0.198	0.542	4.186	
		QFM -0.5	0.089	0.272	0.784	6.395	
		QFM -1	0.128	0.366	1.104	9.411	
Source: Residue after 8% melting of DMM at QFM+1							
Mineral			Ol	Opx	Cpx	Sp	
Mode			63.43	24.78	10.04	1.74	
Ti (µg/g)			294.31				
Y (µg/g)			1.59				
V (µg/g)			39.14				

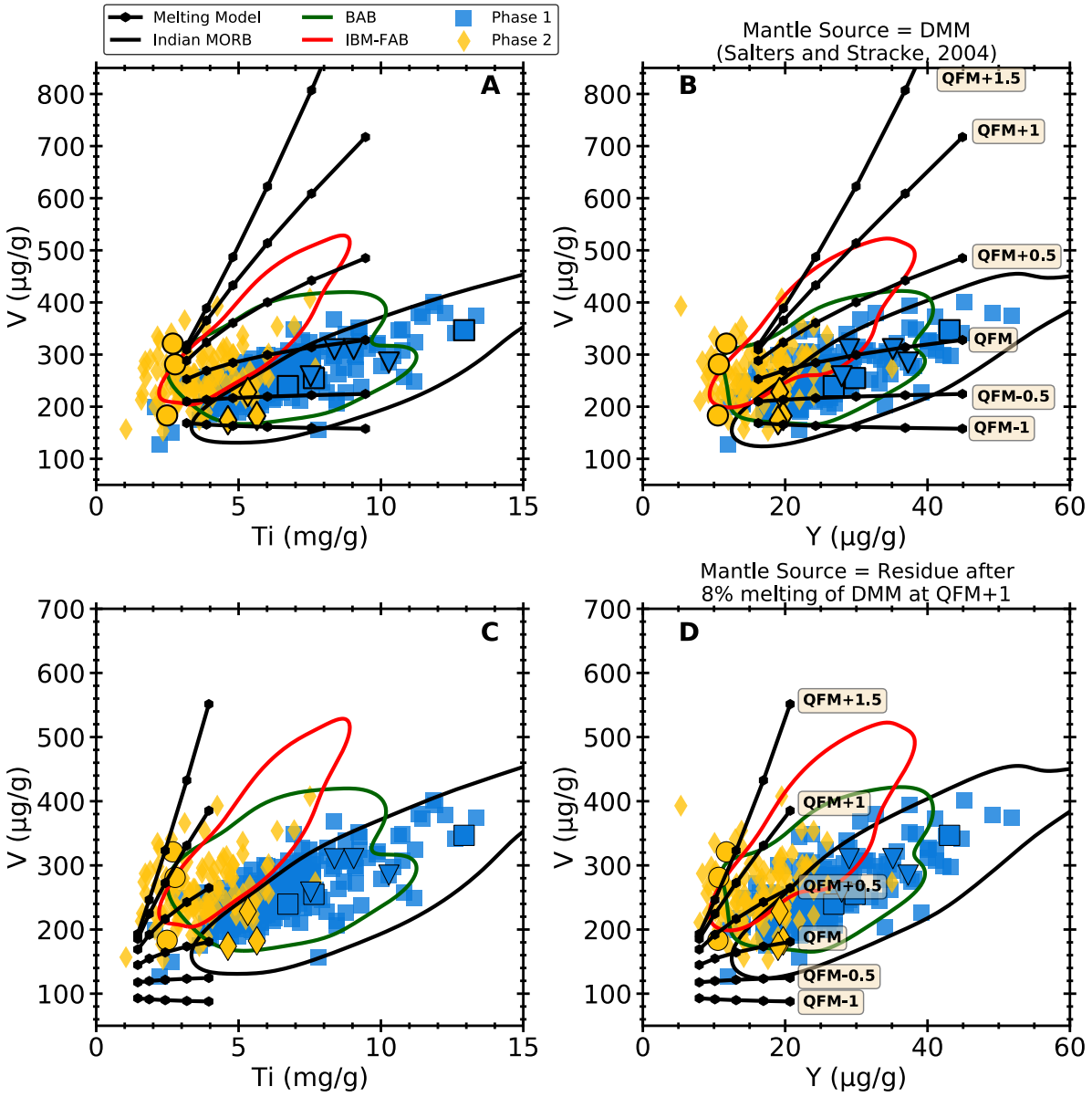

Fig. 5.10 V-Ti-Y systematics of primitive Phase 1 and Phase 2 lavas and dikes with non-modal fractional melting trends at varying oxygen fugacity. (A) – V vs. Ti with melting trends of a DMM source. (B) – V vs. Y with melting trends of a DMM source. (C) – V vs. Ti with melting trends of an 8% residue DMM source melted at QFM+1. (D) – V vs. Y with melting trends of an 8% residue DMM source melted at QFM+1. Oman data are from 'Oman DB' which include >1200 published and unpublished data compiled by Christopher Macleod and used with permission. Indian MORB, Back-arc basin (BAB) and Izu-Bonin-Mariana Fore-arc (FAB) basalt fields are defined by a kernel density contour that contains 95% of the data. Indian MORB and BAB data are taken from the compilation of Gale et al. (2013) and references therein. IBM-FAB data are from Reagan et al. (2010) and Shervais et al. (2019). Solid grey lines represent constant Ti/V or V/Y depending on the panel. DMM source composition is from Salters and Stracke (2004), mineral modes are from Workman and Hart (2005), and melt modes were taken from Niu (1997). Melting trends (solid black lines) shown in panels A and B represent 0.1% to 25% melting, with each circle representing a 5% increment. In panels C-D, melting increments are 0.1, 5, 10, and 17%.

This implies that the mantle source of Phase 1 shares broadly similar redox conditions to that of average MORB. However, Fig. 5.10 also demonstrates that there is a notable portion of primitive Phase 1 data, with Ti/V and V/Y more comparable to that of back arc and fore arc basalts. Thus, suggesting there is greater variability in source depletion and redox state of Phase 1 than typically observed in MORB, which would require the presence of water (Koepke et al., 2021).Most primitive Phase 2 lavas and dikes possess low Ti/V and high V/Y comparable to those observed in subduction zone basalts, which indicates they are probably derived from a depleted, oxidised source (Fig. 5.10). The generation of most Phase 2 primitive magmas requires either; (i) extreme depletion (20-25%) of a DMM source at QFM or above, or (ii) re-melting of a depleted residue produced from melting DMM under oxidising conditions (Fig. 5.10). The latter scenario provides a better fit for bulk the of data and can explain the entire range of variation observed in primitive Phase 2 magmas (Fig. 5.10).

When combined with geochronology (Rioux et al., 2012; Rioux et al., 2013), V-Ti-Y systematics indicate that the transition to a depleted, oxidised mantle source occurred extremely rapidly. The V-Ti-Y systematics of Phase 2 are consistent with the previous observation that their Ti isotope evolution occurred under very hydrous conditions (>2 wt.% H_2O; Fig. 5.9). Interestingly, another important caveat to consider is that whilst V-Ti-Y suggest redox state of Phase 1 is MORB-like, their Ti isotope evolution requires the presence of elevated water contents (~0.5 wt.% H_2O; Fig. 5.8). This juxtaposition requires that water was added to the Phase 1 mantle source prior to the onset of magmatic differentiation. A recent combination of experimental data and phase equilibria modelling by Koepke et al. (2021) suggests that not only is the widespread presence of water in the Phase 1 mantle source is highly plausible, it is necessary to explain the presence of wehrlitic phase assemblages (olivine + clinopyroxene) in the plutonic crust of the Oman ophiolite.

5.7 Conclusions: The geodynamic setting of the Oman Ophiolite

The implications of the coupled Ti isotope and trace element systematics of the Oman ophiolite indicate:

i. The Ti isotope fractionation pathways of Phase 1 required H_2O contents in their parental magmas far greater than those found in modern MORB magmas. Phase 2 exhibit Ti isotope signatures comparable to modern hydrous arc magmas. This is further corroborated by their Ti.V and V/Y systematics which suggest Phase 2 parental magmas are produced by melting a highly depleted mantle source under oxidising conditions, and hence the presence of significant amounts of H_2O.
ii. Whilst Ti/V and V/Y systematics suggest Phase 1 mantle sources were generated under redox conditions broadly comparable to that of average MORB, as evidence by Ti isotopes, the evolution of Phase 1 magmas occurred under more hydrous conditions. This is likely the result of the progressive hydration of an initially dry upwelling mantle column during the early stages of subduction initiation.

The data presented in this chapter provide strong evidence for a 'moist' to wet transition in the Oman ophiolite, and thus progressive development of a subduction signature. When combined with current constraints from geochronology, this progression occurred extremely rapidly over a period of ~1-2 Myr (Rioux et al., 2012; Rioux et al., 2013). The absence of direct geologic evidence for an arc complex existing concurrent with the onset of Phase 1 magmatism would argue against back arc basin origin (e.g. Pearce et al., 1984). However, many have begun to draw parallels between the Oman ophiolite and Izu-Bonin-Mariana system (e.g. Stern et al., 2012; MacLeod et al., 2013; Ishizuka et al., 2014), particularly as current evidence suggest the onset of subduction initiation was rapid in both localities (Crameri et al., 2020 and references therein). Therefore, the coupled Ti isotope and trace element systematics presented in this chapter contribute to providing further evidence that the Oman ophiolite formed

as consequence of rapid subduction initiation, originating as spreading centre associated with a nascent subduction zone.

Chapter 6: Synthesis and Outlook

6.1 Summary and Concluding Remarks

Mass dependent variations in Titanium isotopes show great potential as a novel geochemical tool with which to investigate magmatic processes. This study builds upon the foundations of previous work that demonstrated Ti isotope fractionation during magmatic differentiation is primarily due to Fe-Ti oxide-melt equilibria (e.g. Millet et al., 2016; Deng et al., 2019; Johnson et al., 2019).

To enhance our understanding of the controls and mechanics of Ti isotope fractionation during magmatic differentiation this study has expanded the current Ti isotope dataset to include several well-characterised mafic to felsic differentiation suites from contrast tectonic settings. Differentiated lavas from intraplate settings display a greater magnitude of Ti isotope fractionation at a given SiO_2 content relative to lavas from both mid-ocean ridge and subduction zone settings. The high TiO_2 contents of the parental magmas of intraplate lavas enables them to crystallise both ilmenite and Ti-rich titanomagnetite in high modal abundance, which combined with extreme levels of fractional crystallisation (>80%) produces significant Ti isotope fractionation during magmatic differentiation. In contrast tholeiitic and arc magmas have lower parental TiO_2 contents, with titanomagnetite being the dominant Fe-Ti oxide phase. In addition, hydrous calc-alkaline arc magmas display elevated $\delta^{49/47}Ti$ values at a given Mg# relative to tholeiitic magmas form both mid ocean ridge and subduction zone settings. This is the manifestation of earlier Fe-Ti oxide saturation in hydrous calc-alkaline magmas due the suppression of plagioclase in the presence of increased water contents. The additional control of water contents on Ti isotope fractionation trends suggests Ti isotope could be applied as a novel isotopic proxy to elucidate the geodynamic setting of ancient volcanism.

Measurements of Fe-Ti oxide mineral separates have confirmed that Fe-Ti oxides are isotopically light relative to silicate melt and minerals (Johnson et al., 2019). However, there is currently no measurements of individual Fe-Ti oxide phases such

as ilmenite, titanomagnetite and rutile. Extracting pure Fe-Ti oxides phases from mineral separates is often complicated by the fact that these phases are often intergrown or possess similar densities and magnetic properties. This study utilises a novel micro-mill technique to sample individual Fe-Ti oxide-groundmass and glass pairs in-situ from a range of natural and experimental samples, with the aim to provide more robust quantitative constraints on the Ti isotope fractionation factors of different Fe-Ti oxides. The Ti isotope composition of Fe-Ti oxide phases is consistently isotopically lighter than their host groundmass or silicate melt. Ilmenite and rutile possess relatively homogeneous Ti isotope compositions with ilmenite being isotopically lighter compared to rutile. This difference is primarily reflective of small differences in their Ti-O bond length, with ilmenite possessing slightly longer Ti-O bonds and hence a stronger preference for lighter isotopes. The titanomagnetite Ti isotope fractionation increases as a function of TiO_2 contents with $\Delta^{49/47}Ti_{titanomagnetite\text{-}melt}$ values at 1000 K ranging up to -1.12‰ in Ti-rich titanomagnetite (~23 wt.% TiO_2) from Heard Island compared to -0.64‰ in Santorini (~13 wt.% TiO_2). This dichotomy could result from strain due to exchange of smaller Fe^{3+} ions with larger Fe^{2+} and Ti^{4+} ions during magnetite-ulvöspinel solid solution creating a weaker crystal lattice in Ti-rich titanomagnetite. The results presented in this study are consistent with Ti isotope fractionation factors inferred from analyses of mineral separates and ab-initio calculations (e.g. Leitzke et al., 2018; Johnson et al., 2019; Mandl, 2019; Wang et al., 2020). The data from this study enables the calculation of Ti isotope fractionation factors as a function of both temperature and TiO_2 content in the case of titanomagnetite. This enables these fractionation factors to be used in combination with Ti isotope inter-mineral fractionation factors for silicate minerals recalculated from previous ab-initio studies to successfully model the behaviour of Ti isotopes during partial melting of Earth's mantle as well as fractional crystallisation of magmas from distinct magma series. This work provides the foundation for Ti isotopes to develop into a mature petrologic tool that can be applied to model a range of magmatic processes.

The constraints on the behaviour and mechanics of Ti isotope fractionation from Chapters 3 and 4 provide the framework by which the efficacy of Ti isotopes as a novel tool to identify the tectonic setting of past volcanism in the geologic record. During this study Ti isotope measurements were performed on a temporally and spatially representative set of lavas and dikes from the Oman-UAE ophiolite to deduce the geodynamic setting in which it formed. The Oman ophiolite was chosen as the focus of this study due to its recognition as the best preserved and largest ophiolite complex available for study. There is long-standing and contentious debate surrounding its geodynamic context of formation, which hinges on two competing hypotheses: (i) the ophiolite formed at an open-ocean mid-ocean ridge, and thus a unique, invaluable direct analogue for modern fast-spreading oceanic ridges; or (ii) it formed as spreading centre in a marginal basin above a nascent subduction zone, analogous to fore-arc spreading centres such as the Izu-Bonin-Mariana system. Ti isotope systematics observed in the earliest phase of magmatism, Phase 1, which is compositionally like Indian MORB, requires the presence of H_2O contents far greater than has currently been observed in any mid-ocean ridge basalt, thus ruling out a scenario whereby Phase 1 magmas were formed at a true mid ocean ridge setting. Additionally, magmas from the second stage of magmatism, Phase 2, display Ti isotope systematics comparable to hydrous arc magmas. Furthermore, additional context is provided through modelling of the incompatible and redox-sensitive trace element systematics (V-Ti-Y) of Phase 1 and Phase 2 primitive magmas. V-Ti-Y systematics demonstrate that Phase 2 magmas are derived from a highly depleted oxidised source which is consistent with their Ti isotope systematics. However, V-Ti-Y systematics of Phase 1 suggest the redox state of its mantle source is similar to that of average MORB, and most primitive Phase 1 magmas can be produced by melting of a depleted MORB mantle (DMM) source. When considered in conjunction with the Ti isotope compositions of Phase 1, this indicates a progressive hydration of the Phase 1 mantle source prior to or contemporaneous with the onset of magmatic differentiation. Thus, the combined Ti isotope and trace element investigation

presented in this study provides convincing evidence for a rapid moist to wet transition in the Oman ophiolite and the progressive maturation of a subduction zone signature. Additionally, when these results are placed within a geochronological context the data suggest that from the onset of subduction initiation the formation of the subduction zone occurred within 2 Myr.

6.2 Outlook and Potential for Future Work

The work in this thesis has investigated the mechanics and controls that influence mass dependent Ti isotope fractionation during magmatic processes. The results demonstrate the efficacy of Ti isotopes as a novel tool that can be utilised to trace magmatic differentiation and probe the geodynamic setting of ancient volcanism. In addition, the calculation of Ti isotope Fe-Ti oxide-melt fractionation factors provide the foundation for further petrologic modelling.

Constraints provided from mantle melting models in Chapter 4 indicate, the degree of melting exerts no resolvable influence on the Ti isotope composition of the terrestrial mantle. However, There is still debate surrounding the Ti isotope composition of mid ocean ridge basalts (MORB), with Deng et al. (2018) arguing that enriched MORB are isotopically heavier with respect to normal MORB due to mantle recycling of isotopically light cumulates formed during continental crust formation in the Archean. However, this interpretation is controversial and relies on a limited number of samples. To fully address this issue, a comprehensive Ti isotope study of a global database of well-characterised MORB lavas and glasses from all Earth's oceans is required. The Ti isotope systematics would also need to be coupled with constraints from precise radiogenic isotope ratios such as Pb/Pb, Sm-Nd and Rb-Sr to identify if there is indeed resolvable variation between the Ti isotope compositions of different MORB's.

A recent investigation by Klaver et al. (2021) observed small resolvable variations in the Ti isotope compositions of detrital marine sediments, which was interpreted to the result of hydrodynamic sorting of Fe-Ti oxides during sediment

transport. Thus this has implications for models of crustal evolution that use Ti isotope as a proxy for the proportion of felsic crust (e.g. Greber et al., 2017a), with hydrodynamic sorting possessing the ability to introduce bias into such models (Klaver et al., 2021). This work also raises an additional question on the influence of sediment contributions to the Ti isotope composition of subduction zone lavas, as the introduction of sediment into subduction zone mantle sources has important implications for its bulk chemical and isotopic composition (e.g. Othman et al., 1989; Elliott et al., 1997; Plank and Langmuir, 1998; Rapp et al., 2008; Andersen et al., 2015). Klaver et al. (2021) demonstrated that eastern Mediterranean Sea sediment of distinct provenance also have different Ti isotope compositions. A potential future application could be to conduct a Ti isotope study of volcanic arc lavas where the degree and provenance of their sediment input is well-constrained. A combined Ti isotope study of arc lavas and associated detrital sediment could be used to constrain if sediment input can influence the Ti isotope composition of subduction zone lavas.

Bibliography

Aarons S. M., Reimink J. R., Greber N. D., Heard A. W., Zhang Z. and Dauphas N. (2020) Titanium isotopes constrain a magmatic transition at the Hadean-Archean boundary in the Acasta Gneiss Complex. *Sci. Adv.* **6**.

Abily B., Ceuleneer G. and Launeau P. (2011) Synmagmatic normal faulting in the lower oceanic crust: Evidence from the Oman ophiolite. *Geology* **39**, 391–394.

Ackerson M. R., Cody G. D. and Mysen B. O. (2020) 29 Si solid state NMR and Ti K-edge XAFS pre-edge spectroscopy reveal complex behavior of Ti in silicate melts. *Prog. earth Planet. Sci.* **7**, 1–11.

Akimoto S., Katsura T. and Yoshida M. (1957) Magnetic properties of $TiFe_2O_4$-Fe_3O_4. *J. Geomagn. Geoelectr.* **9**, 165–178.

Alabaster T., Pearce J. A. and Malpas J. (1982) The volcanic stratigraphy and petrogenesis of the Oman ophiolite complex. *Contrib. to Mineral. Petrol.* **81**, 168–183.

Albarède F. and Beard B. (2004) Analytical methods for non-traditional isotopes. *Rev. Mineral. geochemistry* **55**, 113–152.

Albarede F., Telouk P., Blichert-Toft J., Boyet M., Agranier A. and Nelson B. (2004) Precise and accurate isotopic measurements using multiple-collector ICPMS. *Geochim. Cosmochim. Acta* **68**, 2725–2744.

Andersen M. B., Elliott T., Freymuth H., Sims K. W. W., Niu Y. and Kelley K. A. (2015) The terrestrial uranium isotope cycle. *Nature* **517**, 356–359.

Andrén H., Rodushkin I., Stenberg A., Malinovsky D. and Baxter D. C. (2004) Sources of mass bias and isotope ratio variation in multi-collector ICP-MS: optimization of instrumental parameters based on experimental observations. *J. Anal. At. Spectrom.* **19**, 1217–1224.

Andújar J., Scaillet B., Pichavant M. and Druitt T. H. (2015) Differentiation conditions of a basaltic magma from Santorini, and its bearing on the production of andesite in arc settings. *J. Petrol.* **56**, 765–794.

Andújar J., Scaillet B., Pichavant M. and Druitt T. H. (2016) Generation conditions of dacite and rhyodacite via the crystallization of an andesitic magma. Implications for the plumbing system at Santorini (Greece) and the origin of tholeiitic or calc-alkaline differentiation trends in arc magmas. *J. Petrol.* **57**, 1887–1920.

Anonymous (1972) Penrose field conference on ophiolites. *Geotimes* **17**, 24–25.

Van Baalen M. R. (1993) Titanium mobility in metamorphic systems: a review. *Chem. Geol.* **110**, 233–249.

Bacon C. R. and Hirschmann M. M. (1988) Mg/Mn partitioning as a test for equilibrium between coexisting Fe-Ti oxides. *Am. Mineral.* **73**, 57–61.

Barling J. (1994) Origin and evolution of a high-Ti ocean island basalt suite: the Laurens Peninsula Series, Heard Island, Indian Ocean. *Mineral. Mag.* **58**, 49–50.

Barling J. (1990) The petrogenesis of the Newer Lavas of Heard Island, southern Indian Ocean. Monash University.

Barling J. and Goldstein S. L. (1990) Extreme isotopic variations in Heard Island lavas and the nature of mantle reservoirs. *Nature* **348**, 59–62.

Barling J., Goldstein S. L. and Nicholls I. A. N. A. (1994) Geochemistry of Heard Island (southern Indian Ocean): Characterization of an enriched mantle component and implications for enrichment of the sub-Indian Ocean mantle. *J. Petrol.* **35**, 1017–1053.

Barth T. F. W. and Posnjak E. (1932) Spinel structures: with and without variate atom equipoints. *Zeitschrift Für Krist. Mater.* **82**, 325–341.

Barton M. and Huijsmans J. P. P. (1986) Post-caldera dacites from the Santorini volcanic complex, Aegean Sea, Greece: an example of the eruption of lavas of near-constant composition over a 2,200 year period. *Contrib. to Mineral. Petrol.* **94**, 472–495.

Bas Le M. J., Maitre R. W. L. E., Streckeisen A., Zanettin B. and Rocks I. S. on the S. of I. (1986) A chemical classification of volcanic rocks based on the total alkali-silica diagram. *J. Petrol.* **27**, 745–750.

Bédard J. H. (2014) Parameterizations of calcic clinopyroxene—Melt trace element

partition coefficients. *Geochemistry, Geophys. Geosystems* **15**, 303–336.

Bédard J. H. (2005) Partitioning coefficients between olivine and silicate melts. *Lithos* **83**, 394–419.

Bédard J. H. (2007) Trace element partitioning coefficients between silicate melts and orthopyroxene: parameterizations of D variations. *Chem. Geol.* **244**, 263–303.

Bédard J. H. (2006) Trace element partitioning in plagioclase feldspar. *Geochim. Cosmochim. Acta* **70**, 3717–3742.

Belgrano T. M. and Diamond L. W. (2019) Subduction-zone contributions to axial volcanism in the Oman–UAE ophiolite. *Lithosphere* **11**, 399–411.

Belgrano T. M., Diamond L. W., Vogt Y., Biedermann A. R., Gilgen S. A. and Al-Tobi K. (2019) A revised map of volcanic units in the Oman ophiolite: insights into the architecture of an oceanic proto-arc volcanic sequence. *Solid Earth* **10**, 1181–1217.

Belgrano T. M., Tollan P. M., Marxer F. and Diamond L. W. (2021) Paleobathymetry of submarine lavas in the Samail and Troodos ophiolites: Insights from volatiles in glasses and implications for hydrothermal systems. *J. Geophys. Res. Solid Earth* **126**, e2021JB021966.

Benoit M., Ceuleneer G. and Polvé M. (1999) The remelting of hydrothermally altered peridotite at mid-ocean ridges by intruding mantle diapirs. *Nature* **402**, 514–518.

Berglund M. and Wieser M. E. (2011) Isotopic compositions of the elements 2009 (IUPAC Technical Report). *Pure Appl. Chem.* **83**, 397–410.

Berndt J., Koepke J. and Holtz F. (2005) An experimental investigation of the influence of water and oxygen fugacity on differentiation of MORB at 200 MPa. *J. Petrol.* **46**, 135–167.

Berry A. J. and O'Neill H. S. C. (2021) Oxygen Content, Oxygen Fugacity, the Oxidation State of Iron, and Mid-Ocean Ridge Basalts. *Magma Redox Geochemistry*, 155–163.

Bigeleisen J. (1965) Chemistry of Isotopes: Isotope chemistry has opened new areas of chemical physics, geochemistry, and molecular biology. *Science,* **147**(3567), 463–471.

Bigeleisen J. and Mayer M. G. (1947) Calculation of equilibrium constants for isotopic exchange reactions. *J. Chem. Phys.* **15**, 261–267.

Blundy J. and Cashman K. (2008) Petrologic reconstruction of magmatic system variables and processes. *Rev. Mineral. Geochemistry* **69**, 179–239.

Bonnand P., Parkinson I. J. and Anand M. (2016) Mass dependent fractionation of stable chromium isotopes in mare basalts: Implications for the formation and the differentiation of the Moon. *Geochim. Cosmochim. Acta* **175**, 208–221.

Bosi F., Hålenius U. and Skogby H. (2009) Crystal chemistry of the magnetite-ulvospinel series. *Am. Mineral.* **94**, 181–189.

Boudier F., Nicolas A., Ildefonse B. and Jousselin D. (1997) EPR microplates, a model for the Oman ophiolite. *Terra Nov.* **9**, 79–82.

Bragg W. H. (1915) The structure of magnetite and the spinels. *Nature* **95**, 561.

Brown I. D. (2016) *The chemical bond in inorganic chemistry: the bond valence model*., Oxford University Press.

Bryan W. B., Finger L. W. t and Chayes F. (1969) Estimating proportions in petrographic mixing equations by least-squares approximation. *Science (80-.).* **163**, 926–927.

Burkhardt C., Hin R. C., Kleine T. and Bourdon B. (2014) Evidence for Mo isotope fractionation in the solar nebula and during planetary differentiation. *Earth Planet. Sci. Lett.* **391**, 201–211.

Campbell I. H. (2001) Identification of ancient mantle plumes. *Spec. Pap. Soc. Am.*, 5–22.

Canales J. P., Detrick R. S., Bazin S., Harding A. J. and Orcutt J. A. (1998) Off-axis crustal thickness across and along the East Pacific Rise within the MELT area. *Science,* **280(**5367**)**, 1218–1221.

Canales J. P., Toomey D. R. and Wilcock W. S. D. (2003) Segment-scale variations in the crustal structure of 150–300 kyr old fast spreading oceanic crust (East Pacific Rise, 8 15′ N–10 5′ N) from wide-angle seismic refraction profiles. *Geophys. J. Int.* **152**, 766–794.

Canil D. (1999) Vanadium partitioning between orthopyroxene, spinel and silicate melt and the redox states of mantle source regions for primary magmas. *Geochim. Cosmochim. Acta* **63**, 557–572.

Cann J. R. (1970) Rb, Sr, Y, Zr and Nb in some ocean floor basaltic rocks. *Earth Planet. Sci. Lett.* **10**, 7–11.

Carmichael I. S. E. (1966) The iron-titanium oxides of salic volcanic rocks and their associated ferromagnesian silicates. *Contrib. to Mineral. Petrol.* **14**, 36–64.

Carr M. J. and Gazel E. (2017) Igpet software for modeling igneous processes: examples of application using the open educational version. *Mineral. Petrol.* **111**, 283–289.

Chamberlain K. J., Barclay J., Preece K., Brown R. J. and Davidson J. P. (2016) Origin and evolution of silicic magmas at ocean islands: Perspectives from a zoned fall deposit on Ascension Island, South Atlantic. *J. Volcanol. Geotherm. Res.* **327**, 349–360.

Chamberlain K. J., Barclay J., Preece K. J., Brown R. J. and Davidson J. P. (2019) Lower crustal heterogeneity and fractional crystallization control evolution of small-volume magma batches at ocean island volcanoes (Ascension Island, South Atlantic). *J. Petrol.* **60**, 1489–1522.

Charlier B. L. A., Ginibre C., Morgan D., Nowell G. M., Pearson D. G., Davidson J. P. and Ottley C. J. (2006) Methods for the microsampling and high-precision analysis of strontium and rubidium isotopes at single crystal scale for petrological and geochronological applications. *Chem. Geol.* **232**, 114–133.

Chen C., Dai W., Wang Z., Liu Y., Li M., Becker H. and Foley S. F. (2019) Calcium isotope fractionation during magmatic processes in the upper mantle. *Geochim. Cosmochim. Acta* **249**, 121–137.

Clague D. A., Caress D. W., Dreyer B. M., Lundsten L., Paduan J. B., Portner R. A., Spelz-Madero R., Bowles J. A., Castillo P. R. and Guardado-France R. (2018) Geology of the Alarcon Rise, Southern Gulf of California. *Geochemistry, Geophys. Geosystems* **19**, 807–837.

Clarke I., McDougall I. and Whitford D. J. (1983) Volcanic evolution of heard and Mc-Donald Islands, Southern Indian Ocean. In *Antarctic earth science. International symposium. 4* pp. 631–635.

Clayton R. N., Grossman L. and Mayeda T. K. (1973) A component of primitive nuclear composition in carbonaceous meteorites. *Science,***182(**4111**)**, 485–488.

Clayton R. N., Onuma N. and Mayeda T. K. (1976) A classification of meteorites based on oxygen isotopes. *Earth Planet. Sci. Lett.* **30**, 10–18.

Coleman R. G. (1981) Tectonic setting for ophiolite obduction in Oman. *J. Geophys. Res. Solid Earth* **86**, 2497–2508.

Coogan L. A., Jenkin G. R. T. and Wilson R. N. (2007) Contrasting cooling rates in the lower oceanic crust at fast-and slow-spreading ridges revealed by geospeedometry. *J. Petrol.* **48**, 2211–2231.

Coplen T. B. (2011) Guidelines and recommended terms for expression of stable-isotope-ratio and gas-ratio measurement results. *Rapid Commun. mass Spectrom.* **25**, 2538–2560.

Craddock P. R. and Dauphas N. (2011) Iron isotopic compositions of geological reference materials and chondrites. *Geostand. Geoanalytical Res.* **35**, 101–123.

Crameri F., Magni V., Domeier M., Shephard G. E., Chotalia K., Cooper G., Eakin C. M., Grima A. G., Gürer D. and Király Á. (2020) A transdisciplinary and community-driven database to unravel subduction zone initiation. *Nat. Commun.* **11**, 1–14.

Daly R. A. (1914) *Igneous rocks and their origin*.,

Dauphas N., Burkhardt C., Warren P. H. and Fang-Zhen T. (2014a) Geochemical arguments for an Earth-like Moon-forming impactor. *Philos. Trans. R. Soc. A Math. Phys. Eng. Sci.* **372**, 20130244.

Dauphas N., John S. G. and Rouxel O. (2017) 11 Iron Isotope Systematics. *Non-Traditional Stable Isot.*, 415–510.

Dauphas N., Pourmand A. and Teng F.-Z. (2009) Routine isotopic analysis of iron by HR-MC-ICPMS: How precise and how accurate? *Chem. Geol.* **267**, 175–184.

Dauphas N., Roskosz M., Alp E. E., Neuville D. R., Hu M. Y., Sio C. K., Tissot F. L. H., Zhao J., Tissandier L. and Médard E. (2014b) Magma redox and structural controls on iron isotope variations in Earth's mantle and crust. *Earth Planet. Sci. Lett.* **398**, 127–140.

Dauphas N. and Rouxel O. (2006) Mass spectrometry and natural variations of iron isotopes. *Mass Spectrom. Rev.* **25**, 515–550.

Davis A. M., Zhang J., Greber N. D., Hu J., Tissot F. L. H. and Dauphas N. (2018) Titanium isotopes and rare earth patterns in CAIs: Evidence for thermal processing and gas-dust decoupling in the protoplanetary disk. *Geochim. Cosmochim. Acta* **221**, 275–295.

Debret B., Millet M.-A., Pons M.-L., Bouilhol P., Inglis E. and Williams H. (2016) Isotopic evidence for iron mobility during subduction. *Geology* **44**, 215–218.

Dempsey S. (2013) Geochemistry of volcanic rocks from the Sunda Arc.

Deng Z., Chaussidon M., Savage P., Robert F., Pik R. and Moynier F. (2019) Titanium isotopes as a tracer for the plume or island arc affinity of felsic rocks. *Proc. Natl. Acad. Sci.* **116**, 1132–1135.

Deng Z., Moynier F., Sossi P. A. and Chaussidon M. (2018) Bridging the depleted MORB mantle and the continental crust using titanium isotopes. *Geochem. Perspect. Lett.* **9**, 11–15.

Dhuime B., Wuestefeld A. and Hawkesworth C. J. (2015) Emergence of modern continental crust about 3 billion years ago. *Nat. Geosci.* **8**, 552–555.

Dietz L. A., Paghugki C. F. and Land G. A. (1962) Internal Standard Technique for Precise Isotopic Abundance Measurments in Thermal Ionization Mass Spectrometry. *Anal. Chem.* **34**, 709–710.

Dixon J. E. and Clague D. A. (2001) Volatiles in basaltic glasses from Loihi Seamount, Hawaii: Evidence for a relatively dry plume component. *J. Petrol.* **42**, 627–654.

Dodson M. H. (1963) A theoretical study of the use of internal standards for precise isotopic analysis by the surface ionization technique: Part I-General first-order algebraic solutions. *J. Sci. Instrum.* **40**, 289.

Dodson M. H. (1970) Simplified equations for double-spiked isotopic analyses. *Geochim. Cosmochim. Acta* **34**, 1241–1244.

Druitt T. H. (2014) New insights into the initiation and venting of the Bronze-Age eruption of Santorini (Greece), from component analysis. *Bull. Volcanol.* **76**, 1–21.

Druitt T. H., Edwards L., Mellors R. M., Pyle D. M., Sparks R. S. J., Lanphere M., Davies M. and Barreirio B. (1999) Santorini volcano. *Geol. Soc. Mem.* **19**.

Eiler J. M., Bergquist B., Bourg I., Cartigny P., Farquhar J., Gagnon A., Guo W., Halevy I., Hofmann A. and Larson T. E. (2014) Frontiers of stable isotope geoscience. *Chem. Geol.* **372**, 119–143.

Elliott T., Plank T., Zindler A., White W. and Bourdon B. (1997) Element transport from slab to volcanic front at the Mariana arc. *J. Geophys. Res. Solid Earth* **102**, 14991–15019.

Epov V. N., Malinovskiy D., Vanhaecke F., Bégué D. and Donard O. F. X. (2011) Modern mass spectrometry for studying mass-independent fractionation of heavy stable isotopes in environmental and biological sciences. *J. Anal. At. Spectrom.* **26**, 1142–1156.

Ernewein M., Pflumio C. and Whitechurch H. (1988) The death of an accretion zone as evidenced by the magmatic history of the Sumail ophiolite (Oman). *Tectonophysics* **151**, 247–274.

Faak K., Coogan L. A. and Chakraborty S. (2015) Near conductive cooling rates in the upper-plutonic section of crust formed at the East Pacific Rise. *Earth Planet. Sci. Lett.* **423**, 36–47.

Fabbro G. N., Druitt T. H. and Scaillet S. (2013) Evolution of the crustal magma plumbing system during the build-up to the 22-ka caldera-forming eruption of Santorini (Greece). *Bull. Volcanol.* **75**, 1–22.

Farges F. and Brown G. E. (1997) Coordination chemistry of titanium (IV) in silicate glasses and melts: IV. XANES studies of synthetic and natural volcanic glasses and tektites at ambient temperature and pressure. *Geochim. Cosmochim. Acta* **61**, 1863–1870.

Farges F., Brown G. E., Navrotsky A., Gan H. and Rehr J. J. (1996a) Coordination chemistry of Ti (IV) in silicate glasses and melts: II. Glasses at ambient temperature and pressure. *Geochim. Cosmochim. Acta* **60**, 3039–3053.

Farges F., Brown G. E. and Rehr J. J. (1996b) Coordination chemistry of Ti (IV) in silicate glasses and melts: I. XAFS study of titanium coordination in oxide model compounds. *Geochim. Cosmochim. Acta* **60**, 3023–3038.

Feig S. T., Koepke J. and Snow J. E. (2010) Effect of oxygen fugacity and water on phase equilibria of a hydrous tholeiitic basalt. *Contrib. to Mineral. Petrol.* **160**, 551–568.

Feig S. T., Koepke J. and Snow J. E. (2006) Effect of water on tholeiitic basalt phase equilibria: an experimental study under oxidizing conditions. *Contrib. to Mineral. Petrol.* **152**, 611–638.

Feng C., Qin T., Huang S., Wu Z. and Huang F. (2014) First-principles investigations of equilibrium calcium isotope fractionation between clinopyroxene and Ca-doped orthopyroxene. *Geochim. Cosmochim. Acta* **143**, 132–142.

Field L., Blundy J., Calvert A. and Yirgu G. (2013) Magmatic history of Dabbahu, a composite volcano in the Afar Rift, Ethiopia. GSA *Bulletin,* **125**, 128–147.

Fietzke J. and Eisenhauer A. (2006) Determination of temperature-dependent stable strontium isotope (88Sr/86Sr) fractionation via bracketing standard MC-ICP-MS. *Geochemistry, Geophys. Geosystems* **7**.

Floyd P. A. and Winchester J. A. (1978) Identification and discrimination of altered and metamorphosed volcanic rocks using immobile elements. *Chem. Geol.* **21**, 291–306.

Fox J. M., McPhie J., Carey R. J., Jourdan F. and Miggins D. P. (2021) Construction of an intraplate island volcano: The volcanic history of Heard Island. *Bull. Volcanol.* **83**, 1–21.

Fujino K. (1974) Cation distribution and local variation of site symmetry in solid solution series, Fe_3O_4-Fe_2TiO_4. *Mineral. J.* **7**, 472–488.

Gaetani G. A. and Grove T. L. (1997) Partitioning of moderately siderophile elements among olivine, silicate melt, and sulfide melt: Constraints on core formation in

the Earth and Mars. *Geochim. Cosmochim. Acta* **61**, 1829–1846.

Gaetani G. A., Grove T. L. and Bryan W. B. (1993) The influence of water on the petrogenesis of subductionrelated igneous rocks. *Nature* **365**, 332–334.

Gale A., Dalton C. A., Langmuir C. H., Su Y. and Schilling J. (2013) The mean composition of ocean ridge basalts. *Geochemistry, Geophys. Geosystems* **14**, 489–518.

Galer S. J. G. and Abouchami W. (1998) Practical application of lead triple spiking for correction of instrumental mass discrimination. *Miner. Mag. A* **62**, 491–492.

Gall L., Williams H., Siebert C. and Halliday A. (2012) Determination of mass-dependent variations in nickel isotope compositions using double spiking and MC-ICPMS. *J. Anal. At. Spectrom.* **27**, 137–145.

Gardner J. E., Thomas R. M. E., Jaupart C. and Tait S. (1996) Fragmentation of magma during Plinian volcanic eruptions. *Bull. Volcanol.* **58**, 144–162.

Gazoni E. and Clark C. (2018) openpyxl-A Python library to read/write Excel 2010 xlsx/xlsm files. *Retrieved from.(accessed 20 April 2016) http//openpyxl. readthedocs. org/en/default*.

Gertisser R., Preece K. and Keller J. (2009) The Plinian Lower Pumice 2 eruption, Santorini, Greece: magma evolution and volatile behaviour. *J. Volcanol. Geotherm. Res.* **186**, 387–406.

Ghiorso M. S. and Evans B. W. (2008) Thermodynamics of rhombohedral oxide solid solutions and a revision of the Fe-Ti two-oxide geothermometer and oxygen-barometer. *Am. J. Sci.* **308**, 957–1039.

Ghiorso M. S. and Gualda G. A. R. (2015) An H 2 O–CO 2 mixed fluid saturation model compatible with rhyolite-MELTS. *Contrib. to Mineral. Petrol.* **169**, 1–30.

Ghiorso M. S., Hirschmann M. M., Reiners P. W. and Kress V. C. (2002) The pMELTS: A revision of MELTS for improved calculation of phase relations and major element partitioning related to partial melting of the mantle to 3 GPa. *Geochemistry, Geophys. Geosystems* **3**, 1–35.

Ghiorso M. S. and Prissel K. B. (2020) ENKI Cloud App: Implementation of the Fe-Ti Oxide Geothermooxybarometer of Ghiorso and Evans, 2008.

Godard M., Bosch D. and Einaudi F. (2006) A MORB source for low-Ti magmatism in the Semail ophiolite. *Chem. Geol.* **234**, 58–78.

Godard M., Dautria J. and Perrin M. (2003) Geochemical variability of the Oman ophiolite lavas: Relationship with spatial distribution and paleomagnetic directions. *Geochemistry, Geophys. Geosystems* **4**(6), 8609.

Goodenough K. M., Styles M. T., Schofield D., Thomas R. J., Crowley Q. C., Lilly R. M., McKervey J., Stephenson D. and Carney J. N. (2013) Architecture of the Oman–UAE ophiolite: evidence for a multi-phase magmatic history. In *Lithosphere Dynamics and Sedimentary Basins: The Arabian Plate and Analogues* Springer. pp. 23–42.

Goodenough K. M., Thomas R. J., Styles M. T., Schofield D. I. and MacLeod C. J. (2014) Records of ocean growth and destruction in the Oman–UAE ophiolite. *Elements* **10**, 109–114.

De Graaff S. J., Goodenough K. M., Klaver M., Lissenberg C. J., Jansen M. N., Millar I. and Davies G. R. (2019) Evidence for a moist to wet source transition throughout the Oman-UAE ophiolite, and implications for the geodynamic history. *Geochemistry, Geophys. Geosystems* **20**, 651–672.

Greaney A. T., Rudnick R. L., Helz R. T., Gaschnig R. M., Piccoli P. M. and Ash R. D. (2017) The behavior of chalcophile elements during magmatic differentiation as observed in Kilauea Iki lava lake, Hawaii (vol 210, pg 71, 2017). *Geochim. Cosmochim. Acta* **245**, 643–644.

Greber N. D., Dauphas N., Bekker A., Ptáček M. P., Bindeman I. N. and Hofmann A. (2017a) Titanium isotopic evidence for felsic crust and plate tectonics 3.5 billion years ago. *Science,* **357**(6357), 1271–1274.

Greber N. D., Dauphas N., Puchtel I. S., Hofmann B. A. and Arndt N. T. (2017b) Titanium stable isotopic variations in chondrites, achondrites and lunar rocks. *Geochim. Cosmochim. Acta* **213**, 534–552.

Greber N. D., Pettke T., Vilela N., Lanari P. and Dauphas N. (2021) Titanium isotopic compositions of bulk rocks and mineral separates from the Kos magmatic suite:

Insights into fractional crystallization and magma mixing processes. *Chem. Geol.*, 120303.

Grove T. L., Elkins-Tanton L. T., Parman S. W., Chatterjee N., Müntener O. and Gaetani G. A. (2003) Fractional crystallization and mantle-melting controls on calc-alkaline differentiation trends. *Contrib. to Mineral. Petrol.* **145**, 515–533.

Gualda G. A. R., Ghiorso M. S., Lemons R. V and Carley T. L. (2012) Rhyolite-MELTS: a modified calibration of MELTS optimized for silica-rich, fluid-bearing magmatic systems. *J. Petrol.* **53**, 875–890.

Haase K. M., Freund S., Beier C., Koepke J., Erdmann M. and Hauff F. (2016) Constraints on the magmatic evolution of the oceanic crust from plagiogranite intrusions in the Oman ophiolite. *Contrib. to Mineral. Petrol.* **171**, 1–16.

Harker A. (1909) *The natural history of igneous rocks*., Methuen & Company.

Harris C. R., Millman K. J., van der Walt S. J., Gommers R., Virtanen P., Cournapeau D., Wieser E., Taylor J., Berg S. and Smith N. J. (2020) Array programming with NumPy. *Nature* **585**, 357–362.

Helz R. T. (1987) Differentiation behavior of Kilauea Iki lava lake, Kilauea Volcano, Hawaii: an overview of past and current work. *Magmat. Process. Physicochem. Princ.* **1**, 241–258.

Helz R. T., Kirschenbaum H. K., Marinenko J. W. and Qian R. (1994) *Whole-rock analyses of core samples from the 1967, 1975, 1979 and 1981 drillings of Kilauea Iki lava lake, Hawaii*., US Geological Survey,.

Henderson C. M. B. and Foland K. A. (1996) Ba-and Ti-rich primary biotite from the Brome alkaline igneous complex, Monteregian Hills, Quebec; mechanisms of substitution. *Can. Mineral.* **34**, 1241–1252.

Henstock T. J., Woods A. W. and White R. S. (1993) The accretion of oceanic crust by episodic sill intrusion. *J. Geophys. Res. Solid Earth* **98**, 4143–4161.

Hill E., Wood B. J. and Blundy J. D. (2000) The effect of Ca-Tschermaks component on trace element partitioning between clinopyroxene and silicate melt. *Lithos* **53**, 203–215.

Hill P. S. and Schauble E. A. (2008) Modeling the effects of bond environment on equilibrium iron isotope fractionation in ferric aquo-chloro complexes. *Geochim. Cosmochim. Acta* **72**, 1939–1958.

Hin R. C., Coath C. D., Carter P. J., Nimmo F., Lai Y.-J., von Strandmann P. A. E. P., Willbold M., Leinhardt Z. M., Walter M. J. and Elliott T. (2017) Magnesium isotope evidence that accretional vapour loss shapes planetary compositions. *Nature* **549**, 511–515.

Hoare L., Klaver M., Saji N. S., Gillies J., Parkinson I. J., Lissenberg C. J. and Millet M.-A. (2020) Melt chemistry and redox conditions control titanium isotope fractionation during magmatic differentiation. *Geochim. Cosmochim. Acta* **282**, 38–54.

Horita J., Cole D. R., Polyakov V. B. and Driesner T. (2002) Experimental and theoretical study of pressure effects on hydrogen isotope fractionation in the system brucite-water at elevated temperatures. *Geochim. Cosmochim. Acta* **66**, 3769–3788.

Höskuldsson Á., Óskarsson N., Pedersen R., Grönvold K., Vogfjörð K. and Ólafsdóttir R. (2007) The millennium eruption of Hekla in February 2000. *Bull. Volcanol.* **70**, 169–182.

Howarth G. H. and Prevec S. A. (2013) Hydration vs. oxidation: Modelling implications for Fe–Ti oxide crystallisation in mafic intrusions, with specific reference to the Panzhihua intrusion, SW China. *Geosci. Front.* **4**, 555–569.

Huang F., Glessner J., Ianno A., Lundstrom C. and Zhang Z. (2009) Magnesium isotopic composition of igneous rock standards measured by MC-ICP-MS. *Chem. Geol.* **268**, 15–23.

Huang S., Farkaš J. and Jacobsen S. B. (2010) Calcium isotopic fractionation between clinopyroxene and orthopyroxene from mantle peridotites. *Earth Planet. Sci. Lett.* **292**, 337–344.

Huijsmans J. P. P. and Barton M. (1989) Polybaric geochemical evolution of two shield volcanoes from Santorini, Aegean Sea, Greece: evidence for zoned magma

chambers from cyclic compositional variations. *J. Petrol.* **30**, 583–625.

Huijsmans J. P. P., Barton M. and Salters V. J. M. (1988) Geochemistry and evolution of the calc-alkaline volcanic complex of Santorini, Aegean Sea, Greece. *J. Volcanol. Geotherm. Res.* **34**, 283–306.

Inglis E. C., Creech J. B., Deng Z. and Moynier F. (2018) High-precision zirconium stable isotope measurements of geological reference materials as measured by double-spike MC-ICPMS. *Chem. Geol.* **493**, 544–552.

Ishikawa T., Nagaishi K. and Umino S. (2002) Boninitic volcanism in the Oman ophiolite: Implications for thermal condition during transition from spreading ridge to arc. *Geology* **30**, 899–902.

Ishizuka O., Tani K. and Reagan M. K. (2014) Izu-Bonin-Mariana forearc crust as a modern ophiolite analogue. *Elements* **10**, 115–120.

Jansen M. N., Lissenberg C. J., Klaver M., de Graaff S. J., Koornneef J. M., Smeets R. J., MacLeod C. J. and Davies G. R. (2018) Isotopic variation in Semail Ophiolite lower crust reveals crustal-level melt aggregation. *Geochemical Perspect. Lett.* **8**, 37–42.

Jicha B. R., Singer B. S. and Valentine M. J. (2013) 40Ar/39Ar geochronology of subaerial Ascension Island and a re-evaluation of the temporal progression of basaltic to rhyolitic volcanism. *J. Petrol.* **54**, 2581–2596.

Johnson A. C., Aarons S. M., Dauphas N., Nie N. X., Zeng H., Helz R. T., Romaniello S. J. and Anbar A. D. (2019) Titanium isotopic fractionation in Kilauea Iki lava lake driven by oxide crystallization. *Geochim. Cosmochim. Acta* **264**, 180–190.

Keil K. (2010) Enstatite achondrite meteorites (aubrites) and the histories of their asteroidal parent bodies. *Geochemistry* **70**, 295–317.

Kelemen P. B., Koga K. and Shimizu N. (1997) Geochemistry of gabbro sills in the crust-mantle transition zone of the Oman ophiolite: Implications for the origin of the oceanic lower crust. *Earth Planet. Sci. Lett.* **146**, 475–488.

Kemner F., Haase K. M., Beier C., Krumm S. and Brandl P. A. (2015) Formation of andesite melts and Ca-rich plagioclase in the submarine Monowai volcanic system, Kermadec arc. *Geochemistry, Geophys. Geosystems* **16**, 4130–4152.

Kessel R., Schmidt M. W., Ulmer P. and Pettke T. (2005) Trace element signature of subduction-zone fluids, melts and supercritical liquids at 120–180 km depth. *Nature* **437**, 724–727.

Kinzler R. J. and Grove T. L. (1993) Corrections and further discussion of the primary magmas of mid-ocean ridge basalts, 1 and 2. *J. Geophys. Res. Solid Earth* **98**, 22339–22347.

Klaver M. (2016) Dynamics of magma generation and differentiation in the central-eastern Aegean arc:: A geochemical and petrological study of Quaternary arc volcanism in Greece, PhD Thesis, Vrije Universiteit Amsterdam.

Klaver M., Carey S., Nomikou P., Smet I., Godelitsas A. and Vroon P. (2016a) A distinct source and differentiation history for Kolumbo submarine volcano, Santorini volcanic field, Aegean arc. *Geochemistry, Geophys. Geosystems* **17**, 3254–3273.

Klaver M. and Coath C. D. (2019) Obtaining accurate isotopic compositions with the double spike technique: Practical considerations. *Geostand. Geoanalytical Res.* **43**, 5–22.

Klaver M., Davies G. R. and Vroon P. Z. (2016b) Subslab mantle of African provenance infiltrating the Aegean mantle wedge. *Geology* **44**, 367–370.

Klaver M., Ionov D. A., Takazawa E. and Elliott T. (2020) The non-chondritic Ni isotope composition of Earth's mantle. *Geochim. Cosmochim. Acta* **268**, 405–421.

Klaver M., MacLennan S. A., Ibañez-Mejia M., Tissot F. L. H., Vroon P. Z. and Millet M.-A. (2021) Reliability of detrital marine sediments as proxy for continental crust composition: The effects of hydrodynamic sorting on Ti and Zr isotope systematics. *Geochim. Cosmochim. Acta, **310**, 221-239*.

Klemme S., Prowatke S., Hametner K. and Günther D. (2005) Partitioning of trace elements between rutile and silicate melts: implications for subduction zones. *Geochim. Cosmochim. Acta* **69**, 2361–2371.

Koepke J., Feig S. T., Berndt J. and Neave D. A. (2021) Wet magmatic processes during the accretion of the deep crust of the Oman Ophiolite paleoridge: Phase diagrams and petrological records. *Tectonophysics*, 229051.

Koepke J. and Zhang C. (2020) Axial Melt-Lens Dynamics at Fast Spreading Midocean Ridges. *Dyn. magma Evol.*, 179–206.

Kommescher S., Fonseca R. O. C., Kurzweil F., Thiemens M. M., Münker C. and Sprung P. (2020) Unravelling lunar mantle source processes via the Ti isotope composition of lunar basalts. *Geochemical Perspect. Lett.* **13**, 13–18.

Kress V. C. and Carmichael I. S. E. (1991) The compressibility of silicate liquids containing Fe 2 O 3 and the effect of composition, temperature, oxygen fugacity and pressure on their redox states. *Contrib. to Mineral. Petrol.* **108**, 82–92.

Larsen K. K., TRINqUIER A., Paton C., Schiller M., Wielandt D., Ivanova M. A., Connelly J. N., Nordlund Å., Krot A. N. and Bizzarro M. (2011) Evidence for magnesium isotope heterogeneity in the solar protoplanetary disk. *Astrophys. J. Lett.* **735**, L37.

Laubier M., Grove T. L. and Langmuir C. H. (2014) Trace element mineral/melt partitioning for basaltic and basaltic andesitic melts: An experimental and laser ICP-MS study with application to the oxidation state of mantle source regions. *Earth Planet. Sci. Lett.* **392**, 265–278.

Laumonier M., Scaillet B., Pichavant M., Champallier R., Andujar J. and Arbaret L. (2014) On the conditions of magma mixing and its bearing on andesite production in the crust. *Nat. Commun.* **5**, 1–12.

Lee C.-T. A., Leeman W. P., Canil D. and Li Z.-X. A. (2005) Similar V/Sc systematics in MORB and arc basalts: implications for the oxygen fugacities of their mantle source regions. *J. Petrol.* **46**, 2313–2336.

Leitzke F. P., Fonseca R. O. C., Göttlicher J., Steininger R., Jahn S., Prescher C. and Lagos M. (2018) Ti K-edge XANES study on the coordination number and oxidation state of Titanium in pyroxene, olivine, armalcolite, ilmenite, and silicate glass during mare basalt petrogenesis. *Contrib. to Mineral. Petrol.* **173**, 1–17.

Lepage L. D. (2003) ILMAT: an Excel worksheet for ilmenite-magnetite geothermometry and geobarometry. *Comput. Geosci.* **29**, 673–678.

Leya I., Schönbächler M., Wiechert U., Krähenbühl U. and Halliday A. N. (2008)

Titanium isotopes and the radial heterogeneity of the solar system. *Earth Planet. Sci. Lett.* **266**, 233–244.

Lin J. and Morgan J. P. (1992) The spreading rate dependence of three-dimensional mid-ocean ridge gravity structure. *Geophys. Res. Lett.* **19**, 13–16.

Lippard S. J. (1986) The ophiolite of northern Oman. *Geol. Soc. London Mem.* **11**, 178.

Lissenberg C. J., Bedard J. H. and van Staal C. R. (2004) The structure and geochemistry of the gabbro zone of the Annieopsquotch ophiolite, Newfoundland: implications for lower crustal accretion at spreading ridges. *Earth Planet. Sci. Lett.* **229**, 105–123.

Loocke M. (2016) The role of the axial melt lens in crustal accretion at fast-spreading mid-ocean ridges. PhD Thesis, Cardiff University.

Lu D., Zhang T., Yang X., Su P., Liu Q. and Jiang G. (2017) Recent advances in the analysis of non-traditional stable isotopes by multi-collector inductively coupled plasma mass spectrometry. *J. Anal. At. Spectrom.* **32**, 1848–1861.

Lucic G., Berg A. and Stix J. (2016) Water-rich and volatile-undersaturated magmas at Hekla volcano, Iceland. *Geochemistry, Geophys. Geosystems* **17**, 3111–3130.

Lundstrom C. C., Shaw H. F., Ryerson F. J., Williams Q. and Gill J. (1998) Crystal chemical control of clinopyroxene-melt partitioning in the Di-Ab-An system: implications for elemental fractionations in the depleted mantle. *Geochim. Cosmochim. Acta* **62**, 2849–2862.

Maclennan J., Hulme T. and Singh S. C. (2005) Cooling of the lower oceanic crust. *Geology* **33**, 357–366.

MacLeod C. J., Johan Lissenberg C. and Bibby L. E. (2013) "Moist MORB" axial magmatism in the Oman ophiolite: The evidence against a mid-ocean ridge origin. *Geology* **41**, 459–462.

Madsen J. A., Detrick R. S., Mutter J. C., Buhl P. and Orcutt J. A. (1990) A two-and three-dimensional analysis of gravity anomalies associated with the East Pacific Rise at 9° N and 13° N. *J. Geophys. Res. Solid Earth* **95**, 4967–4987.

Mallmann G. and O'Neill H. S. C. (2009) The crystal/melt partitioning of V during

mantle melting as a function of oxygen fugacity compared with some other elements (Al, P, Ca, Sc, Ti, Cr, Fe, Ga, Y, Zr and Nb). *J. Petrol.* **50**, 1765–1794.

Mandl M. B. (2019) Titanium isotope fractionation on the Earth and moon: constraints on magmatic processes and moon formation. ETH Zurich.

Mastrobuono-Battisti A., Perets H. B. and Raymond S. N. (2015) A primordial origin for the compositional similarity between the Earth and the Moon. *Nature* **520**, 212–215.

Mattauch J. and Herzog R. (1934) Über einen neuen Massenspektrographen. *Zeitschrift für Phys.* **89**, 786–795.

McDonough W. F., Stosch H.-G. and Ware N. G. (1992) Distribution of titanium and the rare earth elements between peridotitic minerals. *Contrib. to Mineral. Petrol.* **110**, 321–328.

McDonough W. F. and Sun S.-S. (1995) The composition of the Earth. *Chem. Geol.* **120**, 223–253.

Melekhova E., Blundy J., Robertson R. and Humphreys M. C. S. (2015) Experimental evidence for polybaric differentiation of primitive arc basalt beneath St. Vincent, Lesser Antilles. *J. Petrol.* **56**, 161–192.

Michaud V., Clocchiatti R. and Sbrana S. (2000) The Minoan and post-Minoan eruptions, Santorini (Greece), in the light of melt inclusions: chlorine and sulphur behaviour. *J. Volcanol. Geotherm. Res.* **99**, 195–214.

Millet M.-A. and Dauphas N. (2014) Ultra-precise titanium stable isotope measurements by double-spike high resolution MC-ICP-MS. *J. Anal. At. Spectrom.* **29**, 1444–1458.

Millet M.-A., Dauphas N., Greber N. D., Burton K. W., Dale C. W., Debret B., Macpherson C. G., Nowell G. M. and Williams H. M. (2016) Titanium stable isotope investigation of magmatic processes on the Earth and Moon. *Earth Planet. Sci. Lett.* **449**, 197–205.

Millet M., Tutt C. M., Handler M. R. and Baker J. A. (2014) Processes and time scales of dacite magma assembly and eruption at Tauhara volcano, Taupo Volcanic

Zone, New Zealand. *Geochemistry, Geophys. Geosystems* **15**, 213–237.

Mills K. C. (1993) The influence of structure on the physico-chemical properties of slags. *ISIJ Int.* **33**, 148–155.

Miyashiro A. (1973) The Troodos ophiolitic complex was probably formed in an island arc. *Earth Planet. Sci. Lett.* **19**, 218–224.

Moore J. G. (1970) Water content of basalt erupted on the ocean floor. *Contrib. to Mineral. Petrol.* **28**, 272–279.

Moores E. M. and Kellogg L. H. (2000) contingency": A resolution of the" ophiolite conundrum". *Ophiolites Ocean. crust New insights from F. Stud. Ocean Drill. Progr.* **349**, 3.

Morgan J. P. and Chen Y. J. (1993) The genesis of oceanic crust: Magma injection, hydrothermal circulation, and crustal flow. *J. Geophys. Res. Solid Earth* **98**, 6283–6297.

Müller T., Koepke J., Garbe-Schönberg C.-D., Dietrich M., Bauer U. and Wolff P. E. (2017) Anatomy of a frozen axial melt lens from a fast-spreading paleo-ridge (Wadi Gideah, Oman ophiolite). *Lithos* **272**, 31–45.

Mysen B. O. and Richet P. (2018) *Silicate glasses and melts*., Elsevier.

Nandedkar R. H., Ulmer P. and Müntener O. (2014) Fractional crystallization of primitive, hydrous arc magmas: an experimental study at 0.7 GPa. *Contrib. to Mineral. Petrol.* **167**, 1–27.

Nanne J. A. M., Millet M.-A., Burton K. W., Dale C. W., Nowell G. M. and Williams H. M. (2017) High precision osmium stable isotope measurements by double spike MC-ICP-MS and N-TIMS. *J. Anal. At. Spectrom.* **32**, 749–765.

Nicholls I. A. (1971) Petrology of Santorini Volcano, Cyclades, Greece. *J. Petrol.* **12**, 67–119.

Nicolas A. (2012) *Structures of ophiolites and dynamics of oceanic lithosphere*., Springer Science & Business Media.

Nicolas A., Boudier F., Ildefonse B. and Ball E. (2000) Accretion of Oman and United Arab Emirates ophiolite–Discussion of a new structural map. *Mar. Geophys. Res.*

21, 147–180.

Nicolas A., Reuber I. and Benn K. (1988) A new magma chamber model based on structural studies in the Oman ophiolite. *Tectonophysics* **151**, 87–105.

Nie N. X., Dauphas N., Alp E. E., Zeng H., Sio C. K., Hu J. Y., Chen X., Aarons S. M., Zhang Z. and Tian H.-C. (2021) Iron, magnesium, and titanium isotopic fractionations between garnet, ilmenite, fayalite, biotite, and tourmaline: Results from NRIXS, ab initio, and study of mineral separates from the Moosilauke metapelite. *Geochim. Cosmochim. Acta* **302**, 18–45.

Niederer F. R., Papanastassiou D. A. and Wasserburg G. J. (1980) Endemic isotopic anomalies in titanium. *Astrophys. J. Lett.* **240**, L73–L77.

Niemeyer S. and Lugmair G. W. (1984) Titanium isotopic anomalies in meteorites. *Geochim. Cosmochim. Acta* **48**, 1401–1416.

Nier A. O. (1940) A mass spectrometer for routine isotope abundance measurements. *Rev. Sci. Instrum.* **11**, 212–216.

Nishikawa S. (1915) Structure of some crystals of spinel group. *Proc. Tokyo Math. Soc. 2nd Ser.* **8**, 199-209.

Niu Y. (1997) Mantle melting and melt extraction processes beneath ocean ridges: evidence from abyssal peridotites. *J. Petrol.* **38**, 1047–1074.

O'Neil J. R. (1986) Theoretical and experimental aspects of isotopic fractionation. *Rev. Mineral.* **16**, 1–40.

O'Neill H. S. C. and Navrotsky A. (1983) Simple spinels; crystallographic parameters, cation radii, lattice energies, and cation distribution. *Am. Mineral.* **68**, 181–194.

Oberti R., Ungaretti L., Cannillo E. and Hawthorne F. C. (1992) The behaviour of Ti in amphiboles; I, Four-and six-coordinate Ti in richterite. *Eur. J. Mineral.* **4**, 425–439.

Oeser M., Dohmen R., Horn I., Schuth S. and Weyer S. (2015) Processes and time scales of magmatic evolution as revealed by Fe–Mg chemical and isotopic zoning in natural olivines. *Geochim. Cosmochim. Acta* **154**, 130–150.

Oeser M., Ruprecht P. and Weyer S. (2018) Combined Fe-Mg chemical and isotopic zoning in olivine constraining magma mixing-to-eruption timescales for the

continental arc volcano Irazú (Costa Rica) and Cr diffusion in olivine. *Am. Mineral. J. Earth Planet. Mater.* **103**, 582–599.

Okube M., Oshiumi T., Nagase T., Miyawaki R., Yoshiasa A., Sasaki S. and Sugiyama K. (2018) Site occupancy of Fe^{2+}, Fe^{3+} and Ti^{4+} in titanomagnetite determined by valence-difference contrast in synchrotron X-ray resonant scattering. *J. Synchrotron Radiat.* **25**, 1694–1702.

Orians K. J., Boyle E. A. and Bruland K. W. (1990) Dissolved titanium in the open ocean. *Nature* **348**, 322–325.

Othman D. Ben, White W. M. and Patchett J. (1989) The geochemistry of marine sediments, island arc magma genesis, and crust-mantle recycling. *Earth Planet. Sci. Lett.* **94**, 1–21.

Pallister J. S. (1984) Parent magmas of the Semail ophiolite, Oman. *Geol. Soc. London, Spec. Publ.* **13**, 63–70.

Palme H. and O'Neill H. (2014) Cosmochemical Estimates of Mantle Composition. Planets, Asteriods, Comets and The Solar System, Volume 2 of Treatise on Geochemistry . Edited by Andrew M. Davis.

Papanastassiou D. A. and Brigham C. A. (1989) The identification of meteorite inclusions with isotope anomalies. *Astrophys. J.* **338**, L37–L40.

Papike J. J., Karner J. M. and Shearer C. K. (2005) Comparative planetary mineralogy: Valence state partitioning of Cr, Fe, Ti, and V among crystallographic sites in olivine, pyroxene, and spinel from planetary basalts. *Am. Mineral.* **90**, 277–290.

Papike J. J., Simon S. B., Burger P. V, Bell A. S., Shearer C. K. and Karner J. M. (2016) Chromium, vanadium, and titanium valence systematics in Solar System pyroxene as a recorder of oxygen fugacity, planetary provenance, and processes. *Am. Mineral.* **101**, 907–918.

Parman S. W., Grove T. L., Kelley K. A. and Plank T. (2011) Along-arc variations in the pre-eruptive H2O contents of Mariana arc magmas inferred from fractionation paths. *J. Petrol.* **52**, 257–278.

Pearce C. I., Henderson C. M. B., Telling N. D., Pattrick R. A. D., Charnock J. M., Coker

V. S., Arenholz E., Tuna F. and van der Laan G. (2010) Fe site occupancy in magnetite-ulvospinel solid solutions: A new approach using X-ray magnetic circular dichroism. *Am. Mineral.* **95**, 425–439.

Pearce J. A. (2008) Geochemical fingerprinting of oceanic basalts with applications to ophiolite classification and the search for Archean oceanic crust. *Lithos* **100**, 14–48.

Pearce J. A. (2014) Immobile element fingerprinting of ophiolites. *Elements* **10**, 101–108.

Pearce J. A. (1982) Trace element characteristics of lavas from destructive plate boundaries. *Orog. andesites Relat. rocks*, 528–548.

Pearce J. A., Alabaster T., Shelton A. W. and Searle M. P. (1981) The Oman ophiolite as a Cretaceous arc-basin complex: evidence and implications. *Philos. Trans. R. Soc. London. Ser. A, Math. Phys. Sci.* **300**, 299–317.

Pearce J. A. and Cann J. R. (1973) Tectonic setting of basic volcanic rocks determined using trace element analyses. *Earth Planet. Sci. Lett.* **19**, 290–300.

Pearce J. A., Lippard S. J. and Roberts S. (1984) Characteristics and tectonic significance of supra-subduction zone ophiolites. *Geol. Soc. London, Spec. Publ.* **16**, 77–94.

Pearce J. A. and Norry M. J. (1979) Petrogenetic implications of Ti, Zr, Y, and Nb variations in volcanic rocks. *Contrib. to Mineral. Petrol.* **69**, 33–47.

Pearce J. A. and Parkinson I. J. (1993) Trace element models for mantle melting: application to volcanic arc petrogenesis. *Geol. Soc. London, Spec. Publ.* **76**, 373–403.

Pearce J. A. and Reagan M. K. (2019) Identification, classification, and interpretation of boninites from Anthropocene to Eoarchean using Si-Mg-Ti systematics. *Geosphere* **15**, 1008–1037.

Pearce J. A. and Robinson P. T. (2010) The Troodos ophiolitic complex probably formed in a subduction initiation, slab edge setting. *Gondwana Res.* **18**, 60–81.

Peccerillo A. and Taylor S. R. (1976) Geochemistry of Eocene calc-alkaline volcanic rocks from the Kastamonu area, northern Turkey. *Contrib. to Mineral. Petrol.* **58**, 63–81.

Petit J. C. J., De Jong J., Chou L. and Mattielli N. (2008) Development of Cu and Zn isotope MC-ICP-MS measurements: Application to suspended particulate matter and sediments from the Scheldt Estuary. *Geostand. Geoanalytical Res.* **32**, 149–166.

Pietruszka A. J. and Reznik A. D. (2008) Identification of a matrix effect in the MC-ICP-MS due to sample purification using ion exchange resin: An isotopic case study of molybdenum. *Int. J. Mass Spectrom.* **270**, 23–30.

Pik R., Marty B. and Hilton D. R. (2006) How many mantle plumes in Africa? The geochemical point of view. *Chem. Geol.* **226**, 100–114.

Plank T. and Langmuir C. H. (1998) The chemical composition of subducting sediment and its consequences for the crust and mantle. *Chem. Geol.* **145**, 325–394.

Platzner I. T., Habfast K., Walder A. J. and Goetz A. (1997) Modern isotope ratio mass spectrometry.

Polyakov V. B. (2009) Equilibrium iron isotope fractionation at core-mantle boundary conditions. *Science,* **323**(5916), 912–914.

Polyakov V. B. and Kharlashina N. N. (1994) Effect of pressure on equilibrium isotopic fractionation. *Geochim. Cosmochim. Acta* **58**, 4739–4750.

Portner R. A., Dreyer B. M. and Clague D. A. (2021) Mid-ocean-ridge rhyolite (MORR) eruptions on the East Pacific Rise lack the fizz to pop. *Geology* **49**, 377–381.

Preece K., Mark D. F., Barclay J., Cohen B. E., Chamberlain K. J., Jowitt C., Vye-Brown C., Brown R. J. and Hamilton S. (2018) Bridging the gap: 40Ar/39Ar dating of volcanic eruptions from the 'Age of Discovery.' *Geology* **46**, 1035–1038.

Prytulak J. and Elliott T. (2007) TiO_2 enrichment in ocean island basalts. *Earth Planet. Sci. Lett.* **263**, 388–403.

Prytulak J., Nielsen S. G., Ionov D. A., Halliday A. N., Harvey J., Kelley K. A., Niu Y. L., Peate D. W., Shimizu K. and Sims K. W. W. (2013) The stable vanadium isotope composition of the mantle and mafic lavas. *Earth Planet. Sci. Lett.* **365**, 177–189.

Prytulak J., Sossi P. A., Halliday A. N., Plank T., Savage P. S. and Woodhead J. D. (2016) Stable vanadium isotopes as a redox proxy in magmatic systems. *Geochemical Perspect. Lett*, ***3***, *75-84.*

Rapp R. P., Irifune T., Shimizu N., Nishiyama N., Norman M. D. and Inoue T. (2008) Subduction recycling of continental sediments and the origin of geochemically enriched reservoirs in the deep mantle. *Earth Planet. Sci. Lett.* **271**, 14–23.

Reagan M. K., Ishizuka O., Stern R. J., Kelley K. A., Ohara Y., Blichert-Toft J., Bloomer S. H., Cash J., Fryer P. and Hanan B. B. (2010) Fore-arc basalts and subduction initiation in the Izu-Bonin-Mariana system. *Geochemistry, Geophys. Geosystems* **11**.

Reck H., Behrend F., Dobe F., Georgalas G., Hondros D., Liatsikas N., Van Padang M. N., Quenstedt W. and Schuster J. (1936) *Santorin: der Werdegang eines Inselvulkans und sein Ausbruch 1925-1928: ergebnisse einer Deutsch-Griechischen Arbeitsgemeinschaft*.,

Reubi O. and Blundy J. (2009) A dearth of intermediate melts at subduction zone volcanoes and the petrogenesis of arc andesites. *Nature* **461**, 1269–1273.

Richter F. M., Davis A. M., DePaolo D. J. and Watson E. B. (2003) Isotope fractionation by chemical diffusion between molten basalt and rhyolite. *Geochim. Cosmochim. Acta* **67**, 3905–3923.

Richter F. M., Watson E. B., Mendybaev R. A., Teng F.-Z. and Janney P. E. (2008) Magnesium isotope fractionation in silicate melts by chemical and thermal diffusion. *Geochim. Cosmochim. Acta* **72**, 206–220.

Rickwood P. C. (1989) Boundary lines within petrologic diagrams which use oxides of major and minor elements. *Lithos* **22**, 247–263.

Rioux M., Bowring S., Kelemen P., Gordon S., Dudás F. and Miller R. (2012) Rapid crustal accretion and magma assimilation in the Oman-UAE ophiolite: High precision U-Pb zircon geochronology of the gabbroic crust. *J. Geophys. Res. Solid Earth* **117**.

Rioux M., Bowring S., Kelemen P., Gordon S., Miller R. and Dudás F. (2013) Tectonic development of the Samail ophiolite: High-precision U-Pb zircon geochronology and Sm-Nd isotopic constraints on crustal growth and emplacement. *J. Geophys. Res. Solid Earth* **118**, 2085–2101.

Roskosz M., Sio C. K. I., Dauphas N., Bi W., Tissot F. L. H., Hu M. Y., Zhao J. and Alp

E. E. (2015) Spinel–olivine–pyroxene equilibrium iron isotopic fractionation and applications to natural peridotites. *Geochim. Cosmochim. Acta* **169**, 184–199.

le Roux P. J., Shirey S. B., Hauri E. H., Perfit M. R. and Bender J. F. (2006) The effects of variable sources, processes and contaminants on the composition of northern EPR MORB (8–10 N and 12–14 N): Evidence from volatiles (H2O, CO2, S) and halogens (F, Cl). *Earth Planet. Sci. Lett.* **251**, 209–231.

Rudge J. F., Reynolds B. C. and Bourdon B. (2009) The double spike toolbox. *Chem. Geol.* **265**, 420–431.

Rzehak L. J. A., Kommescher S., Kurzweil F., Sprung P., Leitzke F. P. and Fonseca R. O. C. (2021) The redox dependence of titanium isotope fractionation in synthetic Ti-rich lunar melts. *Contrib. to Mineral. Petrol.* **176**, 1–16.

Salinas-Sanchez A., Garcia-Munoz J. L., Rodriguez-Carvajal J., Saez-Puche R. and Martinez J. L. (1992) Structural characterization of R_2BaCuO_5 (R= Y, Lu, Yb, Tm, Er, Ho, Dy, Gd, Eu and Sm) oxides by X-ray and neutron diffraction. *J. Solid State Chem.* **100**, 201–211.

Salters V. J. M. and Stracke A. (2004) Composition of the depleted mantle. *Geochemistry, Geophys. Geosystems* **5**.

Samat M. H., Ali A. M. M., Taib M. F. M., Hassan O. H. and Yahya M. Z. A. (2016) Hubbard U calculations on optical properties of 3d transition metal oxide TiO_2. *Results Phys.* **6**, 891–896.

Sandstrom D. R., Lytle F. W., Wei P. S. P., Greegor R. B., Wong J. and Schultz P. (1980) Coordination of Ti in TiO_2 - SiO_2 glass by X-ray absorption spectroscopy. *J. Non. Cryst. Solids* **41**, 201–207.

Savage P. S., Georg R. B., Williams H. M., Burton K. W. and Halliday A. N. (2011) Silicon isotope fractionation during magmatic differentiation. *Geochim. Cosmochim. Acta* **75**, 6124–6139.

Schauble E. A. (2004) Applying stable isotope fractionation theory to new systems. *Rev. Mineral. geochemistry* **55**, 65–111.

Schoenberg R., Merdian A., Holmden C., Kleinhanns I. C., Haßler K., Wille M. and

Reitter E. (2016) The stable Cr isotopic compositions of chondrites and silicate planetary reservoirs. *Geochim. Cosmochim. Acta* **183**, 14–30.

Searle M. and Cox J. (1999) Tectonic setting, origin, and obduction of the Oman ophiolite. *Geol. Soc. Am. Bull.* **111**, 104–122.

Sedler I. K., Feenstra A. and Peters T. (1994) An X-ray powder diffraction study of synthetic (Fe, Mn) 2TiO4 spinel. *Eur. J. Mineral.*, 873–886.

Shannon R. D. (1976) Revised effective ionic radii and systematic studies of interatomic distances in halides and chalcogenides. *Acta Crystallogr. Sect. A Cryst. physics, diffraction, Theor. Gen. Crystallogr.* **32**, 751–767.

Shellnutt J. G., Zhou M.-F. and Zellmer G. F. (2009) The role of Fe–Ti oxide crystallization in the formation of A-type granitoids with implications for the Daly gap: an example from the Permian Baima igneous complex, SW China. *Chem. Geol.* **259**, 204–217.

Shervais J. W. (1982) Ti-V plots and the petrogenesis of modern and ophiolitic lavas. *Earth Planet. Sci. Lett.* **59**, 101–118.

Shervais J. W., Reagan M., Haugen E., Almeev R. R., Pearce J. A., Prytulak J., Ryan J. G., Whattam S. A., Godard M. and Chapman T. (2019) Magmatic response to subduction initiation: Part 1. Fore-arc basalts of the Izu-Bonin arc from IODP Expedition 352. *Geochemistry, Geophys. Geosystems* **20**, 314–338.

Simon J. I. and DePaolo D. J. (2010) Stable calcium isotopic composition of meteorites and rocky planets. *Earth Planet. Sci. Lett.* **289**, 457–466.

Simon S. B. and Sutton S. R. (2017) Valence of Ti, V, and Cr in Apollo 14 aluminous basalts 14053 and 14072. *Meteorit. Planet. Sci.* **52**, 2051–2066.

Simon S. B. and Sutton S. R. (2018) Valences of Ti, Cr, and V in Apollo 17 high-Ti and very low-Ti basalts and implications for their formation. *Meteorit. Planet. Sci.* **53**, 2138–2154.

Sisson T. W. and Grove T. L. (1993) Experimental investigations of the role of H 2 O in calc-alkaline differentiation and subduction zone magmatism. *Contrib. to Mineral. Petrol.* **113**, 143–166.

Snyder G. A., Taylor L. A. and Neal C. R. (1992) A chemical model for generating the sources of mare basalts: Combined equilibrium and fractional crystallization of the lunar magmasphere. *Geochim. Cosmochim. Acta* **56**, 3809–3823.

Soddy F. (1913) Intra-atomic charge. *Nature* **92**, 399–400.

Sossi P. A., Foden J. D. and Halverson G. P. (2012) Redox-controlled iron isotope fractionation during magmatic differentiation: an example from the Red Hill intrusion, S. Tasmania. *Contrib. to Mineral. Petrol.* **164**, 757–772.

Sossi P. A. and O'Neill H. S. C. (2017) The effect of bonding environment on iron isotope fractionation between minerals at high temperature. *Geochim. Cosmochim. Acta* **196**, 121–143.

Sossi P. A., Prytulak J. and O'Neill H. S. C. (2018) Experimental calibration of vanadium partitioning and stable isotope fractionation between hydrous granitic melt and magnetite at 800 C and 0.5 GPa. *Contrib. to Mineral. Petrol.* **173**, 1–18.

Staudigel H., Plank T., White B. and Schmincke H. (1996) Geochemical fluxes during seafloor alteration of the basaltic upper oceanic crust: DSDP Sites 417 and 418. *Subduction top to bottom* **96**, 19–38.

Stern R. J., Reagan M., Ishizuka O., Ohara Y. and Whattam S. (2012) To understand subduction initiation, study forearc crust: To understand forearc crust, study ophiolites. *Lithosphere* **4**, 469–483.

Stout M. Z. and Bayliss P. (1980) Crystal structure of two ferrian ulvospinels from British Columbia. *Can. Mineral.* **18**, 339–341.

Szymanowski D., Ellis B. S., Wotzlaw J.-F. and Bachmann O. (2019) Maturation and rejuvenation of a silicic magma reservoir: High-resolution chronology of the Kneeling Nun Tuff. *Earth Planet. Sci. Lett.* **510**, 103–115.

Taboada T., Cortizas A. M., García C. and García-Rodeja E. (2006) Particle-size fractionation of titanium and zirconium during weathering and pedogenesis of granitic rocks in NW Spain. *Geoderma* **131**, 218–236.

Tang M., Chen K. and Rudnick R. L. (2016) Archean upper crust transition from mafic to felsic marks the onset of plate tectonics. *Science (80-.).* **351**, 372–375.

Tatsumi Y. and Suzuki T. (2009) Tholeiitic vs calc-alkalic differentiation and evolution of arc crust: constraints from melting experiments on a basalt from the Izu–Bonin–Mariana Arc. *J. Petrol.* **50**, 1575–1603.

Teng F.-Z. (2017) Magnesium isotope geochemistry. *Rev. Mineral. Geochemistry* **82**, 219–287.

Teng F.-Z., Dauphas N. and Watkins J. M. (2017) Non-traditional stable isotopes: retrospective and prospective. *Rev. Mineral. geochemistry* **82**, 1–26.

Teng F.-Z., Li W.-Y., Ke S., Marty B., Dauphas N., Huang S., Wu F.-Y. and Pourmand A. (2010) Magnesium isotopic composition of the Earth and chondrites. *Geochim. Cosmochim. Acta* **74**, 4150–4166.

Thiemens M. H. (2006) History and applications of mass-independent isotope effects. *Annu. Rev. Earth Planet. Sci.* **34**, 217–262.

Thiemens M. H. (1999) Mass-independent isotope effects in planetary atmospheres and the early solar system. *Science (80-.).* **283**, 341–345.

Thomson J. J. (1913) On the appearance of helium and neon in vacuum tubes. *Nature* **90**, 645–647.

Tiepolo M., Oberti R., Zanetti A., Vannucci R. and Foley S. F. (2007) Trace-element partitioning between amphibole and silicate melt. *Rev. Mineral. Geochemistry* **67**, 417–452.

Timm C., Graham I. J., de Ronde C. E. J., Leybourne M. I. and Woodhead J. (2011) Geochemical evolution of Monowai volcanic center: New insights into the northern Kermadec arc subduction system, SW Pacific. *Geochemistry, Geophys. Geosystems* **12**.

Todd E., Gill J. B. and Pearce J. A. (2012) A variably enriched mantle wedge and contrasting melt types during arc stages following subduction initiation in Fiji and Tonga, southwest Pacific. *Earth Planet. Sci. Lett.* **335**, 180–194.

Toplis M. J. and Carroll M. R. (1995) An experimental study of the influence of oxygen fugacity on Fe-Ti oxide stability, phase relations, and mineral—melt equilibria in ferro-basaltic systems. *J. Petrol.* **36**, 1137–1170.

Toplis M. J. and Carroll M. R. (1996) Differentiation of ferro-basaltic magmas under conditions open and closed to oxygen: implications for the Skaergaard intrusion and other natural systems. *J. Petrol.* **37**, 837–858.

Trinquier A., Elliott T., Ulfbeck D., Coath C., Krot A. N. and Bizzarro M. (2009) Origin of nucleosynthetic isotope heterogeneity in the solar protoplanetary disk. *Science,* **324**(5925), 374–376.

Urey H. C. (1948) Oxygen isotopes in nature and in the laboratory. *Science.* **108(**2810**)**, 489–496.

Urey H. C. (1947) The thermodynamic properties of isotopic substances. *J. Chem. Soc.*, 562–581.

Valley J. W. and Cole D. R. (2018) Stable isotope geochemistry. *Rev Mineral Geochem*, Mineralogical Society of America and the Geochemical Society, Washington D.C.

VanTongeren J. A., Hirth G. and Kelemen P. B. (2015) Constraints on the accretion of the gabbroic lower oceanic crust from plagioclase lattice preferred orientation in the Samail ophiolite. *Earth Planet. Sci. Lett.* **427**, 249–261.

VanTongeren J. A., Kelemen P. B. and Hanghøj K. (2008) Cooling rates in the lower crust of the Oman ophiolite: Ca in olivine, revisited. *Earth Planet. Sci. Lett.* **267**, 69–82.

Vera E. E., Mutter J. C., Buhl P., Orcutt J. A., Harding A. J., Kappus M. E., Detrick R. S. and Brocher T. M. (1990) The structure of 0-to 0.2-my-old oceanic crust at 9° N on the East Pacific Rise from expanded spread profiles. *J. Geophys. Res. Solid Earth* **95**, 15529–15556.

Virtanen P., Gommers R., Oliphant T. E., Haberland M., Reddy T., Cournapeau D., Burovski E., Peterson P., Weckesser W. and Bright J. (2020) SciPy 1.0: fundamental algorithms for scientific computing in Python. *Nat. Methods* **17**, 261–272.

Walder A. J., Platzner I. and Freedman P. A. (1993) Isotope ratio measurement of lead, neodymium and neodymium–samarium mixtures, hafnium and hafnium–lutetium mixtures with a double focusing multiple collector inductively coupled plasma mass spectrometer. *J. Anal. At. Spectrom.* **8**, 19–23.

Walter M. J. (1998) Melting of garnet peridotite and the origin of komatiite and depleted lithosphere. *J. Petrol.* **39**, 29–60.

Wang W., Huang S., Huang F., Zhao X. and Wu Z. (2020) Equilibrium inter-mineral titanium isotope fractionation: Implication for high-temperature titanium isotope geochemistry. *Geochim. Cosmochim. Acta* **269**, 540–553.

Wang W., Zhou C., Qin T., Kang J.-T., Huang S., Wu Z. and Huang F. (2017) Effect of Ca content on equilibrium Ca isotope fractionation between orthopyroxene and clinopyroxene. *Geochim. Cosmochim. Acta* **219**, 44–56.

Warren P. H. and Wasson J. T. (1979) The origin of KREEP. *Rev. Geophys.* **17**, 73–88.

Washington H. S. (1926) Santorini eruption of 1925. *Bull. Geol. Soc. Am.* **37**, 349–384.

Wasserburg G. J., Papanastassiou D. A., Nenow E. V and Bauman C. A. (1969) A programmable magnetic field mass spectrometer with on-line data processing. *Rev. Sci. Instrum.* **40**, 288–295.

Waychunas G. A. (1987) Synchrotron radiation XANES spectroscopy of Ti in minerals; effects of Ti bonding distances, Ti valence, and site geometry on absorption edge structure. *Am. Mineral.* **72**, 89–101.

Weber G. and Castro J. M. (2017) Phase petrology reveals shallow magma storage prior to large explosive silicic eruptions at Hekla volcano, Iceland. *Earth Planet. Sci. Lett.* **466**, 168–180.

Wechsler B. A., Lindsley D. H. and Prewitt C. T. (1984) Crystal structure and cation distribution in titanomagnetites ($Fe_{3-x}Ti_xO_4$). *Am. Mineral.* **69**, 754–770.

Wechsler B. A. and Prewitt C. T. (1984) Crystal structure of ilmenite ($FeTiO_3$) at high temperature and at high pressure. *Am. Mineral.* **69**, 176–185.

Weis D., Kieffer B., Maerschalk C., Barling J., De Jong J., Williams G. A., Hanano D., Pretorius W., Mattielli N. and Scoates J. S. (2006) High-precision isotopic characterization of USGS reference materials by TIMS and MC-ICP-MS. *Geochemistry, Geophys. Geosystems* **7**.

Whitney D. L. and Evans B. W. (2010) Abbreviations for names of rock-forming minerals. *Am. Mineral.* **95**, 185–187.

Williams H. M., McCammon C. A., Peslier A. H., Halliday A. N., Teutsch N., Levasseur S. and Burg J.-P. (2004) Iron isotope fractionation and the oxygen fugacity of the mantle. *Science,* **304**(5677), 1656–1659.

Williams N. H. (2015) *Titanium isotope cosmochemistry*. PhD Thesis, The University of Manchester (United Kingdom).

Williams N. H., Fehr M. A., Parkinson I. J., Mandl M. B. and Schönbächler M. (2021) Titanium isotope fractionation in solar system materials. *Chem. Geol.* **568**, 120009.

Wombacher F., Eisenhauer A., Heuser A. and Weyer S. (2009) Separation of Mg, Ca and Fe from geological reference materials for stable isotope ratio analyses by MC-ICP-MS and double-spike TIMS. *J. Anal. At. Spectrom.* **24**, 627–636.

Woodhead J. (2002) A simple method for obtaining highly accurate Pb isotope data by MC-ICP-MS. *J. Anal. At. Spectrom.* **17**, 1381–1385.

Woosley S. E. and Weaver T. A. (1995) *The evolution and explosion of massive Stars II: Explosive hydrodynamics and nucleosynthesis*., Lawrence Livermore National Lab., CA (United States).

Workman R. K. and Hart S. R. (2005) Major and trace element composition of the depleted MORB mantle (DMM). *Earth Planet. Sci. Lett.* **231**, 53–72.

Wu C. C. and Mason T. O. (1981) Thermopower measurement of cation distribution in magnetite. *J. Am. Ceram. Soc.* **64**, 520–522.

Wu H., He Y., Bao L., Zhu C. and Li S. (2017) Mineral composition control on inter-mineral iron isotopic fractionation in granitoids. *Geochim. Cosmochim. Acta* **198**, 208–217.

Yang L. (2009) Accurate and precise determination of isotopic ratios by MC-ICP-MS: A review. *Mass Spectrom. Rev.* **28**, 990–1011.

Young E. D. and Galy A. (2004) The isotope geochemistry and cosmochemistry of magnesium. *Rev. Mineral. Geochemistry* **55**, 197–230.

Young E. D., Galy A. and Nagahara H. (2002) Kinetic and equilibrium mass-dependent isotope fractionation laws in nature and their geochemical and cosmochemical significance. *Geochim. Cosmochim. Acta* **66**, 1095–1104.

Young E. D., Kuramoto K., Marcus R. A., Yurimoto H. and Jacobsen S. B. (2008) Mass-independent oxygen isotope variation in the solar nebula. *Rev. Mineral. Geochemistry* **68**, 187–218.

Young E. D., Manning C. E., Schauble E. A., Shahar A., Macris C. A., Lazar C. and Jordan M. (2015) High-temperature equilibrium isotope fractionation of non-traditional stable isotopes: Experiments, theory, and applications. *Chem. Geol.* **395**, 176–195.

Zellmer G., Turner S. and Hawkesworth C. (2000) Timescales of destructive plate margin magmatism: new insights from Santorini, Aegean volcanic arc. *Earth Planet. Sci. Lett.* **174**, 265–281.

Zhang J., Dauphas N., Davis A. M. and Pourmand A. (2011) A new method for MC-ICPMS measurement of titanium isotopic composition: Identification of correlated isotope anomalies in meteorites. *J. Anal. At. Spectrom.* **26**, 2197–2205.

Zhao X., Tang S., Li J., Wang H., Helz R., Marsh B., Zhu X. and Zhang H. (2020) Titanium isotopic fractionation during magmatic differentiation. *Contrib. to Mineral. Petrol.* **175**, 1–16.

List of Electronic Appendices

The following list of electronic appendices containing all the data reported in this thesis is listed below and can be accessed using the following link: https://github.com/lhoare-geo/Liam-Hoare-Cardiff-University-2021-Ti-Isotope-Thesis-Appendices.git

- Appendix E1 – Compilation of Titanium isotope compositions of geo-reference materials
- Appendix E2 – Titanium isotope, major and trace element compositions of magmatic differentiation suites from Chapter 3.
- Appendix E3 – Mineral Chemistry for Fe-Ti oxides and reference standards, along with Titanium isotope compositions for oxides, groundmass and glass, parameters used for fractional crystallisation models
- Appendix E4 – Titanium isotope, major and trace element compositions of Oman Ophiolite lava and dike samples from Chapter 5.